ADVANCES IN COPPER-BASED CHEMISTRY FOR RETRO DYE-SENSITIZED SOLAR CELLS AND EMERGING THIN-FILM MATERIALS IN OPTOELECTRONICS

By

Samhita Kaushik

A DISSERTATION

Submitted to
Michigan State University
in partial fulfillment of the requirements
for the degree of

Chemistry – Doctor of Philosophy

ABSTRACT

Copper complexes, being known to have interesting chemistry, are exploited as photosensitizers and redox shuttles in dye-sensitized solar cells (DSSCs). In the most successful example, using Cu(II/I)(tmby)₂ as a redox shuttle achieves a 13.7% power conversion efficiency (PCE) under 1 sun and 34% under 1000 lux. In these systems, however, base additives like 4-tert-butylpyridine (TBP) are shown to undergo ligand exchange reactions with certain Cu²⁺ centers, resulting in a loss of solution potential and hindering the exploitation of copper redox shuttles to their full potential. In this thesis, an investigation of a new class of copper complexes with sterically crowded ligands is discussed. Uniquely, showing the potential of these complexes to act simultaneously as chromophores and redox shuttles offers the possibility of dramatically higher efficiencies. The role of TBP in ligand exchange and redox reactions is examined, using cyclic voltammetry, UV-Vis absorption spectroscopy, and ¹H NMR measurements. In addition, describing the details of this reaction and how it maps onto dye-sensitized solar cell performance as both a chromophore and redox shuttle, along with future directions.

In the latter part of this thesis, a novel class of organic single-crystal thin films is explored, advancing the field of optoelectronics by developing highly ordered organic materials. Offering exceptional electronic and optical properties, these single-crystal organic solid crystals are positioned as promising candidates for a range of high-performance optical and electronic devices, paving the way for new applications in next-generation optoelectronic systems and impacting fields such as displays, sensors, and photonic circuits.

Copyright by SAMHITA KAUSHIK 2025 This thesis is dedicated to Ma, Deta and Megha. Thank you for always believing in me.

ACKNOWLEDGMENTS

I am immensely grateful to Tom (Dr. Thomas Hamann), whose mentorship has been invaluable to my growth as both a researcher and a person. His guidance, encouragement, and support through every part of this journey have been instrumental, and I thank him deeply for welcoming me into his group and for believing in me through both the highs and lows of research. Without his positivity and support, I may have lost sight of my dreams far too easily. I am certain I will carry the skills and traits I have learned from him throughout my life. If I ever have the opportunity to mentor someone, he is exactly the example I would strive to follow.

I would also like to thank my committee members for their guidance, which has helped me stay on course. I am thankful to the entire Hamann group, my research family. Special thanks to Austin for helping me kick-start my Ph.D. journey, and to Eric, Pin, Soumik, Xiaoyin, Femi, Chellammal, and Michael for being such supportive and inspiring peers.

I am incredibly thankful for my friends that I met at MSU, especially Hannah and Christina, for their unwavering support. Finally, my deepest gratitude goes to my family—my mom, dad, and sister—who patiently listened to my stories about chemistry and research despite having willingly chosen different paths. Their support through every part of these years has meant the world to me.

TABLE OF CONTENTS

Chapter 1: Introduction to Photovoltaics Research and Dye Sensitized Solar Cells	1
1.1 Motivation for Photovoltaics to Mitigate Energy Crisis	1
1.2 Evolution of DSSCs: A Historical Perspective	
1.3 Components and Mechanism of Dye-sensitized solar cells	
1.4 Challenges of DSSCs	
1.5 New photochemical conversion scheme	
REFERENCES	30
Chapter 2: Retro Cells	35
2.1 Background	
2.2 DSSCs with [Cu(dsbtmp) ₂] ^{+/2+}	
2.3 Retro Cells: Results and Discussion	
2.4 Conclusion	61
2.5 Materials	62
2.6 Synthesis	62
2.7 Device Fabrication	66
2.8 Instrumentation	67
2.9 Electrochemistry	68
2.10 Room Temperature Spectroscopy	68
2.11 Single Crystal X-Ray Crystallography	
2.12 Light harvesting efficiency (LHE)	
2.13 Cyclic voltammetry	
REFERENCES	76
Chapter 3: Charge Separation and Base Additives	79
3.1 Bases in DSSCs	
3.2 Retro cells and charge separation	
3.3 Future Directions	87
REFERENCES	89
Chapter 4: Determining Limiting Electron Transfer Processes in Retro Cells	92
4.1 Theory and Discussion	
4.2 Preparation of ZrO ₂ paste	107
4.3 Modification to photoanode fabrication	
4.4 Modification to sandwiching method	
4.5 Future directions	108
REFERENCES	112
Chapter 5: Charge Collection Efficiency, Recombination and Self Exchange Kinetics	116
5.1 Introduction.	
5.2 Measurement of self-exchange rate for copper complexes	
5.3 Reorganization Energy	
5.4 Future Work	
REFERENCES	

Chapter 6: BiVO ₄ - Liquid Junction Solar Cells	132
6.1 Introduction	132
6.2 Methodology	135
6.3 Results and Discussion	
6.4 Conclusion and Future Directions	144
REFERENCES	146
Chapter 7: Exploring 2D Organic Single Crystals: Properties, Synthesis, and Applications	
7.1 Introduction	
7.2 Solution Based Methods for crystal growth	
7.3 Motivation Behind the Work	156
7.4 Experimental and discussion	159
7.5 Conclusion	
7.6 Future Directions	173
REFERENCES	175
APPENDIX	180

Chapter 1: Introduction to Photovoltaics

Research and Dye Sensitized Solar Cells

1.1 Motivation for Photovoltaics to Mitigate Energy

Crisis

The global energy crisis represents one of the most pressing challenges of the 21st century, characterized by growing energy demand, dwindling fossil fuel reserves, and increasing concerns about climate change.^{1,2} In the past few decades, governments worldwide have made collective commitments to mitigate the progression of global warming. Despite heightened diplomatic efforts, the impacts of climate change are already evident, with projections indicating worsening conditions in the future.³

Through initiatives like the Kyoto Protocol and the Paris Agreement, nations have pledged to reduce greenhouse gas emissions. However, carbon dioxide levels in the atmosphere continue to escalate, leading to accelerated global warming. It is cautioned that if this trend persists unchecked, it could result in catastrophic environmental consequences, including substantial sea-level rise, unprecedented droughts and floods, and extensive biodiversity loss.³

Following the negotiation of the Paris accord in 2015, numerous countries party to the agreement have bolstered their climate objectives. This has been manifested through commitments to emission reductions and assistance for vulnerable nations in adapting to extreme weather events, as evidenced in the annual UN climate conferences, notably the Conference of the Parties (COP). Nevertheless, the non-attendance of key figures such as U.S. President Joe Biden and Chinese

President Xi Jinping at the COP28 summit in Dubai, UAE, has sparked concerns regarding the future climate commitments of the world's leading greenhouse gas emitters.³

The Paris Agreement stands as the most significant global climate accord to date, mandating all nations to establish emission reduction targets, known as nationally determined contributions (NDCs).³ These targets are aimed at preventing global average temperatures from surpassing 2°C above preindustrial levels, with endeavors to limit the increase to 1.5°C.⁴ Additionally, the agreement strives for achieving global net-zero emissions, wherein the amount of greenhouse gases emitted is balanced by removal from the atmosphere, by the latter half of the century. This concept, also referred to as climate neutrality or carbon neutrality, is pivotal in mitigating further climate disruption.

Analysis of ice core data reveals that the Earth's average temperature is presently increasing at a rate unprecedented in the past eight hundred thousand years. Scientists attribute this phenomenon primarily to human activities over the last century and a half, notably the combustion of fossil fuels and widespread deforestation. These activities have significantly amplified the concentration of heat-trapping greenhouse gases, particularly carbon dioxide, in the atmosphere, resulting in accelerated global warming.

In this context, the adoption of renewable energy sources, particularly solar energy, has emerged as a pivotal strategy to mitigate the impacts of the energy crisis and transition towards a sustainable energy future. It has emerged as a promising solution to address the global challenges of climate change, energy security, and environmental sustainability. As the world transitions towards a low-carbon future, renewable solar energy research plays a crucial role in driving innovation, improving efficiency, and reducing costs associated with solar technologies. The immense potential of solar energy is highlighted by the fact that the sunlight reaching the Earth's surface in

just one hour could satisfy global energy needs for an entire year.⁵ At the forefront of solar energy technologies are silicon-based solar cells, which currently dominate the photovoltaic (PV) market, constituting approximately 93% of total PV installations⁵. These highly efficient PV devices, based on crystalline silicon, have achieved remarkable efficiencies, reaching up to 26.7%,⁵ closely approaching the theoretical efficiency limit of 31% proposed by Shockley and Queisser in 1961 (Figure 1.1). Figure 1.2 shows some of the efficiencies of different research cells. The report is maintained by NREL.

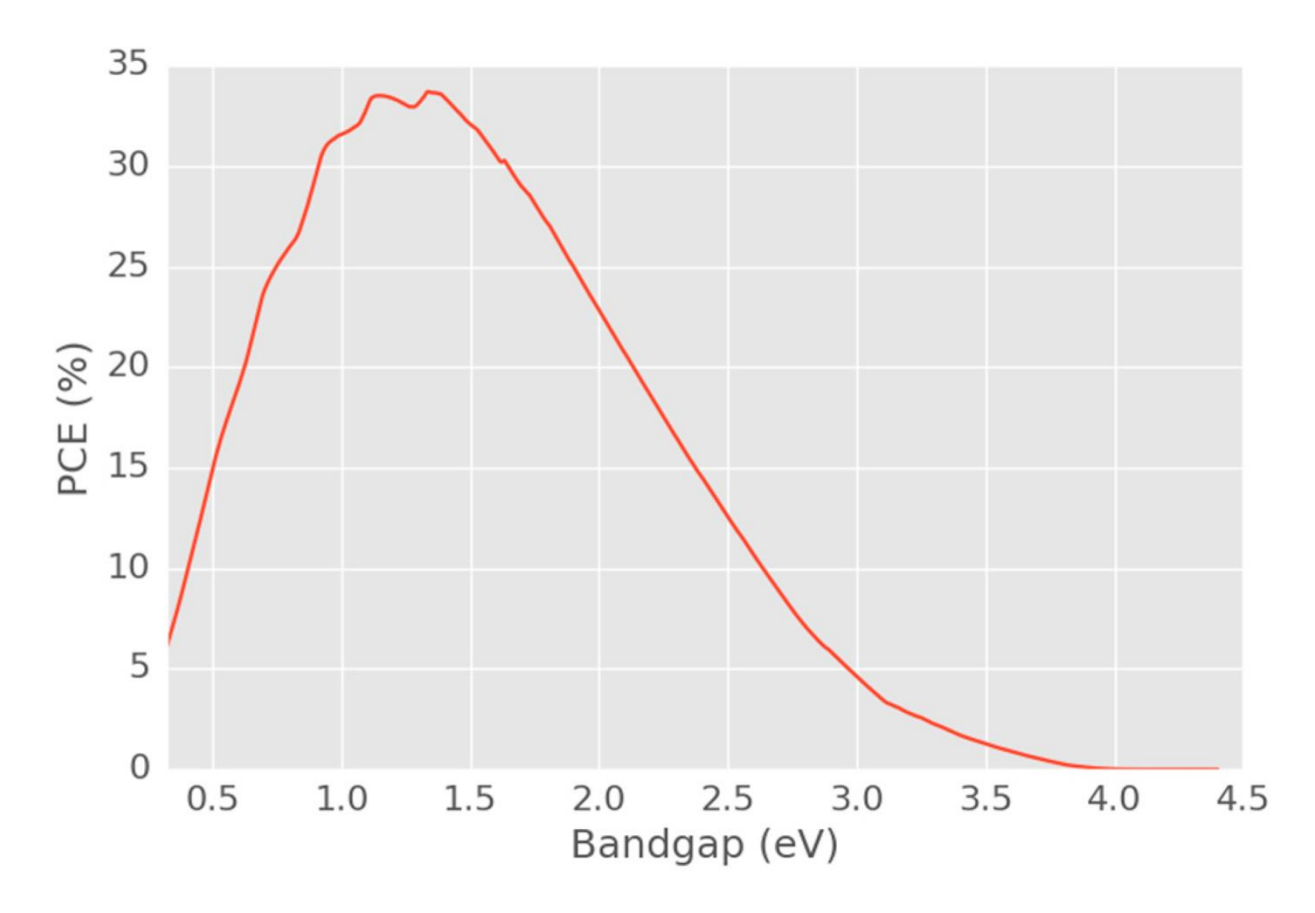


Figure 1.1: Shockley–Queisser limit at 1.2 eV which is 33.7%.

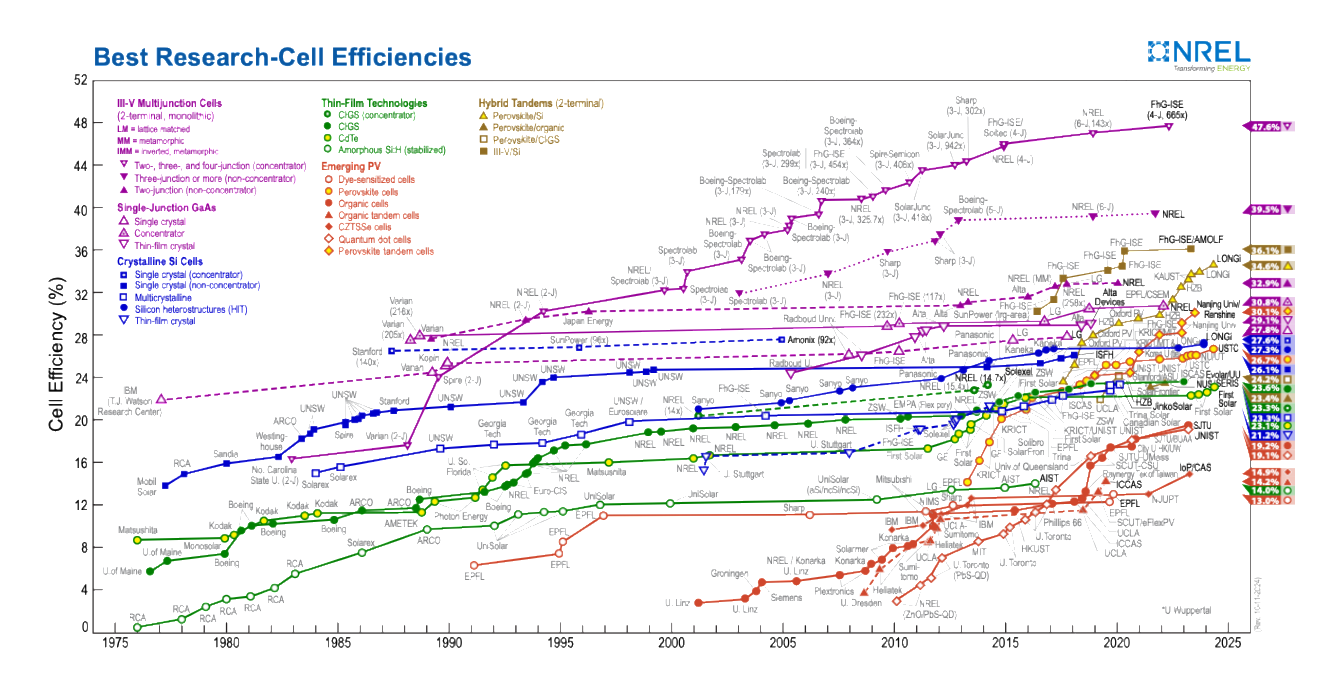


Figure 1.2: NREL's chart of the highest confirmed conversion efficiencies for research cells for a range of photovoltaic technologies, plotted from 1976 to the present.

PV devices directly convert sunlight into electricity without the need for combustion or moving parts, making them highly versatile and applicable in various environments. However, the production of silicon-based solar cells necessitates extremely pure silicon, obtained through costly high-temperature and high-vacuum processes. These constraints have spurred the exploration of alternative PV technologies utilizing low-cost materials and fabrication methods. Among these alternatives, Dye-Sensitized Solar Cells (DSSCs) have emerged as a promising contender.

DSSCs offer several advantages over traditional silicon-based solar cells. They can be fabricated using cost-effective techniques, enabling large-scale production.^{7,8} Moreover, DSSC fabrication processes are compatible with roll-to-roll techniques, facilitating the creation of large-area devices on flexible substrates, including textiles and paper. These characteristics make DSSCs suitable for applications in wearable electronics and building-integrated photovoltaics.^{5,6,9}

Another notable advantage of DSSCs is their semi-transparency and ability to be produced in various colors. This feature, coupled with their flexibility, enhances their appeal for architectural

integration into various surfaces beyond conventional rooftops. Furthermore, DSSCs exhibit exceptional performance under indoor lighting conditions, achieving efficiencies of up to 28.9% under 1000 lux illumination, making them suitable for powering small electronic devices autonomously. ^{10,11}

While silicon-based solar cells continue to dominate the PV market, the emergence of DSSCs presents a compelling alternative with distinct advantages, including cost-effectiveness, flexibility, and high performance under various conditions. Continued research and development in this field hold the promise of further advancing solar energy utilization and accelerating the transition towards a sustainable energy future.

1.2 Evolution of DSSCs: A Historical Perspective

Photosensitization with the help of a dye is a technique originating from early silver halide studies. ^{12,13} It became a robust field of research with profound implications for modern solar cell technology. Moser first observed sensitization of a semiconductor under sub-band gap illumination while experimenting with silver halides coated in erythrosine back in 1887. ¹⁴ Building upon Moser's observations, Gurney and Mott proposed in 1927 a mechanism for dye-sensitization of crystalline semiconductors involving electron transfer from the excited state of the sensitizer into the conduction band of the semiconductor. ¹⁵ This notion was later validated in 1968 by Gerischer, who conducted electrochemical studies confirming electron transfer upon illumination of dyes interfaced with semiconductors such as ZnO. ¹⁶ It was discovered that organic dyes in electrochemical cells could generate electricity when illuminated. Early experiments involved extracting chlorophyll from spinach, leading to the synthesis of chlorophyll-sensitized zinc oxide electrodes in 1972. ¹⁷

However, early attempts at dye-sensitized photoelectrochemical cells encountered limitations. These cells relied on the diffusion of dissolved sensitizers to the semiconductor surface for electron injection, resulting in low photocurrents due to the majority of photoexcited dyes relaxing back to their ground state before injection could occur. To address this, researchers began functionalizing dyes with substituents allowing them to anchor to the semiconductor surface, thereby improving injection yields. Osa and Fujihira pioneered covalent linking of dyes to semiconductors in 1976, but despite this advancement, low photocurrents persisted due to poor light absorption by the monolayer of dye.¹⁸

Transition metal sensitizers emerged as a pivotal development in dye-sensitized solar cell (DSSC) technology. Initial reports utilizing complexes like [Ru(bpy)₃]²⁺ showcased promising properties yet faced challenges such as diffusion constraints and poor internal conversion efficiencies.¹⁹ Subsequent research focused on optimizing the porosity of electrodes, culminating in the discovery of nanoporous titanium dioxide. A breakthrough occurred in 1985 when Grätzel and Brian O' Regan sensitized a polycrystalline anatase TiO₂ electrode with [Ru(bpy)₂(dcbpy)]²⁺, alongside a hydroquinone "supersensitizer," achieving remarkable external quantum efficiencies and injection yields.^{20–22} They termed these devices "dye-sensitized solar cells (DSSCs)" or "Grätzel cells" and worked on them in UC Berkeley and further developed them at Ecole Polytechnique Fédèrale de Lausanne (EPFL). Subsequent refinements, including enhancing surface roughness and modifying the regenerating molecule, led to notable improvements in incident photo-to-current efficiencies and power conversion efficiencies. This helped in increasing efficiencies to 10% by 1993.²³ The subsequent decades saw incremental improvements, with ruthenium-based sensitizers and iodide/triiodide redox shuttles dominating until 2010 when alternative redox shuttles emerged.

Thus, the journey of DSSCs intersects with the broader history of photovoltaics, tracing back to Edmond Becquerel's observations in 1839. Subsequent investigations by Vogel, Moser, and Gerischer laid the groundwork for understanding sensitization mechanisms and charge separation in semiconductors. Despite early progress, practical challenges persisted, including limited light harvesting efficiency and planar electrode configurations.

Organic sensitizers coupled with outer-sphere redox shuttles pushed efficiencies beyond 15%, but progress stagnated below 16% in recent years.^{24,25} Understanding fundamental processes within DSSCs and addressing limitations are critical for unlocking their full potential and achieving higher efficiencies.

1.3 Components and Mechanism of Dye-sensitized solar cells

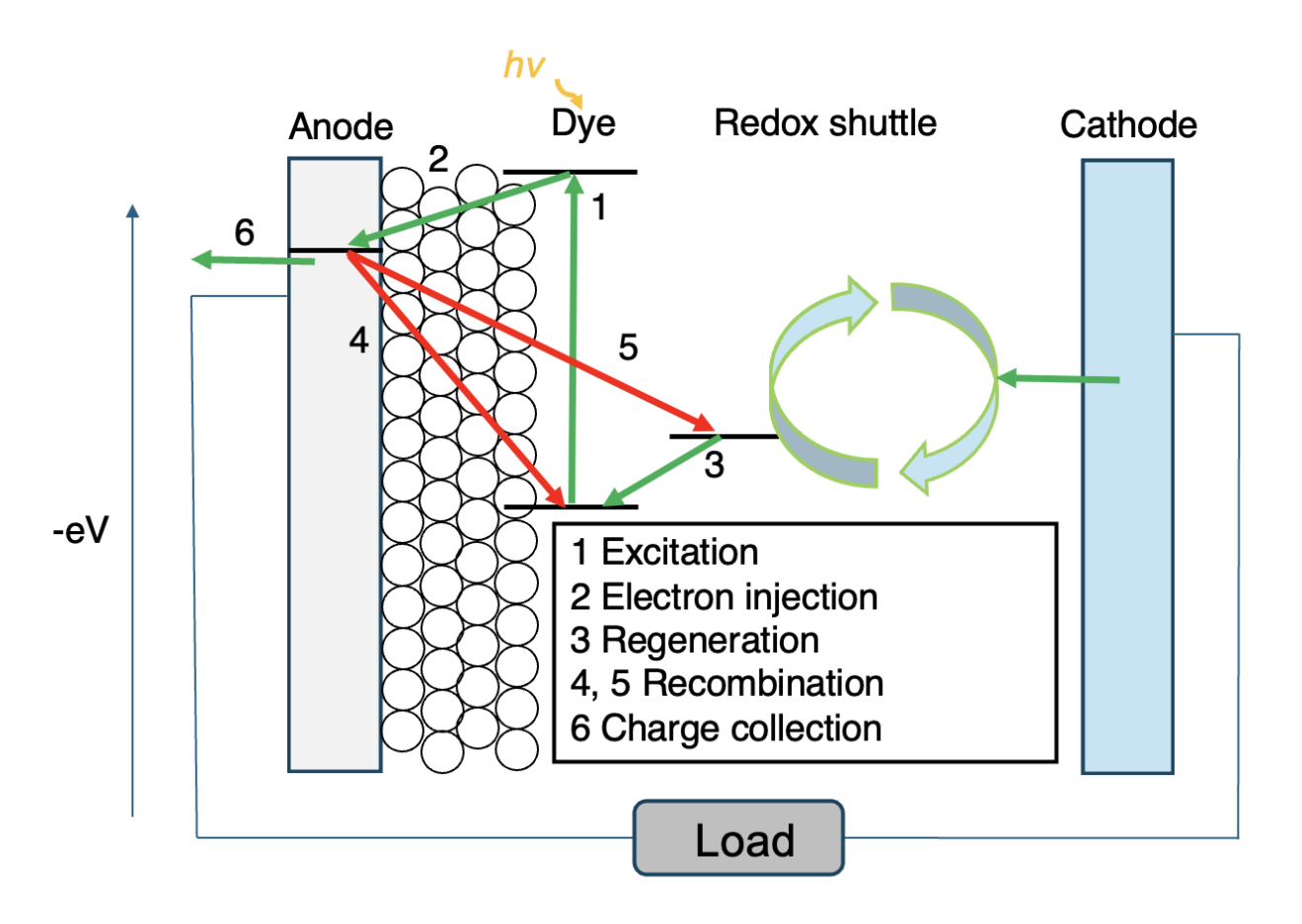


Figure 1.3: Schematic of the basic components and operating principles of a DSSC.

DSSCs comprise several key components that work together to harness sunlight and convert it into electrical energy. These components include the semiconductor electrode, sensitizing dye, electrolyte, counter electrode, and conductive substrate. Each component plays a crucial role in the overall functioning of the DSSC, contributing to its efficiency and performance.

Semiconductor Electrode:

The semiconductor electrode serves as the substrate for anchoring the sensitizing dye molecules and facilitating charge transport within the DSSC. Commonly used semiconductor materials include titanium dioxide (TiO₂) and zinc oxide (ZnO), chosen for their favorable electronic properties, stability, and abundance. The semiconductor electrode is typically in the form of a porous film or nanoparticle layer, providing a large surface area for dye adsorption and maximizing light absorption.

Sensitizing Dye:

The sensitizing dye is a crucial component of DSSCs responsible for absorbing photons from incident sunlight and initiating the generation of charge carriers. Sensitizing dyes are typically organic molecules or metal complexes with conjugated pi-electron systems, allowing for efficient light absorption and charge transfer. Commonly used sensitizing dyes include ruthenium-based complexes, porphyrins, phthalocyanines, and organic dyes. The choice of sensitizing dye influences the spectral absorption properties and light-harvesting efficiency of the DSSC.

Electrolyte:

The electrolyte facilitates ion transport within the DSSC, maintaining charge balance and enabling efficient charge transfer at the electrode-electrolyte interface. Liquid electrolytes based on organic solvents or ionic liquids are commonly employed in DSSC configurations. The electrolyte also plays a critical role in preventing charge recombination and ensuring the stability and longevity of the DSSC. Additionally, the electrolyte may contain redox shuttle species that mediate the transfer of electrons between the semiconductor electrode and the counter electrode.

Counter Electrode:

The counter electrode completes the electrical circuit of the DSSC and catalyzes the reduction of the redox shuttle species present in the electrolyte. Commonly used materials for the counter electrode include platinum, carbon, and other conductive materials with high catalytic activity and stability. The counter electrode serves as the site for the reduction reactions that regenerate the sensitizing dye molecules and complete the charge transfer process within the DSSC.

Light Absorption in DSSCs

The first step in the operation of DSSCs involves the absorption of photons from incident sunlight by the sensitizing dye molecules immobilized on the surface of the semiconductor electrode. This process is critical as it initiates the generation of charge carriers within the device. The choice of sensitizing dye plays a crucial role in determining the spectral absorption properties and light-harvesting efficiency of the DSSC.

Sensitizing dyes used in DSSCs typically possess a complex molecular structure consisting of a light-absorbing chromophore group conjugated with electron-donating and electron-withdrawing substituents. The chromophore group, often a metal complex or an organic dye molecule, is responsible for absorbing photons from sunlight. Commonly employed sensitizing dyes include ruthenium-based complexes, porphyrins, phthalocyanines, and organic dyes.

Upon absorption of a photon, the sensitizing dye undergoes a transition from its ground state to an excited state. This transition is characterized by the promotion of an electron from the highest occupied molecular orbital (HOMO) to the lowest unoccupied molecular orbital (LUMO) or higher energy orbitals within the molecular structure of the dye. The energy of the absorbed photon must exceed the bandgap of the semiconductor material to facilitate this transition effectively. The absorption spectrum of the sensitizing dye determines the range of wavelengths of incident sunlight that can be absorbed, thereby influencing the overall efficiency of the DSSC. Sensitizing dyes are typically chosen or designed to have absorption spectra that overlap with the solar spectrum, maximizing light absorption and enhancing the device's power conversion efficiency.

Charge Generation and Separation

Following light absorption, the sensitizing dye enters an excited state characterized by the presence of an electron in a higher energy orbital. This photoexcited state of the dye serves as the precursor for charge carrier generation within the DSSC.

Upon photoexcitation, the excited-state dye undergoes a series of rapid internal processes, including vibrational relaxation and intersystem crossing, leading to the formation of a long-lived charge-separated state. In this state, an electron is transferred from the excited dye molecule to the conduction band of the semiconductor electrode, leaving behind a positively charged dye molecule or "hole" in the ground state.

The mechanism of charge separation in DSSCs is governed by the relative energy levels of the dye molecules and the semiconductor electrode. The energy of the excited-state dye must exceed the conduction band edge of the semiconductor material for efficient electron transfer to occur. Additionally, the energetics of the dye-semiconductor interface play a crucial role in facilitating charge separation and preventing charge recombination.

The charge-separated state generated upon photoexcitation represents the primary mechanism by which DSSCs convert photon energy into electrical energy. Efficient charge separation is essential for maximizing the photocurrent and overall efficiency of the device.

Charge Transport and Collection

Once generated, the free electrons in the conduction band of the semiconductor electrode migrate through the material under the influence of an external electric field. Simultaneously, the positively charged dye molecules or "holes" diffuse through the electrolyte towards the counter electrode.

The migration of electrons through the semiconductor electrode is facilitated by the electronic band structure of the material, which allows for efficient transport of charge carriers. In DSSCs,

semiconductor materials with high electron mobility and conductivity, such as titanium dioxide (TiO₂) and zinc oxide (ZnO), are commonly employed to facilitate rapid charge transport.

Meanwhile, at the counter electrode, the electrons are consumed in reduction reactions facilitated by the redox shuttle present in the electrolyte. The redox shuttle acts as a mediator, facilitating the transfer of electrons from the semiconductor electrode to the counter electrode, where they participate in reduction reactions, completing the charge transfer circuit.

The overall efficiency of charge transport and collection in DSSCs is influenced by factors such as the morphology and surface properties of the semiconductor electrode, the composition and properties of the electrolyte, and the kinetics of electron transfer at the electrode-electrolyte interface. Optimizing these factors is essential for maximizing the efficiency and performance of DSSCs.

Charge Recombination and Loss Mechanisms

Despite the efforts to minimize charge recombination and loss mechanisms, some fraction of the photoexcited electrons and holes recombine before reaching the respective electrodes, leading to a decrease in the overall efficiency of the DSSC. In DSSCs, recombination is a critical loss mechanism where photogenerated charge carriers do not contribute to useful electrical power. One pathway involves the excited dye molecule, which, before injecting an electron into the TiO₂ conduction band, can decay back to its ground state either radiatively (emitting light) or nonradiatively (dissipating energy as heat). This process prevents electron injection and reduces efficiency. Once an electron is injected into the TiO₂, it can recombine via two primary routes. The first is recombination with the oxidized dye molecule. In this case, the injected electron travels back to the dye, neutralizing it before the dye can be regenerated by the redox mediator. This direct recombination competes with the desired electron transport through the TiO₂ network to the

external circuit. The second recombination pathway involves the injected electron reacting with the oxidized form of the redox mediator. This process, referred to as recombination in the electrolyte, bypasses the dye regeneration step and wastes the energy that would otherwise drive the external circuit.

Both recombination pathways reduce the efficiency of DSSCs by shortening the lifetime of photoinjected electrons and lowering the achievable photocurrent. Strategies to mitigate these losses include optimizing dye design, surface passivation of TiO₂ to reduce recombination sites, and engineering the redox mediator to suppress electron recombination rates. Various strategies have been proposed to mitigate charge recombination and loss mechanisms in DSSCs, including the design of semiconductor electrodes with optimized morphology and surface properties, the use of redox shuttles with fast kinetics and low recombination rates, and the development of novel sensitizing dyes with improved charge separation properties. Additionally, advances in device engineering and fabrication techniques have contributed to minimizing losses and enhancing the efficiency of DSSCs.

TiO₂ has a presence of surface defects. Among these, oxygen vacancies are the most common and significantly influence the electronic properties of the material. Oxygen vacancies occur when an oxygen atom is removed from the lattice, leaving behind two unpaired electrons. These electrons, initially part of the O 2p orbital, are transferred into the conduction band formed by Ti 3d orbitals. The presence of these vacancies creates localized donor-like electronic states, which lie just below the conduction band edge. These states can trap electrons, altering the electronic structure and introducing additional recombination pathways.

For a traditional DSSCs with TiO₂ and iodide/ triiodide as redox shuttles, conditions of recombination have been well studied. Regeneration of the sensitizer by iodide plays a critical role

in preventing the recombination of conduction band electrons with the oxidized dye in DSSCs. During this process, iodide ions (Γ) donate electrons to the oxidized dye, regenerating its ground state and enabling continuous photon absorption. The oxidation of iodide results in the formation of triiodide (Γ) ions, which diffuse a short distance (less than 50 μ m) through the electrolyte to the cathode. The cathode, coated with a thin layer of platinum catalyst, facilitates the reduction of Γ 0 back to Γ 1, completing the regenerative cycle.

Under standard working conditions, as detailed in a study by O'Regan and Durrant, the system operates with specific concentrations and behaviors. For instance, each TiO₂ particle contains about 10 electrons on average, but more than 90% of these electrons are trapped rather than in the conduction band. An 18 nm diameter TiO₂ particle hosts approximately 600 dye molecules, with each molecule absorbing a photon once per second, resulting in an electron injection flux of around 600 electrons per second into the particle. Despite this flux, under operational conditions, only one dye molecule per 150 TiO₂ particles exists in an oxidized state at any given time.

The electrolyte composition and solute distribution are also finely balanced. In the pore volume around a single TiO₂ particle, there are typically about 1000 I⁻ ions and 200 I₃⁻ ions, with the overall solute volume fraction in the mesoporous system ranging from 10–20%. The concentration of free iodine (I₂) is exceptionally low, less than 1 μM, corresponding to approximately one free iodine molecule for every 10,000 TiO₂ particles. These parameters collectively highlight the intricate balance of charge transport and regeneration dynamics in DSSCs, critical for their efficiency and functionality.

In order to understand the electron transfer processes and the loss mechanisms in DSSCs better, it is vital to introduce Marcus theory that explains a lot of the kinetics in DSSCs. Marcus theory provides a framework to understand electron transfer reactions, describing the interplay of

thermodynamics, molecular reorganization, and solvent dynamics. 26,27 It models how electrons transfer between a donor and an acceptor, either within a molecule or between molecules, and how this process is influenced by energy changes and system reorganization. The driving force for the reaction is characterized by the free energy change (ΔG^0), representing the thermodynamic favorability. A more negative ΔG^0 corresponds to a more energetically favorable reaction.

Central to Marcus theory is the concept of reorganization energy (λ), which accounts for structural and environmental changes required for electron transfer. These changes include molecular adjustments (inner-sphere reorganization) and rearrangement of surrounding solvent molecules (outer-sphere reorganization). The total reorganization energy represents the energy required to distort the system to a configuration compatible with the charge distribution of the products. The activation energy (E_a) for the electron transfer reaction, which determines the rate, depends on the balance between ΔG^0 and λ . $^{26,28-30}$ Marcus derived an expression for E_a as:

This equation shows that E_a is minimized when ΔG^0 is close to - λ , where the reaction becomes most efficient.

The potential energy surfaces of the reactants and products in Marcus theory are approximated as parabolas due to the harmonic nature of molecular vibrations. Electron transfer occurs when these parabolas intersect, corresponding to the transition state where the energies of the donor and acceptor are equal. The rate of electron transfer (k_{ET}) is given by:

$$k_{ET} = A \exp(-E_a / (k_B T))$$

 $E_a = ((\lambda + \Delta G^0)^2) / (4\lambda)$

where A is the pre-exponential factor representing electronic coupling between the donor and acceptor, k_B is Boltzmann's constant, and T is the temperature. This equation shows that k_{ET}

depends exponentially on the activation energy, highlighting the importance of minimizing E_a for faster electron transfer.

A significant prediction of Marcus theory is the inverted region, which occurs when ΔG^o becomes more negative than $-\lambda$. In this regime, despite the reaction being highly favorable, the rate of electron transfer decreases because the energy barrier (E_a) grows again, as the system must distort more extensively to reach the transition state. This counterintuitive result was experimentally confirmed and underscores the balance between driving force and reorganization energy.

Marcus theory can be extended to include the effect of electronic coupling, which describes how strongly the donor and acceptor are electronically connected. This coupling is essential in determining the actual rate of electron transfer. The rate constant for electron transfer (k_{ET}) including electronic coupling is given by:

$$k_{ET} = |H_{DA}|^2 / \hbar \sqrt{(\pi / \lambda k_B T)} \exp[-(\lambda + \Delta G^0)^2 / (4 \lambda k_B T)]$$

Here, $|H_{DA}|$ is the electronic coupling matrix element, representing the strength of the interaction between the donor and acceptor. \hbar is the reduced Planck's constant, λ is the reorganization energy (including both inner-sphere and outer-sphere contributions), k_B is Boltzmann's constant, T is the temperature in Kelvin, and ΔG^0 is the free energy change of the reaction. The inclusion of $|H_{DA}|$ highlights that the rate of electron transfer is proportional to the square of the coupling strength. A higher $|H_{DA}|$ leads to faster electron transfer, as it facilitates efficient overlap of the donor and acceptor electronic states. This equation also shows that the electron transfer rate depends on the thermodynamics (ΔG^0), the system's reorganization energy (λ), and the temperature. For weak coupling systems (non-adiabatic), this equation is especially relevant, as $|H_{DA}|$ becomes the

bottleneck for the reaction. In contrast, in strong coupling systems (adiabatic), the rate is determined more by the energy landscape than by the coupling strength.

The recombination and regeneration rates for the various dyes with cobalt polypyridine redox couples were determined using transient absorption spectroscopy on a nanosecond laser setup and were analyzed by Marcus theory. They are anticipated to occur within the Marcus inverted region, as the driving force for recombination exceeds the reorganization energy expected for the process in various sensitizers bound to titanium dioxide. Reorganization energies around 1 eV have been estimated for several DSSC dyes. When these dyes are bound to TiO2, the reorganization energy is reduced. In this paper, Marcus theory was also utilized to describe the regeneration of the oxidized dye molecules by cobalt(II) complexes. The theory provided a framework to understand the electron transfer dynamics between the dye molecules and the cobalt(II) complexes, explaining the factors that influence the regeneration process, including reorganization energies and the driving force for the reaction.

The following figure summarizes the various kinetics in DSSCs.³⁴

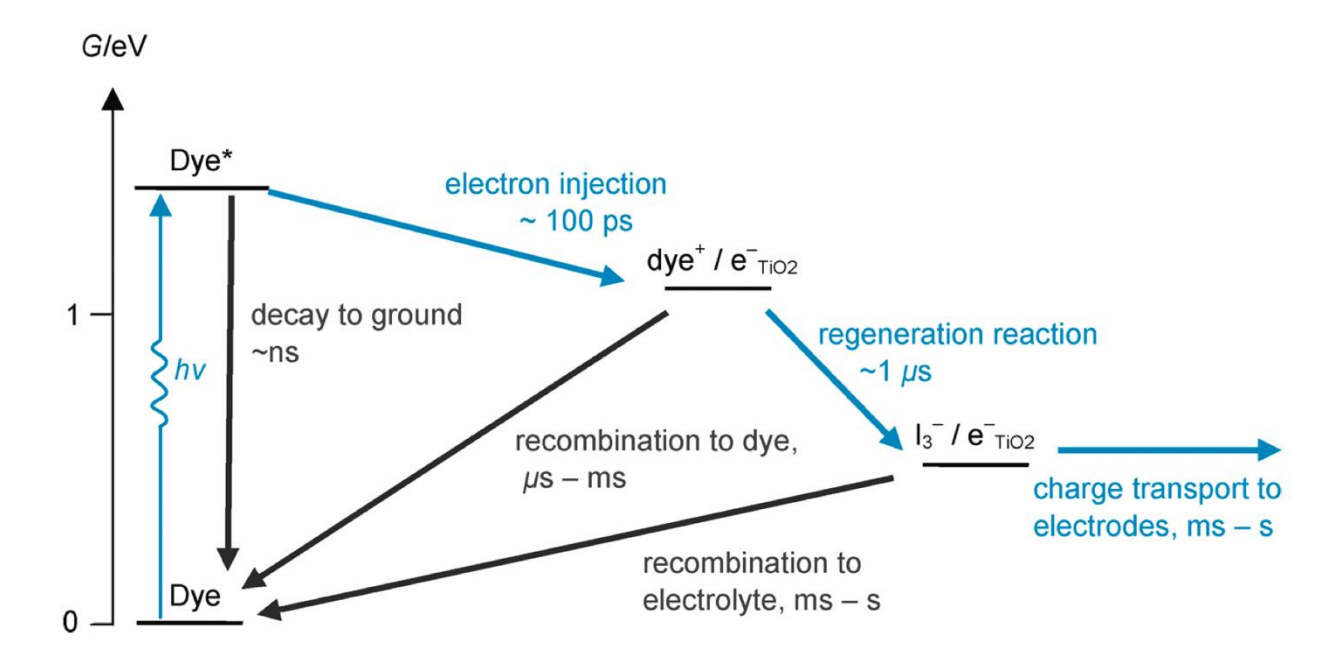


Figure 1.4: Illustration of the kinetics of DSSC function and has been reproduced from the reference 34.³⁴

Although the figure provides a general overview of the kinetics timescale in DSSCs, it does not fully represent the actual processes occurring within the cell. In fact, recent studies have shown results that contradict this depiction. A study by Jouko Korppi-Tommol et al. showed that in a solvent, electron injection from two different dyes occurs on a femto- to picosecond timescale, whereas in the electrolyte, the process slows considerably, extending into the nanosecond timescale. Another paper presents femtosecond to nanosecond transient absorption (TA) data on electron injection in DSSCs fabricated with low volatility, commercially relevant electrolytes, both with and without added lithium. The results span an extended time range (300 fs–6.3 ns) and an extended wavelength range (800–1400 nm) for both N719 and C106 dyes. Kinetics were measured on both TiO₂ and noninjecting ZrO₂. Using the latter, the spectra and absorption coefficient of N719* across the wavelength range were determined. An isosbestic point was observed in the TA spectra on TiO₂ near 900 nm for all cells, present from less than 1 ps to more than 1 ns. The paper shows how measurements near this isosbestic point can give a false impression of uniformly

femtosecond injection dynamics in DSSCs. A comparison of dynamics measured at 1200 nm with mid-IR transient absorption measured at 5100 nm confirms that a majority of the electron injection occurs slowly (>10 ps) in these commercially relevant cells. This indicates that the timescale of electron processes in dye-sensitized solar cells (DSSCs) is strongly influenced by the specific combination of components used in the cell. The interaction between the dye, semiconductor material, and electrolyte plays a crucial role in determining how quickly electrons are injected into the conduction band of the semiconductor. Variations in factors such as dye type, electrolyte composition, and the presence of additives like lithium can lead to significant differences in the electron injection dynamics. As shown in the study, the measured electron injection timescales varied depending on these factors, highlighting the importance of optimizing each component to achieve the desired performance in DSSCs. This variability emphasizes that the overall electron transfer process cannot be understood in isolation but must consider the combined effect of all materials and additives used in the cell.³⁴⁻³⁶

Semiconductor Electrode Preparation:

The semiconductor electrode serves as the foundation of the DSSC, providing a platform for anchoring sensitizing dye molecules and facilitating charge transport. One of the most commonly used materials for semiconductor electrodes is titanium dioxide (TiO₂), known for its favorable electronic properties and stability. The fabrication of TiO₂ electrodes typically begins with the deposition of a thin film or layer onto a conductive substrate.

One method for preparing TiO₂ electrodes is the doctor-blade technique, which involves spreading a paste containing TiO₂ nanoparticles onto a conductive substrate, such as fluorine-doped tin oxide (FTO) glass, using a doctor blade or similar apparatus. The substrate is then heated to anneal the TiO₂ film and remove any residual solvents, resulting in a porous and uniform electrode structure.

Alternatively, TiO₂ electrodes can be fabricated using screen printing, spray coating, or spin coating techniques, each offering unique advantages in terms of film thickness control, homogeneity, and scalability. Regardless of the fabrication method, the goal is to achieve a porous and high-surface-area electrode structure that allows for efficient dye adsorption and charge transport.

Dye Adsorption:

Once the semiconductor electrode is prepared, the next step in DSSC fabrication involves immobilizing sensitizing dye molecules onto its surface. The choice of sensitizing dye is critical, as it determines the spectral absorption properties and light-harvesting efficiency of the DSSC. Commonly used sensitizing dyes include ruthenium-based complexes, porphyrins, phthalocyanines, and organic dyes.

Sensitizing dye molecules are typically dissolved or dispersed in a suitable solvent or electrolyte solution, forming a dye bath or suspension. The semiconductor electrode is then immersed or coated with the dye solution, allowing the dye molecules to adsorb onto its surface through coordination or chemical bonding interactions. The duration of dye immersion or coating, as well as the concentration of dye solution, can influence the amount and distribution of dye molecules on the electrode surface.

To enhance dye adsorption and coverage, various techniques such as vacuum infiltration, soaking, or thermal treatment may be employed. Additionally, strategies such as co-sensitization, where multiple dye molecules are used in combination, can be explored to broaden the spectral absorption range and improve light harvesting efficiency.

Electrolyte Preparation:

The electrolyte plays a crucial role in DSSC operation, facilitating ion transport, maintaining charge balance, and mediating charge transfer processes within the device. Liquid electrolytes based on organic solvents or ionic liquids are commonly used in DSSC configurations due to their favorable properties such as high ionic conductivity and compatibility with sensitizing dyes.

The preparation of DSSC electrolytes typically involves mixing suitable redox shuttle species, such as iodide/triiodide (I-/I3-) or cobalt-based complexes, with a solvent or electrolyte solution. The redox shuttle species undergo reversible redox reactions, shuttling electrons between the semiconductor electrode and the counter electrode during device operation.

Additional components such as electrolyte additives, co-solvents, and stabilizers may be included to optimize the electrolyte composition and enhance device performance. Careful consideration must be given to the choice of electrolyte components to ensure compatibility with other DSSC materials and minimize degradation over time.

Counter Electrode Fabrication:

The counter electrode serves as the site for reduction reactions that regenerate sensitizing dye molecules and complete the charge transfer process within the DSSC. Commonly used materials for the counter electrode include platinum, carbon, and conductive polymers, chosen for their high catalytic activity and stability.

The fabrication of the counter electrode typically involves depositing a thin film or layer of the counter electrode material onto a conductive substrate, such as FTO glass or stainless steel. Techniques such as sputtering, thermal evaporation, or electrodeposition may be employed to achieve the desired electrode morphology and thickness.

Once fabricated, the counter electrode is often treated or modified to enhance its catalytic activity and promote efficient charge transfer at the electrode-electrolyte interface. For example, platinum electrodes may be annealed or subjected to surface treatments to increase their surface area and improve catalytic performance.

Assembly and Sealing:

The final step in DSSC fabrication involves assembling the various components into a functional solar cell and sealing the device to prevent moisture ingress and electrolyte leakage. The semiconductor electrode, sensitizing dye-coated side facing outward, is sandwiched with the counter electrode, separated by a spacer to maintain a defined electrolyte volume.

The assembled DSSC is then sealed using a suitable encapsulation material or sealing method, such as thermoplastic sealing, epoxy resin encapsulation, or glass frit sealing. The sealing process ensures the long-term stability and durability of the DSSC by protecting sensitive components from environmental factors and preventing electrolyte evaporation or leakage.

1.4 Challenges of DSSCs

Some of the challenges faced by DSSCs despite being an important contender amongst photovoltaics are discussed below.

Stability and Durability:

Ensuring the stability and durability of DSSCs presents a significant challenge, particularly in harsh environmental conditions and prolonged operation. DSSCs are susceptible to degradation mechanisms such as dye desorption, electrolyte leakage, corrosion, and chemical degradation of components. Sensitizing dyes may degrade over time due to exposure to light, moisture, and temperature fluctuations, leading to reduced light absorption and device efficiency. Electrolyte instability can result in leakage, evaporation, or chemical reactions that degrade performance and

compromise device integrity. Semiconductor electrodes and counter electrodes may undergo corrosion or degradation under operating conditions, leading to decreased electron transport and catalytic activity. Improving stability requires the development of robust materials and interfaces, protective coatings, and encapsulation techniques to shield DSSCs from environmental factors and prevent degradation over time. Additionally, advancements in electrolyte formulation, redox shuttle chemistry, and device design may enhance stability and prolong device lifespan.

Scalability and Manufacturing:

Scaling up DSSC manufacturing to commercial production levels presents significant challenges in terms of cost, scalability, and reproducibility. Conventional fabrication techniques for DSSCs, such as doctor-blade coating, screen printing, and spray coating, may be limited in terms of throughput, uniformity, and cost-effectiveness. Achieving high-throughput and large-area deposition of semiconductor electrodes and sensitizing dyes while maintaining uniformity and performance remains a major hurdle. Additionally, ensuring reproducibility and consistency in device performance across large production batches is challenging due to variations in materials, processing conditions, and equipment. Developing scalable and cost-effective manufacturing processes, automation technologies, and quality control measures is essential for the commercialization and mass production of DSSCs. Integration with existing solar cell manufacturing infrastructure and supply chains may facilitate the adoption and scalability of DSSC technology in the renewable energy market.

Cost-Effectiveness and Competitiveness:

The cost-effectiveness and competitiveness of DSSCs relative to other solar cell technologies, particularly silicon-based photovoltaics, represent significant challenges in commercialization and market penetration. While DSSCs offer advantages such as low material costs, ease of fabrication,

and flexibility in design, they still face cost barriers associated with materials, fabrication, encapsulation, and durability. Achieving cost parity with conventional solar cells requires reducing material costs, optimizing fabrication processes, improving device efficiency and stability, and scaling up production volumes. Additionally, DSSCs must compete with established solar technologies in terms of performance, reliability, and bankability to gain market acceptance and attract investment. Overcoming cost and competitiveness challenges may require collaboration between academia, industry, and government to drive innovation, reduce barriers to entry, and accelerate the commercialization of DSSCs as a viable renewable energy solution.

Research by Tajamul Hussain Syed and Wei Wei provides insights into the manufacturing costs of DSSCs. For a reference DSSC module (shown in Table 1), the total manufacturing cost is estimated at USD 22.4 per m². This includes USD 16.5 per m² for materials like glass, frames, laminating films, junction boxes, and testing, along with USD 5.9 per m² for cell processing, which accounts for utilities, labor, equipment depreciation, and maintenance.³⁷

When compared to perovskite solar cells, the costs differ significantly. Perovskite cells have a processing cost of USD 8 per m² and material costs of USD 29 per m². Additionally, perovskite cells are more cost-effective in processing than other PV technologies like CIGS and CdTe, which have processing costs of USD 29 per m² and USD 27 per m², respectively.³⁷

Table 1: Reproduced from the journal article by Tajamul Hussain Syed and Wei Wei. This represents the cost distribution for various materials used in DSSCs³⁷

Component	Raw Material	Price (USD/kg)	Weight (g/m²)	Material Cost (USD/m ²)
Glass	3 mm Glass	0.8–1.1	7500	7.0000
FTO	FTO	550-900	1.790	1.2980
Counter Electrode	AC	0.60-5.50	40	0.0240
Counter Electrode	WS ₂	10–50	20	0.2000
Photo Electrode	TiO ₂	2–4	16	0.0320
Photo Electrode	N719 C ₅₈ H ₈₆ N ₈ O ₈ RuS ₂	2–5	4	0.0080
Electrolyte	lodine	20-50	0.45	0.0090
Electrolyte	Lithium iodide	12–20	0.15	0.0017
Electrolyte	4-tert-Butylpyridine C ₉ H ₁₃ N	7–8	1.68	0.0118
Electrolyte	$C_8H_{15}IN_2$	29–80	7.10	0.2058
Electrolyte	CH ₅ N ₃ CHNS	10–30	0.26	0.0026
Electrolyte	C ₅ H ₉ N	10–25	5.3	0.053
Electrolyte	CH ₃ CN	5–10	29.65	0.1482
Junction Box	-	-	-	7.500

Material Selection and Optimization:

The selection and optimization of materials represent a significant challenge in the development of DSSCs. Each component of the DSSC, including the semiconductor electrode, sensitizing dye, electrolyte, counter electrode, and conductive substrates, must be carefully chosen and tailored to maximize device performance. Semiconductor electrodes, commonly made of titanium dioxide (TiO₂) or zinc oxide (ZnO) nanoparticles, require high surface area, excellent electron transport properties, and stability under operational conditions. Sensitizing dyes need to exhibit efficient light absorption, charge separation, and redox properties while maintaining stability and compatibility with the semiconductor. The electrolyte must possess high ionic conductivity, stability, and redox shuttle capabilities to facilitate charge transport and prevent degradation. Counter electrodes must have high catalytic activity and stability to promote efficient reduction reactions. Additionally, conductive substrates should provide mechanical support and serve as

current collectors while being transparent to allow sunlight to reach the active components.

Achieving optimal performance requires a thorough understanding of material properties and interactions, as well as extensive experimentation and optimization.

Efficiency Enhancement:

Improving the efficiency of DSSCs remains a significant challenge in the field. While DSSCs have demonstrated relatively high efficiency compared to other thin-film solar cell technologies, such as organic photovoltaics (OPVs) and perovskite solar cells, they still lag behind conventional silicon-based solar cells. Enhancing efficiency requires addressing various factors, including light absorption, charge generation, separation, transport, and collection. Efforts to improve light absorption involve optimizing the spectral response of sensitizing dyes, increasing dye loading on semiconductor electrodes, and broadening the absorption spectrum to capture a wider range of sunlight. Improving charge generation and separation requires minimizing charge recombination losses and enhancing the lifetime of photoexcited states. Efficient charge transport and collection rely on optimizing the morphology and structure of semiconductor electrodes and reducing interface resistances. Additionally, strategies such as tandem or multi-junction DSSCs and integrating complementary photovoltaic materials may further enhance efficiency by utilizing multiple absorption bands and maximizing light utilization.

1.5 New photochemical conversion scheme

Efficiency in dye-sensitized solar cells (DSSCs) differs markedly from other photovoltaic technologies due to inherent energy losses occurring during various cell processes. In particular, substantial research efforts are directed towards minimizing the significant energy loss associated with dye regeneration, a crucial step in DSSC operation. One innovative approach to mitigate these energy losses involves eliminating one electron-transfer process, specifically dye regeneration. In

such scenarios, the dye remains in solution, enabling the oxidized form, post-charge injection, to diffuse to the counter electrode before undergoing reduction (recombination). This dissertation focuses on the drive to eliminate the regeneration loss as well as the conventional step of dye soaking during DSSC fabrication, a time-consuming process that potentially impacts the overall cost-effectiveness of DSSCs. The aim is to integrate the dye and electrolyte into a single component, thereby removing an electron transfer reaction, and ultimately enhancing the efficiency and viability of DSSCs.

This ambitious goal presents several challenging constraints, particularly concerning the properties and behavior of the dye. However, recent advancements in the field, particularly with copper complexes, offer promising avenues for exploration. In early stages of DSSC research, Ru(II) polypyridyl complexes were studied as photosensitizers. However, the disadvantage of using Ruthenium as a sensitizer is their low abundance in nature. This has led to the use of copper complexes as an alternative. McMillin and coworkers studied bis(1,10- phenanthroline) copper complexes in solution and showed the photoredox behavior for this complex. 12 The complex was also shown to have a metal to ligand charge transfer (MLCT) band of high extinction coefficient. These properties of the copper complex paved the way to their usage as photosensitizers in DSSCs. In 1994, copper complexes used as photosensitizer were first reported. 13 They studied bis(2,9diphenyl-1,10-phenanthroline)copper(I) but the photocurrent generated was low (0.6 mA/cm). Further studies to modify the complex were then carried out. Sandroni and coworkers in 2014 reported DSSCs using heteroleptic copper sensitzers having the best efficiency of 4.66% so far. 14 Copper complexes have also been widely used as redox shuttles in DSSCs as well. In 2005, Hattori used copper complexes as a redox couples in DSSCs for the first time.¹³ This led to research on other copper complexes like $[Cu^{+/2+}(tmby)_2](TFSI)_{1/2}$ (tmby = 4,4',6,6'-tetramethyl-2,2'-

bipyridine; TFSI =bis(trifluoromethylsulfonyl)imide) redox couple, generating the best efficiency of 13.1%. ¹⁵

Notably, research conducted by Castellano's group has resulted in the synthesis of copper complexes with exceptionally long excited-state lifetimes, exceeding 1 microsecond. This extended lifetime suggests that within a titanium dioxide (TiO₂) framework, each excited chromophore may encounter the TiO₂ surface before reverting to its original state. Such a phenomenon opens up the possibility of facilitating charge injection without the necessity of dye attachment to the surface, thus potentially streamlining the DSSC fabrication process.

The potential of these copper complexes to eliminate the requirement for dye attachment to the surface for charge injection represents a significant advancement in DSSC technology. By allowing the oxidized chromophore to diffuse to the counter electrode for reduction, this approach simplifies the fabrication process while potentially improving device performance and efficiency. However, the oxidized chromophore's role as an effective electron acceptor raises concerns about the possibility of energy loss through the electron transfer mechanism due to recombination. ^{17–19} Therefore, managing the competition between recombination and oxidized species diffusion is imperative for ensuring optimal DSSC performance.

To address this challenge, one proposed solution involves introducing a ligand exchange reaction of the oxidized chromophore. This reaction is hypothesized to prevent recombination, thereby preserving the energy of the injected electrons and maximizing device efficiency. By carefully controlling the kinetics and thermodynamics of this reaction, researchers aim to strike a balance between recombination suppression and efficient charge transfer, ultimately leading to improved DSSC performance. Such ligand exchanges have been previously studied in other systems.²⁰

Furthermore, the investigation of related copper complexes as redox shuttles presents additional opportunities for enhancing DSSC efficiency. Previous studies have demonstrated the excellent performance of copper complexes in facilitating electron transport and regeneration, ^{21–26} making them attractive candidates for integration into a single-component DSSC configuration, which we term as "Retro Cells". By leveraging the dual functionality of copper complexes as both sensitizers and redox shuttles, researchers can potentially simplify DSSC fabrication and improve device performance simultaneously.

Thus, the integration of copper complexes into DSSC technology holds significant promise for overcoming existing challenges and advancing the field. By eliminating the need for dye attachment to the surface and introducing innovative approaches to manage electron transfer and recombination, researchers aim to improve DSSC efficiency and viability for widespread commercial adoption. The following chapters will examine and explore this new photochemical conversion scheme.

REFERENCES

- (1) COP28: assessment of commitments to climate and development financing, global health and gender equality. https://focus2030.org/COP28-assessment-of-commitments-to-climate-and-development-financing-global (accessed 2024-05-04).
- (2) Calvin, K.; Dasgupta, D.; Krinner, G.; Mukherji, A.; Thorne, P. W.; Trisos, C.; Romero, J.; Aldunce, P.; Barrett, K.; Blanco, G.; Cheung, W. W. L.; Connors, S.; Denton, F.; Diongue-Niang, A.; Dodman, D.; Garschagen, M.; Geden, O.; Hayward, B.; Jones, C.; Jotzo, F.; Krug, T.; Lasco, R.; Lee, Y.-Y.; Masson-Delmotte, V.; Meinshausen, M.; Mintenbeck, K.; Mokssit, A.; Otto, F. E. L.; Pathak, M.; Pirani, A.; Poloczanska, E.; Pörtner, H.-O.; Revi, A.; Roberts, D. C.; Roy, J.; Ruane, A. C.; Skea, J.; Shukla, P. R.; Slade, R.; Slangen, A.; Sokona, Y.; Sörensson, A. A.; Tignor, M.; van Vuuren, D.; Wei, Y.-M.; Winkler, H.; Zhai, P.; Zommers, Z.; Hourcade, J.-C.; Johnson, F. X.; Pachauri, S.; Simpson, N. P.; Singh, C.; Thomas, A.; Totin, E.; Alegría, A.; Armour, K.; Bednar-Friedl, B.; Blok, K.; Cissé, G.; Dentener, F.; Eriksen, S.; Fischer, E.; Garner, G.; Guivarch, C.; Haasnoot, M.; Hansen, G.; Hauser, M.; Hawkins, E.; Hermans, T.; Kopp, R.; Leprince-Ringuet, N.; Lewis, J.; Ley, D.; Ludden, C.; Niamir, L.; Nicholls, Z.; Some, S.; Szopa, S.; Trewin, B.; van der Wijst, K.-I.; Winter, G.; Witting, M.; Birt, A.; Ha, M. IPCC, 2023: Climate Change 2023: Synthesis Report. Contribution of Working Groups I, II and III to the Sixth Assessment Report of the Intergovernmental Panel on Climate Change [Core Writing Team, H. Lee and J. Romero Switzerland. 2023. https://doi.org/10.59327/IPCC/AR6-(Eds.)]. IPCC, Geneva, 9789291691647.
- (3) The Paris Agreement Publication | UNFCCC. https://unfccc.int/documents/184656 (accessed 2024-05-04).
- (4) Masson-Delmotte, V.; Zhai, P.; Pörtner, H.-O.; Roberts, D.; Skea, J.; Shukla, P. R.; Pirani, A.; Moufouma-Okia, W.; Péan, C.; Pidcock, R.; Connors, S.; Matthews, J. B. R.; Chen, Y.; Zhou, X.; Gomis, M. I.; Lonnoy, E.; Maycock, T.; Tignor, M.; Waterfield, T. Global Warming of 1.5°C An IPCC Special Report on the Impacts of Global Warming of 1.5°C above Pre-Industrial Levels and Related Global Greenhouse Gas Emission Pathways, in the Context of Strengthening the Global Response to the Threat of Climate Change, Sustainable Development, and Efforts to Eradicate Poverty Summary for Policymakers Technical Summary Frequently Asked Questions Glossary Edited by Science Officer Science Assistant Graphics Officer Working Group I Technical Support Unit. 2019.
- Victoria, M.; Haegel, N.; Peters, I. M.; Sinton, R.; Jäger-Waldau, A.; del Cañizo, C.; Breyer, C.; Stocks, M.; Blakers, A.; Kaizuka, I.; Komoto, K.; Smets, A. Solar Photovoltaics Is Ready to Power a Sustainable Future. Joule **2021**, 5 (5), 1041–1056. https://doi.org/10.1016/J.JOULE.2021.03.005.
- (6) Roger A. Messenger; Amir Abtahi. Photovoltaic Systems Engineering, Fourth Edition, Fourth.; CRC Press, 2017.
- (7) Carella, A.; Borbone, F.; Centore, R. Research Progress on Photosensitizers for DSSC. Front Chem **2018**, 6 (SEP), 416256. https://doi.org/10.3389/FCHEM.2018.00481/BIBTEX.

- (8) Kharche, N. R. Future Directions and Emerging Trends: Technological Innovations in Solar Energy Integration. https://services.igi-global.com/resolvedoi/resolve.aspx?doi=10.4018/979-8-3693-7822-9.ch002 **1AD**, 39–58. https://doi.org/10.4018/979-8-3693-7822-9.CH002.
- (9) Saifullah, M.; Ahn, S.; Gwak, J.; Ahn, S.; Kim, K.; Cho, J.; Park, J. H.; Eo, Y. J.; Cho, A.; Yoo, J. S.; Yun, J. H. Development of Semitransparent CIGS Thin-Film Solar Cells Modified with a Sulfurized-AgGa Layer for Building Applications. J Mater Chem A Mater **2016**, 4 (27), 10542–10551. https://doi.org/10.1039/C6TA01909A.
- (10) Freitag, M.; Teuscher, J.; Saygili, Y.; Zhang, X.; Giordano, F.; Liska, P.; Hua, J.; Zakeeruddin, S. M.; Moser, J. E.; Grätzel, M.; Hagfeldt, A. Dye-Sensitized Solar Cells for Efficient Power Generation under Ambient Lighting. Nature Photonics 2017 11:6 **2017**, 11 (6), 372–378. https://doi.org/10.1038/nphoton.2017.60.
- (11) Yeoh, M. E.; Chan, K. Y. A Review on Semitransparent Solar Cells for Real-Life Applications Based on Dye-Sensitized Technology. IEEE J Photovolt **2021**, 11 (2), 354–361. https://doi.org/10.1109/JPHOTOV.2020.3047199.
- (12) Meggers, W. F.; Stimson, F. J. Dyes for Photographic Sensitizing. J Opt Soc Am **1920**, 4 (3), 91. https://doi.org/10.1364/JOSA.4.000091.
- (13) Quina, F. H.; Silva, G. T. M. The Photophysics of Photosensitization: A Brief Overview. J Photochem Photobiol **2021**, 7, 100042. https://doi.org/10.1016/J.JPAP.2021.100042.
- (14) Moser, J. Notiz Über Verstärkung Photoelektrischer Ströme Durch Optische Sensibilisirung. Monatsh Chem **1887**, 8 (1), 373. https://doi.org/10.1007/BF01510059.
- (15) Gurney, R. W.; Mott, N. F. The Theory of the Photolysis of Silver Bromide and the Photographic Latent Image. Proc R Soc Lond A Math Phys Sci **1938**, 164 (917), 151–167. https://doi.org/10.1098/RSPA.1938.0011.
- (16) Gerischer, H.; Michel-Beyerle, M. E.; Rebentrost, F.; Tributsch, H. Sensitization of Charge Injection into Semiconductors with Large Band Gap. Electrochim Acta **1968**, 13 (6), 1509–1515. https://doi.org/10.1016/0013-4686(68)80076-3.
- (17) TRIBUTSCH, H.; CALVIN, M. ELECTROCHEMISTRY OF EXCITED MOLECULES: PHOTO-ELECTROCHEMICAL REACTIONS OF CHLOROPHYLLS. Photochem Photobiol **1971**, 14 (2), 95–112. https://doi.org/10.1111/J.1751-1097.1971.TB06156.X.
- (18) Osa, T.; Fujihira, M. Photocell Using Covalently-Bound Dyes on Semiconductor Surfaces. Nature 1976 264:5584 **1976**, 264 (5584), 349–350. https://doi.org/10.1038/264349a0.
- (19) Aghazada, S.; Nazeeruddin, M. K. Ruthenium Complexes as Sensitizers in Dye-Sensitized Solar Cells. Inorganics 2018, Vol. 6, Page 52 **2018**, 6 (2), 52. https://doi.org/10.3390/INORGANICS6020052.
- (20) Augustynski, J.; Vlachopoulos, N.; Liska, P.; GräTzel, M. Very Efficient Visible Light Energy Harvesting and Conversion by Spectral Sensitization of High Surface Area Polycrystalline Titanium Dioxide Films. J Am Chem Soc **1988**, 110 (4), 1216–1220. https://doi.org/10.1021/JA00212A033/ASSET/JA00212A033.FP.PNG_V03.

- (21) Desilvestro, J.; Grätzel, M.; Kavan, L.; Moser, J.; Augustynski, J. Highly Efficient Sensitization of Titanium Dioxide. J Am Chem Soc **1985**, 107 (10), 2988–2990. https://doi.org/10.1021/JA00296A035/ASSET/JA00296A035.FP.PNG V03.
- O'Regan, B.; Grätzel, M. A Low-Cost, High-Efficiency Solar Cell Based on Dye-Sensitized Colloidal TiO2 Films. Nature **1991**, 353 (6346), 737–740. https://doi.org/10.1038/353737A0.
- (23) Nazeeruddin, M. K.; Kay, A.; Rodicio, I.; Humphry-Baker, R.; Müller, E.; Liska, P.; Vlachopoulos, N.; Grätzel, M. Conversion of Light to Electricity by Cis-X2Bis (2,2'-Bipyridyl-4,4'-Dicarboxylate) Ruthenium (II) Charge-Transfer Sensitizers (X = Cl-, Br-, I-, CN-, and SCN-) on Nanocrystalline TiO2 Electrodes. J Am Chem Soc **1993**, 115 (14), 6382–6390. https://doi.org/10.1021/JA00067A063.
- (24) Mathew, S.; Yella, A.; Gao, P.; Humphry-Baker, R.; Curchod, B. F. E.; Ashari-Astani, N.; Tavernelli, I.; Rothlisberger, U.; Nazeeruddin, M. K.; Grätzel, M. Dye-Sensitized Solar Cells with 13% Efficiency Achieved through the Molecular Engineering of Porphyrin Sensitizers. Nature Chemistry 2014 6:3 2014, 6 (3), 242–247. https://doi.org/10.1038/nchem.1861.
- (25) Kakiage, K.; Aoyama, Y.; Yano, T.; Oya, K.; Fujisawa, J. I.; Hanaya, M. Highly-Efficient Dye-Sensitized Solar Cells with Collaborative Sensitization by Silyl-Anchor and Carboxy-Anchor Dyes. Chemical Communications **2015**, 51 (88), 15894–15897. https://doi.org/10.1039/C5CC06759F.
- (26) Marcus, R. A.; Sutin, N. Electron Transfers in Chemistry and Biology. Biochimica et Biophysica Acta (BBA) Reviews on Bioenergetics **1985**, 811 (3), 265–322. https://doi.org/10.1016/0304-4173(85)90014-X.
- (27) Bisquert, J.; Marcus, R. A. Device Modeling of Dye-Sensitized Solar Cells. **2013**, 325–395. https://doi.org/10.1007/128_2013_471.
- (28) Marcus, R. A. Electron Transfer Reactions in Chemistry. Theory and Experiment*. Protein Electron Transfer **2020**, 249–272. https://doi.org/10.1201/9781003076803-10.
- (29) Marcus, R. A. On the Theory of Oxidation-Reduction Reactions Involving Electron Transfer. I. J Chem Phys **1956**, 24 (5), 966–978. https://doi.org/10.1063/1.1742723.
- (30) Barbara, P. F.; Meyer, T. J.; Ratner, M. A. Contemporary Issues in Electron Transfer Research. Journal of Physical Chemistry **1996**, 100 (31), 13148–13168. https://doi.org/10.1021/JP9605663.
- (31) Feldt, S. M.; Lohse, P. W.; Kessler, F.; Nazeeruddin, M. K.; Grätzel, M.; Boschloo, G.; Hagfeldt, A. Regeneration and Recombination Kinetics in Cobalt Polypyridine Based Dye-Sensitized Solar Cells, Explained Using Marcus Theory. Physical Chemistry Chemical Physics **2013**, 15 (19), 7087–7097. https://doi.org/10.1039/C3CP50997D.
- (32) Soman, S.; Pradhan, S. C.; Yoosuf, M.; Vinayak, M. V.; Lingamoorthy, S.; Gopidas, K. R. Probing Recombination Mechanism and Realization of Marcus Normal Region Behavior in DSSCs Employing Cobalt Electrolytes and Triphenylamine Dyes. Journal of Physical Chemistry C **2018**, 122 (25), 14113–14127. https://doi.org/10.1021/ACS.JPCC.8B01325.

- (33) Chou, M.; Creutz, C.; Sutin, N. Rate Constants and Activation Parameters for Outer-Sphere Electron-Transfer Reactions and Comparisons with the Predictions of Marcus Theory. J Am Chem Soc **2002**, 99 (17), 5615–5623. https://doi.org/10.1021/JA00459A014.
- (34) Listorti, A.; O'Regan, B.; Durrant, J. R. Electron Transfer Dynamics in Dye-Sensitized Solar Cells. Chemistry of Materials **2011**, 23 (15), 3381–3399. https://doi.org/10.1021/CM200651E/ASSET/IMAGES/MEDIUM/CM-2011-00651E 0010.GIF.
- (35) Antila, L. J.; Myllyperkio, P.; Mustalahti, S.; Lehtivuori, H.; Korppi-Tommola, J. Injection and Ultrafast Regeneration in Dye-Sensitized Solar Cells. Journal of Physical Chemistry C **2014**, 118 (15), 7772–7780. https://doi.org/10.1021/JP4124277/SUPPL_FILE/JP4124277_SI_001.PDF.
- Juozapavicius, M.; Kaucikas, M.; Dimitrov, S. D.; Barnes, P. R. F.; Van Thor, J. J.; O'Regan, B. C. Evidence for "Slow" Electron Injection in Commercially Relevant Dye-Sensitized Solar Cells by Vis-NIR and IR Pump-Probe Spectroscopy. Journal of Physical Chemistry C 2013, 117 (48), 25317–25324. https://doi.org/10.1021/JP408989Q/SUPPL_FILE/JP408989Q_SI_001.PDF.
- (37) Syed, T. H.; Wei, W. Technoeconomic Analysis of Dye Sensitized Solar Cells (DSSCs) with WS2/Carbon Composite as Counter Electrode Material. Inorganics 2022, Vol. 10, Page 191 **2022**, 10 (11), 191. https://doi.org/10.3390/INORGANICS10110191.
- (38) McMillin, D. R.; Buckner, M. T.; Ahn, B. Tae. A Light-Induced Redox Reaction of Bis(2,9-Dimethyl-1,10-Phenanthroline)Copper(I). Inorg Chem **2002**, 16 (4), 943–945. https://doi.org/10.1021/IC50170A046.
- (39) Shigeki Hattori; Yuji Wada; Shozo Yanagida, and; Fukuzumi*, S. Blue Copper Model Complexes with Distorted Tetragonal Geometry Acting as Effective Electron-Transfer Mediators in Dye-Sensitized Solar Cells. J Am Chem Soc **2005**, 127 (26), 9648–9654. https://doi.org/10.1021/JA0506814.
- (40) Sandroni, M.; Favereau, L.; Planchat, A.; Akdas-Kilig, H.; Szuwarski, N.; Pellegrin, Y.; Blart, E.; Bozec, H. le; Boujtita, M.; Odobel, F. Heteroleptic Copper(I)–Polypyridine Complexes as Efficient Sensitizers for Dye Sensitized Solar Cells. J Mater Chem A Mater **2014**, 2 (26), 9944–9947. https://doi.org/10.1039/C4TA01755B.
- (41) Cao, Y.; Liu, Y.; Zakeeruddin, S. M.; Hagfeldt, A.; Grätzel, M. Direct Contact of Selective Charge Extraction Layers Enables High-Efficiency Molecular Photovoltaics. Joule **2018**, 2 (6), 1108–1117. https://doi.org/10.1016/j.joule.2018.03.017.
- (42) McCusker, C. E.; Castellano, F. N. Design of a Long-Lifetime, Earth-Abundant, Aqueous Compatible Cu(I) Photosensitizer Using Cooperative Steric Effects. Inorg Chem **2013**, 52 (14), 8114–8120. https://doi.org/10.1021/IC401213P.
- (43) Huang, S. Y.; Schlichthörl, G.; Nozik, A. J.; Grätzel, M.; Frank, A. J. Charge Recombination in Dye-Sensitized Nanocrystalline TiO2 Solar Cells. Journal of Physical Chemistry B **1997**, 101 (14), 2576–2582. https://doi.org/10.1021/JP962377Q.

- (44) Ondersma, J. W.; Hamann, T. W. Recombination and Redox Couples in Dye-Sensitized Solar Cells. Coord Chem Rev **2013**, 257 (9–10), 1533–1543. https://doi.org/10.1016/J.CCR.2012.09.010.
- (45) Xie, Y.; Baillargeon, J.; Hamann, T. W. Kinetics of Regeneration and Recombination Reactions in Dye-Sensitized Solar Cells Employing Cobalt Redox Shuttles. Journal of Physical Chemistry C 2015, 119 (50), 28155–28166. https://doi.org/10.1021/ACS.JPCC.5B08244.
- (46) Wang, Y.; Hamann, T. W. Improved Performance Induced by in Situ Ligand Exchange Reactions of Copper Bipyridyl Redox Couples in Dye-Sensitized Solar Cells. Chemical Communications **2018**, 54 (87), 12361–12364. https://doi.org/10.1039/C8CC07191H.
- (47) Karpacheva, M.; Malzner, F. J.; Wobill, C.; Büttner, A.; Constable, E. C.; Housecroft, C. E. Cuprophilia: Dye-Sensitized Solar Cells with Copper(I) Dyes and Copper(I)/(II) Redox Shuttles. Dyes and Pigments **2018**, 156, 410–416. https://doi.org/10.1016/j.dyepig.2018.04.033.
- (48) Fürer, S. O.; Milhuisen, R. A.; Kashif, M. K.; Raga, S. R.; Acharya, S. S.; Forsyth, C.; Liu, M.; Frazer, L.; Duffy, N. W.; Ohlin, C. A.; Funston, A. M.; Tachibana, Y.; Bach, U. The Performance-Determining Role of Lewis Bases in Dye-Sensitized Solar Cells Employing Copper-Bisphenanthroline Redox Mediators. Adv Energy Mater 2020, 10 (37), 2002067. https://doi.org/10.1002/AENM.202002067.
- (49) Rodrigues, R. R.; Lee, J. M.; Taylor, N. S.; Cheema, H.; Chen, L.; Fortenberry, R. C.; Delcamp, J. H.; Jurss, J. W. Copper-Based Redox Shuttles Supported by Preorganized Tetradentate Ligands for Dye-Sensitized Solar Cells. Dalton Transactions **2020**, 49 (2), 343–355. https://doi.org/10.1039/C9DT04030G.
- (50) Devdass, A.; Watson, J.; Firestone, E.; Hamann, T. W.; Delcamp, J. H.; Jurss, J. W. An Efficient Copper-Based Redox Shuttle Bearing a Hexadentate Polypyridyl Ligand for DSCs under Low-Light Conditions. ACS Appl Energy Mater **2022**, 5 (5), 5964–5973. https://doi.org/10.1021/ACSAEM.2C00344.
- (51) Higashino, T.; Imahori, H. Emergence of Copper(I/II) Complexes as Third-Generation Redox Shuttles for Dye-Sensitized Solar Cells. ACS Energy Lett **2022**, 7 (6), 1926–1938. https://doi.org/10.1021/ACSENERGYLETT.2C00716.
- (52) Sayah, D.; Ghaddar, T. H. Investigation of Ethylisopropyl Sulfone Medium with a Copper-Based Redox Electrolyte for Ambient Light Dye-Sensitized Solar Cells: Achieving High Efficiency and Enduring Long-Term Stability. ACS Appl Energy Mater **2023**, 6 (23), 11924–11933. https://doi.org/10.1021/ACSAEM.3C02067.

Chapter 2: Retro Cells

2.1 Background

Since the emergence of Grätzel-type dye-sensitized solar cells (DSSCs) as an economical and accessible means of harnessing solar energy for electricity generation, there has been a concerted effort to enhance their photo-conversion efficiency (PCE) by optimizing each constituent. Notably, extensive research has focused on improving both the sensitizer and the redox mediators. Ruthenium based dyes such as N719, N3, CYC-B11 and black dye are one of the best-known photosensitizers in DSSCs. These dyes give excellent power conversion efficiencies (PCE) with iodide/triiodide redox couple, but their PCE lowers with transition metal based redox couples. The usage of these dyes is also limited by the rarity and costliness of ruthenium, prompting exploration into Earth-abundant alternatives. Pioneering work by Sauvage and colleagues marked the utilization of copper(I) complexes as sensitizers, driven by the similarity in photophysical properties between copper(I) and ruthenium(II) complexes. In recent years, there has been a surge in research dedicated to leveraging inexpensive and environmentally friendly copper(I) complexes as sensitizers in DSSCs. Odobel et. al synthesized a copper(I) complex with 4,4'-dicarboxylic acid-6,6'-dimesityl-2,2'-bipyridine as the anchoring ligand and 4,4'-bis(N,N-diethylaminestyryl)-6,6'dimethyl-2,2'-bipyridine as the ancillary ligand that demonstrate remarkable PCE, unparalleled among coordination complexes of first-row transition metals. They also showed that the DSSCs performed better compared to control cells with N719 dye.

In 2005, Fukuzumi and colleagues pioneered the use of copper complexes as redox shuttles in DSSCs. They evaluated the photovoltaic properties of N719 ruthenium dye-based DSSCs alongside a range of complexes, including [Cu(phen)₂]^{1+/2+} and [Cu(dmp)₂]^{1+/2+}. Since then,

significant advancements in the performance of copper(II/I) redox mediators have been achieved through ligand structure tailoring, co-sensitization strategies, and innovative device architectures. Notably, Grätzel et al. reported a DSSC utilizing a Cu(II)/Cu(I) redox-based electrolyte, achieving an exceptional PCE of 13.1%. Recent work on copper polypyridyl complexes as redox shuttles has led to DSSCs with efficiencies up to 15%. These redox shuttles are interesting because they can act as fast reducing agents, thus minimizing the energy penalty of the dye regeneration step, however they are also slow enough acceptors to allow quantitative charge collection. We have shown the reason complexes like [Cu(dmbpy)₂]^{2+/+} (dmbpy = 6,6'-dimethyl-2,2'-bipyridine) are slow acceptors is a ligand exchange reaction of an exogenous base, e.g. tert-butyl pyridine (TBP), with the Cu(II) complexes. We note that the Cu(I) redox shuttles can have significant competitive absorption due to MLCT bands in the visible region. Indeed, this is sometimes taken advantage of to utilize copper complexes as earth abundant transition metal chromophores for DSSCs.

With the goals of using earth abundant metals for designing DSSCs as well as with the knowledge of copper complexes being successful candidates as photosensitizers and redox shuttles in DSSCs, the development of full-copper DSSCs were explored by several groups. 1,2 However, the inevitable competition for absorption between the dye and the redox shuttle poses a limitation on such systems, potentially hindering them from reaching their maximum efficiency. To overcome such a limitation, the subsequent paragraphs introduce a new system.

In pioneering work, Clark and Sutin investigated the sensitization of single crystal TiO_2 electrodes using ruthenium tris(4,7-dimethyl-1,10-phenanthroline), $[Ru(dmphen)_3]^{2+}$. They found that photoexcited $[Ru(dmphen)_3]^{2+}$ within an effective diffusion distance of 59 nm, determined by the 1.74 µs excited state lifetime, τ , of the Ru sensitizer, inject electrons into the TiO_2 conduction band with essentially unity quantum yield. The photocurrent was ultimately limited by the small fraction

of excited sensitizer molecules within this diffusion distance from the flat electrode. Modern DSSCs utilize a mesoporous TiO₂ photoanode where the pore size is on the order of 10-30ß nm, determined by the TiO₂ nanoparticle size and preparation conditions. In this case, all photoexcited sensitizers with a µs lifetime would diffuse to a TiO₂ surface and allow charge separation. Ruthenium polypyridyl complexes are good electron acceptors, however, and fast recombination limits charge collection for such systems. While band-bending in single crystal TiO₂ can inhibit such recombination losses, there is no band-bending in nanoparticle TiO₂ electrodes and recombination by interfacial electron transfer is a critical limitation. This is the reason that kinetically slow redox shuttles are generally utilized to reduce the oxidized chromophores and allow efficient charge collection.

Castellano has reported a series of copper complexes with long excited state lifetimes and strong absorbance in the visible region analogous to Ru polypyridyl analogs. For example, [Cu(dsbtmp)₂]⁺ (dsbtmp=bis(2,9-di(sec-butyl)-3,4,7,8-tetramethyl-1,10-phenanthroline) was shown to have excited-state lifetimes >1 µs in a variety of solvents (Figure 2.1 (b)). A molar absorptivity of 7400 M⁻¹ cm⁻¹ at 445 nm allows good visible light absorption within a ca. 10 micron TiO₂ mesoporous electrode. These attributes suggest the possibility of using [Cu(dsbtmp)₂]⁺ dissolved in solution as a sensitizer for TiO₂. Diffusion of the oxidized [Cu(dsbtmp)₂]²⁺ to the counter electrode would complete the circuit. Such a solar cell, which we term "Retro Cell", would be advantageous as it eliminates the energy loss of the dye regeneration step, eliminates the time intensive dye absorption step, and may decrease instability due to dye desorption. In order to be successful, recombination losses to [Cu(dsbtmp)₂]²⁺ must be minimized to allow good charge collection. Herein we report the first example of a retro cell, identify rate

limiting steps in photocurrent generation and future directions to advance the efficiency and application scope.

2.2 DSSCs with $[Cu(dsbtmp)_2]^{+/2+}$

(a)

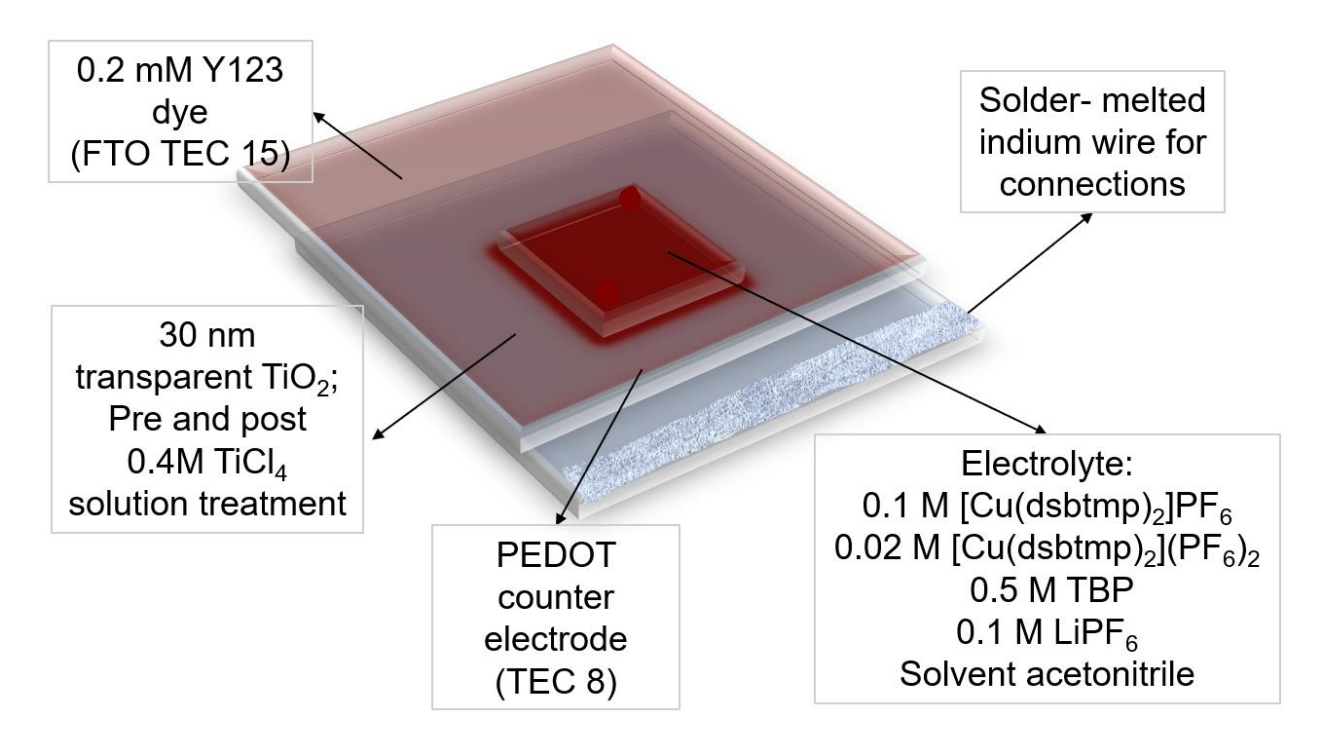


Figure 2.1: (a) Representation of DSSC employing Y123 dye and [Cu(dsbtmp)₂]^{+/2+} with TBP as the base additive. (b) Structure of [Cu(dsbtmp)₂]⁺ (dsbtmp=bis(2,9-di(sec-butyl)-3,4,7,8-tetramethyl-1,10-phenanthroline) (c) Structure of Y123 dye (d) UV-Vis Absorption spectrum of dye Y123 reproduced from reference 4.⁴

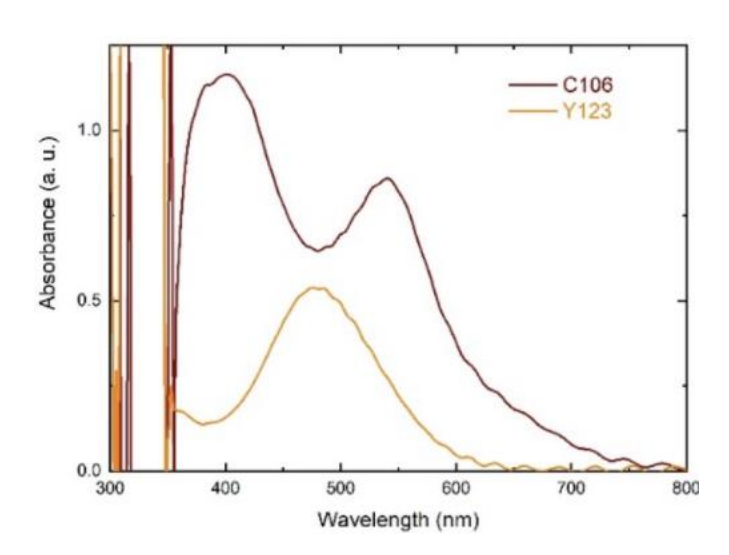
Figure 2.1 (cont'd)

(c)

$$C_6H_{13}O$$
 OC_6H_{13}
 $C_6H_{13}C_6H_{13}$
 $C_6H_{13}O$

Figure 2.1 (cont'd)

(d)



The [Cu(dsbtmp)₂]⁺ complex was synthesized according to a previously reported method.⁵ The Cu(II) form was prepared by oxidation with an equimolar solution of nitrosonium hexafluorophosphate, NOPF₆ and [Cu(dsbtmp)₂]⁺ in dichloromethane in an inert atmosphere. Detailed synthetic methods and characterization are provided in section 2.6. Before working on the fabrication and principles of retro cells, a study on using the copper complexes as redox shuttles in a regular DSSC was carried out. The conditions used for the cells are summarized in figure 2.1. 3-{6-{4-[bis(2',4'-dihexyloxybiphenyl-4-yl)amino-]phenyl}-4,4-dihexyl-cyclopenta-[2,1-b:3,4-b']dithiphene-2-yl}-2-cyanoacrylic acid, also known as Y123 (Figure 2.1 (c)) was chosen for this set. It has a $E^0 = 0.45 \text{ V}$ vs Fc^+/Fc and has been used before in other similar systems. The redox shuttle has a $E^0 = 0.43 \text{ V}$ vs Fc^+/Fc , as measured from the cyclic voltammograms in Figure 2.5. Previously Y123 has achieved a 10% solar cell efficiency and has demonstrated exceptional device stability under high-temperature conditions.^{6,7} This dye has also previously copper redox shuttles.^{7–9} Highly DSSCs with porous been in ethylenedioxythiophene) (PEDOT) counter electrodes, which have been proven to be successful

for various redox couples in previous studies, has been used here. 10,11 The electrolyte consisted of 0.1 M [Cu(dsbtmp)₂](PF₆), 0.02 M [Cu(dsbtmp)₂](PF₆)₂, 0.5M TBP and 0.1 M LiPF₆ in dry acetonitrile. A detailed description of the synthesis of the materials and the characteristics of the copper complexes is discussed in section 2.5. The performance DSSCs is evaluated using several key parameters that provide insights into their efficiency and functionality. Among these, J-V curves and incident photon-to-current efficiency (IPCE) measurements are the most commonly used techniques. 12 J-V curves, or current density-voltage curves, are obtained by measuring the current density (J) generated by the cell as a function of the applied voltage (V) under illumination. These curves provide critical information about the cell's short-circuit current density (J_{sc}), opencircuit voltage (V_{oc}), fill factor (FF), and overall power conversion efficiency (PCE). The J_{sc} represents the maximum current density generated when the cell is short-circuited, while the V_{oc} is the maximum voltage produced when no current flows through the circuit. The fill factor is a measure of the cell's electrical performance and is defined as the ratio of the maximum power output to the product of J_{sc} and V_{oc}. The PCE, calculated as the ratio of the electrical power output to the incident solar power input, indicates the overall efficiency of the DSSC in converting sunlight into electricity. These measurements are typically conducted under standardized conditions using a solar simulator with an irradiance of 1000 W/m², simulating one sun illumination. IPCE, or incident photon-to-current efficiency, measures the efficiency of a DSSC in converting incident photons at specific wavelengths into electrical current. This parameter is wavelength-dependent and provides insight into the spectral response of the cell. The IPCE is calculated as the ratio of the photocurrent generated by the cell to the number of incident photons at a given wavelength, expressed as a percentage. IPCE measurements help identify how efficiently the dye sensitizer absorbs light and injects electrons into the semiconductor across the

visible and near-infrared regions. By analyzing the IPCE spectrum, researchers can assess the dye's light-harvesting capabilities and the overall photo response of the device.

The current density vs voltage (J-V) plots for light (when the light is on) and dark (when the light is turned off) conditions under AM 1.5G (100 mW cm⁻²) light is given in figure 2.2 (a). The cells showed an average open circuit voltage (V_{OC}) of 0.79 V (± 0.033 V), an average short circuit current densities (J_{SC}) of 2.78 mA/cm² (\pm 0.068 mA/cm²) and an efficiency (η) of 1.37 %. The cells were also tested without TBP in the electrolyte, and they resulted in negligible values for both V_{OC} and J_{SC} and thus overall efficiency. The IPCE and the integrated current density for the set of devices is given in figure 2.2 (b). Dye Y123 has an absorption maximum at 530 nm as shown in Figure 2.1 (d). Current transient measurements are used to investigate the dynamic processes of charge generation, transport, and recombination under time-dependent conditions. These measurements involve monitoring the photocurrent (or dark current) over time in response to a sudden change in illumination or applied voltage. They provide insights into the kinetics of charge carriers and the efficiency of processes within the DSSC. The current transient plot in figure 2.2 (c) for the devices were carried out where the light was turned on and off with a time interval of 5 s within the processes. It shows a drop in current immediately after the light is turned on. This indicates mass transport limitations in the devices.

(a)

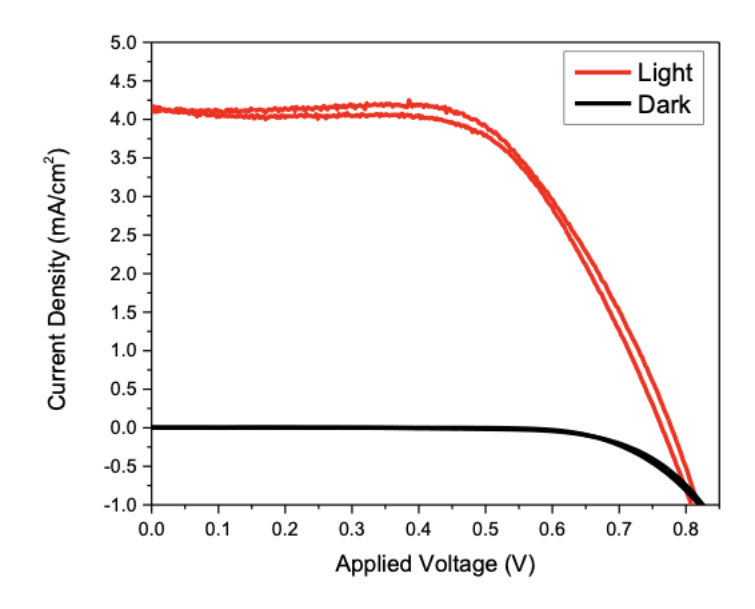
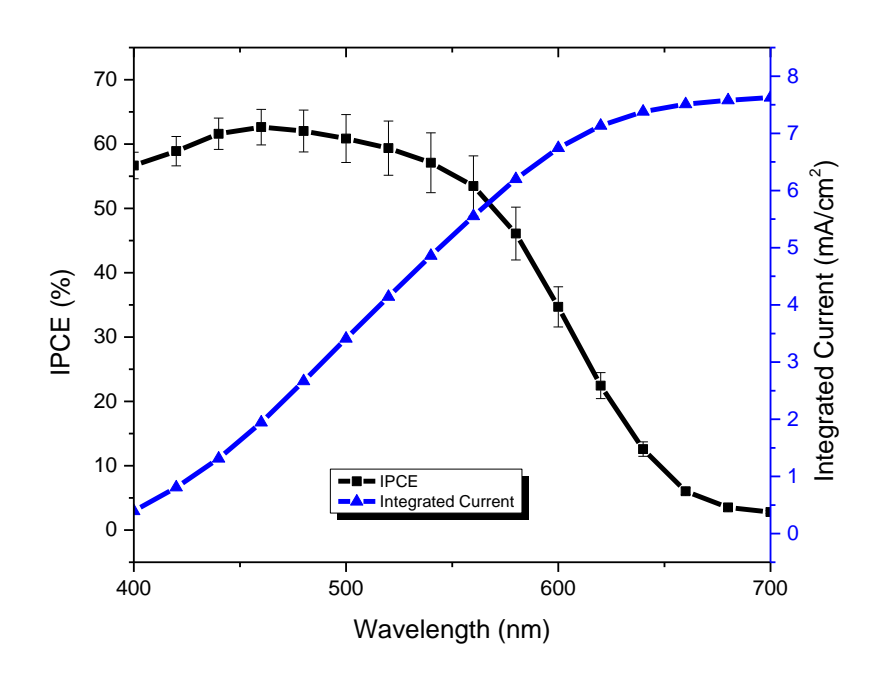


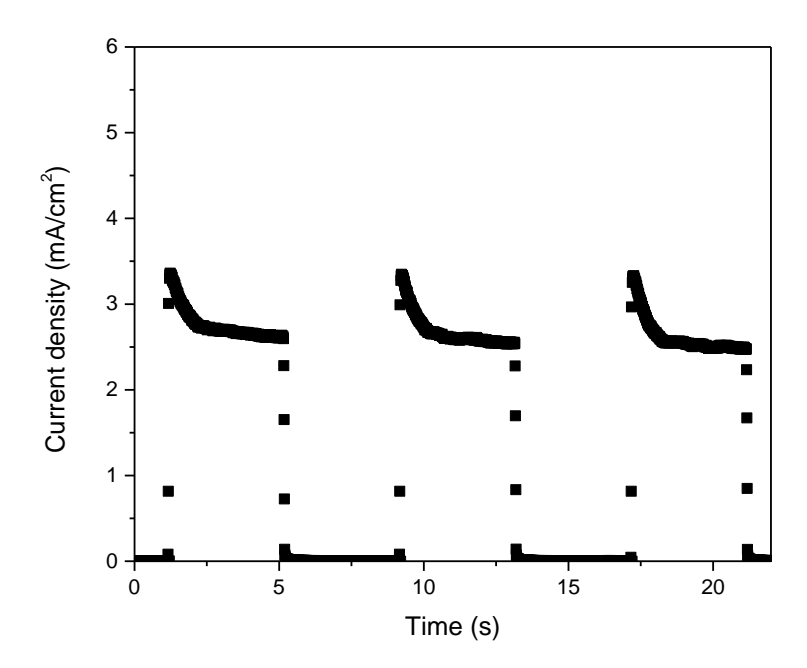
Figure 2.2: (a) Current density vs applied voltage characteristics measured under 100mW/cm² illumination (red) when the light is turned off and under dark conditions (black) when the light is turned off, for DSSCs with [Cu(dsbtmp)₂]^{+/2+} and TBP in the electrolytic solution. (b) Incident photon-to-current conversion efficiency (black squares) and integrated current density (blue triangles) for DSSCs with [Cu(dsbtmp)₂]^{+/2+} and TBP (c) Transient current vs time plot under short circuit conditions for DSSCs with [Cu(dsbtmp)₂]^{+/2+} and TBP under white light (the light is alternatively turned on and off at 5s time intervals.

Figure 2.2 (cont'd)

(b)

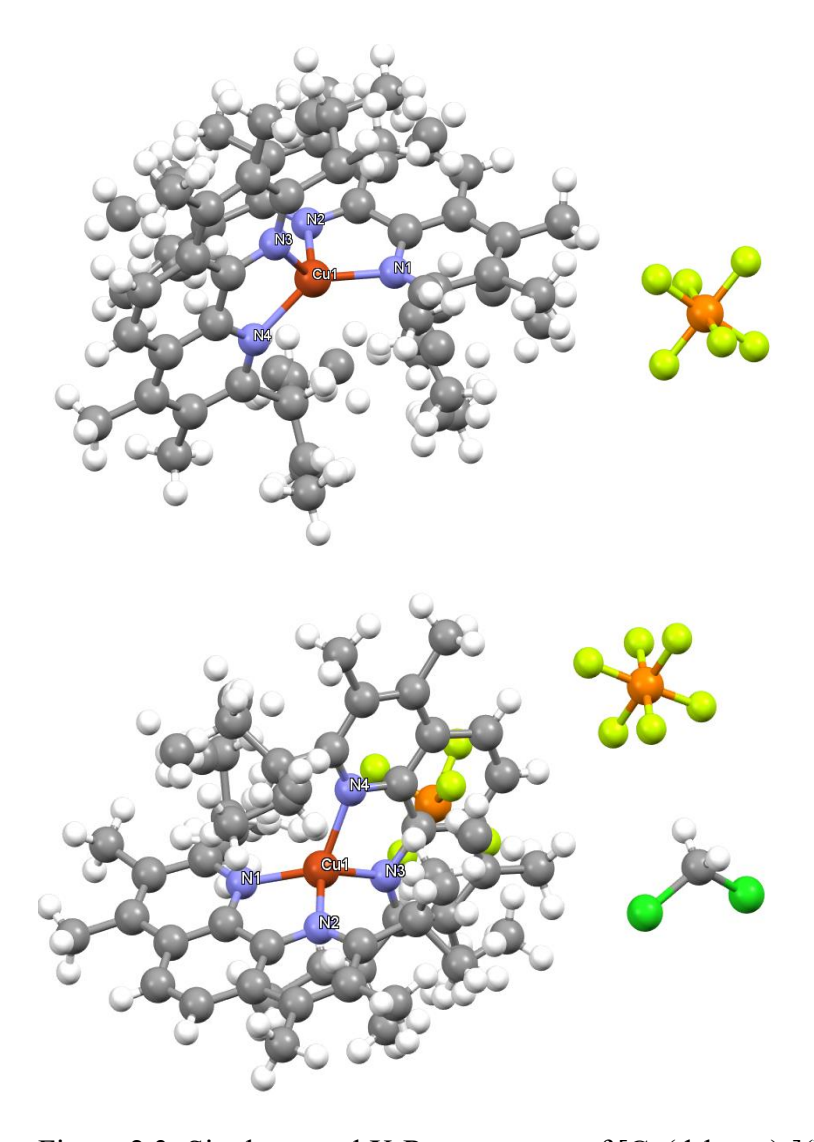


(c)



2.3 Retro Cells: Results and Discussion

The crystal structures of $[Cu(dsbtmp)_2]^+$ and $[Cu(dsbtmp)_2]^{2+}$ are shown below in Figure 2.3. These structures have been obtained for the first time and has been not reported in literature before to the best of our knowledge. The bite angles of the Cu(I) center are 81.78° and 82.02° , which is quite different from tetrahedral structures typical of Cu(I) bipyridyl complexes, which we attribute to the steric bulk of the dsbtmp ligands. The Cu(II) center has bite angles of 84.5° and 84.2° . The structure of the complex was determined by calculating the four-coordinate geometry index, τ_4 as introduced by Houser et al.¹³ The index was found to be 0.7208. This indicates a pseudodisphenoidal (seesaw) geometry for both the copper centers. Cu(I) complexes are generally tetrahedral, which undergo a Jahn-Teller distortion upon oxidation from a d^{10} to d^9 configuration, which typically leads to flattening of the d^9 complex. In a disphenoidal complex, however, no Jahn-Teller distortion is expected, consistent with the similar measured bond lengths and bond angles of both Cu(I) and Cu(II) centers. Some properties of the copper centers are listed in Table 2.1.



 $Figure\ 2.3:\ Single\ crystal\ X-Ray\ structure\ of\ [Cu(dsbtmp)_2](PF_6)\ and\ [Cu(dsbtmp)_2](PF_6)_2.$

Table 2.1: Selected bond lengths and bond angles of [Cu(dsbtmp)₂](PF₆)₂ and [Cu(dsbtmp)₂](PF₆)₂

Complex	Bond	Bond Length	Bond	Bond Angle
		(Å)		(degree)
[Cu(dsbtmp) ₂](PF ₆)	Cu1-N1	2.022(2)	N1-Cu1-N2	81.79(9)
	Cu1-N2	2.088(2)	N1-Cu1-N3	124.80(9)
	Cu1-N3	2.074(2)	N1-Cu1-N4	139.42(9)
	Cu1-N4	2.038(2)	N2-Cu1-N3	111.42(9)
[Cu(dsbtmp) ₂](PF ₆) ₂	Cu1-N1	1.961(6)	N1-Cu1-N2	84.5(3)
	Cu1-N2	2.010(8)	N1-Cu1-N4	120.0(2)
	Cu1-N3	1.959(5)	N1-Cu1-N3	138.4(3)
	Cu1-N4	2.027(7)	N2-Cu1-N3	113.8(3)

Two sets of retro cells were fabricated with electrolytes containing 0.1 M [Cu(dsbtmp)₂](PF₆), 0.05 M [Cu(dsbtmp)₂](PF₆)₂ and 0.1 M LiPF₆ in dry acetonitrile. TBP is an electrolyte additive that is typically employed in DSSCs, which has shown to induce a shift in the conduction band (CB) edge of TiO₂ towards more negative potentials.¹⁴ Furthermore, the steric hindrance offered by the tert-butyl group has been documented to play a significant role in reducing recombination through the shielding effect it exerts on TiO₂ surface.¹⁵ In case of copper electrolytes in DSSCs, it has also been shown that TBP undergoes ligand substitution reactions with some Cu(II) species which results in reduction of recombination and improvement in device performance.¹⁶ Therefore,

in one set of cells, 0.5 M TBP was introduced to compare the behavior to the control set without TBP.

The photocurrent density vs applied voltage (J–V) response of the retro cells, both with and without TBP, under AM 1.5G (100 mW cm⁻²) light are displayed in Figure 2.4 (a). The cells with TBP showed an average open circuit voltage (V_{OC}) of 0.65 V (\pm 0.023 V), an average short circuit current densities (J_{SC}) of 0.097 mA/cm² (\pm 0.020 mA/cm²) and an efficiency (η) of 0.045%. The cells without TBP resulted in negligible values for both V_{OC} (0.2 V) and J_{SC} (0.03 mA/cm²) and thus overall efficiency. Notably, the inclusion of TBP yielded a substantial improvement in device performance, emphasizing the significant role played by TBP in the cell configuration which we discuss further below.

IPCE measurements were performed to assess the spectral response of DSSCs; the results are displayed in Figure 2.4 (b). The peak in the 400-450 nm region resembles the absorption spectrum of [Cu(dsbtmp)₂]⁺ (Figure 2.5 (b)) indicating that the photocurrent in the retro cells is derived from the excitation of the Cu(I) species. The current densities derived from the integration of IPCE data in Figure 2.4 (b) are consistent with the J-V measurements, thus indicating the IPCE captures the behavior of the J-V measurements. The IPCE can be described by the product of the light harvesting efficiency, η_{LH} , the charge separation efficiency, η_{sep} , and the charge collection efficiency η_{cc} :

$$IPCE(\lambda) = \eta_{LH}(\lambda) \times \eta_{sep} \times \eta_{cc}(\lambda) \ (1)$$

The light harvesting efficiency (η_{LH}), shown in Figure 2.4 (d), is defined as the percent of incident photons absorbed by the copper complex (dye) in the solar cell. It is determined from the absorption profile of the complex and is described in detail in the Supporting Information. It is interesting to note that the η_{LH} is high in the region 400-500 nm but the IPCE is relatively low in

the same region. Division of the IPCE by η_{LH} is the absorbed photon-to-current efficiency, APCE, or internal quantum yield which is shown in Figure 2.4 (d).

The charge separation efficiency is determined by the diffusion of excited sensitizers to the TiO_2 surface, thus the diffusion coefficient and the excited state lifetime of the sensitizers, and the injection efficiency, which are all independent of wavelength. The charge collection efficiency is controlled by recombination via back electron transfer, and is a function of the electron diffusion length, L_n , film thickness, d, and the absorption coefficient which gives rise to a dependence on wavelength. At longer wavelengths, ca. 450 - 550 nm, where the absorption by Cu(I) decreases, the electrons are injected into TiO_2 farther from the substrate and therefore must diffuse longer distances to be collected. If charge collection is limited by fast recombination, the APCE at these wavelengths would be negligible. The fact that the APCE is relatively flat in this region suggests good charge collection. The open circuit photovoltage is also related to rate of recombination; the relatively large V_{oc} for cells with TBP is thus consistent with slow recombination and good charge collection.

The excited state lifetime was found to be 1.5 μ s by time resolved emission spectroscopy measurements in acetonitrile with 10 mM solution, consistent with prior reports.⁵ The diffusion coefficient was found to be 6.2×10^{-5} cm² s⁻¹ by analysis of cyclic voltammograms shown in Figure 2.12. Thus, an excited state diffusion length of 96.1 nm is predicted. Assuming the TiO₂ pore size is on the order of the nanoparticle size of ~25 nm, all excited chromophores should collide with the TiO₂ surface at least once. We therefore suggest the photocurrent and overall efficiency is limited by η_{sep} , which we primarily attribute to a poor charge injection efficiency at contact. One reason for this may be due to the weak coupling between the complex and the semiconductor,

which is distance dependent. This is due to the bulky tert-butyl group present in the complex as a result of substitution, which is shown in the following text.

(a)

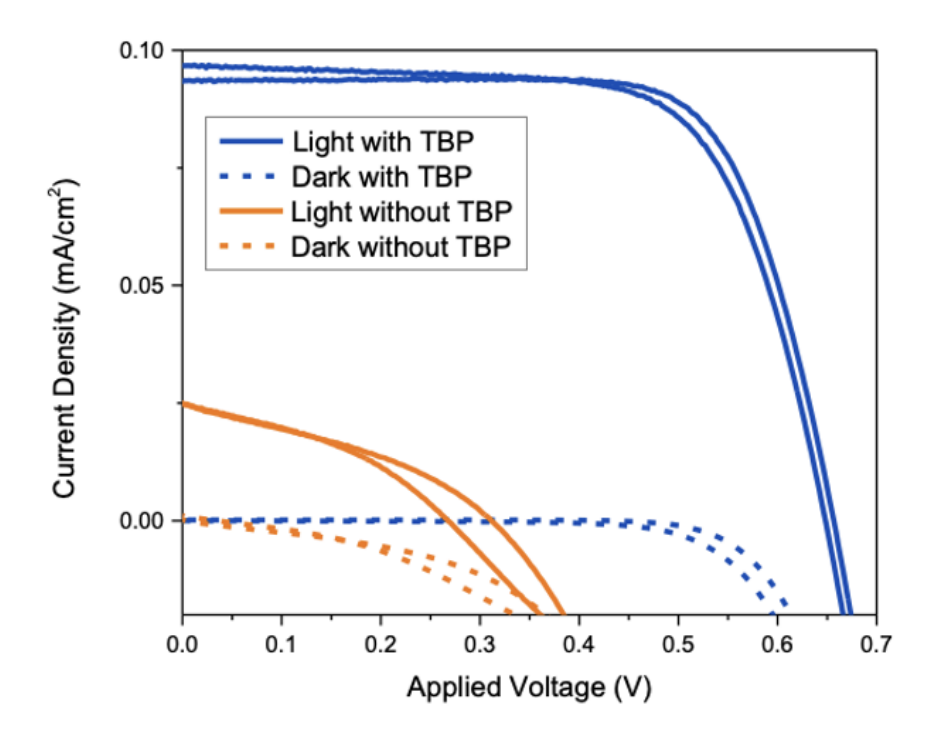
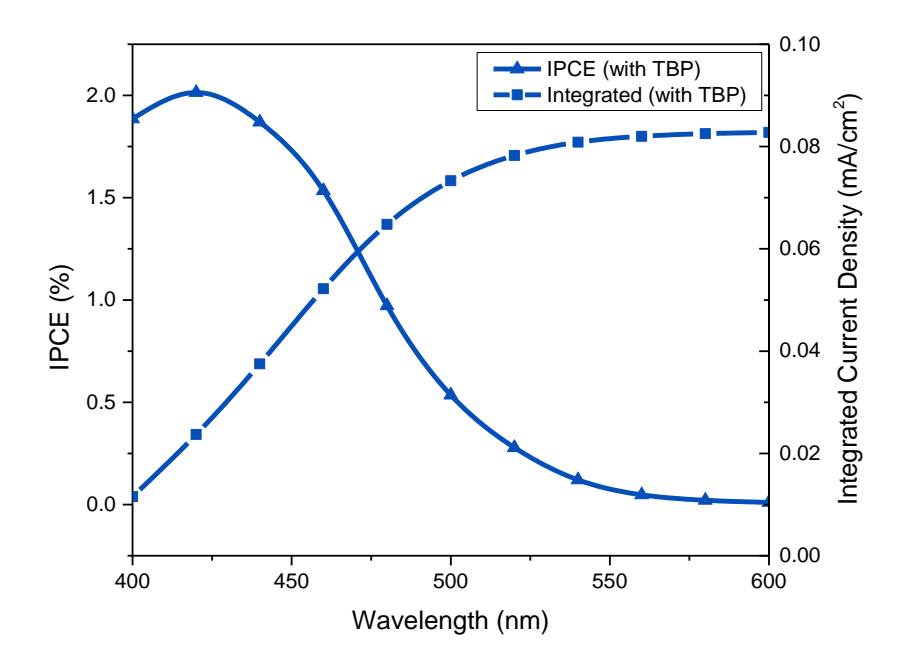


Figure 2.4: (a) Current density vs applied voltage characteristics of retro cells measured under 100mW/cm² illumination (solid lines) and under dark conditions (dotted lines) for [Cu(dsbtmp)₂]^{+/2+} with TBP (dark blue) and without TBP (orange) in the electrolytic solution. (b) Incident photon-to-current conversion efficiency (triangles) and integrated current density (squares) for [Cu(dsbtmp)₂]^{+/2+} retro cells with TBP (c) Incident photon-to-current conversion efficiency (triangles) and integrated current density (solid line) for [Cu(dsbtmp)₂]^{+/2+} retro cells without TBP (d) Light harvesting efficiency and internal quantum efficiency of [Cu(dsbtmp)₂]^{+/2+}.

Figure 2.4 (cont'd)

(b)



(c)

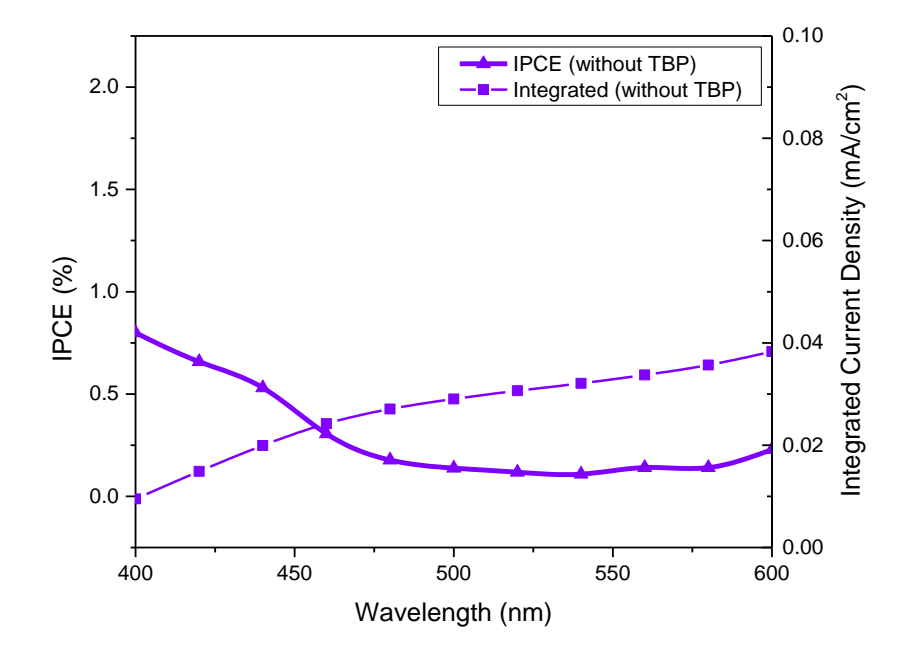
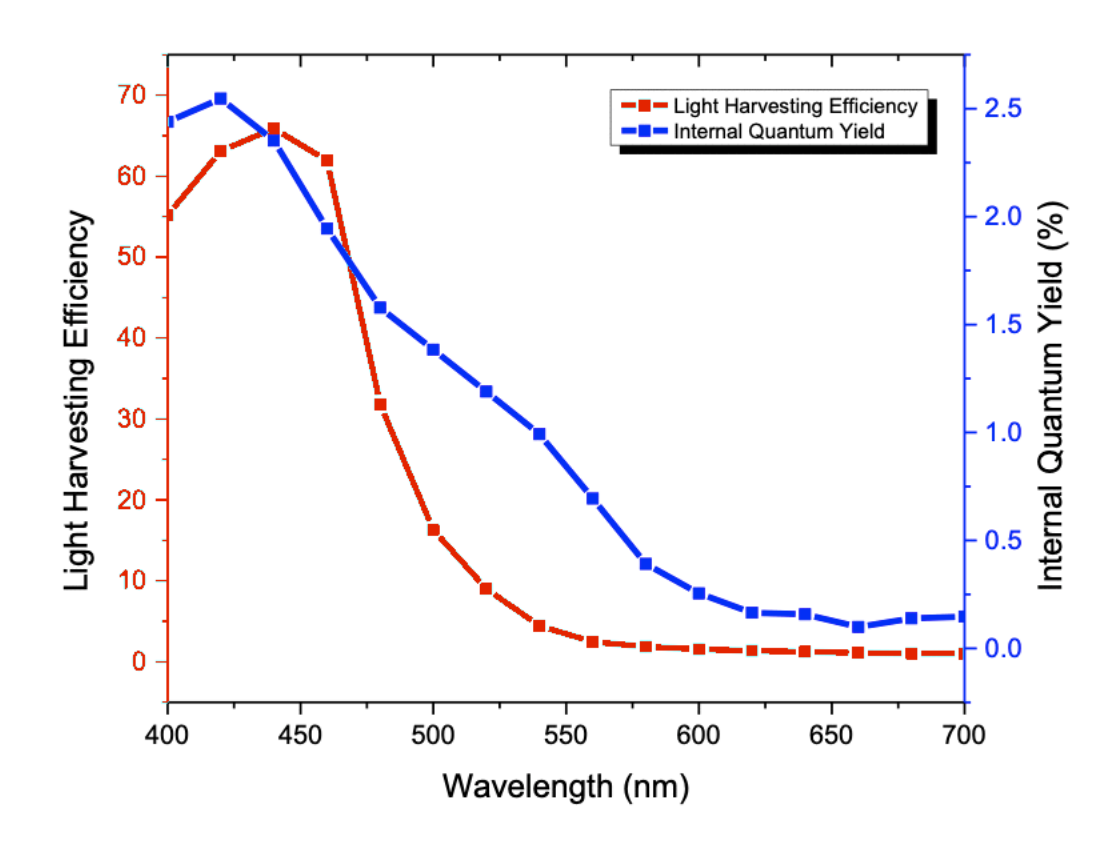


Figure 2.4 (cont'd)

(d)



The presence of TBP has a dramatic effect on the photocurrent and photovoltage that cannot be explained by shifting the band edge or steric hinderance of recombination. Therefore, the interaction of TBP with the copper complexes is likely the dominant effect. The solution potential of the electrolyte without TBP was found to be 0.463 V vs Fc⁺/Fc, consistent with expectations of the Nernst equation. The Nernst equation relates the electrochemical potential of a system to the concentrations of its chemical species. It is crucial in understanding and predicting the behavior of electrochemical cells, including dye-sensitized solar cells (DSSCs), batteries, and other systems involving redox reactions. ^{17–19}

The Nernst equation is written as:

$$E = E^{\circ} - (RT / nF) \ln Q$$

In this equation, E is the cell potential at a given state, and E° represents the standard electrode potential, which applies when all reactants and products are at their standard states, typically 1 M concentration or 1 atm pressure. R is the universal gas constant, equal to 8.314 J mol⁻¹ K⁻¹, and T is the absolute temperature in Kelvin. The term n represents the number of electrons transferred in the redox reaction, while F is the Faraday constant, equal to 96485 C mol⁻¹. Finally, Q is the reaction quotient, the ratio of the concentrations (or partial pressures) of products to reactants raised to their stoichiometric coefficients.

At standard temperature (298 K), the equation is often simplified to:

$$E = E^{\circ} - (0.059 / n) \log Q$$

Here, log Q uses base-10 logarithms, and the constant 0.059 V arises from substituting the values for R, T, and F.

Upon the addition of TBP to the electrolyte, however the solution potential shifts to -0.013 V vs

Fc⁺/Fc. Because the counter electrode is poised at the solution potential and serves as the reference in the 2-electrode configuration, a negative shift in solution potential represents a loss in voltage. The V_{oc} goes up by 300 mV, however, with TBP, even with the nearly ~500 mV change in solution potential. Thus, the Fermi level in TiO₂ at open circuit increases by an incredible 800 mV. A negative 270 mV change in solution potential upon addition of TBP to [Cu(dmbpy)₂]^{2+/+} and a negative 190 mV change in solution potential for [Cu(PDTO)]^{2+/+}, where PDTO is 1,8-bis(2'-pyridyl)-3,6-dithiaoctane, were also reported and attributed to a ligand exchange. ^{16,20} The large change in solution potential observed here thus also suggests a change in composition of the redox active species in the electrolyte. Titrations of the Cu(I) and Cu(II) species with TBP were therefore independently conducted and monitored by cyclic voltammetry (CV) and UV-vis absorption spectroscopy. TBP has no noticeable impact on the Cu(I) species on the timescales of the

measurements, as seen in Figure 2.6 (a). Titrations of the Cu(II) species with TBP, however, indicate a significant effect on the voltammograms and UV-Vis spectra, which are shown in Figure 2.5 (a) and Figure 2.5 (b), respectively. In the CVs, the cathodic return wave diminishes significantly upon addition of TBP. It is hypothesized that TBP substitutes one or both dsbtmp ligands, analogous to prior reports of the less sterically hindered [Cu(dmbpy)₂]^{2+/+}. ¹⁶

(a)

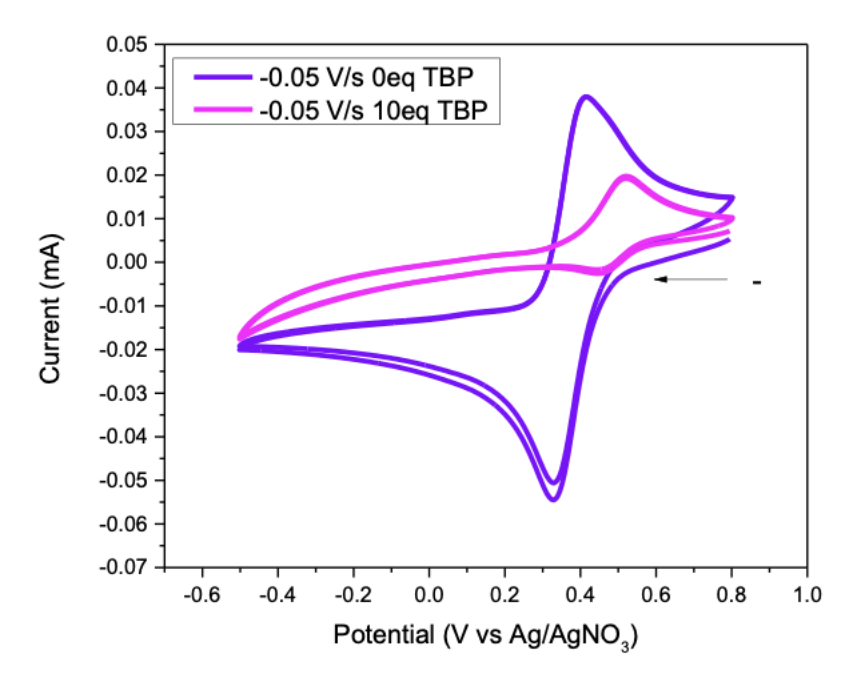
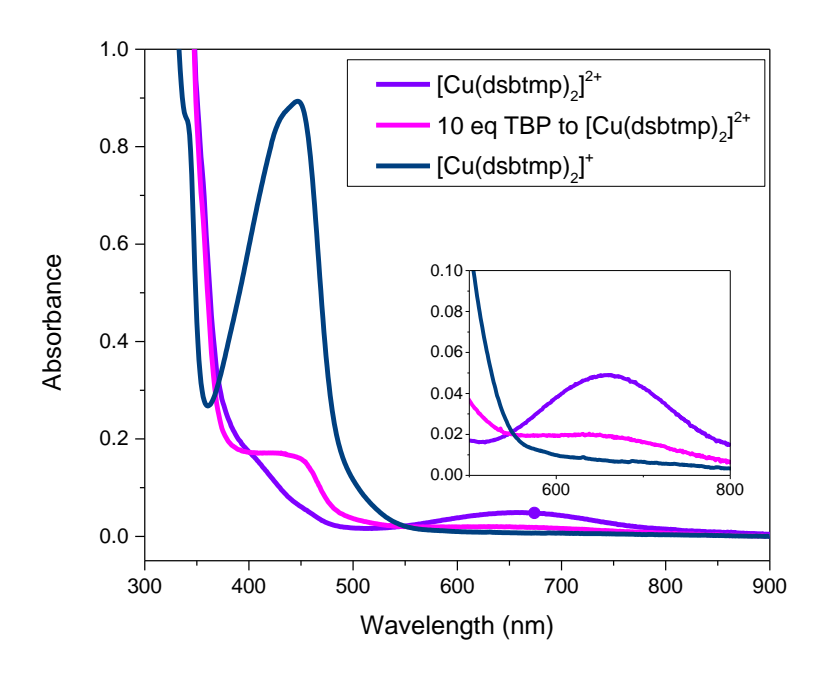


Figure 2.5: (a) Cyclic voltammogram of titration of TBP (equivalents in legend) to 2mM $[Cu(dsbtmp)_2]^{2+}$ in acetonitrile with a scan rate of 0.05 V/s (b) UV-Vis spectra of 0.2 mM each of $[Cu(dsbtmp)_2]^{2+}$ and $[Cu(dsbtmp)_2]^{2+}$ and $[Cu(dsbtmp)_2]^{2+}$ and 20 mM TBP (10 eq).

Figure 2.5 (cont'd)

(b)



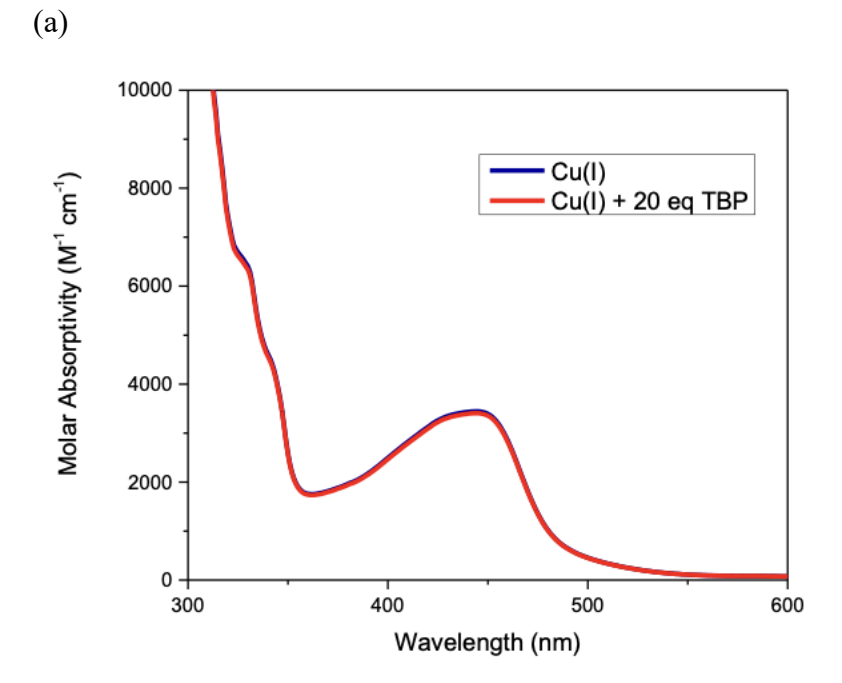
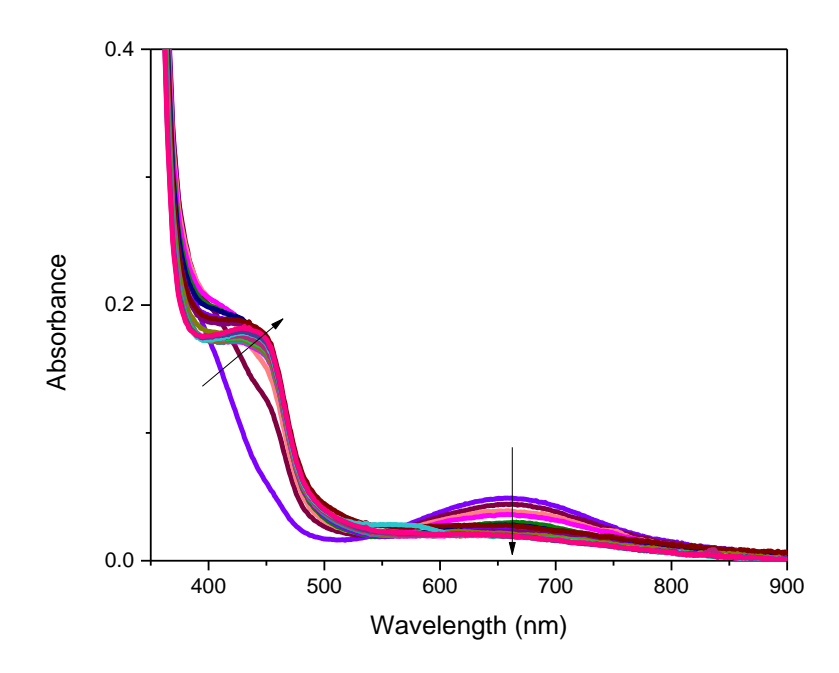


Figure 2.6: (a) UV-Vis spectra showing titration of 20 equiv. TBP to 0.25 mM [Cu(dsbtmp)₂]⁺ in acetonitrile (b) UV-Vis spectra showing titration of TBP (arrow indicates increase in equivalents by 1 from 0 equiv. to 20 equiv.) to 0.25 mM [Cu(dsbtmp)₂]²⁺ in acetonitrile.

Figure 2.6 (cont'd)

(b)



[Cu(dsbtmp)₂]⁺ has its characteristic metal-to-ligand charge transfer (MLCT) peak at 450 nm while the [Cu(dsbtmp)₂]²⁺ absorbs at 660 nm (LMCT) as seen in the UV-vis spectrum in Figure 2.5 (b). Upon titration of various equivalents of TBP to [Cu(dsbtmp)₂]²⁺, the peak at 660 nm disappears concurrent with the growth of a new peak at 450 nm. The presence of an isosbestic point in the spectra indicates the formation of one new species from the [Cu(dsbtmp)₂]²⁺ in the UV-vis measurement timescale. The new species cannot be attributed to the [Cu(dsbtmp)₂]⁺, as the line shape and the absorption coefficients are different. In a previous report we showed displacement of dmbpy ligands of [Cu(dmbpy)₂]²⁺ by TBP to make the [Cu(TBP)₄]²⁺ complex.¹⁶ In order to test this possibility, [Cu(TBP)₄]^{+/2+} complexes were synthesized by previously reported methods.²¹ The UV-vis absorption spectra of the [Cu(TBP)₄]^{+/2+} species are shown in Figure 2.7. [Cu(TBP)₄]²⁺ has a peak at 580 nm and does not match that of the unknown species (Figure 2.5 (b)).

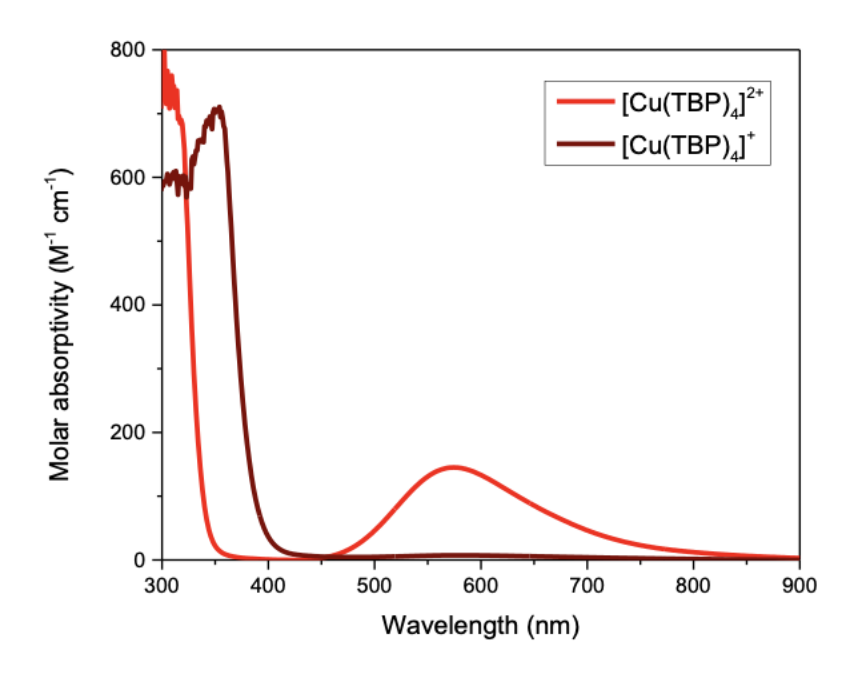


Figure 2.7: UV-Vis spectra of [Cu(TBP)₄]^{2+/+}in acetonitrile.

 1 H-NMR studies were therefore carried out to identify the intermediate species formed. The 1 H-NMR of the [Cu(dsbtmp)₂]²⁺ (Figure 2.8) consists of several broad peaks which is typical of a paramagnetic complex. Upon addition of TBP to the Cu(II) species, peaks assigned to free dsbtmp ligand appear in the spectra. There were some additional peaks in the aromatic region from 7-9 ppm that could not be assigned but are likely from the new complex which is formed (Figure 2.8 (b)). Quantitative 1 H-NMR studies were carried out in which 2.8 mM [Cu(dsbtmp)₂]²⁺ was titrated with 10 equivalents of TBP and a known volume (1 μL) of 1,2-dichloroethane (DCE) was added to the solution (Figure 2.8 (c)). By integrating the aromatic ligand peak at 8.33 ppm and the DCE peak at 3.83 ppm, it was found that 50% of the ligand dissociates from [Cu(dsbtmp)₂]²⁺ which implies that [Cu(dsbtmp)(TBP)_x]^{y+} is the unknown product. To understand the nature of the Cu center of the [Cu(dsbtmp)(TBP)_x]^{y+} species, EPR studies were carried out. The EPR in Figure 2.13 has gx, gy and gz values of 2.2806, 2.1305 and 2.0243 and an R-value of 0.7075 which is indicative of a Cu(II) center. This experiment implies that the species that is formed is the [Cu(dsbtmp)(TBP)_x]²⁺. Thus, the partial ligand substituted complex is crucial in reducing

recombination and enhancing the performance of the retro cells. A schematic to summarize the retro cell and its energy correlations has been shown in figure 2.9.

(a)

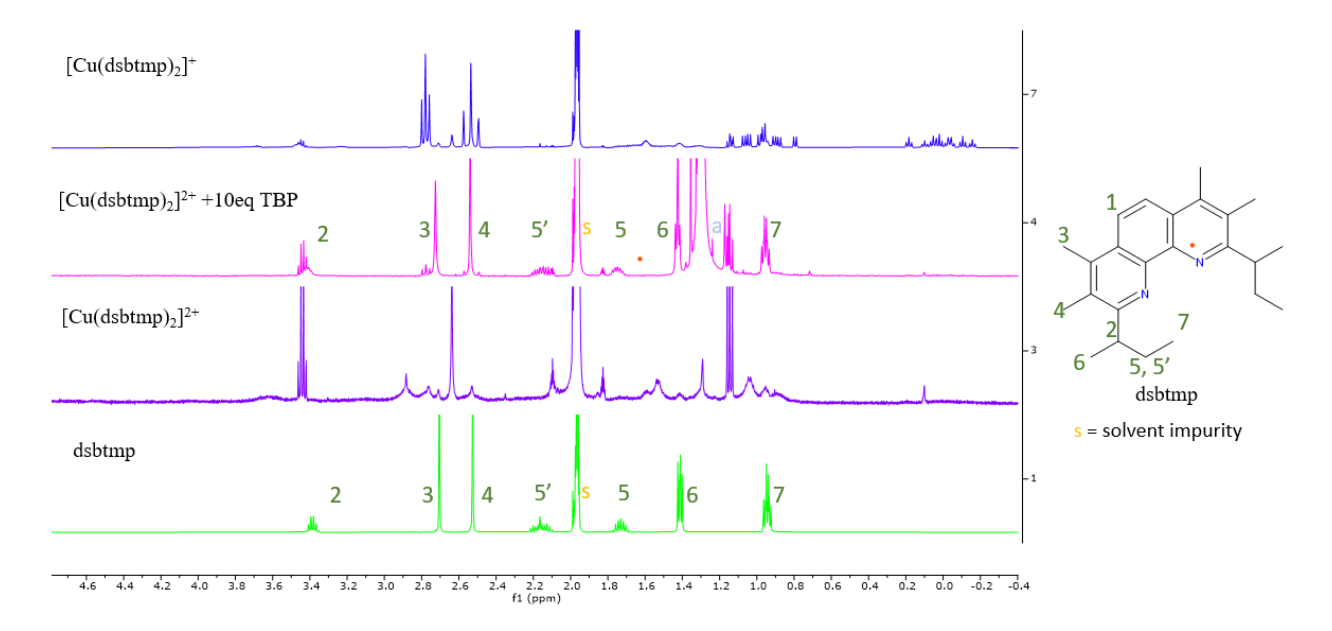
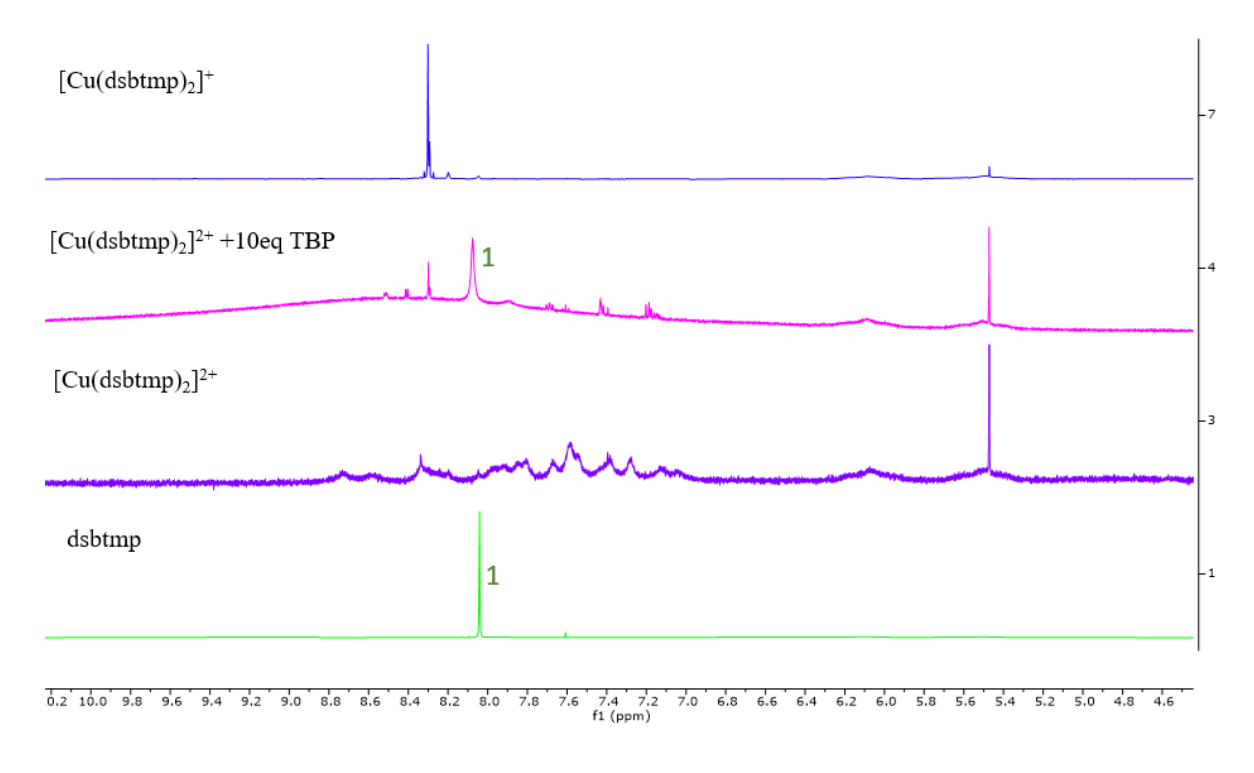


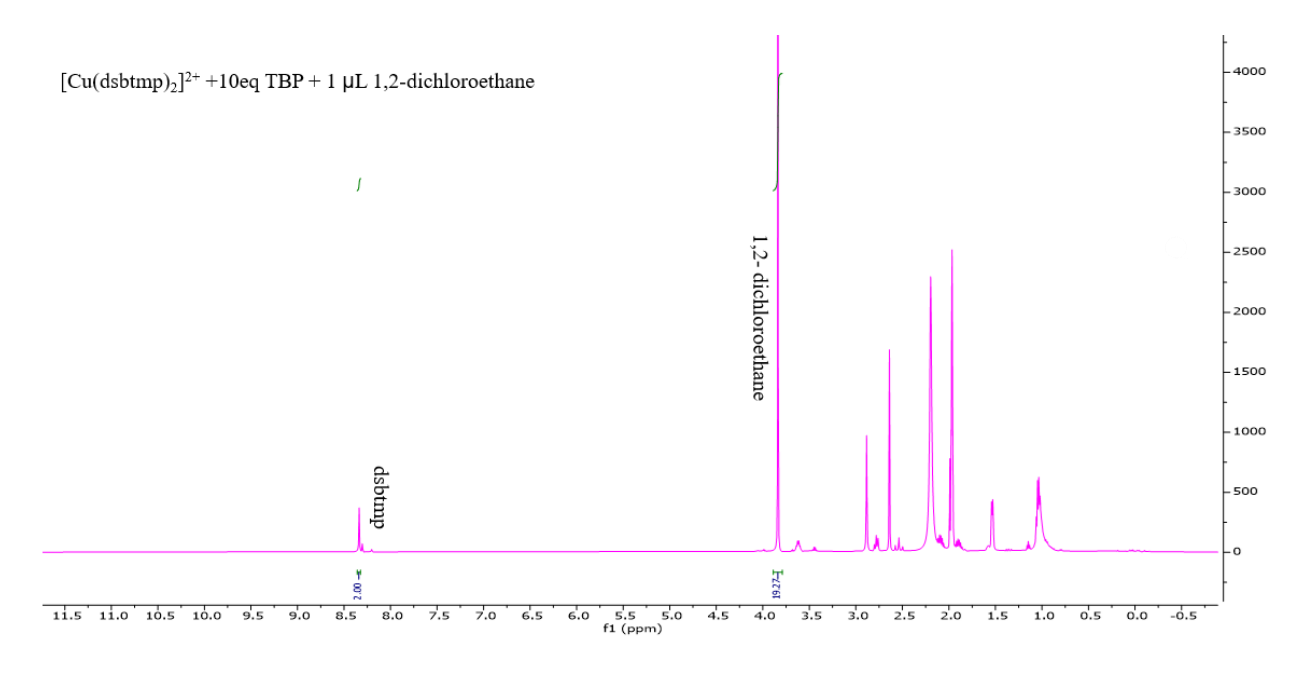
Figure 2.8: (a),(b) ¹H-NMR of dsbtmp, [Cu(dsbtmp)₂]²⁺, [Cu(dsbtmp)₂]⁺ and mixture of 10 equiv. TBP and [Cu(dsbtmp)₂]²⁺in deuterated acetonitrile (b) ¹H-NMR of a mixture of 1,2-dicloroethane, 10 equiv. TBP and [Cu(dsbtmp)₂]²⁺in deuterated acetonitrile (c) ¹H-NMR of a mixture of 1,2-dicloroethane, 10 equiv. TBP and 2.8 mM [Cu(dsbtmp)₂]²⁺in deuterated acetonitrile.

Figure 2.8 (cont'd)

(b)



(c)



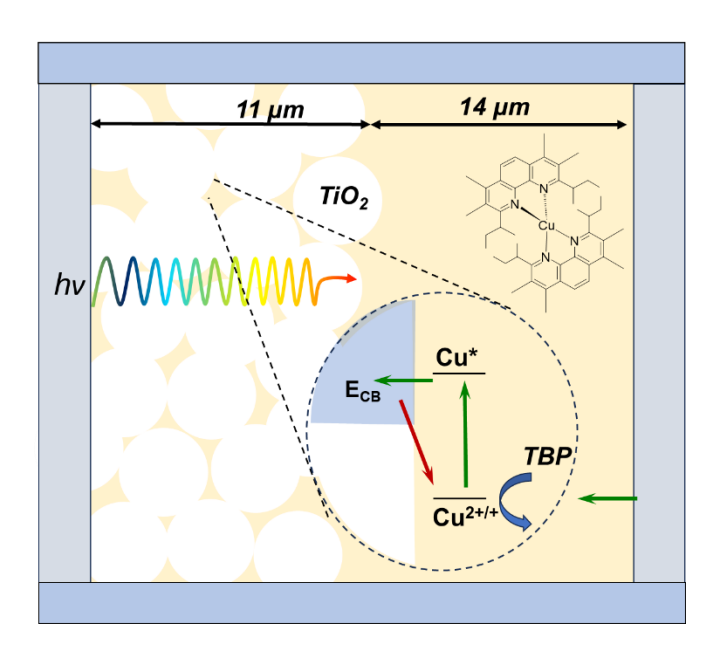


Figure 2.9: Schematic of a retro cell. Following light absorption by the copper complex in the mesoporous photoanode, the excited dye ($E^* = -1.46 \text{ V}$ vs $Fc^{+/0}$) will diffuse to the TiO_2 surface and inject an electron into the conduction band ($E_{CB} = -1.161 \text{ V}$ to -1.336 V vs Fc in acetonitrile 37), and the oxidized dye will diffuse to the counter electrode or be intercepted by TBP in solution.

2.4 Conclusion

In conclusion, the study explores the viability of a new type of solar energy conversion system termed retro cells. $[Cu(dsbtmp)_2]^{2+/+}$ were incorporated as the dye/redox shuttle for the devices and they were measured with and without the base additive TBP. The results demonstrate a remarkable enhancement in device performance with the addition of TBP, showcasing improved V_{OC} , J_{SC} , and η . The study investigates the impact of TBP on the electrolyte, revealing a substantial change in solution potential as well as other spectroscopic changes, suggesting ligand substitution reactions with the Cu(II) species. The ligand substituted complex is a poor acceptor species and hence the recombination is slow. This indicates that slow recombination is essential for device performance. Despite this, the persistence of low currents remains a challenge, primarily attributed to poor

charge separation efficiency. Ongoing efforts are directed towards addressing this issue, with attempts to increase charge separation as the key focus of our current research.

2.5 Materials

All reagents were sourced from commercial suppliers and used as received without further purification. Tetramethyl-1,10-phenanthroline, toluene, sec-butyl-lithium, dichloromethane, manganese dioxide, magnesium sulfate, n- hexane, tetrakis(acetonitrile)copper(I) hexafluorophosphate, diethyl ether, nitrosonium hexafluorophosphate, titanium(IV) chloride solution, ethanol, hydrochloric acid (HCl) and hexachloroplatinic(IV) acid (H₂PtCl₆) were obtained from Sigma Aldrich. Celite was obtained from Jade Scientific.

2,9-di(sec-butyl)-3,4,7,8-tetramethyl-1,10-phenanthroline,dsbtmp and bis(2,9-di(sec-butyl)-3,4,7,8-tetramethyl-1,10-phenanthroline)copper(I) hexafluorophosphate, [Cu(dsbtmp)₂](PF₆) were made following protocols established in the literature.¹⁰ Specific modifications to the synthetic procedures have been detailed in the Supplementary section.

2.6 Synthesis

2,9-Di(sec-butyl)-3,4,7,8-tetramethyl-1,10-phenanthroline (dsbtmp)

The 2,9-di(sec-butyl)-3,4,7,8-tetramethyl-1,10-phenanthroline was synthesized as described in the literature. Tetramethyl-1,10-phenanthroline (8.46 mmol, 2g) was suspended in 30 mL of anhydrous toluene and then was reacted with sec-butyl-lithium (30 ml of 1.45 M) under nitrogen atmosphere at 0°C and stirred overnight at room temperature. The reaction was quenched with water (20.0 ml) and the organic layer was separated. The aqueous layer was extracted three times with dichloromethane (20.0 ml), and the combined organic layers were treated with excess manganese dioxide (50.0 g). This was stirred overnight. It was then gravity filtered through celite.

The filtrate was dried with magnesium sulfate, filtered and the solvent was removed by rotary evaporation. The product was recrystallized with n-hexane. The yield of this reaction is 67% (1.67 g). 1 H NMR (500 MHz, CDCl₃) δ 7.91 (s, 2H), 3.29 (q, J = 6.7, 2H), 2.66 (s, 6H), 2.49 (s, 6H), 2.24 – 2.06 (m, 2H), 1.77 (m, 2H), 1.48 (dd, J = 6.7, 4.4 Hz, 6H), 0.99 (m, 6H).

Scheme 1: Synthesis of 2,9-Di(sec-butyl)-3,4,7,8-tetramethyl-1,10-phenanthroline (dsbtmp)

Bis(2,9-di(sec-butyl)-3,4,7,8-tetramethyl-1,10-phenanthroline)copper(I) hexafluorophosphate

([Cu(dsbtmp)₂](PF₆))

literature. 10 The synthesized described in the copper complex was as Tetrakis(acetonitrile)copper(I) hexafluorophosphate (0.260 g, 0.68 mmol) and dsbtmp (0.5 g, 1.43 mmol) were added to 10mL DCM. The solution was stirred overnight, and the product was precipitated with diethyl ether. The product was then obtained by decantation. The yield of this reaction is 80.4% (0.49 g). ¹H NMR (500 MHz, CDCl₃) δ 8.21 (s, 2H), 3.42 – 3.72 (m, 2H), 2.71 (m, 6H), 2.54 (t, J = 19.1 Hz, 6H), 1.28 (d, J = 13.1 Hz, 4H), 1.12 - 0.77 (m, 6H), 0.24 - -0.17 (m, 6H), 0.6H). Elemental analysis: found (calculated) for C₄₈H₆₄CuF₆N₄P: C, 63.99 (63.66); H, 7.26 (7.12); N, 6.16 (6.19).

$$[Cu(CH_3CN)_4]PF_6$$

Scheme 2: Synthesis of bis(2,9-di(sec-butyl)-3,4,7,8-tetramethyl-1,10-phenanthroline)copper(I) hexafluorophosphate

Bis(2,9-di(sec-butyl)-3,4,7,8-tetramethyl-1,10-phenanthroline)copper(II) bis(hexafluorophosphate) ([Cu(dsbtmp)₂](PF₆)₂)

A solution of [Cu(dsbtmp)₂](PF₆) (0.2 g, 0.24 mmol) of 2mL of dichloromethane was prepared. Another solution of nitrosonium hexafluorophosphate, NOPF₆ (0.15 g, 0.24 mmol) in 2mL dichloromethane was prepared. Both the solutions were mixed, and the reaction was stirred for 30 minutes. The product was precipitated using diethyl ether and then filtered. The yield of this reaction was 78% (0.19 g). Elemental analysis: found (calculated) for C₄₈H₆₄CuF₁₂N₄P₂: C, 54.94 (54.88); H, 6.28 (6.14); N, 5.39 (5.33).

Scheme 3: Synthesis of bis(2,9-di(sec-butyl)-3,4,7,8-tetramethyl-1,10-phenanthroline)copper(II) bis(hexafluorophosphate)

Scheme 4: Synthetic scheme for bis(2,9-di(sec-butyl)-3,4,7,8-tetramethyl-1,10-phenanthroline)copper(II) bis(hexafluorophosphate)summarized from the reactions above

2.7 Device Fabrication

A retro cell consists of a fluorine doped tin oxide (FTO) glass substrate layered with TiO₂ that functions as the photoanode. The thickness of the TiO₂ layer was 8 μ m as determined by profilometry. Another FTO glass substrate layered with Pt catalyst acts as the cathode. These glass substrates are sandwiched together, and the electrolyte is injected through pre-drilled holes on the cathode. The holes are sealed with a cover slip using Surlyn sheets as the sealant. FTO-coated glass (8 Ω sq⁻¹ (TEC 8)) was purchased from Pilkington North America. TiO₂ paste was purchased from Greatcell Solar Materials Pty Ltd. Surlyn with a dimension of 25 μ m was procured from Solaronix. The TEC 8 FTO substrates were sectioned into pieces measuring 1.5 cm by 2 cm. These sections underwent a 15-minute sonication process in soapy DI water, followed by manual scrubbing using Kimwipes. Subsequently, a 10-minute sonication in DI water, along with rinsing in acetone and a 10-minute sonication in isopropanol, was carried out. After air-drying, the sections were immersed in an aqueous 40 mM TiCl₄ solution at 70 °C for 30 minutes. Following this, the sections were promptly rinsed with 18 M Ω water and subjected to annealing, involving heating from room temperature to 500 °C, followed by a 30-minute hold at 500 °C.

Then, a specific area of 0.36 cm² was layered with a commercial 30 nm TiO₂ nanoparticle paste (DSL 30NRD) by doctor blading. The resultant transparent films were allowed to sit undisturbed for a period of 10 minutes before being placed within a 100 °C oven for 15 minutes. The oven's temperature was then incrementally increased, reaching 325 °C for 5 minutes, followed by 375 °C for 5 minutes, 450 °C for 5 minutes, and finally, 500 °C for 15 minutes.

For making a platinum counter electrode, the following steps were undertaken: firstly, two holes were drilled into a sheet of TEC 8 FTO. The FTO was then sonicated in a soap solution, followed by a 5-minute sonication in DI water. It was then rinsed with a 0.1M HCl solution in ethanol (~1

mL concentrated HCl in 100 ml) and subjected to a 10-minute sonication in an acetone bath. Following this, any residual organic contaminants were removed by heating the material in air at approximately 400°C for about 15 minutes. The next step was coating it with around 0.5 drop/cm² of a 5mM H₂PtCl₆ solution in isopropanol. The material was then quickly tilted to spread the solution and allowed to dry without exposure to a breeze for a duration of 5 minutes. Lastly, the material was subjected to a heat treatment at 380°C for 20 minutes, after which it was removed from the heat source and allowed to cool while covered in ambient conditions. The assembly process involved sandwiching the working and counter electrodes using 25 µm surlyn films. This was accomplished by placing them onto a hotplate at 140 °C and applying pressure while the Surylyn melted. Contact was established with the TiO₂ electrode by gently scratching its edge with sandpaper and then applying melted indium. Similarly, melted indium was applied to the counter electrode. The indium was left to dry for 15 minutes. Then, the cells were filled with electrolyte via one of two predrilled holes and then sealed. This sealing process was executed by employing 25 µm surlyn, backed by a glass coverslip, and applying heat to achieve an airtight seal. Two sets of electrolytic conditions were measured. For the first set, the electrolyte consisted of

Two sets of electrolytic conditions were measured. For the first set, the electrolyte consisted of 0.15 M Cu(I), 0.01 M Cu(II) and 0.1 M lithium hexafluorophosphate (LiPF₆) in dry acetonitrile. For the second set, the electrolyte consisted of 0.15 M Cu(I), 0.01 M Cu(II), 0.1 M LiPF₆ and 0.5 M 4-tert-butyl pyridine(TBP) in dry acetonitrile. Cells were measured approximately 1 hour after fabrication. Six solar cells were measured for each electrolyte condition.

2.8 Instrumentation

An AM 1.5 solar filter was employed to replicate sunlight conditions at 100 mW cm⁻², and the light intensity was calibrated using an accredited reference cell system (Oriel Reference Solar Cell & Meter). In order to prevent direct excitation of the TiO₂ during light measurements, a 400 nm

long-pass filter was incorporated. A black mask, with an open area measuring 0.12 cm², was placed on the cell which acts as the active region. The devices' solution potential was determined by immersing a platinum wire and the Ag/AgNO₃ electrode into the electrolyte, while subsequently measuring the potential between these electrodes. For monochromatic light used in IPCE (incident photon-to-current efficiency) measurements, a monochromator (Horiba Jobin Yvon MicroHR) coupled with a 450 W xenon arc light source was used. The photon flux of the light directed onto the samples was measured via a laser power meter (Nova II Ophir). IPCE measurements were conducted in 20 nm intervals across the range of 400 to 600 nm, focusing on the short circuit current.

2.9 Electrochemistry

All the electrochemical measurements were performed using 0.1M lithium hexafluorophosphate in acetonitrile. They were carried out in an inert atmosphere in the glovebox. The cyclic voltammetry measurements were performed using a µAutolabIII potentiostat with a three-electrode system- glassy carbon as the working electrode, platinum mesh as a counter electrode and Ag/AgNO₃ as the reference electrode. The cyclic voltammetry measurements were carried out using 2mM solution of each complex.

2.10 Room Temperature Spectroscopy

Absorption spectra for the complexes were acquired using a PerkinElmer Lambda 35 UV-vis spectrometer and 1 cm path length quartz cuvettes at 480 nm min⁻¹. Solution concentration of 0.2mM was used for each complex. Steady state emission spectra were obtained using Horiba Jobin Yvon Fluorolog Spectrofluorometer. The measurements were performed at room temperature.

Time resolved emission measurements for the complexes were carried out in Edinburgh Instruments LP980 transient Absorption Spectrometer. The measurements were carried out using 10mM solution of each complex using acetonitrile as the solvent. Transient absorption data was collected under the guidance of Dr. Karl Nielsen using an ultrafast laser spectroscopy setup designed to capture excited-state dynamics with high temporal resolution. The measurements involved femtosecond pump-probe techniques, where a pump pulse excited the sample, and a delayed probe pulse monitored the resulting transient absorption changes over time. This allowed for the characterization of excited-state lifetimes, charge carrier dynamics, and energy transfer processes. Data acquisition and analysis required precise calibration, background correction, and kinetic modeling to extract meaningful insights. Given the technical complexity, Dr. Nielsen's expertise was instrumental in optimizing experimental parameters and ensuring accurate interpretation of results.

2.11 Single Crystal X-Ray Crystallography

Single crystals were grown in dichloromethane with slow diethyl ether diffusion over the course of three days. A suitable crystal with dimensions $0.12 \times 0.12 \times 0.05$ mm³ was selected and mounted on a nylon loop with paratone oil on a XtaLAB Synergy, Dualflex, HyPix diffractometer. The crystal was kept at a steady T = 100.00(10) K during data collection. The structure was solved with the ShelXT (Sheldrick, 2015) solution program using dual methods and by using Olex2 1.3 (Dolomanov et al., 2009) as the graphical interface. The model was refined with ShelXL 2018/3 (Sheldrick, 2015) using full matrix least squares minimization on F^2 .

2.12 Light harvesting efficiency (LHE)

LHE was calculated using the following equation:

A=-logT, where A is the absorbance and T is the transmittance of the incident light.

LHE= 1-R-T, where R is the reflectance of the substrate. The reflectance of the electrodes were previously found to be 20%. ¹⁷

Transmittance is the ratio of transmitted light through the solar cell to the total incident light on the solar cell. About 80% of the incident light goes through the TiO₂/electrolyte layer, thus the equation becomes:

LHE= 1-R-T = 1 - 0.2 - T= 0.8 - T= $0.8 - 0.8 (10^{-A*P})$ where P is the porosity of the TiO₂ film (50%)

= $0.8 - 0.8 \ (10^{-} e^{*C^*l^*P})$ where ϵ is the molar absorptivity of the electrolyte, C is the concentration of the electrolytic solution, l is the path length of light through TiO₂ film measured by profilometry (11 μ m).

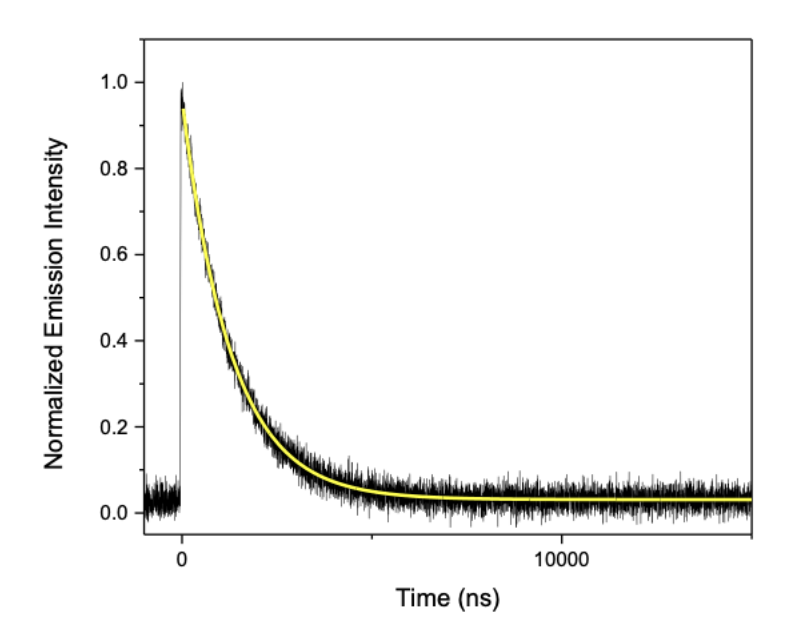


Figure 2.10: Time-resolved emission spectrum of 2mM [Cu(dsbtmp)₂](PF₆) in acetonitrile.

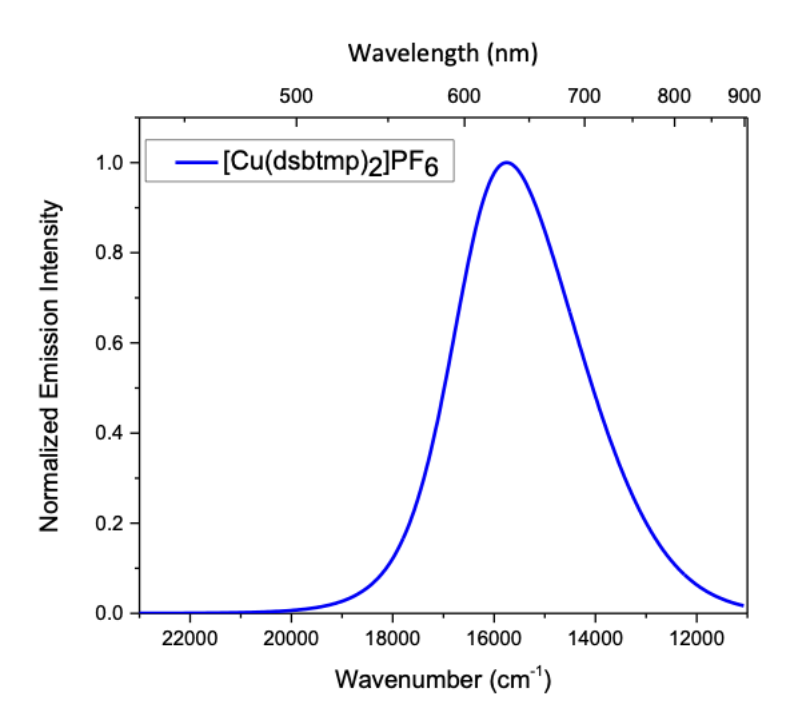


Figure 2.11: Steady-state emission spectrum of 2mM [Cu(dsbtmp)₂](PF₆) in acetonitrile.

2.13 Cyclic voltammetry

Cyclic voltammograms of $[Cu(dsbtmp)_2](PF_6)$ were measured at different scan rates, as shown in Figure 2.12 (a). The peak current vs square root of scan rate was plotted, shown in Figure 2.12 (b). The potentials are reported relative to $Fc^{+/0}$.

$$i_p = 0.446 nFAC^0 \left(\frac{nFvD}{RT}\right)^{1/2}$$
 (1)

where n is the number of electrons transferred in the redox reaction, A is the surface area of the electrode, C^0 is the concentration of the bulk solution and D is the diffusion coefficient of analyte. Equation 1 and the slope of the plot in Figure 2.12 (b) was used to calculate the diffusion coefficient, which was found to be 6.2×10^{-5} cm² s⁻¹.

The diffusion length or the distance of diffusion of a species is given by the following equation 18:

$$L = (D.\tau)^{1/2} \tag{2}$$

where L is the diffusion length; D is the diffusion coefficient of the species and τ is the lifetime in seconds.

For excited [Cu(dsbtmp)₂](PF₆), the diffusion length is found to be 60 nm. The lifetime of the complex was measured to be 1.5 µs from time resolved emission spectrum of the complex as shown in figure 2.10, which aligned with that reported in literature.¹⁰ The diffusion length provides insight into the distance over which the excited molecules can diffuse within the retro cells before the semiconductor is reached, facilitating the injection of an electron into the semiconductor's conduction band. This diffusion to the semiconductor must occur before it decays to its ground state. Usually, TiO₂ nanoparticles that are used as semiconductors in DSSCs have a size of about 25 nm, which indicates that these excited copper complexes should have sufficient time for diffusion and charge injection into the semiconductor.

(a)

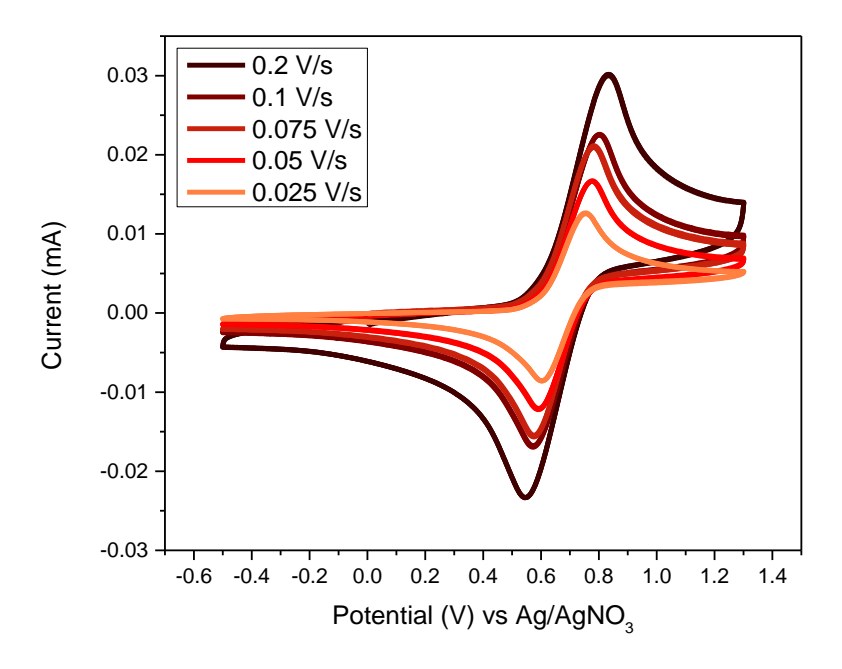
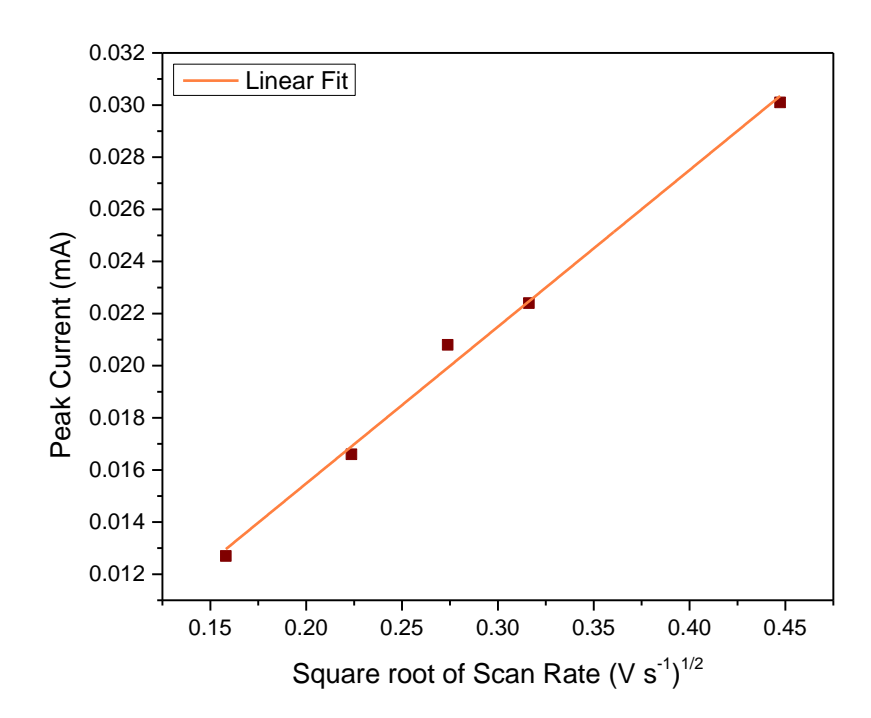


Figure 2.12: (a) Cyclic voltammogram of $[Cu(dsbtmp)_2]^{2+}$ in acetonitrile with different scan rates shown in legend (b) Scan rate dependence (peak current vs square root of scan rate) of $[Cu(dsbtmp)_2]^{2+}$ in acetonitrile.

Figure 2.12 (cont'd)

(b)



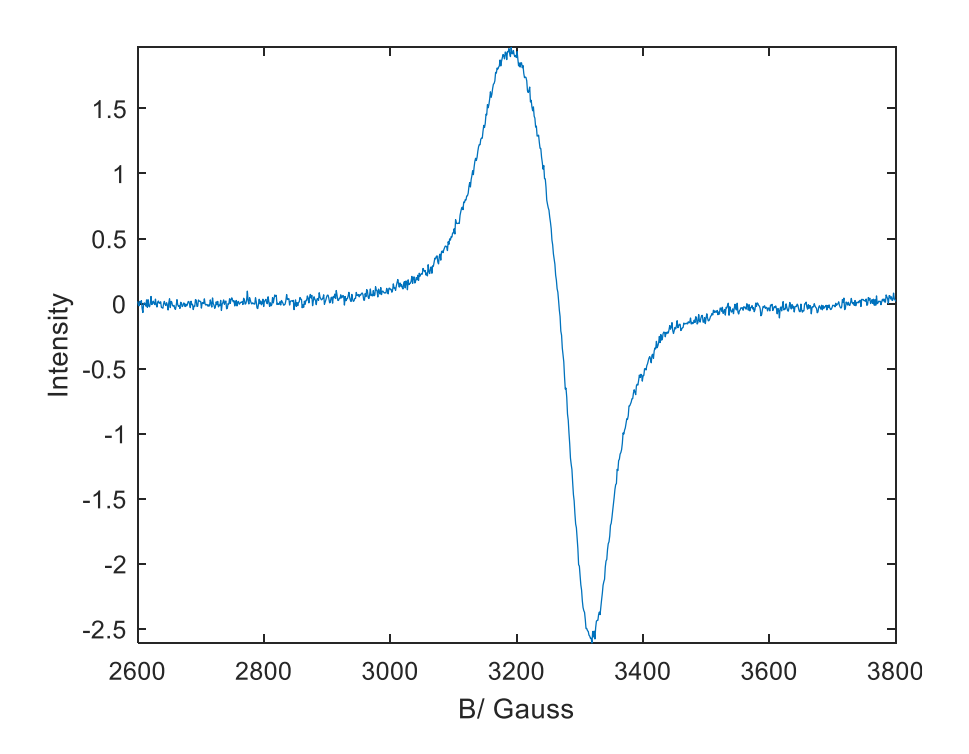


Figure 2.13: EPR of a mixture of [Cu(dsbtmp)₂]²⁺ and 20 equiv. TBP in acetonitrile.

REFERENCES

- (1) Dragonetti, C.; Magni, M.; Colombo, A.; Melchiorre, F.; Biagini, P.; Roberto, D. Coupling of a Copper Dye with a Copper Electrolyte: A Fascinating Springboard for Sustainable Dye-Sensitized Solar Cells. ACS Appl Mater Interfaces **2018**, 1 (2), 751–756. https://doi.org/10.1021/ACSAEM.7B00196/ASSET/IMAGES/LARGE/AE-2017-00196R 0003.JPEG.
- (2) Karpacheva, M.; Malzner, F. J.; Wobill, C.; Büttner, A.; Constable, E. C.; Housecroft, C. E. Cuprophilia: Dye-Sensitized Solar Cells with Copper(I) Dyes and Copper(I)/(II) Redox Shuttles. Dyes and Pigments **2018**, 156, 410–416. https://doi.org/10.1016/J.DYEPIG.2018.04.033.
- (3) Clark, W. D. K.; Sutin, N. Spectral Sensitization of N-Type TiO2 Electrodes by Polypyridineruthenium(II) Complexes. J Am Chem Soc 1977, 99 (14), 4676–4682. https://doi.org/10.1021/ja00456a025.
- (4) Barichello, J.; Gullace, S.; Cusimano, A.; Di Marco, G.; Matteocci, F.; Calogero, G. A Photoelectrochemical Study of Hybrid Organic and Donor—Acceptor Dyes as Sensitizers for Dye-Sensitized Solar Cells. Applied Sciences 2022, Vol. 12, Page 3159 **2022**, 12 (6), 3159. https://doi.org/10.3390/APP12063159.
- (5) McCusker, C. E.; Castellano, F. N. Design of a Long-Lifetime, Earth-Abundant, Aqueous Compatible Cu(I) Photosensitizer Using Cooperative Steric Effects. Inorg Chem **2013**, 52 (14), 8114–8120. https://doi.org/10.1021/ic401213p.
- (6) Saygili, Y.; Söderberg, M.; Pellet, N.; Giordano, F.; Cao, Y.; Munoz-García, A. B.; Zakeeruddin, S. M.; Vlachopoulos, N.; Pavone, M.; Boschloo, G.; Kavan, L.; Moser, J. E.; Grätzel, M.; Hagfeldt, A.; Freitag, M. Copper Bipyridyl Redox Mediators for Dye-Sensitized Solar Cells with High Photovoltage. J Am Chem Soc 2016, 138 (45), 15087–15096. https://doi.org/10.1021/JACS.6B10721/ASSET/IMAGES/LARGE/JA-2016-107219 0009.JPEG.
- (7) Rodrigues, R. R.; Lee, J. M.; Taylor, N. S.; Cheema, H.; Chen, L.; Fortenberry, R. C.; Delcamp, J. H.; Jurss, J. W. Copper-Based Redox Shuttles Supported by Preorganized Tetradentate Ligands for Dye-Sensitized Solar Cells. Dalton Transactions **2020**, 49 (2), 343–355. https://doi.org/10.1039/C9DT04030G.
- (8) Cao, Y.; Saygili, Y.; Ummadisingu, A.; Teuscher, J.; Luo, J.; Pellet, N.; Giordano, F.; Zakeeruddin, S. M.; Moser, J. E.; Freitag, M.; Hagfeldt, A.; Grätzel, M. 11% Efficiency Solid-State Dye-Sensitized Solar Cells with Copper(II/I) Hole Transport Materials. Nat Commun **2017**, 8. https://doi.org/10.1038/NCOMMS15390.
- (9) Yum, J. H.; Baranoff, E.; Kessler, F.; Moehl, T.; Ahmad, S.; Bessho, T.; Marchioro, A.; Ghadiri, E.; Moser, J. E.; Yi, C.; Nazeeruddin, M. K.; Grätzel, M. A Cobalt Complex Redox Shuttle for Dye-Sensitized Solar Cells with High Open-Circuit Potentials. Nat Commun **2012**, 3. https://doi.org/10.1038/NCOMMS1655.
- (10) Tian, H.; Yu, Z.; Hagfeldt, A.; Kloo, L.; Sun, L. Organic Redox Couples and Organic Counter Electrode for Efficient Organic Dye-Sensitized Solar Cells. J Am Chem Soc **2011**,

- 133 (24), 9413–9422. https://doi.org/10.1021/JA2030933/SUPPL_FILE/JA2030933_SI_001.PDF.
- (11) Sapp, S. A.; Elliott, C. M.; Contado, C.; Caramori, S.; Bignozzi, C. A. Substituted Polypyridine Complexes of Cobalt(II/III) as Efficient Electron-Transfer Mediators in Dye-Sensitized Solar Cells. J Am Chem Soc **2002**, 124 (37), 11215–11222. https://doi.org/10.1021/JA027355Y.
- (12) Hagfeldt, A.; Boschloo, G.; Sun, L.; Kloo, L.; Pettersson, H. Dye-Sensitized Solar Cells. Chem Rev **2010**, 110 (11), 6595–6663. https://doi.org/10.1021/CR900356P.
- (13) Yang, L.; Powell, D. R.; Houser, R. P. Structural Variation in Copper(I) Complexes with Pyridylmethylamide Ligands: Structural Analysis with a New Four-Coordinate Geometry Index, T4. Dalton Transactions **2007**, No. 9, 955–964. https://doi.org/10.1039/B617136B.
- (14) Nazeeruddin, M. K.; Kay, A.; Rodicio, I.; Humphry-Baker, R.; Müller, E.; Liska, P.; Vlachopoulos, N.; Grätzel, M. Conversion of Light to Electricity by Cis-X2Bis (2,2'-Bipyridyl-4,4'-Dicarboxylate) Ruthenium (II) Charge-Transfer Sensitizers (X = Cl-, Br-, I-, CN-, and SCN-) on Nanocrystalline TiO2 Electrodes. J Am Chem Soc 1993, 115 (14), 6382–6390. https://doi.org/10.1021/JA00067A063/ASSET/JA00067A063.FP.PNG_V03.
- (15) Boschloo, G.; Häggman, L.; Hagfeldt, A. Quantification of the Effect of 4-Tert-Butylpyridine Addition to I -/I3- Redox Electrolytes in Dye-Sensitized Nanostructured TiO2 Solar Cells. Journal of Physical Chemistry B **2006**, 110 (26), 13144–13150. https://doi.org/10.1021/JP0619641/SUPPL_FILE/JP0619641SI20060515_124641.PDF.
- (16) Wang, Y.; Hamann, T. W. Improved Performance Induced by in Situ Ligand Exchange Reactions of Copper Bipyridyl Redox Couples in Dye-Sensitized Solar Cells. Chemical Communications **2018**, 54 (87), 12361–12364. https://doi.org/10.1039/C8CC07191H.
- (17) Stock, J. T.; Orna, M. V; of the History of Chemistry, A. C. Society. D.; of Analytical Chemistry, A. C. Society. D.; Meeting, A. C. Society.; John T. Stock, M. V. O. Electrochemistry, Past and Present, Copyright. Electrochemistry, Past and Present 1989.
- (18) Morrison, S. R. Electrochemistry at Semiconductor and Oxidized Metal Electrodes. Electrochemistry at Semiconductor and Oxidized Metal Electrodes 1980. https://doi.org/10.1007/978-1-4613-3144-5.
- (19) Bard, A. J.; Faulkner, L. R. Allen J. Bard and Larry R. Faulkner, Electrochemical Methods: Fundamentals and Applications, New York: Wiley, 2001, 2nd Ed. Russian Journal of Electrochemistry **2002**, 38 (12), 1364–1365. https://doi.org/10.1023/A:1021637209564.
- (20) Hoffeditz, W. L.; Katz, M. J.; Deria, P.; Cutsail, G. E.; Pellin, M. J.; Farha, O. K.; Hupp, J. T. One Electron Changes Everything. A Multispecies Copper Redox Shuttle for Dye-Sensitized Solar Cells. Journal of Physical Chemistry C **2016**, 120 (7), 3731–3740. https://doi.org/10.1021/ACS.JPCC.6B01020/SUPPL_FILE/JP6B01020_SI_002.CIF.
- (21) Kim, T. Y.; Suh, E. H.; Firestone, E.; Raithel, A. L.; Xu, C. Q.; Ke, X.; Yun, D. J.; Jang, J.; McCracken, J.; Hamann, T. W. Metal Complex Molecular Solids Showing Band-like Transport Driven by In Situ Ligand Exchange. Chemistry of Materials **2023**, 35, 41.

- https://doi.org/10.1021/ACS.CHEMMATER.3C00686/ASSET/IMAGES/LARGE/CM3C00686-0007.JPEG.
- (22) Xie, Y.; Baillargeon, J.; Hamann, T. W. Kinetics of Regeneration and Recombination Reactions in Dye-Sensitized Solar Cells Employing Cobalt Redox Shuttles. Journal of Physical Chemistry C **2015**, 119 (50), 28155–28166. https://doi.org/10.1021/ACS.JPCC.5B08244.

Chapter 3: Charge Separation and Base Additives

3.1 Bases in DSSCs

The idea of copper complexes as redox couples in DSSCs stemmed from the pivotal role of blue copper proteins in nature, acting as proficient mediators for electron transfer within the photosynthetic system.^{1,2} These proteins create an environment that facilitates electron transfer by constraining the geometric transition from the preferred tetrahedral coordination of Cu(I) to the square-planar Cu(II), thereby reducing the energy barrier associated with this oxidation process. In an attempt to replicate this natural mechanism, Hattori et al. achieved efficiencies of up to 1.4% under 100 mW cm⁻² solar irradiation in DSSCs. The redox shuttle that was used in their study was [Cu(dmp)₂][CF₃SO₃]_{1/2} (2,9-dimethyl-1,10-phenanthroline).³ The electrolytes utilized in most DSSCs investigations so far share a common feature: they incorporate 4-tert-butylpyridine (TBP) and Li⁺-salts as additives.^{3,4}

In 1993, Grätzel and his colleagues first introduced TBP into DSSCs revealing a significant enhancement in the open-circuit voltage (V_{oc}) when combined with LiI-based electrolytes.⁵ The study revealed a shift in the titania band edge towards higher energy levels. Further studies by Haque et al. delved into the impact of TBP and lithium cations on the shift of TiO₂ conduction band and trap levels, as well as on recombination kinetics between electrons in TiO₂ and oxidized dye molecules.⁶ The observed changes in kinetics were attributed to alterations in TiO₂ energy levels. By employing charge extraction and electron lifetime measurements, this enhancement could be ascribed to the displacement of the TiO₂ band edge towards negative potentials, responsible for 60% of the voltage increase, along with a lengthening of the electron lifetime, contributing to the remaining 40%.⁷ In-depth analysis via in situ Raman spectroscopy

demonstrated TBP's binding to the titania surface, potentially interacting with iodine or dye molecules, further supported by surface analysis studies proposing a defect covering hypothesis. Extensive research by Kusama, Arakawa, and collaborators explored the effects of nitrogendonating additives, including pyrimidines, aminotriazoles, quinolines, benzimidazoles, alkylaminopyridines, alkylpyridines and aminothiazoles. The effects of these additives were found to involve both the titania surface and interactions with redox couple components. Computational studies supported experimental findings, indicating a shift in the TiO₂ conduction band to higher energies due to nitrogen-containing additives, consistent with experimental observations.

In case of copper electrolytes in DSSCs, it has also been shown that TBP undergoes ligand substitution reactions with some Cu(II) species which results in reduction of recombination and improvement in device performance. The outstanding reported performance, with an energy conversion efficiency of approximately 15%, observed for [Cu(dmbpy)₂]^{2+/+} (dmbpy = 6,6'-dimethyl-2,2'-bipyridine) in DSSCs, can be elucidated by a ligand exchange reaction involving the Cu(II) species. This phenomenon was investigated, demonstrating that the presence of TBP in [Cu(dmbpy)₂]^{2+/+} electrolytes induces a ligand substitution reaction with [Cu(dmbpy)₂]²⁺, yielding the [Cu(TBP)_x]²⁺/[Cu(dmbpy)₂]⁺ redox species in solution. This ligand exchange has several implications, with the primary one being the formation of a less effective electron acceptor, [Cu(TBP)_x]²⁺, which mitigates recombination, thereby enabling quantitative charge collection. While Cu(I) d¹⁰ complexes typically exhibit a tetrahedral geometry with four-coordinate arrangements, Cu(II) d⁹ complexes often adopt a 5–6 coordinate structure characterized by a flattened Jahn–Teller distorted geometry. In this geometry, the axial ligands are elongated compared to the equatorial Cu-ligand bonds. It's known that Lewis bases can coordinate to Cu(II)

bisphenanthroline complexes, a process that occurs rapidly, within the picosecond time scale, leading to the formation of exciplexes. 11–13

An analogous effect to TBP was observed in literature during the titration of $[Cu(dmp)_2]^{2+}$ with N-methylbenzimidazole (NMBI), another Lewis base known for its similar effects to TBP as an electrolyte additive for DSSCs. However, when $[Cu(dmp)_2]^{2+}$ was titrated with trifluoromethylpyridine (TFMP), only minor spectral changes were observed. 14-17

Ashbrook and Elliott discovered that TBP acts as a kinetic trap for Cu(II) complexes, temporarily inhibiting their reduction to Cu(I) in DSSCs. ¹⁸ Similarly, Saygili et al. and Kavan et al. noted a more intricate electrochemistry in bipyridyl-based redox couples $[Cu(dmby)_2]^{+/2+}$ and $[Cu(tmby)_2]^{+/2+}$ (where dmbpy = 6,6'-dimethyl-2,2'-bipyridine and tmby = 6,6',4,4'-tetramethyl-2,2'-bipyridine), respectively. Moreover, they observed a shift in the redox potential of $[Cu(dmp)_2]^{+/2+}$ with the addition of TBP. ¹⁹

3.2 Retro cells and charge separation

Chapter 2 provides a comprehensive examination of the operation, benefits, and challenges associated with retro cells. One significant concern regarding charge injection in retro cells pertains to the electronic coupling between the dye and the semiconductor. It is hypothesized that upon contact between the photoexcited dye and the TiO₂ surface, charge transfer should occur adiabatically, and injection should be quantitative, a phenomenon observed by Clark and Sutin.²⁰ However, a notable distinction lies in the presence of TBP in the electrolyte. This compound is utilized as a potential-determining additive and has been demonstrated to mitigate recombination by binding to the TiO₂ surface. In conventional DSSCs, this binding does not impede charge separation since the dye is firmly bound to the TiO₂.^{21,22} However, in retro cells, the presence of TBP on the surface may hinder the close proximity of the dye to the surface, potentially serving as

a spacer layer with a tunneling barrier. Consequently, this could substantially diminish the charge injection process. In this study, some Lewis bases have been studied to understand their roles in retro cells (as well as DSSCs) with [Cu(dsbtmp)₂]^{+/2+} complexes and the charge injection challenge has been explored.

The structures of the bases used in this study are given in figure 1. The base 4-tert-butylpyridine (TBP) (figure 1 (a)) was chosen because it is one of the most common bases used in DSSCs. As mentioned in Chapter 2, TBP was found to undergo ligand exchange reaction in presence of [Cu(dsbtmp)₂]^{+/2+}. The other bases were chosen according to structural similarities with TBP. The base 4-(trifluoromethyl)pyridine (TFMP) has electron-withdrawing groups on the tert-butyl positions. Consequently, the study aimed to investigate whether the electronic disparity played a role in ligand exchange. 2,6-di-tert-butylpyridine (DTBP) is more sterically hindered than TBP and was chosen to highlight the effects of sterics on the ligand exchange.

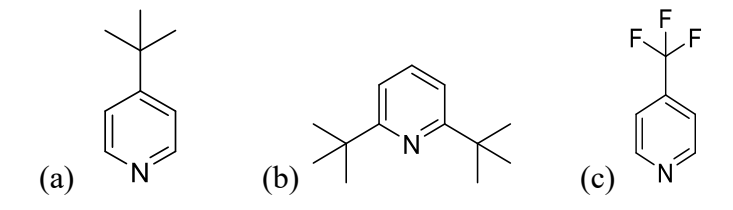


Figure 3.1: Structures of (a) 4-tert-butylpyridine (TBP), (b) 2,6-di-tert-butylpyridine (DTBP) and (c) 4-(trifluoromethyl)pyridine (TFMP).

(a)

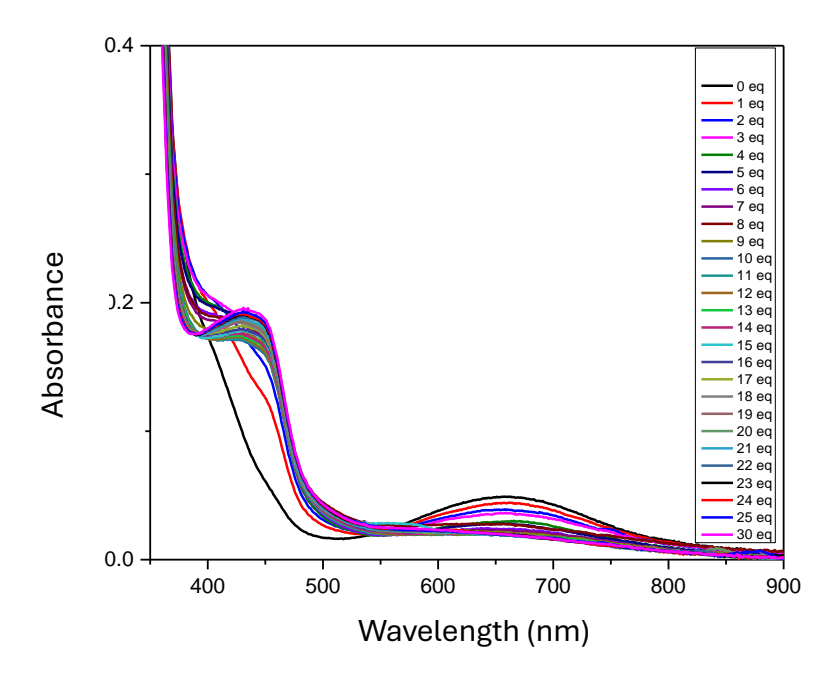
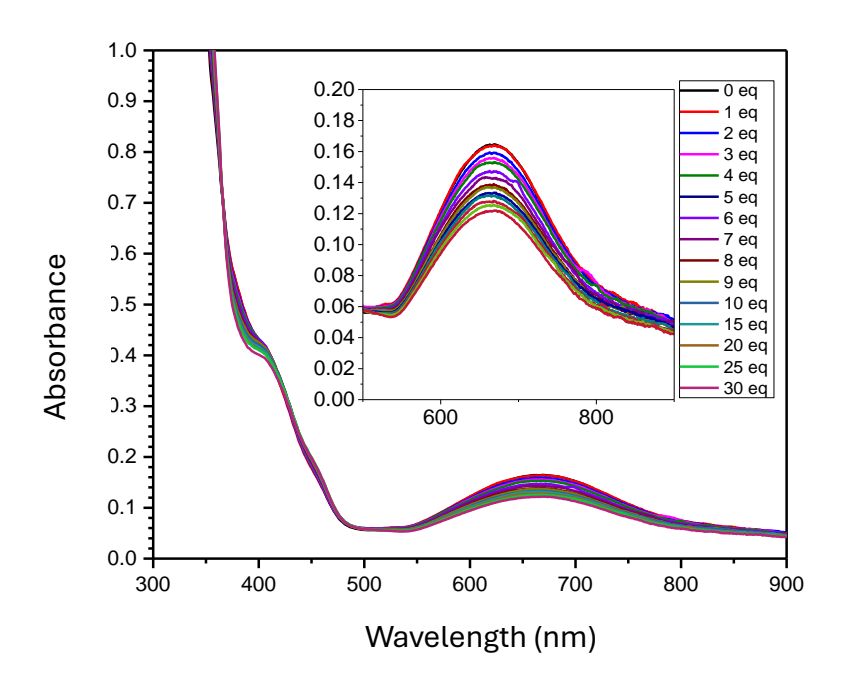


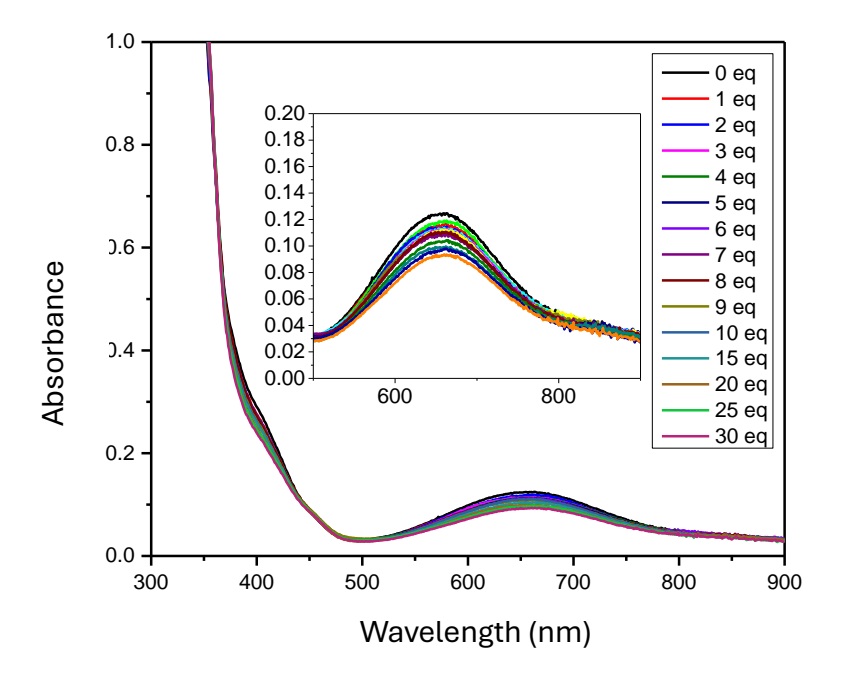
Figure 3.2: UV-Vis spectra showing titration of bases (a) TBP (b) TFMP and (c) DTBP to 0.25 mM [Cu(dsbtmp)₂]²⁺ in acetonitrile. The equivalents of the bases are on the legend.

Figure 3.2 (cont'd)

(b)



(c)



 $Titration \ of \ TBP \ to \ [Cu(dsbtmp)_2]^{2^+} \ had \ a \ dramatic \ effect \ on \ the \ UV-\ Vis \ spectrum. \ [Cu(dsbtmp)_2]^{+^+} \ had \ a \ dramatic \ effect \ on \ the \ UV-\ Vis \ spectrum.$ has its characteristic metal-to-ligand charge transfer (MLCT) peak at 450 nm while the [Cu(dsbtmp)₂]²⁺ absorbs at 660 nm (LMCT) as seen in the UV-vis spectrum in Figure 4 (b). Upon titration of various equivalents of TBP to [Cu(dsbtmp)₂]²⁺, the peak at 660 nm disappears concurrent with the growth of a new peak at 450 nm. The presence of an isosbestic point in the spectra indicates the formation of one new species from the [Cu(dsbtmp)₂]²⁺ in the UV-vis measurement timescale. The new species cannot be attributed to the [Cu(dsbtmp)₂]⁺, as the line shape and the absorption coefficients are different. For the titrations with TFMP and DTBP, no significant changes were observed. The slight changes in the peaks as seen in figure (b) and (c) is due to the effects of dilution. However, no occurrence of new peaks or disappearance of existent peaks were observed. In order to verify the role of these bases in retro cells, devices were made using DTBP in the electrolytic solution. The electrolyte consisted of 0.1 M Cu(I), 0.02 M Cu(II), 0.1 M LiPF₆ and 0.5 M DTBP in dry acetonitrile. The devices, however, performed very poorly, which was predicted based on the fact that the DTBP did not undergo any substitution and is a very bulky ligand. The solution potential before and after addition of DTBP also remained the same (0.43 V vs Fc⁺/Fc) which also indicated the absence of any chemical changes to the solution upon addition.

Using single-crystal ZnO electrodes in contact with osmium redox couples, it has been demonstrated that tert-butyl groups on bpy ligands function as insulating spacers.²³ This leads to a reduction in electronic coupling and, consequently, a decrease in the electron transfer rate constant by approximately 20 times compared to methyl-substituted bpy analog complexes.²⁴ The rationale behind incorporating pyridine was based on the premise that if the tert-butyl group indeed diminishes injection coupling by a factor of 20, as demonstrated in recombination reactions, then

employing these less sterically hindered bases could potentially enhance the photocurrent by a comparable magnitude. This would signify a significant advancement in the proposed system. Thus pyridine, which should possess very similar donor strength and behavior but be less sterically hindered than TBP, was hypothesized as an alternative in retro cells.

(a)

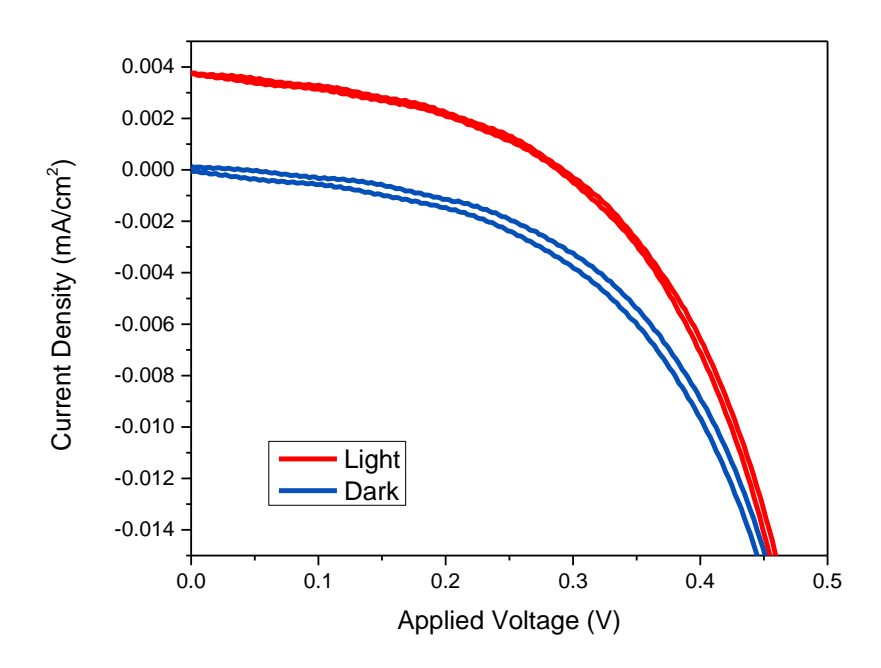
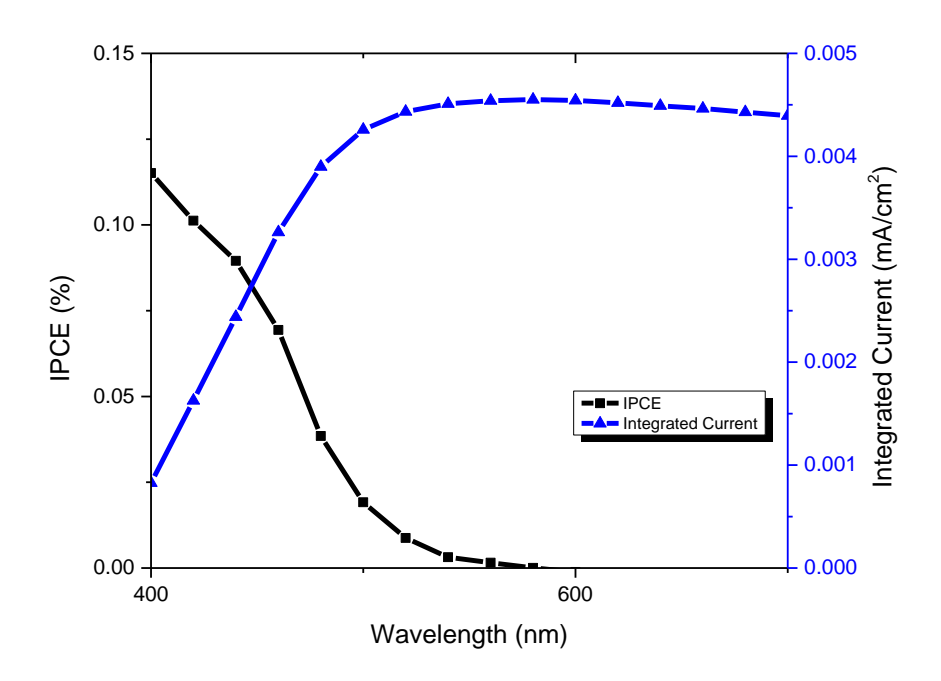


Figure 3.3: (a) Current density vs applied voltage characteristics of retro cells measured under 100mW/cm² illumination (red) and under dark conditions (blue) for [Cu(dsbtmp)₂]^{+/2+} with pyridine (dark blue) as the base additive. (b) Incident photon-to-current conversion efficiency (black squares) and integrated current density (blue triangles) for [Cu(dsbtmp)₂]^{+/2+} retro cells with TBP.

Figure 3.3 (cont'd)

(b)



From the J-V and the IPCE plots in figure 3, it is observed that the devices performed very poorly. Both V_{OC} (0.23 V \pm 0.016 V) and J_{SC} (0.003 mA/cm² \pm 0.001 mA/cm²) and thus overall efficiency was very low.

3.3 Future Directions

Following the preliminary research, an extensive examination needs to be undertaken to delve into the coordination tendencies of a variety of bases. The bases could be varied according to substituents in various position of pyridine, including 4-methylpyridine, 4-benzoylpyridine, 4-dimethylamidopyridine, imidazole, 1-methylimidazole, 1-benzoleimidazole, and methyl benzimidazole. The overarching objective of this comprehensive endeavor is to compile a comprehensive database detailing the interactions between these bases and the copper complexes,

forecast the dynamics of ligand exchange processes, and elucidate the significance of these interactions within the context of retro cells.

REFERENCES

- (1) Adman, E. T. Copper Protein Structures. Adv Protein Chem **1991**, 42, 145–197. https://doi.org/10.1016/S0065-3233(08)60536-7.
- (2) Fürer, S. O.; Milhuisen, R. A.; Kashif, M. K.; Raga, S. R.; Acharya, S. S.; Forsyth, C.; Liu, M.; Frazer, L.; Duffy, N. W.; Ohlin, C. A.; Funston, A. M.; Tachibana, Y.; Bach, U. The Performance-Determining Role of Lewis Bases in Dye-Sensitized Solar Cells Employing Copper-Bisphenanthroline Redox Mediators. Adv Energy Mater **2020**, 10 (37), 2002067. https://doi.org/10.1002/AENM.202002067.
- (3) Cao, Y.; Liu, Y.; Zakeeruddin, S. M.; Hagfeldt, A.; Grätzel, M. Direct Contact of Selective Charge Extraction Layers Enables High-Efficiency Molecular Photovoltaics. Joule **2018**, 2 (6), 1108–1117. https://doi.org/10.1016/J.JOULE.2018.03.017.
- (4) Zhang, W.; Wu, Y.; Bahng, H. W.; Cao, Y.; Yi, C.; Saygili, Y.; Luo, J.; Liu, Y.; Kavan, L.; Moser, J. E.; Hagfeldt, A.; Tian, H.; Zakeeruddin, S. M.; Zhu, W. H.; Grätzel, M. Comprehensive Control of Voltage Loss Enables 11.7% Efficient Solid-State Dye-Sensitized Solar Cells. Energy Environ Sci 2018, 11 (7), 1779–1787. https://doi.org/10.1039/C8EE00661J.
- (5) Nazeeruddin, M. K.; Kay, A.; Rodicio, I.; Humphry-Baker, R.; Müller, E.; Liska, P.; Vlachopoulos, N.; Grätzel, M. Conversion of Light to Electricity by Cis-X2Bis (2,2'-Bipyridyl-4,4'-Dicarboxylate) Ruthenium (II) Charge-Transfer Sensitizers (X = Cl-, Br-, I-, CN-, and SCN-) on Nanocrystalline TiO2 Electrodes. J Am Chem Soc 1993, 115 (14), 6382–6390. https://doi.org/10.1021/JA00067A063/ASSET/JA00067A063.FP.PNG_V03.
- (6) Saif A. Haque, †; Emilio Palomares, †,§; Byung M. Cho, ‡; Alex N. M. Green, †; Narukuni Hirata, †; David R. Klug, ‡ and; James R. Durrant*, †. Charge Separation versus Recombination in Dye-Sensitized Nanocrystalline Solar Cells: The Minimization of Kinetic Redundancy. J Am Chem Soc **2005**, 127 (10), 3456–3462. https://doi.org/10.1021/JA0460357.
- (7) Boschloo, G.; Häggman, L.; Hagfeldt, A. Quantification of the Effect of 4-Tert-Butylpyridine Addition to I -/I3- Redox Electrolytes in Dye-Sensitized Nanostructured TiO2 Solar Cells. Journal of Physical Chemistry B **2006**, 110 (26), 13144–13150. https://doi.org/10.1021/JP0619641/SUPPL_FILE/JP0619641SI20060515_124641.PDF.
- (8) Kusama, H.; Arakawa, H. Influence of Benzimidazole Additives in Electrolytic Solution on Dye-Sensitized Solar Cell Performance. J Photochem Photobiol A Chem **2004**, 162 (2–3), 441–448. https://doi.org/10.1016/S1010-6030(03)00414-3.
- (9) Wang, Y.; Hamann, T. W. Improved Performance Induced by in Situ Ligand Exchange Reactions of Copper Bipyridyl Redox Couples in Dye-Sensitized Solar Cells. Chemical Communications **2018**, 54 (87), 12361–12364. https://doi.org/10.1039/C8CC07191H.
- (10) Ren, Y.; Zhang, D.; Suo, J.; Cao, Y.; Eickemeyer, F. T.; Vlachopoulos, N.; Zakeeruddin, S. M.; Hagfeldt, A.; Grätzel, M. Hydroxamic Acid Pre-Adsorption Raises the Efficiency of

- Cosensitized Solar Cells. Nature 2022 613:7942 **2022**, 613 (7942), 60–65. https://doi.org/10.1038/s41586-022-05460-z.
- (11) Miller, M. T.; Gantzel, P. K.; Karpishin, T. B. Structures of the Copper(I) and Copper(II) Complexes of 2,9-Diphenyl-1,10-Phenanthroline: Implications for Excited-State Structural Distortion. Inorg Chem **1998**, 37 (9), 2285–2290. https://doi.org/10.1021/IC971164S.
- (12) Murphy, B.; Hathaway, B. The Stereochemistry of the Copper(II) Ion in the Solid-State Some Recent Perspectives Linking the Jahn-Teller Effect, Vibronic Coupling, Structure Correlation Analysis, Structural Pathways and Comparative X-Ray Crystallography. Coord Chem Rev **2003**, 243 (1–2), 237–262. https://doi.org/10.1016/S0010-8545(03)00084-5.
- (13) Chen, L. X.; Shaw, G. B.; Novozhilova, I.; Liu, T.; Jennings, G.; Attenkofer, K.; Meyer, G. J.; Coppens, P. MLCT State Structure and Dynamics of a Copper(I) Diimine Complex Characterized by Pump-Probe x-Ray and Laser Spectroscopies and DFT Calculations. J Am Chem Soc **2003**, 125 (23), 7022–7034. https://doi.org/10.1021/JA0294663.
- (14) Kashif, M. K.; Axelson, J. C.; Duffy, N. W.; Forsyth, C. M.; Chang, C. J.; Long, J. R.; Spiccia, L.; Bach, U. A New Direction in Dye-Sensitized Solar Cells Redox Mediator Development: In Situ Fine-Tuning of the Cobalt(II)/(III) Redox Potential through Lewis Base Interactions. J Am Chem Soc 2012, 134 (40), 16646–16653. https://doi.org/10.1021/JA305897K.
- (15) Zhang, C.; Dai, J.; Huo, Z.; Pan, X.; Hu, L.; Kong, F.; Huang, Y.; Sui, Y.; Fang, X.; Wang, K.; Dai, S. Influence of 1-Methylbenzimidazole Interactions with Li+ and TiO2 on the Performance of Dye-Sensitized Solar Cells. Electrochim Acta **2008**, 53 (17), 5503–5508. https://doi.org/10.1016/J.ELECTACTA.2008.03.016.
- (16) Stergiopoulos, T.; Rozi, E.; Karagianni, C. S.; Falaras, P. Influence of Electrolyte Co-Additives on the Performance of Dye-Sensitized Solar Cells. Nanoscale Res Lett **2011**, 6 (1). https://doi.org/10.1186/1556-276X-6-307.
- (17) Ellis, H.; Jiang, R.; Ye, S.; Hagfeldt, A.; Boschloo, G. Development of High Efficiency 100% Aqueous Cobalt Electrolyte Dye-Sensitised Solar Cells. Physical Chemistry Chemical Physics **2016**, 18 (12), 8419–8427. https://doi.org/10.1039/C6CP00264A.
- (18) Ashbrook, L. N.; Elliott, C. M. Dye-Sensitized Solar Cell Studies of a Donor-Appended Bis(2,9-Dimethyl-1, 10-Phenanthroline) Cu(I) Dye Paired with a Cobalt-Based Mediator. Journal of Physical Chemistry C **2013**, 117 (8), 3853–3864. https://doi.org/10.1021/JP3123693.
- (19) Kavan, L.; Saygili, Y.; Freitag, M.; Zakeeruddin, S. M.; Hagfeldt, A.; Grätzel, M. Electrochemical Properties of Cu(II/I)-Based Redox Mediators for Dye-Sensitized Solar Cells. Electrochim Acta **2017**, 227, 194–202. https://doi.org/10.1016/J.ELECTACTA.2016.12.185.
- (20) Clark, W. D. K.; Sutin, N. Spectral Sensitization of N-Type TiO2 Electrodes by Polypyridineruthenium(II) Complexes. J Am Chem Soc **1977**, 99 (14), 4676–4682. https://doi.org/10.1021/ja00456a025.

- (21) Neale, N. R.; Kopidakis, N.; Van De Lagemaat, J.; Grätzel, M.; Frank, A. J. Effect of a Coadsorbent on the Performance of Dye-Sensitized TiO 2 Solar Cells: Shielding versus Band-Edge Movement. Journal of Physical Chemistry B **2005**, 109 (49), 23183–23189. https://doi.org/10.1021/JP0538666/ASSET/IMAGES/MEDIUM/JP0538666E00007.GIF.
- (22) Kopidakis, N.; Neale, N. R.; Frank, A. J. Effect of an Adsorbent on Recombination and Band-Edge Movement in Dye-Sensitized TiO2 Solar Cells: Evidence for Surface Passivation. Journal of Physical Chemistry B 2006, 110 (25), 12485–12489. https://doi.org/10.1021/JP0607364/ASSET/IMAGES/LARGE/JP0607364F00007.JPEG.
- (23) Hamann, T. W.; Brunschwig, B. S.; Lewis, N. S. Comparison of the Self-Exchange and Interfacial Charge-Transfer Rate Constants for Methyl- Versus Tert-Butyl-Substituted Os(III) Polypyridyl Complexes. Journal of Physical Chemistry B **2006**, 110 (50), 25514–25520. https://doi.org/10.1021/JP0649697/ASSET/IMAGES/LARGE/JP0649697F00006.JPEG.
- (24) Xie, Y.; Baillargeon, J.; Hamann, T. W. Kinetics of Regeneration and Recombination Reactions in Dye-Sensitized Solar Cells Employing Cobalt Redox Shuttles. Journal of Physical Chemistry C **2015**, 119 (50), 28155–28166. https://doi.org/10.1021/ACS.JPCC.5B08244.

Chapter 4: Determining Limiting Electron

Transfer Processes in Retro Cells

4.1 Theory and Discussion

The previous chapter introduced the concept of retro cells using [Cu(dsbtmp)₂]^{2+/+} and TBP in acetonitrile. This chapter entails further analysis of retro cells and explores quantification of different parameters that are responsible for the working of these cells. In order to do that, devices were fabricated as mentioned previously in Chapter 2 and measurements of dark and light current vs voltage(J-V), incident photon-to-current efficiency (IPCE) and current transients were carried out for both front as well as back illumination. Here front illumination refers to illumination through the photoanode side and back illumination refers to illumination through the cathode side. The J-V and IPCE plots are given in figure 4.1.

(a)

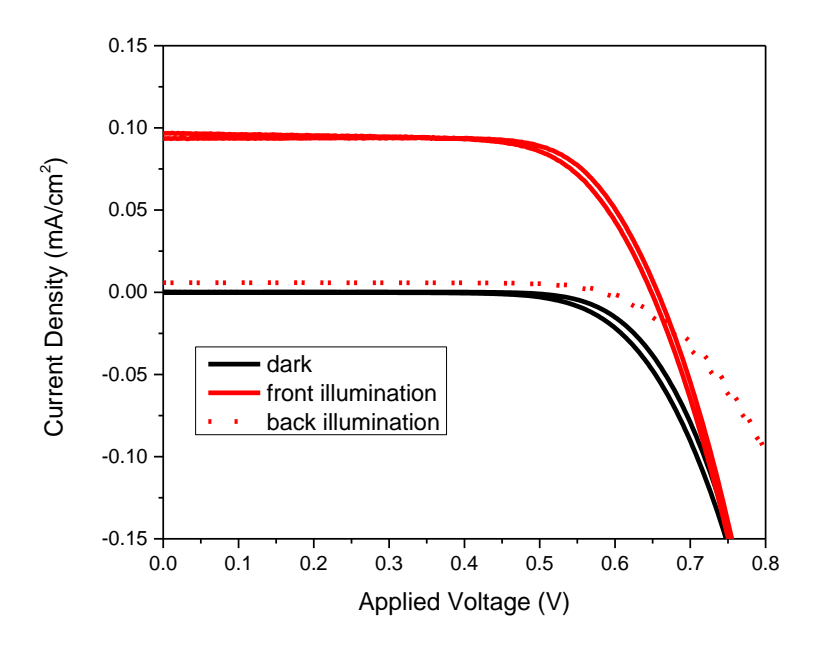
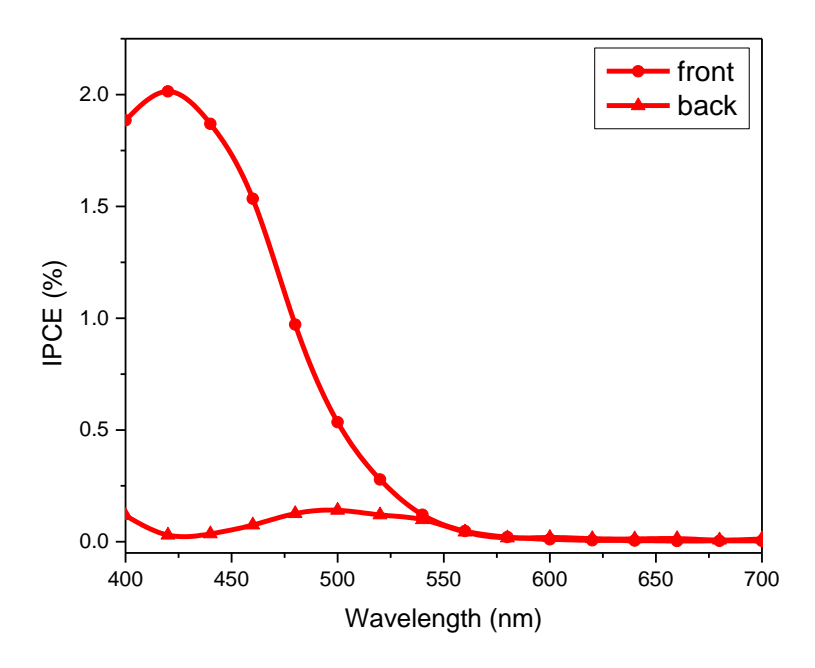


Figure 4.1: (a) Current density vs applied voltage characteristics of retro cells measured under 100mW/cm² illumination front side (solid red line), back side (dotted red line) and under dark conditions (solid black line) for [Cu(dsbtmp)₂]^{+/2+} retro cells with TBP in the electrolytic solution. (b) Incident photon-to-current conversion efficiency for front illumination (circles) and back illumination (triangles) for [Cu(dsbtmp)₂]^{+/2+} retro cells with TBP.

Figure 4.1 (cont'd)

(b)



IPCE in photovoltaic devices, such as DSSCs, is determined by the product of several efficiencies: light harvesting efficiency (η_{LH}), charge collection efficiency (η_{cc}) and charge separation efficiency (η_{sep}).

$$IPCE(\lambda) = \eta_{LH}(\lambda) \; \eta_{CC}(\lambda) \; \eta_{sep} \quad (1)$$

Light harvesting efficiency is defined as the fraction of light intensity absorbed by the dye at a certain wavelength in a DSSC. In accordance with the Lambert–Beer law, the η_{LH} of the cell is governed by the dye's extinction coefficient, the concentration of dye, and the optical path length within the film. Enhancing the η_{LH} relies on the extension of dye absorbance to a broader wavelength spectrum. Thus, η_{LH} is the proportion of incoming photons that are absorbed and is given

LHE =
$$T_{FTO}(1 - 10^{-(A_DP + A_E)})(\frac{A_E}{A_EP + A_D})$$
 (2)

where T_{FTO} is the transmittance of the electrode, A_E is the absorbance of the electrolyte, A_D is the absorbance of the dye molecules and P is the porosity of the photoanode. In case of retro cells, since the dye molecules act as the redox shuttle as well, the equation reduces to:

$$LHE = T_{FTO} (1 - 10^{-\epsilon CdP}) \ (3)$$

where ϵ is the molar absorptivity and C is the concentration of the dye molecules. The light harvesting efficiency is independently measurable. The T_{FTO} was measured by transmission measurement using a UV-Vis spectrometer, the plot of which is given in figure 4.2 (b).

(a)

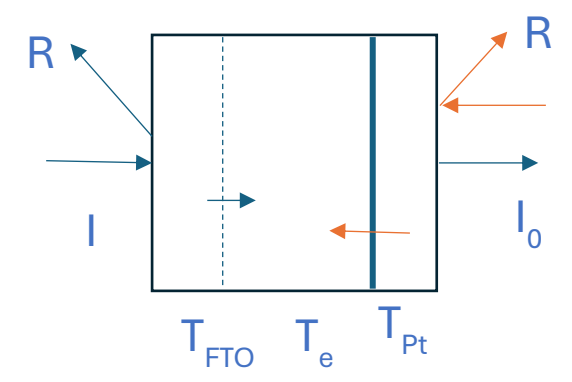
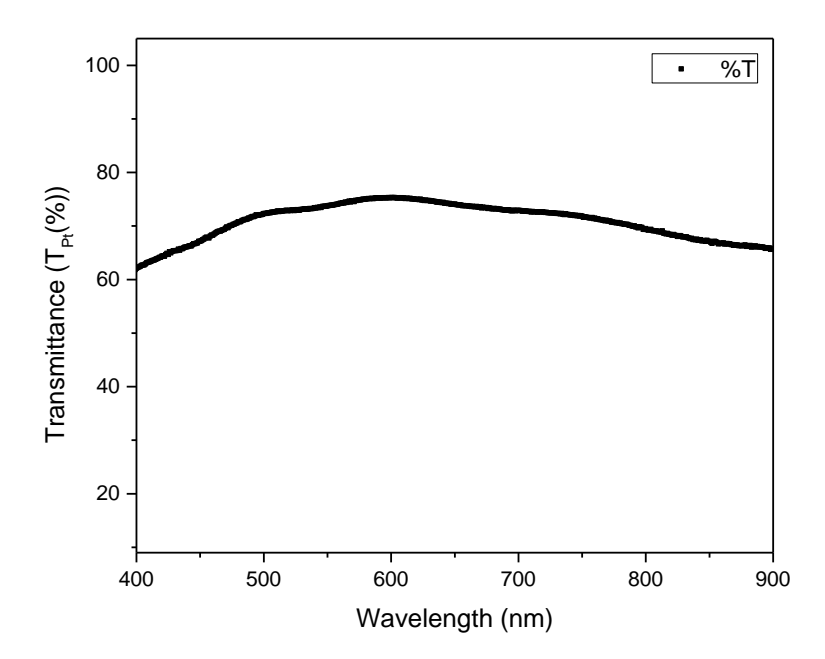


Figure 4.2: (a) Schematic showing the light pathways in the device (b) Transmittance of the FTO glass substrate.

Figure 4.2 (cont'd)

(b)



 η_{CC} quantifies the proportion of photoinjected electrons successfully reaching the electron collector without undergoing recombination. It is given by:^{4–8}

$$\eta_{CC} = \frac{\left[-\text{Ln}\,\varepsilon\,\text{cosh}\left(\frac{d}{\text{Ln}}\right) + \text{sinh}\left(\frac{d}{\text{Ln}}\right) + \text{Ln}\,\varepsilon\,e^{-\varepsilon d}\right]}{(1 - \text{Ln}^2\varepsilon^2)(1 - e^{-\varepsilon d})\text{cosh}\left(\frac{d}{\text{Ln}}\right)} \eqno(4)$$

This equation has been derived previously and reported in literature. The derivation is discussed below but a more detailed discussion can be found in the cited references.

The standard diffusion model operates on the continuity equation for electron concentration which is given by:

$$D\frac{d^2n}{d^2} - \frac{n - n_0}{\tau} + g = 0 \tag{5}$$

where D and τ represent the electron diffusion coefficient and lifetime respectively, n denotes the local electron density, n_0 signifies the equilibrium electron density in the absence of light, g denotes the local electron generation rate. The position coordinate x progresses towards the bulk

of the photoelectrode, with x = 0 positioned at the film edge facing the incoming light. The electron generation rate according to the Beer–Lambert law:

$$g(x,\lambda,d) = \boldsymbol{\phi} \eta_{INJ}(\lambda) \epsilon(\lambda,d) \exp(-\epsilon(\lambda,d)x)$$
 (6)

where ϕ is the photon flux density and η_{INJ} is the electron injection efficiency.

When light illuminates the cell from the photoanode side (front illumination), the boundary conditions for solving the equation at the short circuit condition are as follows:^{4–13}

$$\mathbf{n}(0) = \mathbf{n}_0 \quad (7)$$

$$\frac{dn(x)}{dx} = 0$$
 at x=d (8)

For the opposite direction of light (back illumination), x = 0 at the counter and the conditions are:

$$n(d) = n_0 (9)$$

$$\frac{dn(x)}{dx} = 0$$
 at $x = 0$ (10)

Solving the equations yields expressions for the charge collection efficiency η_{CC} under front and back illuminations: $^{4\text{--}13}$

$$\eta_{CC}(front) = \frac{\left[-\operatorname{Ln}\epsilon\cosh\left(\frac{d}{\operatorname{Ln}}\right) + \sinh\left(\frac{d}{\operatorname{Ln}}\right) + \operatorname{Ln}\epsilon e^{-\epsilon d}\right]\operatorname{Ln}\epsilon}{(1 - \operatorname{Ln}^2\epsilon^2)\left(1 - e^{-\epsilon d}\right)\cosh\left(\frac{d}{\operatorname{Ln}}\right)} \tag{11}$$

$$\eta_{CC}(back) = \frac{\left[\ln \varepsilon \cosh\left(\frac{d}{Ln}\right) + \sinh\left(\frac{d}{Ln}\right) - \ln \varepsilon e^{-\varepsilon d} \right] \ln \varepsilon}{(1 - Ln^2 \varepsilon^2) (1 - e^{-\varepsilon d}) \cosh\left(\frac{d}{Ln}\right)} \quad (12)$$

and
$$Ln = \sqrt{D\tau}$$
 (13)

 η_{CC} is influenced by recombination through back electron transfer and is contingent upon the electron diffusion length (Ln), film thickness (d), and ϵ , thus exhibiting a dependence on both wavelength and direction of incident light.

Analytically solving the equation (5) gives the concentration of conduction band electrons, n at short circuit with boundary conditions (7) and (10). This can be solved for both front and back illumination, where g will be different based on the illumination side.

Charge separation is defined as the extraction of photocarriers to the external circuit. ¹⁴ There's a possibility that some of the photocarriers reaching the collector may not be extracted to the external circuit. The efficiency of charge separation is determined by the movement of excited sensitizers towards the TiO_2 surface, involving factors such as the diffusion coefficient and the lifetime of the sensitizers' excited state, as well as the injection efficiency. These parameters remain unaffected by the wavelength or direction of incident light. Assuming position independence, the effect of η_{sep} cancel out when comparing IPCEs under front and back illuminations. This simplifies the IPCE ratio to primarily reflect the product of charge collection and light harvesting efficiencies. Thus the η_{CC} can be estimated if the IPCE of the cells are measured in both directions. ^{4–13,15–17}

$$\frac{\text{IPCE(front)}.\eta_{\text{LH}}(\text{back})}{\text{IPCE(back)}.\eta_{\text{LH}}(\text{front})} = \frac{n_{\text{cc}}(\text{front})}{n_{\text{cc}}(\text{back})}$$
(14)

For the retro cells containing $[Cu(dsbtmp)_2]^{2+/+}$ and TBP in acetonitrile, the IPCE plots for front and back illumination is given in figure 4.1 (b).

The IPCE for retro cells is given by

$$IPCE=D\frac{\frac{dn(0)}{dx}}{\varphi}$$
 (15)

The ratio of IPCE back and front illumination is given by the following equation, which was solved using equation (17)

$$\begin{split} & \text{IPCE(front)} = \frac{(1\text{-R}) \, L}{n} \, \underbrace{\eta_{\text{inj}} \, \epsilon \, e^{-d} \epsilon (L \, \epsilon \, - \, 1) \, e^{-(d \, \epsilon \, + \, (2/Ln))} + (L \, \epsilon \, + \, 1) \, e^{-d} \epsilon \, - \, 2Ln\epsilon e^{-(d/Ln)}}_{((L_n \, \epsilon \, - \, 1)) \, (e^{-(2/Ln))} + (L \, \epsilon \, + \, 1) \, e^{-d} \epsilon \, - \, 2Ln\epsilon e^{-(d/Ln)}}_{(2d/Ln)} \, \, (16) \\ & \underbrace{\frac{\text{IPCE(back)}}{\text{IPCE(front)}}}_{\text{IPCE(front)}} = \frac{T_n \, T_n \, [(-((Ln \, \epsilon \, + \, 1) \, e^{-d} \, - \, (2Ln \, \epsilon \, e^{-d} \, - \, (2Ln \, e^{-d} \, - \, (2Ln \, \epsilon \, - \, e^{-d} \, - \, (2Ln \, \epsilon \, - \, e^{-d} \, - \, (2Ln \, \epsilon \, - \, e^{-d} \, - \, (2Ln \, \epsilon \, - \, e^{-d} \, - \, (2Ln \, \epsilon \, - \, e^{-d} \, - \, e^{-$$

The T_{Pt} , T_e and ϵ plots are shown in figure 4.3 and figure 4.4. The IPCE(back)/IPCE(front) was then fitted and the plot is given below in figure 4.5.

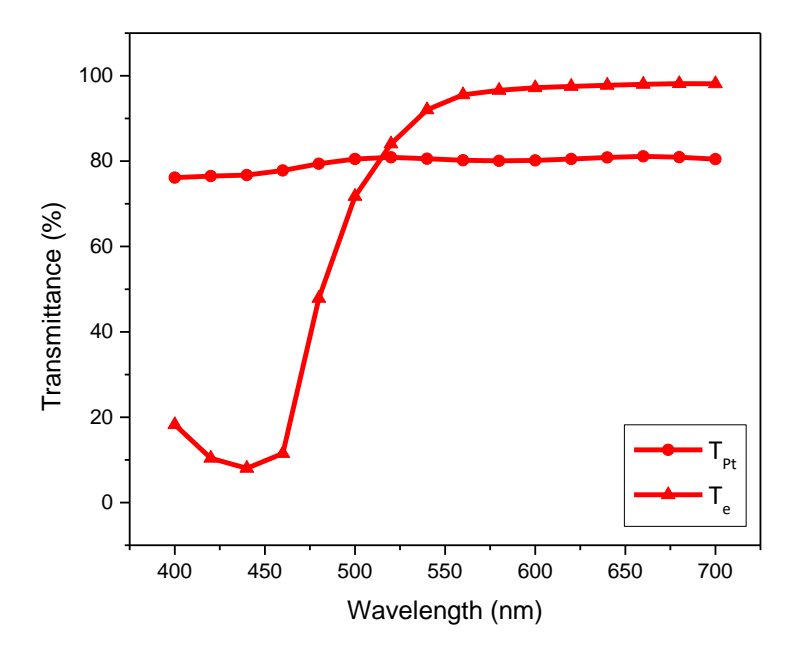


Figure 4.3: Transmittance of counter electrode-Platinized substrate (T_{Pt}) and transmittance of electrolyte (T_e) that is injected in between the photoanode and counter electrode.

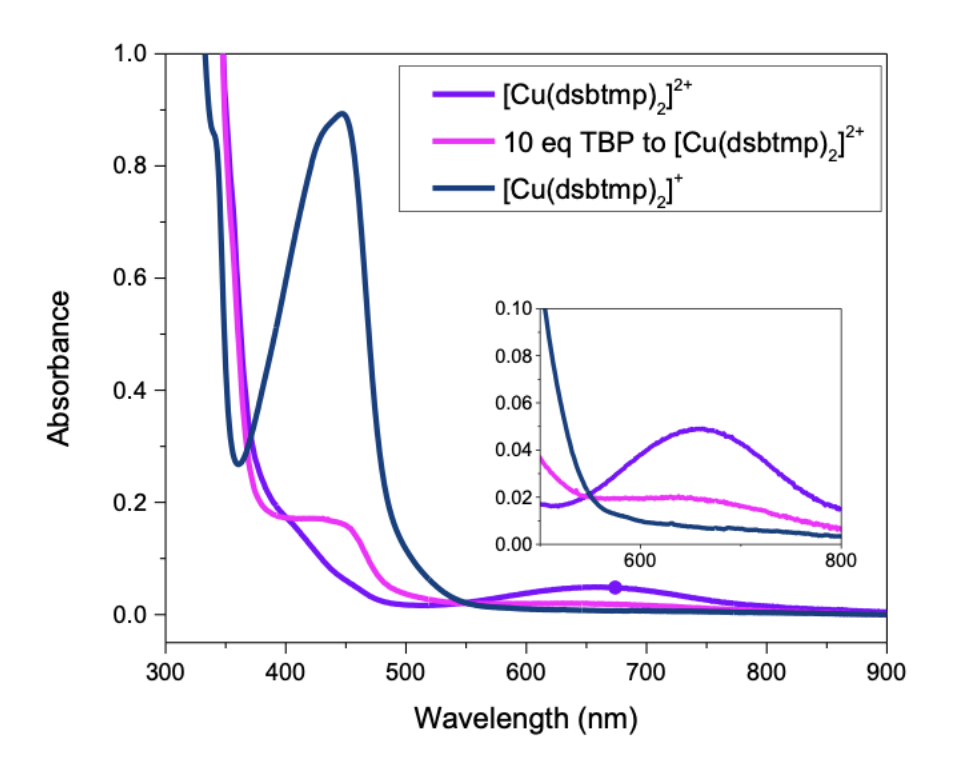


Figure 4.4: UV-Vis spectra of 0.2 mM each of [Cu(dsbtmp)₂]²⁺and [Cu(dsbtmp)₂]⁺and mixture of 2mM [Cu(dsbtmp)₂]²⁺ and 20 mM TBP (10 eq).

The plot in figure 4.5 is the ratio of $\eta_{CC}(front)/\eta_{CC}(back)$ vs wavelength which is derived from:

$$\frac{\text{IPCE(front).T}_{Pt}T_{e}}{\text{IPCE(back)}} = \frac{\eta_{CC}(\text{front})}{\eta_{CC}(\text{back})} \quad (18)$$

Theoretically, if the plot was linear, it would have indicated that η_{CC} was 1. Linearity is not observed in this case which might indicate that charge collection is a limiting factor. However, a more detailed analysis of the plot has revealed the data points from 400-450 nm is far too little and the errors in fitting has not been accounted for to come to this conclusion. In fact, the IPCE and η_{LH} as a function of wavelength, as shown in figure 4.6 has a more reasonable explanation as to what is occurring in the system. The region of 400 nm to 450 nm in the IPCE and η_{LH} vs wavelength plot is similar to the absorption profile of $[Cu(dsbtmp)_2]^+$ as given in figure 4.4. This indicates that the photocurrent in that region is due to the excitation of $[Cu(dsbtmp)_2]^+$. The wavelength range of approximately 450 – 550 nm, where the absorption by Cu(I) diminishes,

electrons are injected into TiO_2 further from the substrate, necessitating longer diffusion distances for collection. If rapid recombination hampers charge collection, IPCE at these wavelengths could be negligible. But this is not the case, indicating that photocurrent is not predominantly limited by charge collection. In fact, the linear relationship between IPCE and η_{LH} in this spectral region suggest charge separation limitations.

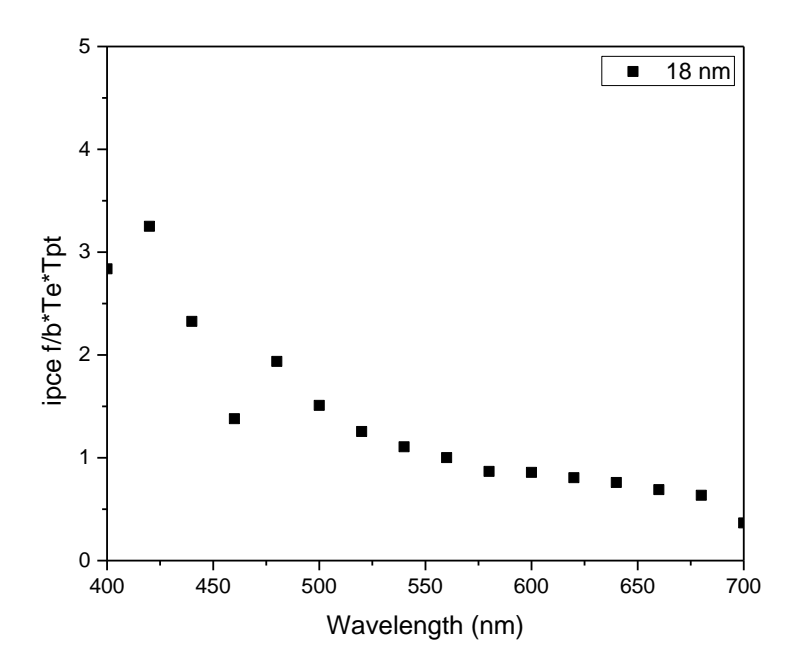


Figure 4.5: Ratio of $\frac{\text{IPCE(front).T}_{Pt}\text{T}_{e}}{\text{IPCE(back)}}$ vs wavelength which gives the ratio of charge collection efficiencies front and back respectively.

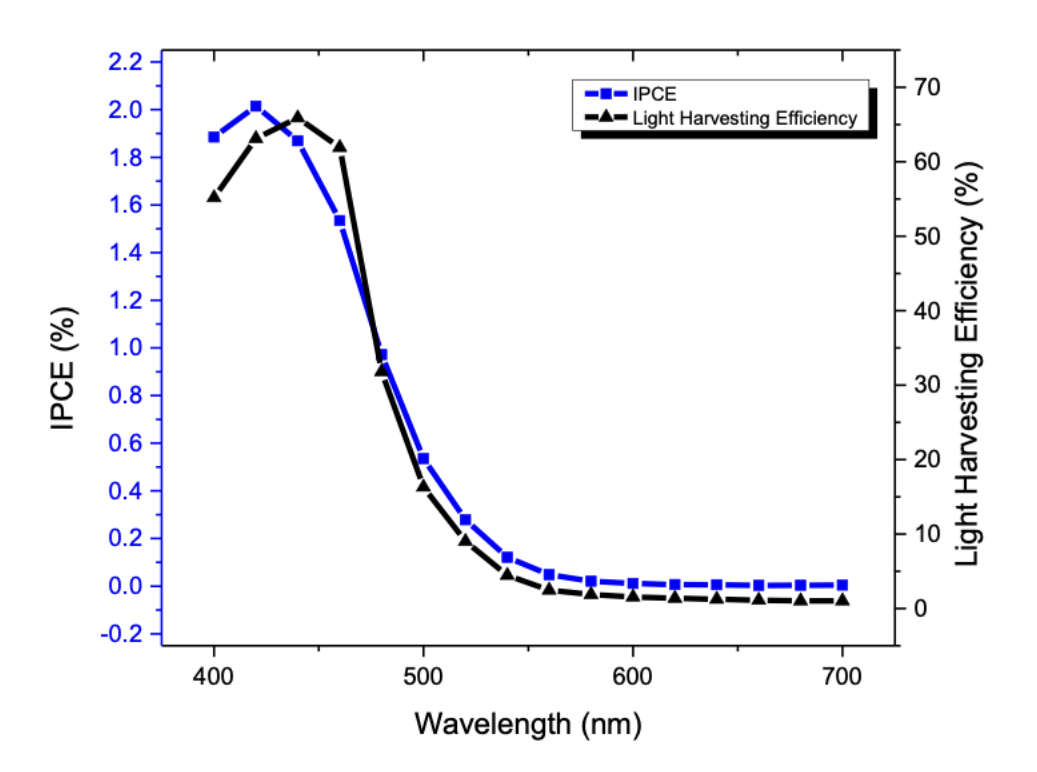
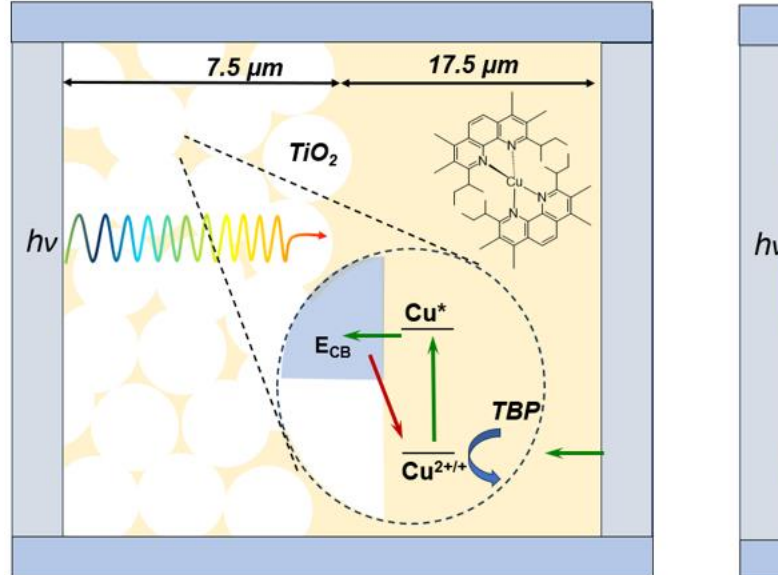


Figure 4.6: Comparison of incident photon-to-current conversion efficiency for front illumination (blue squares) and light harvesting efficiency (black triangles) for [Cu(dsbtmp)₂]^{+/2+} retro cells with TBP.

From figure 4.1 it can be noted that the IPCE (back) values are too low to get a meaningful fit for the IPCE ratio. This is most likely because of the substantial absorption occurring within the bulk electrolyte layer. This layer comprises the same dye solution known for its strong absorption properties. Consequently, when illumination is directed from the backside, only a negligible fraction of photons can effectively penetrate through to reach the photoanode layer, thus impeding the accuracy of measurements. It's noteworthy that the mesoporous TiO_2 photoanode has a thickness of about 7.5 μ m, while it is separated from the counter electrode by a 25 μ m polymer spacer. Therefore, the bulk electrolyte layer can be estimated to have a thickness of approximately 17.5 μ m.

Due to the inability to meaningfully fit the IPCE(back)/IPCE(front), a non-linear fit for IPCE (front) only using equation (16) was carried out instead. However, the fit did not converge, which can be due to multiple factors. One factor could be if the electron diffusion length (Ln) is longer than the thickness of the film (d), which would understandably prevent the fitting of the plot.

As noted above, the bulk electrolyte might have prevented the cells from functioning optimally and so measures to reduce the bulk layer were planned. There have been previous reports of a DSSC architecture in which there is direct contact of the TiO₂ electrode and the counter electrode. This architecture was implemented to reduce the diffusion length of the redox shuttle thereby increasing the cell performance. A similar architecture was implemented for the retro cells in this study to reduce the bulk layer. A pictorial representation of the architecture is given in figure 4.7. The retro cells were fabricated using the method mentioned in Chapter 2. The sandwiching of the electrodes was done by a new method, details of which are given below.



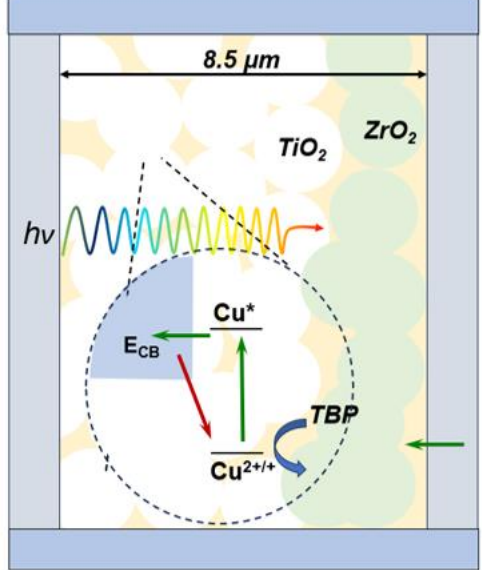


Figure 4.7: Comparison of retro cells with and without Suryln spacer. The first diagram represents a bulk layer of 17.5 μm whereas the second layer shows the addition of a ZrO₂ layer and the fabrication o contact retro cells, that removes the bulk layer.

Sandwiching Contact electrodes in retro cells:

The working and counter electrodes were pressed together using paper binder clips, and UV light-curing glue was applied along the edges where the two electrodes met. After the application of the UV light-curing glue, the cells were exposed to UV light for an hour, during which the glue solidified. Following this, the electrolyte was filled and sealed using the previously mentioned procedure.

The contact retro cells were composed of 0.1 M [Cu(dsbtmp)₂](PF₆), 0.05 M [Cu(dsbtmp)₂](PF₆)₂ 0.5 M TBP and 0.1 M LiPF₆ in dry acetonitrile. The performance of the cells was analyzed by J-V and IPCE measurements given in figure 4.8 (a) and (b) respectively.

(a)

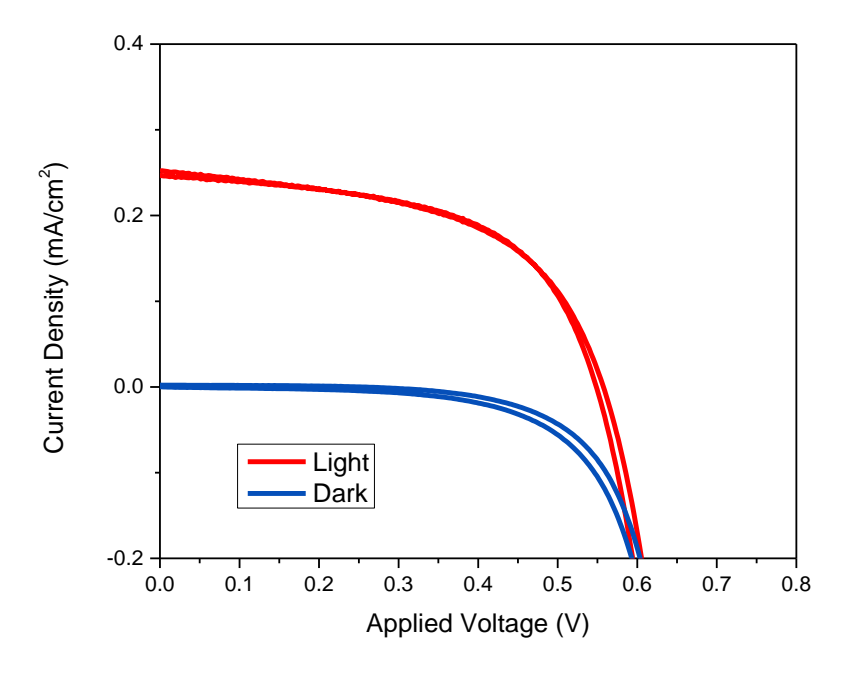
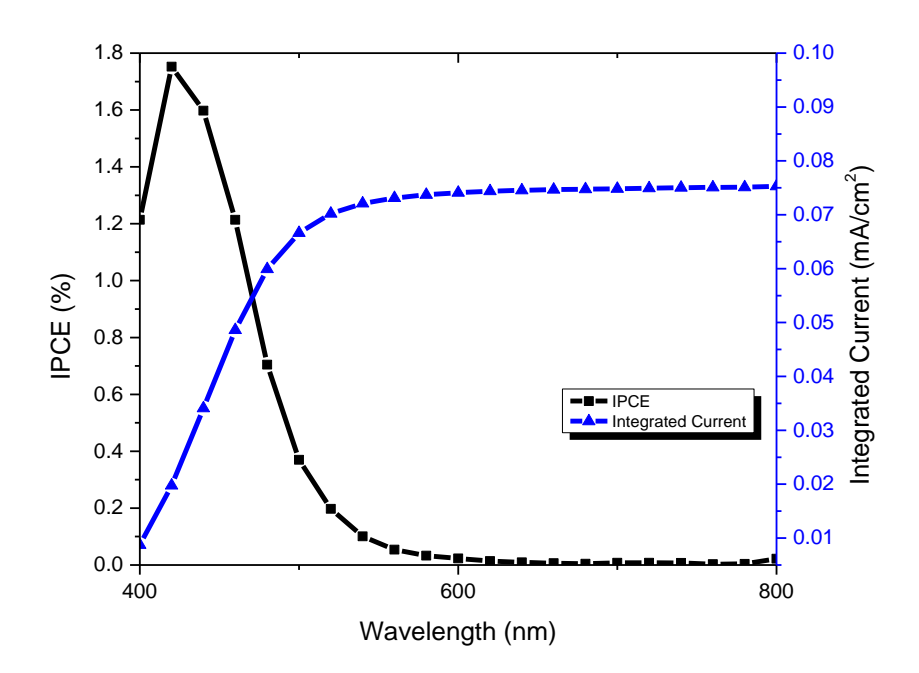


Figure 4.8: (a) Current density vs applied voltage characteristics of retro cells measured under 100mW/cm² illumination front side (solid red line) and under dark conditions (solid blue line) for [Cu(dsbtmp)₂]^{+/2+} retro cells with electrodes in contact and TBP in the electrolytic solution. (b) Incident photon-to-current conversion efficiency for front illumination (black squares) and integrated current density (blue triangles) for [Cu(dsbtmp)₂]^{+/2+} retro cells with electrodes in contact and TBP in the electrolytic solution.

Figure 4.8 (cont'd)

(b)



The cells showed an average open circuit voltage (V_{OC}) of 0.52 V (\pm 0.041 V), an average short circuit current densities (J_{SC}) of 0.24 mA/cm² (\pm 0.04 mA/cm²) and an efficiency (η) of 0.075% (\pm 0.011%). Even though these cells performed better than the retro cells with Surylyn spacer, however, the integrated current from IPCE was unusually low, which is why the conditions of the cell were re-evaluated. The reason for the low IPCE current is unknown but it was realized that shunting, caused by direct contact, might pose a problem and could also contribute to impedance. To address this issue, the deposition of a thin, transparent, insulating ZrO₂ nanoparticle film on top of the mesoporous TiO₂ photoanode might prove beneficial. This film would act as a spacer, preventing shunting when directly pressing the counter electrode to the TiO₂ photoanode. To make the TiO₂/ ZrO₂, the synthesis of ZrO₂ paste had to be standardized and the film had to be characterized.

4.2 Preparation of ZrO₂ paste

A 10% ethyl cellulose solution in ethanol was prepared. The solution was sonicated and then stirred for 12 h. Zirconium (IV) dioxide (10 wt.% in H₂O) was measured upto 6 mL and 20 mL terpineol was added to it. This mixture was stirred for 12 h. After this, 3mL of ethyl cellulose was added to the ZrO₂ -terpineol mixture. After stirring this overnight, the ZrO₂ paste was used for Dr. blading onto the TiO₂ film.

4.3 Modification to photoanode fabrication

The TiO₂ cells were made by Dr. blading followed by heat treatment and the ramping process. After the steps, a second layer of the ZrO₂ paste was Dr. bladed. This was followed by the temperature ramping process as mentioned in Chapter 2.

The thickness of the films were then measured by profilometer. The plots of TiO_2 film, TiO_2/ZrO_2 film and ZrO_2 film is given in figure 4.9.

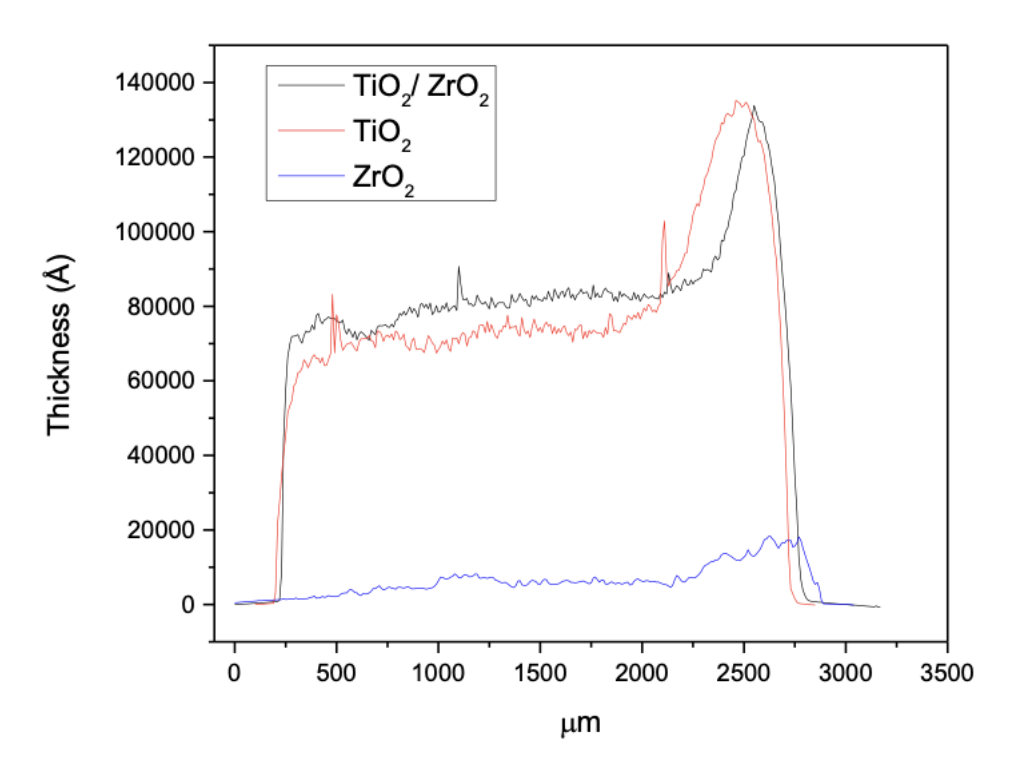


Figure 4.9: Profilometry measurement of thickness of ZrO₂ layer on TiO₂ made by Dr. blading Once the thickness of the films was known, the retro cells using these electrodes were fabricated using standard procedure as described in Chapter 2.

4.4 Modification to sandwiching method

A 1:1 (v/v) mixture of Solaronix Amosil 4R and 4H (2,2'-iminodiethylamine) was prepared separately. The working and counter electrodes were then pressed against each other using paper binder clips, and the epoxy resin was applied along the edges where the two electrodes meet. After the application of the epoxy resin, the cells were placed under constant pressure of the binder clips and put under dark conditions in a desiccator, allowing the resin to cure overnight.

4.5 Future directions

The TiO₂ nanoparticle size will also have a role in contributing to the overall performance of the cells. A preliminary investigation was carried out where retro cells using 18 nm TiO₂ nanoparticles were compared to that of 30 nm TiO₂ particles as shown in figure 4.10. The study suggested that

the 30 nm retro cells and the 18 nm retro cells performed the same on an average, but more in depth studies to analyze them needs to be carried out. Theoretically, if the mechanism in retro cells is limited by charge separation, then existence of smaller pore size in 18 nm nanoparticles than the 30 nm nanoparticles should mean that there will be more collisions per unit time. This should increase the photocurrent in the 18 nm cells as compared to the 30 nm cells.

These measurements were not performed with contact retro cells, which is a study that needs to be carried out in future. From the results above, contact retro cells have a great advantage to enhance the efficiency of these devices due to the reduction of inter-electrode distance and hence the reduction of mass transport losses in the system. Further optimizations may lead to increase in performance of the devices.

(a)

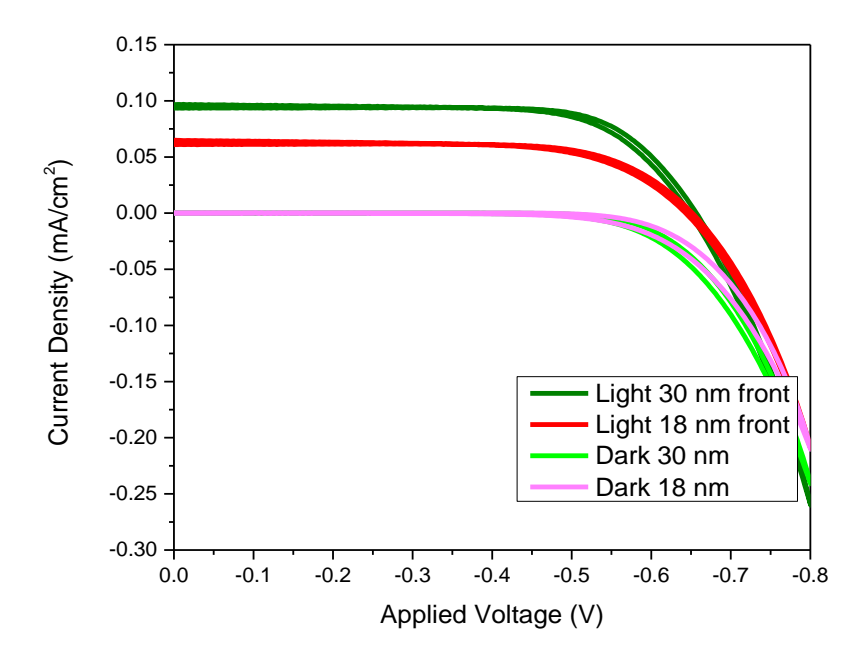
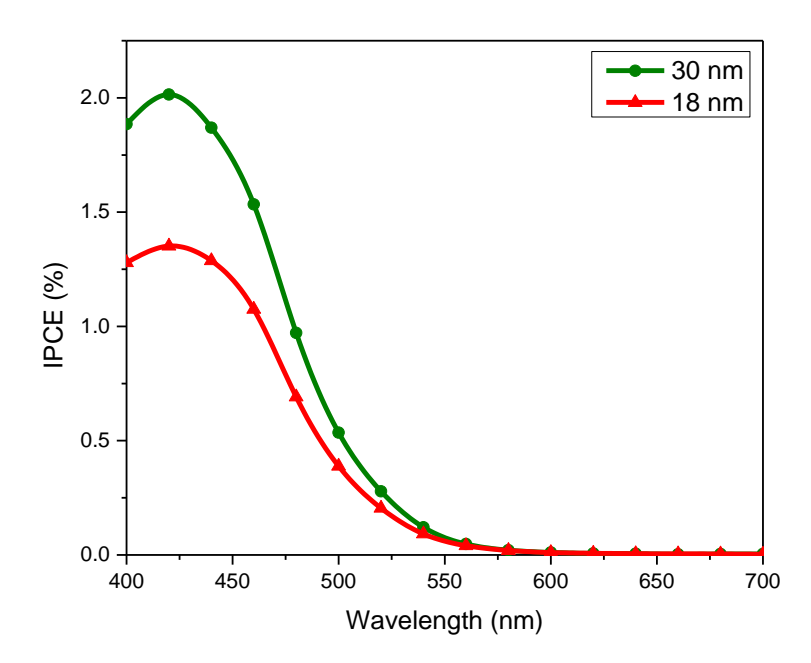


Figure 4.10: (a) Current density vs applied voltage characteristics of retro cells measured under 100mW/cm² illumination front side with 30 nm TiO₂ particles (dark green) and 18 nm TiO₂ particles (red); and under dark conditions: 30 nm TiO₂ particles (light green) and 18 nm TiO₂ particles (pink) for [Cu(dsbtmp)₂]^{+/2+} retro cells with TBP in the electrolytic solution. (b) Incident photon-to-current conversion efficiency for front illumination for [Cu(dsbtmp)₂]^{+/2+} retro cells with TBP with 30 nm TiO₂ particles (green circles) and 18 nm TiO₂ particles (red triangles).

Figure 4.10 (cont'd)

(b)



REFERENCES

- (1) COP28: assessment of commitments to climate and development financing, global health and gender equality. https://focus2030.org/COP28-assessment-of-commitments-to-climate-and-development-financing-global (accessed 2024-05-04).
- (2) Calvin, K.; Dasgupta, D.; Krinner, G.; Mukherji, A.; Thorne, P. W.; Trisos, C.; Romero, J.; Aldunce, P.; Barrett, K.; Blanco, G.; Cheung, W. W. L.; Connors, S.; Denton, F.; Diongue-Niang, A.; Dodman, D.; Garschagen, M.; Geden, O.; Hayward, B.; Jones, C.; Jotzo, F.; Krug, T.; Lasco, R.; Lee, Y.-Y.; Masson-Delmotte, V.; Meinshausen, M.; Mintenbeck, K.; Mokssit, A.; Otto, F. E. L.; Pathak, M.; Pirani, A.; Poloczanska, E.; Pörtner, H.-O.; Revi, A.; Roberts, D. C.; Roy, J.; Ruane, A. C.; Skea, J.; Shukla, P. R.; Slade, R.; Slangen, A.; Sokona, Y.; Sörensson, A. A.; Tignor, M.; van Vuuren, D.; Wei, Y.-M.; Winkler, H.; Zhai, P.; Zommers, Z.; Hourcade, J.-C.; Johnson, F. X.; Pachauri, S.; Simpson, N. P.; Singh, C.; Thomas, A.; Totin, E.; Alegría, A.; Armour, K.; Bednar-Friedl, B.; Blok, K.; Cissé, G.; Dentener, F.; Eriksen, S.; Fischer, E.; Garner, G.; Guivarch, C.; Haasnoot, M.; Hansen, G.; Hauser, M.; Hawkins, E.; Hermans, T.; Kopp, R.; Leprince-Ringuet, N.; Lewis, J.; Ley, D.; Ludden, C.; Niamir, L.; Nicholls, Z.; Some, S.; Szopa, S.; Trewin, B.; van der Wijst, K.-I.; Winter, G.; Witting, M.; Birt, A.; Ha, M. IPCC, 2023: Climate Change 2023: Synthesis Report. Contribution of Working Groups I, II and III to the Sixth Assessment Report of the Intergovernmental Panel on Climate Change [Core Writing Team, H. Lee and J. Romero (Eds.)]. IPCC, Geneva, Switzerland. 2023. https://doi.org/10.59327/IPCC/AR6-9789291691647.
- (3) The Paris Agreement Publication | UNFCCC. https://unfccc.int/documents/184656 (accessed 2024-05-04).
- (4) Masson-Delmotte, V.; Zhai, P.; Pörtner, H.-O.; Roberts, D.; Skea, J.; Shukla, P. R.; Pirani, A.; Moufouma-Okia, W.; Péan, C.; Pidcock, R.; Connors, S.; Matthews, J. B. R.; Chen, Y.; Zhou, X.; Gomis, M. I.; Lonnoy, E.; Maycock, T.; Tignor, M.; Waterfield, T. Global Warming of 1.5°C An IPCC Special Report on the Impacts of Global Warming of 1.5°C above Pre-Industrial Levels and Related Global Greenhouse Gas Emission Pathways, in the Context of Strengthening the Global Response to the Threat of Climate Change, Sustainable Development, and Efforts to Eradicate Poverty Summary for Policymakers Technical Summary Frequently Asked Questions Glossary Edited by Science Officer Science Assistant Graphics Officer Working Group I Technical Support Unit. 2019.
- Victoria, M.; Haegel, N.; Peters, I. M.; Sinton, R.; Jäger-Waldau, A.; del Cañizo, C.; Breyer, C.; Stocks, M.; Blakers, A.; Kaizuka, I.; Komoto, K.; Smets, A. Solar Photovoltaics Is Ready to Power a Sustainable Future. Joule **2021**, 5 (5), 1041–1056. https://doi.org/10.1016/J.JOULE.2021.03.005.
- (6) Roger A. Messenger; Amir Abtahi. Photovoltaic Systems Engineering, Fourth Edition, Fourth.; CRC Press, 2017.
- (7) Carella, A.; Borbone, F.; Centore, R. Research Progress on Photosensitizers for DSSC. Front Chem **2018**, 6 (SEP), 416256. https://doi.org/10.3389/FCHEM.2018.00481/BIBTEX.

- (8) Kharche, N. R. Future Directions and Emerging Trends: Technological Innovations in Solar Energy Integration. https://services.igi-global.com/resolvedoi/resolve.aspx?doi=10.4018/979-8-3693-7822-9.ch002 **1AD**, 39–58. https://doi.org/10.4018/979-8-3693-7822-9.CH002.
- (9) Saifullah, M.; Ahn, S.; Gwak, J.; Ahn, S.; Kim, K.; Cho, J.; Park, J. H.; Eo, Y. J.; Cho, A.; Yoo, J. S.; Yun, J. H. Development of Semitransparent CIGS Thin-Film Solar Cells Modified with a Sulfurized-AgGa Layer for Building Applications. J Mater Chem A Mater **2016**, 4 (27), 10542–10551. https://doi.org/10.1039/C6TA01909A.
- (10) Freitag, M.; Teuscher, J.; Saygili, Y.; Zhang, X.; Giordano, F.; Liska, P.; Hua, J.; Zakeeruddin, S. M.; Moser, J. E.; Grätzel, M.; Hagfeldt, A. Dye-Sensitized Solar Cells for Efficient Power Generation under Ambient Lighting. Nature Photonics 2017 11:6 **2017**, 11 (6), 372–378. https://doi.org/10.1038/nphoton.2017.60.
- (11) Yeoh, M. E.; Chan, K. Y. A Review on Semitransparent Solar Cells for Real-Life Applications Based on Dye-Sensitized Technology. IEEE J Photovolt **2021**, 11 (2), 354–361. https://doi.org/10.1109/JPHOTOV.2020.3047199.
- (12) Meggers, W. F.; Stimson, F. J. Dyes for Photographic Sensitizing. J Opt Soc Am **1920**, 4 (3), 91. https://doi.org/10.1364/JOSA.4.000091.
- (13) Quina, F. H.; Silva, G. T. M. The Photophysics of Photosensitization: A Brief Overview. J Photochem Photobiol **2021**, 7, 100042. https://doi.org/10.1016/J.JPAP.2021.100042.
- (14) Moser, J. Notiz Über Verstärkung Photoelektrischer Ströme Durch Optische Sensibilisirung. Monatsh Chem **1887**, 8 (1), 373. https://doi.org/10.1007/BF01510059.
- (15) Gurney, R. W.; Mott, N. F. The Theory of the Photolysis of Silver Bromide and the Photographic Latent Image. Proc R Soc Lond A Math Phys Sci **1938**, 164 (917), 151–167. https://doi.org/10.1098/RSPA.1938.0011.
- (16) Gerischer, H.; Michel-Beyerle, M. E.; Rebentrost, F.; Tributsch, H. Sensitization of Charge Injection into Semiconductors with Large Band Gap. Electrochim Acta **1968**, 13 (6), 1509–1515. https://doi.org/10.1016/0013-4686(68)80076-3.
- (17) TRIBUTSCH, H.; CALVIN, M. ELECTROCHEMISTRY OF EXCITED MOLECULES: PHOTO-ELECTROCHEMICAL REACTIONS OF CHLOROPHYLLS. Photochem Photobiol **1971**, 14 (2), 95–112. https://doi.org/10.1111/J.1751-1097.1971.TB06156.X.
- (18) Osa, T.; Fujihira, M. Photocell Using Covalently-Bound Dyes on Semiconductor Surfaces. Nature 1976 264:5584 **1976**, 264 (5584), 349–350. https://doi.org/10.1038/264349a0.
- (19) Aghazada, S.; Nazeeruddin, M. K. Ruthenium Complexes as Sensitizers in Dye-Sensitized Solar Cells. Inorganics 2018, Vol. 6, Page 52 **2018**, 6 (2), 52. https://doi.org/10.3390/INORGANICS6020052.
- (20) Augustynski, J.; Vlachopoulos, N.; Liska, P.; GräTzel, M. Very Efficient Visible Light Energy Harvesting and Conversion by Spectral Sensitization of High Surface Area Polycrystalline Titanium Dioxide Films. J Am Chem Soc **1988**, 110 (4), 1216–1220. https://doi.org/10.1021/JA00212A033/ASSET/JA00212A033.FP.PNG_V03.

- (21) Desilvestro, J.; Grätzel, M.; Kavan, L.; Moser, J.; Augustynski, J. Highly Efficient Sensitization of Titanium Dioxide. J Am Chem Soc **1985**, 107 (10), 2988–2990. https://doi.org/10.1021/JA00296A035/ASSET/JA00296A035.FP.PNG V03.
- O'Regan, B.; Grätzel, M. A Low-Cost, High-Efficiency Solar Cell Based on Dye-Sensitized Colloidal TiO2 Films. Nature **1991**, 353 (6346), 737–740. https://doi.org/10.1038/353737A0.
- (23) Nazeeruddin, M. K.; Kay, A.; Rodicio, I.; Humphry-Baker, R.; Müller, E.; Liska, P.; Vlachopoulos, N.; Grätzel, M. Conversion of Light to Electricity by Cis-X2Bis (2,2'-Bipyridyl-4,4'-Dicarboxylate) Ruthenium (II) Charge-Transfer Sensitizers (X = Cl-, Br-, I-, CN-, and SCN-) on Nanocrystalline TiO2 Electrodes. J Am Chem Soc 1993, 115 (14), 6382–6390. https://doi.org/10.1021/JA00067A063.
- (24) Mathew, S.; Yella, A.; Gao, P.; Humphry-Baker, R.; Curchod, B. F. E.; Ashari-Astani, N.; Tavernelli, I.; Rothlisberger, U.; Nazeeruddin, M. K.; Grätzel, M. Dye-Sensitized Solar Cells with 13% Efficiency Achieved through the Molecular Engineering of Porphyrin Sensitizers. Nature Chemistry 2014 6:3 **2014**, 6 (3), 242–247. https://doi.org/10.1038/nchem.1861.
- (25) Kakiage, K.; Aoyama, Y.; Yano, T.; Oya, K.; Fujisawa, J. I.; Hanaya, M. Highly-Efficient Dye-Sensitized Solar Cells with Collaborative Sensitization by Silyl-Anchor and Carboxy-Anchor Dyes. Chemical Communications **2015**, 51 (88), 15894–15897. https://doi.org/10.1039/C5CC06759F.
- (26) McMillin, D. R.; Buckner, M. T.; Ahn, B. Tae. A Light-Induced Redox Reaction of Bis(2,9-Dimethyl-1,10-Phenanthroline)Copper(I). Inorg Chem **2002**, 16 (4), 943–945. https://doi.org/10.1021/IC50170A046.
- (27) Shigeki Hattori; Yuji Wada; Shozo Yanagida, and; Fukuzumi*, S. Blue Copper Model Complexes with Distorted Tetragonal Geometry Acting as Effective Electron-Transfer Mediators in Dye-Sensitized Solar Cells. J Am Chem Soc **2005**, 127 (26), 9648–9654. https://doi.org/10.1021/JA0506814.
- (28) Sandroni, M.; Favereau, L.; Planchat, A.; Akdas-Kilig, H.; Szuwarski, N.; Pellegrin, Y.; Blart, E.; Bozec, H. le; Boujtita, M.; Odobel, F. Heteroleptic Copper(I)–Polypyridine Complexes as Efficient Sensitizers for Dye Sensitized Solar Cells. J Mater Chem A Mater **2014**, 2 (26), 9944–9947. https://doi.org/10.1039/C4TA01755B.
- (29) Cao, Y.; Liu, Y.; Zakeeruddin, S. M.; Hagfeldt, A.; Grätzel, M. Direct Contact of Selective Charge Extraction Layers Enables High-Efficiency Molecular Photovoltaics. Joule **2018**, 2 (6), 1108–1117. https://doi.org/10.1016/j.joule.2018.03.017.
- (30) McCusker, C. E.; Castellano, F. N. Design of a Long-Lifetime, Earth-Abundant, Aqueous Compatible Cu(I) Photosensitizer Using Cooperative Steric Effects. Inorg Chem **2013**, 52 (14), 8114–8120. https://doi.org/10.1021/IC401213P.
- (31) Huang, S. Y.; Schlichthörl, G.; Nozik, A. J.; Grätzel, M.; Frank, A. J. Charge Recombination in Dye-Sensitized Nanocrystalline TiO2 Solar Cells. Journal of Physical Chemistry B **1997**, 101 (14), 2576–2582. https://doi.org/10.1021/JP962377Q.

- (32) Ondersma, J. W.; Hamann, T. W. Recombination and Redox Couples in Dye-Sensitized Solar Cells. Coord Chem Rev **2013**, 257 (9–10), 1533–1543. https://doi.org/10.1016/J.CCR.2012.09.010.
- (33) Xie, Y.; Baillargeon, J.; Hamann, T. W. Kinetics of Regeneration and Recombination Reactions in Dye-Sensitized Solar Cells Employing Cobalt Redox Shuttles. Journal of Physical Chemistry C **2015**, 119 (50), 28155–28166. https://doi.org/10.1021/ACS.JPCC.5B08244.
- (34) Wang, Y.; Hamann, T. W. Improved Performance Induced by in Situ Ligand Exchange Reactions of Copper Bipyridyl Redox Couples in Dye-Sensitized Solar Cells. Chemical Communications **2018**, 54 (87), 12361–12364. https://doi.org/10.1039/C8CC07191H.
- (35) Karpacheva, M.; Malzner, F. J.; Wobill, C.; Büttner, A.; Constable, E. C.; Housecroft, C. E. Cuprophilia: Dye-Sensitized Solar Cells with Copper(I) Dyes and Copper(I)/(II) Redox Shuttles. Dyes and Pigments **2018**, 156, 410–416. https://doi.org/10.1016/j.dyepig.2018.04.033.
- (36) Fürer, S. O.; Milhuisen, R. A.; Kashif, M. K.; Raga, S. R.; Acharya, S. S.; Forsyth, C.; Liu, M.; Frazer, L.; Duffy, N. W.; Ohlin, C. A.; Funston, A. M.; Tachibana, Y.; Bach, U. The Performance-Determining Role of Lewis Bases in Dye-Sensitized Solar Cells Employing Copper-Bisphenanthroline Redox Mediators. Adv Energy Mater **2020**, 10 (37), 2002067. https://doi.org/10.1002/AENM.202002067.
- (37) Rodrigues, R. R.; Lee, J. M.; Taylor, N. S.; Cheema, H.; Chen, L.; Fortenberry, R. C.; Delcamp, J. H.; Jurss, J. W. Copper-Based Redox Shuttles Supported by Preorganized Tetradentate Ligands for Dye-Sensitized Solar Cells. Dalton Transactions 2020, 49 (2), 343–355. https://doi.org/10.1039/C9DT04030G.
- (38) Devdass, A.; Watson, J.; Firestone, E.; Hamann, T. W.; Delcamp, J. H.; Jurss, J. W. An Efficient Copper-Based Redox Shuttle Bearing a Hexadentate Polypyridyl Ligand for DSCs under Low-Light Conditions. ACS Appl Energy Mater **2022**, 5 (5), 5964–5973. https://doi.org/10.1021/ACSAEM.2C00344.
- (39) Higashino, T.; Imahori, H. Emergence of Copper(I/II) Complexes as Third-Generation Redox Shuttles for Dye-Sensitized Solar Cells. ACS Energy Lett **2022**, 7 (6), 1926–1938. https://doi.org/10.1021/ACSENERGYLETT.2C00716.
- (40) Sayah, D.; Ghaddar, T. H. Investigation of Ethylisopropyl Sulfone Medium with a Copper-Based Redox Electrolyte for Ambient Light Dye-Sensitized Solar Cells: Achieving High Efficiency and Enduring Long-Term Stability. ACS Appl Energy Mater **2023**, 6 (23), 11924–11933. https://doi.org/10.1021/ACSAEM.3C02067.

Chapter 5: Charge Collection Efficiency,

Recombination and Self Exchange Kinetics

5.1 Introduction

Charge collection efficiency (η_{CC}) refers to the ability of the electrodes to capture and transport the generated electrons to the external circuit without significant losses due to recombination processes. Recombination is the process of back electron transfer from the conduction band of the semiconductor to the electrolyte. Efficient charge collection ensures that a maximum number of photogenerated carriers contribute to the photocurrent, thereby enhancing the device's performance. The electron diffusion length (Ln) is a term that is associated with charge collection. It calculated as the square root of the product of the electron diffusion coefficient (D) and the recombination time constant (τ) i.e.

$$Ln = \sqrt{D\tau} (1)$$

Alternatively, the electron lifetime, provides a statistical measure of the average distance electrons traverse within the electron-conducting network before undergoing recombination with redox species in the electrolyte. High charge-collection efficiencies necessitate that Ln significantly exceeds the thickness of the film. ^{1–3} In well-optimized DSSCs, the charge-collection efficiency at short circuit typically approaches 100% since recombination at this point is marginal. ^{4–6} Nevertheless, comprehending the charge-collection efficiency for these systems remains inadequately understood.

Theoretically η_{CC} is given by:

$$\eta_{CC} = \frac{\left[-Ln\,\varepsilon\, cosh\left(\frac{d}{Ln}\right) + sinh\left(\frac{d}{Ln}\right) + Ln\,\varepsilon\,e^{-\varepsilon d}\right]}{(1 - Ln^2\varepsilon^2)\left(1 - e^{-\varepsilon d}\right)cosh\left(\frac{d}{Ln}\right)}(2)$$

The derivation of this equation is discussed in Chapter 2. Achieving efficient charge collection hinges on minimizing recombination rates, a process crucial for photovoltaic performance. The mechanism of retro cells, as mentioned in Chapter 2, is similar to earlier works of Clark and Sutin on $[Ru(dmphen)_3]^{2+}$ in single crystals.⁷ A notable distinction between the single crystal electrodes employed by Sutin et al. and the proposed mesoporous electrodes lies in band-bending, which effectively impedes recombination reactions. Band bending refers to the distortion of energy bands near the interface between two materials. In a semiconductor material, the energy bands-valence and conduction bands- represent the allowed energy levels for electrons. When a solution contacts a semiconductor, there is a difference in the fermi levels between the two materials. This difference in fermi levels induces an electric field at the interface, causing the energy bands in the semiconductor to bend or curve. Retro cells utilizing mesoporous TiO_2 however, will be affected by recombination due to the absence of band bending, which in turn will affect the photogenerated charge collection efficiency. This study delves into η_{CC} and the parameters affecting it, in order to understand the mechanism of retro cells better.

 η_{CC} is directly proportional to Ln, with Ln being inversely proportional to the rate constant of electron transfer from the semiconductor to the oxidized form of the redox shuttle, ket. This rate is given by Marcus theory as:⁸

$$k = k_{\text{et,max}} exp\left(-\frac{(\Delta G + \lambda)^2}{4\lambda k_B T}\right) (3)$$

Here, ΔG denotes the driving force for electron transfer, and λ represents the reorganization energy associated with the electron transfer process. The reorganization energy associated with interfacial

reactions can be derived from the reorganization energy of self-exchange reactions. This selfexchange reorganization energy encompasses both outer-sphere (λ_0) and inner-sphere (λ_i) components. To determine the self-exchange rate constants of [Cu(dsbtmp)₂]^{2+/+}, ¹H-NMR line broadening experiments were undertaken. This study aims to establish correlations between selfexchange kinetics and the excited state lifetimes across a range of copper phenanthroline complexes. The objective is to establish a theoretical framework for interpreting recombination reactions retro cells based on fundamental parameters and elucidate the influence of exogenous bases on band positions and rate constants. It is hypothesized that a correlation exists between excited state lifetime and self-exchange kinetics, with steric hindrance induced by ligands potentially prolonging excited state lifetimes and minimizing inner-sphere reorganization energy. The investigation into the rates and mechanisms governing the substitution of one ligand by another within coordination compounds has progressed significantly, reaching a high level of complexity. If a proton partakes in a reversible chemical transformation occurring within a timeframe comparable to its relaxation time, the shape of the NMR line will undergo alterations. Under specific circumstances, it becomes feasible to ascertain the rate of this change based on the line shape. Utilizing NMR to ascertain self-exchange rate constants relies on contrasting the proton spectrum of a diamagnetic species, characterized by sharp peaks and chemical shifts ranging from 0 to 12 ppm, with that of a paramagnetic species, which manifests broad peaks with chemical shifts spanning from -200 to 200 ppm. 9-16 The following paragraph discusses the principles and equations that help us correlate the width of proton peaks to the proton exchange rates in a ¹H-NMR.

Bloch equations (in rotating coordinates) are given by:

$$\frac{dM_z}{dt} = \gamma H_1 \nu - (M_z - M_0) / T_1 (4)$$

$$\frac{\text{d}\nu}{\text{d}t} = \gamma H_1 M_z + (\omega_0 - \omega) u - \frac{\nu}{T_2} (5)$$

$$\frac{du}{dt} = -(\omega_0 - \omega)\nu - \frac{u}{T_2}(6)$$

where vector M is the magnetization induced in a sample when it is placed in a magnetic field, H_0 . M_z is the magnetization along z direction. γ is the gyromagnetic ratio of the nucleus, ω_0 is the precession frequency of the nucleus, ω is the frequency of the field, T_1 and T_2 are the longitudinal and transverse relaxation times respectively. Using the unmodified Bloch equations, it can be shown that line widths are related to the transverse relaxation time as:

$$\Delta v = \frac{1}{\pi T_2} (7)$$

Using this concept, line- broadening in 1 H-NMR can be a powerful tool to understand self-exchange reactions. For slow exchange regime of NMR relaxation processes, the chemical shift difference $\Delta\omega$ follows the condition:

$$\Delta\omega^2\gg \frac{1}{{T_2}^2},\frac{1}{\tau^2}(8)$$

where τ is the lifetime of a nuclear spin in a paramagnetic field.

The self-exchange rate constant for the copper complexes under consideration are thus related to the exchange induced line broadening as:

$$k = \frac{\pi \{\Delta v\}}{[Cu(II)](M)} (9)$$

5.2 Measurement of self-exchange rate for copper

complexes

According to slow exchange conditions, it has previously been established by various experiments that the self-exchange rate is independent of the paramagnetic species in the couple. 9,17,18 Prior to

conducting measurements on the self-exchange rates of the $[Cu(dsbtmp)_2]^{2+/+}$ shuttle, $[Cu(dmp)_2]^{2+/+}$ was initially measured to validate the accuracy of the methodology.

A 2D COSY ¹H-NMR spectrum was obtained for [Cu(dmp)₂]⁺, revealing the absence of coupling between the 2,9 methyl protons and other protons. As coupling could potentially influence the determination of the self-exchange rate, this analysis was imperative to confirm its absence. The line broadening experiment was performed in deuterated acetonitrile and the 2,9 methyl proton singlet at 2.42 ppm (for Cu(I)) was picked for the analysis. Paramagnetic species Cu(II), on the other hand, do not have any such sharp peak at 2.24 ppm. On addition of Cu(II) to a sample of Cu(I), the peak at 2.42 ppm broadens. This phenomenon was utilized to determine the value of self-exchange rate constant according to equation (10), which is a variation of equation (9):

$$k(M^{-1}s^{-1}) = \frac{\pi \left\{fwhm (Hz)\right\}_{para+dia} - \pi \left\{fwhm (Hz)\right\}_{dia}}{[Cu(II)](M)} (10)$$

where fwhm is the full width half maxima

The Cu(II) concentration was varied and the dependence of Cu(II) concentration with linewidth was plotted. The concentration of the diamagnetic species, Cu(I) was kept at a constant value of 10mM. Plots of 1 H-NMR line widths of 10mM [Cu(dmp)₂](PF₆) as a function of temperature at different concentrations of paramagnetic [Cu(dmp)₂](PF₆)₂ is given in figure 5.1. Figure 5.2 is a representative plot of the dependence of the exchange-induced broadening of the Cu(II) linewidth as a function of concentration of Cu(II) at a particular temperature. The self-exchange rate constant, k is measured from this plot according to equation (10). The value of the self-exchange rate constant, k is found to be $(7.49 \pm 0.5) \times 10^4 \text{ M}^{-1} \text{ s}^{-1}$ at 298 K for [Cu(dmp)₂]^{2+/+}. The measurements were carried out at several temperatures- 298 K, 303 K, 308 K, 313 K and 323 K and the data was interpreted. The rate constants at different temperatures are listed in Table 5.1. This complex has been widely studied in literature and its self-exchange rates have also been

measured by various methods by several groups.¹⁹ However, it has been pointed out their there has been discrepancies in the values measured and the values changed with the change in type of study.¹⁹ One of the reasons for this discrepancy might be due to the fact that most of these studies have been carried out in acetonitrile, which is a common solvent system for [Cu(dmp)₂]^{+/2+}. However, there is a possibility of coordination of acetonitrile to the Cu(II) form due to the structural changes that take place when Cu(I) is oxidized to Cu(II), which opens up a coordination site in Cu(II).²⁰ Due to this reason, further investigations need to be carried out to measure a more accurate self-exchange rate constant value, possibly by changing the solvent system into a less coordinating one.

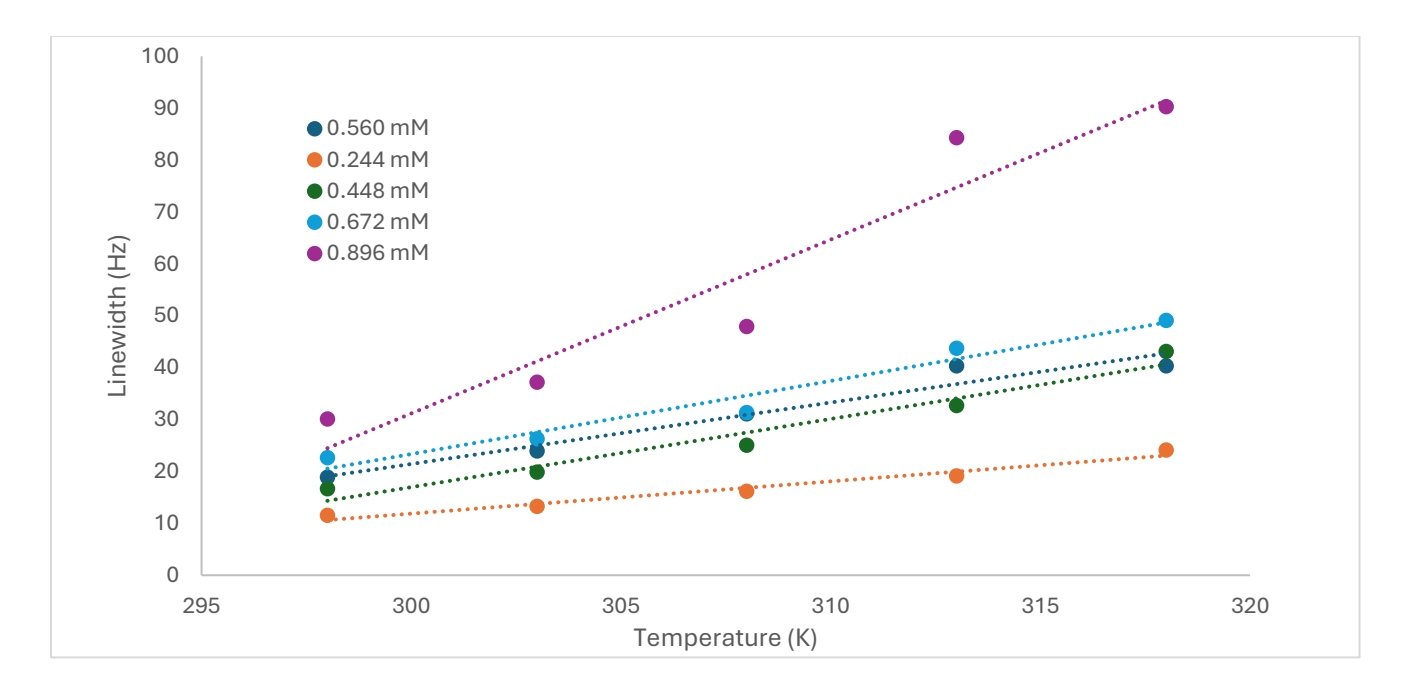


Figure 5.1: Plot of ${}^{1}H$ -NMR line widths of 10mM [Cu(dmp)₂](PF₆) (with different concentrations of corresponding paramagnetic [Cu(dmp)₂](PF₆)₂) vs temperature. The legend shows the different concentrations of [Cu(dmp)₂](PF₆)₂.

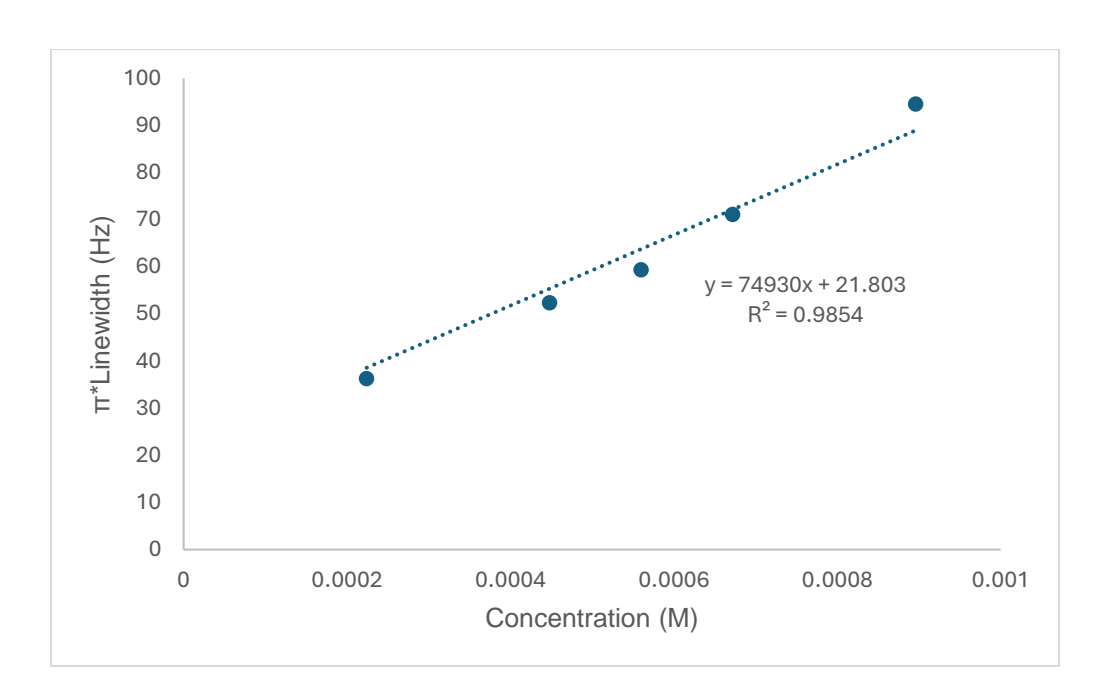


Figure 5.2: Plot of ¹H-NMR line widths of 10mM [Cu(dmp)₂](PF₆) vs concentration of corresponding paramagnetic [Cu(dmp)₂](PF₆)₂ at 308 K.

Table 5.1: Values of self-exchange rate constant for [Cu(dmp)₂]^{+/2+} at different temperatures

Temperature (K)	Self-exchange rate constant, k (M s)
298	$(7.49 \pm 0.5) \times 10^4$
303	$(9.82 \pm 0.7) \times 10^4$
308	$(1.33 \pm 0.2) \times 10^5$
313	$(2.19 \pm 0.4) \times 10^5$
318	$(2.45 \pm 0.5) \times 10^5$

The self-exchange rate constant for the couple [Cu(dsbtmp)₂]^{+/2+} was calculated next. ¹H-NMR data for the species is given in figure 5.3. Diamagnetic species Cu(I) has a sharp peak at 8.22 ppm in the ¹H-NMR spectra when CD₂Cl₂ is used as the solvent. Paramagnetic species Cu(II), on the

other hand, do not have any such sharp peak at 8.22 ppm (figure 7-2). On addition of Cu(II) to a sample of Cu(I), the peak at 8.22 ppm broadens. This phenomenon was utilized to determine the value of self-exchange rate constant according to equation (10). The Cu(II) concentration was varied and the dependence of Cu(II) concentration with linewidth was plotted. The concentration of the diamagnetic species, Cu(I) was kept at a constant value of 10mM. From the plot in figure 5.4 and equation (10), the self-exchange rate constant, k was measured. Plots of ¹H-NMR line widths of 10mM [Cu(dsbtmp)₂](PF₆) as a function of temperature at different concentrations of paramagnetic [Cu(dsbtmp)₂](PF₆)₂ is given in figure 5.5.

The value of the self-exchange rate constant, k is found to be $(7.19 \pm 1.07) \times 10^5 \, M^{-1} \, s^{-1}$ at 298 K. The measurements were carried out at several temperatures- 298 K, 303 K, 308 K, 313 K and 323 K and the data was interpreted. The rate constants at different temperature are listed on Table 5.2. It can be observed that with increase in temperature, the self-exchange rate constant also increases. These values help in further estimating the kinetics of the proposed system. For instance, reorganizational energy of the complexes can be calculated using the self- exchange rate constant which would further help in estimation of rates of recombination of electrons from the semiconductor to the redox couple. This rate constant can also be compared to the self-exchange rate constant value calculated from single-crystal X-ray crystallography data to see if the results are in agreement with each other.

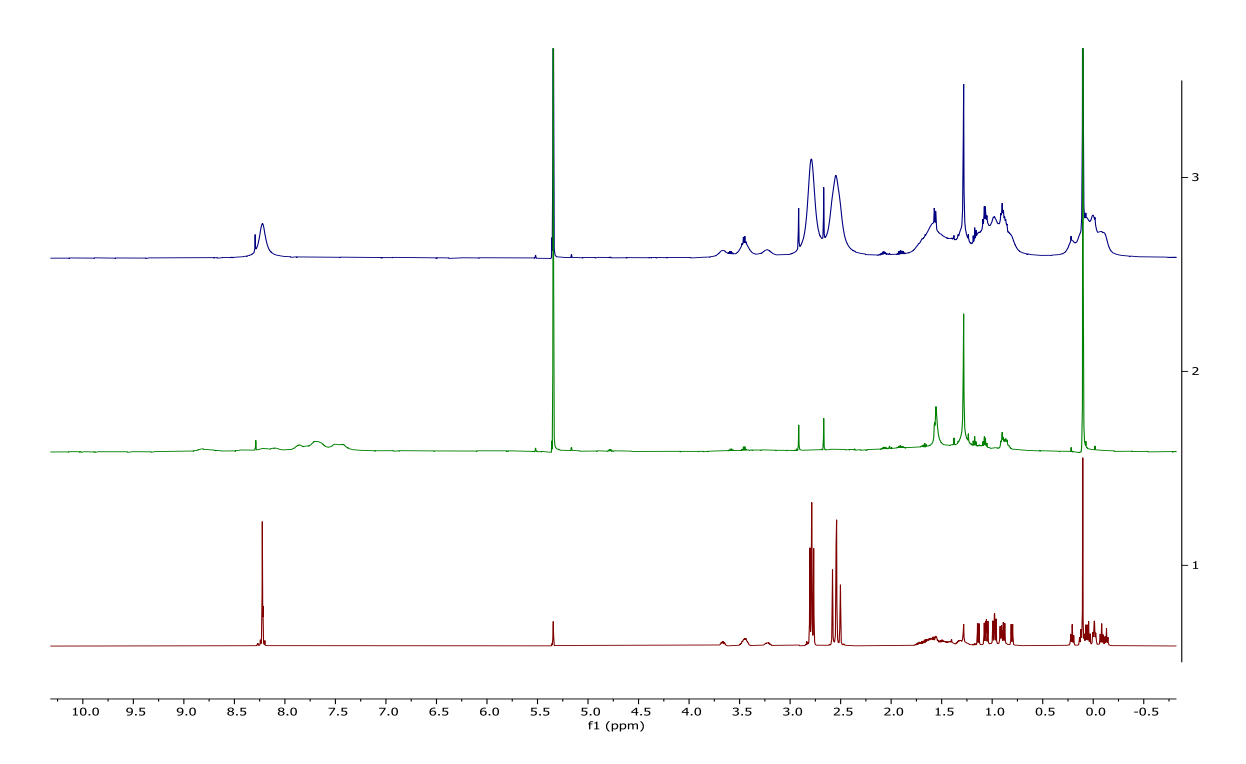


Figure 5.3: (1) ¹H-NMR of [Cu(dsbtmp)₂](PF₆) in CD₂Cl₂. (2) ¹H-NMR of [Cu(dsbtmp)₂](PF₆)₂ in CD₂Cl₂. (3) Mixture of 10mM [Cu(dsbtmp)₂](PF₆) and 1mM [Cu(dsbtmp)₂](PF₆)₂ in CD₂Cl₂.

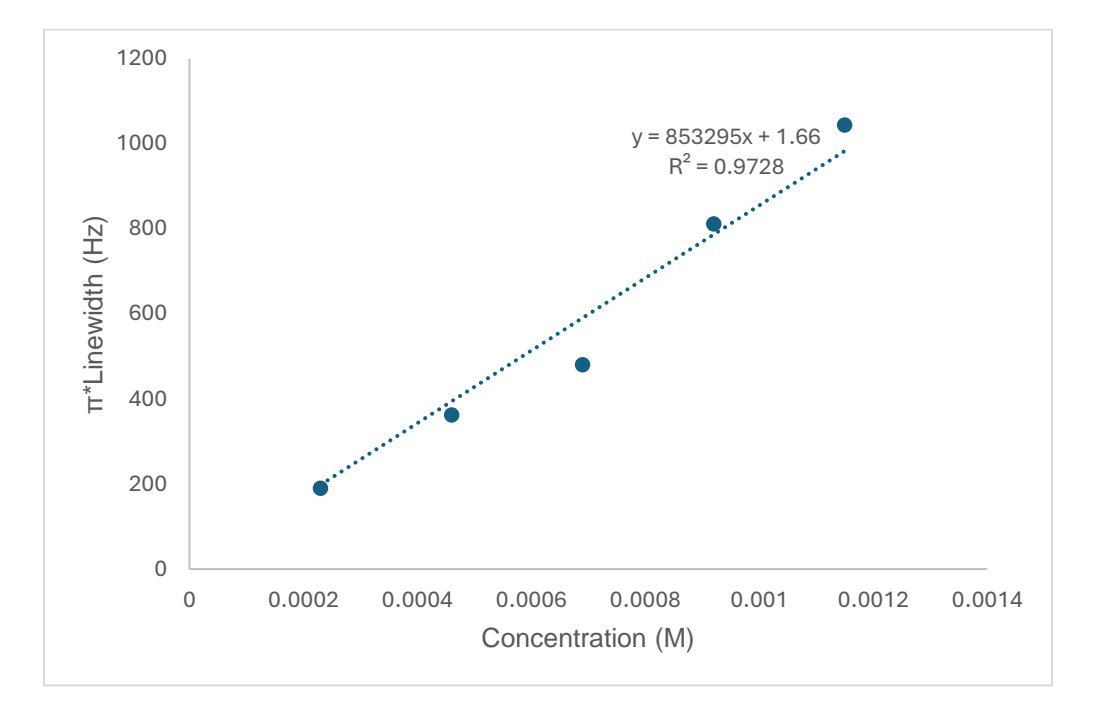


Figure 5.4: Plot of ¹H-NMR line widths of 10mM [Cu(dsbtmp)₂](PF₆) vs concentration of corresponding paramagnetic [Cu(dsbtmp)₂](PF₆)₂ at 308 K.

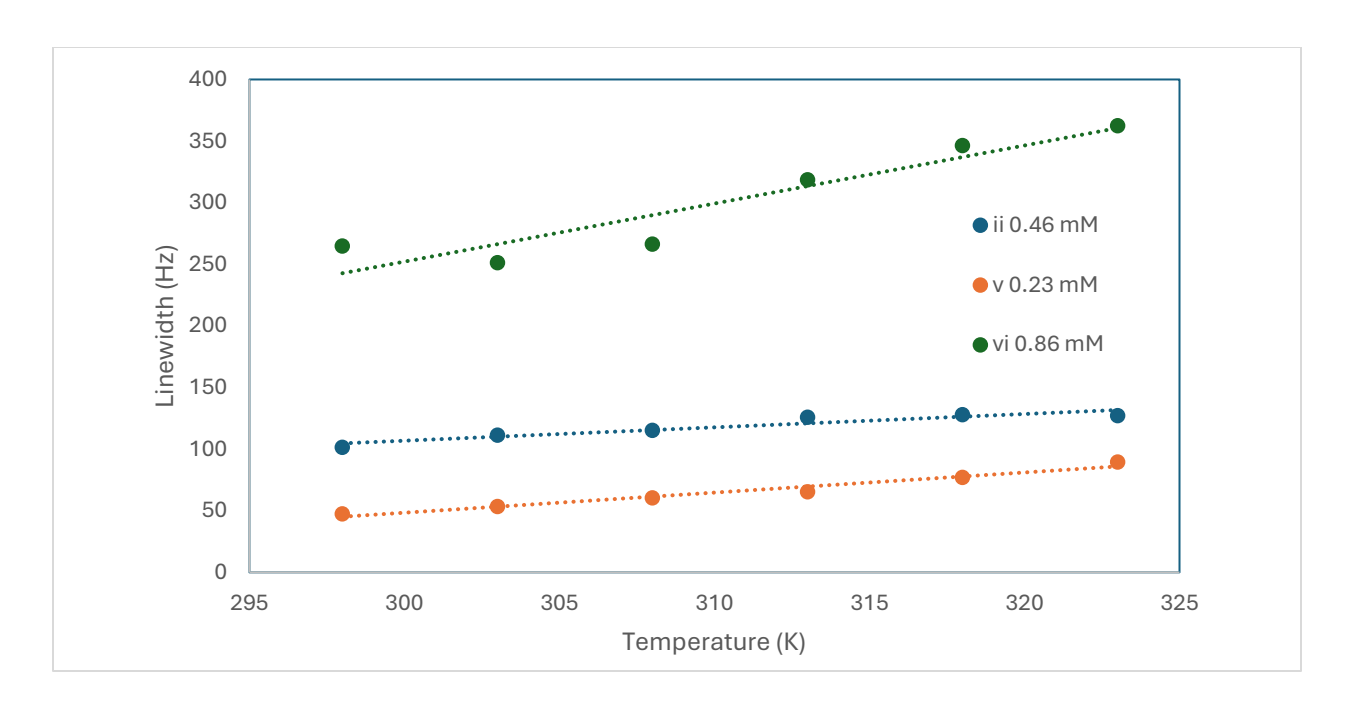


Figure 5.5: Plot of ${}^{1}H$ -NMR line widths of 10mM [Cu(dmp)₂](PF₆) (with different concentrations of corresponding paramagnetic [Cu(dmp)₂](PF₆)₂) vs temperature. The legend shows the different concentrations of [Cu(dmp)₂](PF₆)₂.

Table 5.2: Values of self-exchange rate constant for [Cu(dsbtmp)₂]^{+/2+} at different temperatures

Temperature (K)	Self-exchange rate constant, k (M ⁻¹ s ⁻¹)
298	$(7.19 \pm 1.07) \times 10^5$
303	$(7.71 \pm 1.74) \times 10^5$
308	$(8.53 \pm 0.82) \times 10^5$
313	$(8.76 \pm 1.72) \times 10^5$
318	$(1.00 \pm 0.29) \times 10^6$

5.3 Reorganization Energy

As briefly mentioned above, reorganization energy in transition metal complexes plays a significant role in understanding their electron transfer processes and reactivity. Transition metal complexes often undergo redox reactions involving the transfer of electrons between the metal center and ligands. Reorganization energy quantifies the energetic cost associated with the structural changes that occur during these electron transfer events. Marcus theory provides a framework for understanding electron transfer reactions, including those in transition metal complexes. According to Marcus theory, the rate of electron transfer (k_{ET}) between a donor and acceptor is given by the equation (3).

The reorganization energy encompasses an outer-sphere (λ_0) and an inner-sphere (λ_i) component. The reorganization energy (λ_0) in outer sphere processes accounts for changes in the solvent environment surrounding the donor and acceptor molecules. This includes solvent reorganization and polarization effects as the solvent molecules adjust to accommodate the changing charge distribution. The outer-sphere reorganization energy was assessed using the crystal structure data. The equation for λ_0 is given by:^{8,22–24}

$$\lambda_{o} = \frac{(\Delta q)^{2}}{4 \pi \epsilon_{0}} \left(\frac{1}{2 a_{1}} + \frac{1}{2 a_{2}} - \frac{1}{R} \right) \left(\frac{1}{\epsilon_{op}} - \frac{1}{\epsilon_{sol}} \right)$$

here, q represents the charge transferred, a2 and a1 denote the radii of the two reactants, and R stands for the distance between the centers of the two reactants. ϵ_{op} is ϵ_{0} is the permittivity of free space, the optical dielectric constant and ϵ_{sol} is the dielectric constant of the solvent. The λ_{o} for the $[Cu(dsbtmp)_{2}]^{2+/+}$ solution was calculated to be 0.40 eV.

The reorganization energy in inner sphere processes accounts for the energetic cost associated with changes in the geometry of the donor, acceptor, and intervening ligands during the electron transfer. This includes changes in bond lengths, angles, and coordination environments. $^{25-29}$ λ represents the potential energy necessary to alter the nuclear coordinates of the reactants from their equilibrium positions to the coordinates relevant to the intersection region in an electron transfer process. Here, λ denotes the barrier for the thermal electron-transfer reaction. The rate constant for electron exchange in the high-temperature limit is determined by:

$$k = v_n \exp\left(-\frac{\lambda}{4k_BT}\right)$$

where v_n the effective vibration frequency of the reactants, k_B is the Boltzmann constant and T is the temperature. The v_n is solvent dependent and is usually in the range of $10^{11}-10^{13}~\text{s}^{-1}$. ¹⁷ Solving this equation for the $[\text{Cu}(\text{dsbtmp})_2]^{2^{+/+}}$ solution with the k values from the self- exchange measurement above $((3.8\pm0.2)~\text{x}~10^5~\text{M}^{-1}~\text{s}^{-1})$ at 294.15 K, the λ was found to be 1.26 eV. However, this is an estimated value because of the assumption of the value of v_n .

5.4 Future Work

The measurement for self-exchange rate and reorganization energy is based on a few assumptions. In order to get a more quantitative value, other studies need to be carried out to estimate the accurate value of v_n . One important aspect of the experiments above needs to be pointed out about the ¹H-NMR spectroscopy line-broadening measurements of [Cu(dsbtmp)₂]^{2+/+} as shown in figure 5.6. While carrying out the study, it was noted that the peak at 8.22 ppm for the paramagnetic Cu(I) species was not a pure "singlet" as reported in literature³⁰ but was actually a doublet due to the presence of stereoisomerism of the di-sec-butyl groups. Even though the molecule was predicted to be symmetrical in literature before, but XRD data in Chapter 2 reveals that the geometry is

pseudo-disphenoidal, which explains the splitting of the peak. This limited the accurate the interpretation of peak broadening and introduced uncertainties in rate constant determination. To address this, Cu(II/I) complexes with symmetric ligands, such as [Cu(dipp)₂]^{2+/+} (where dipp is 2,9-diisopropyl-1,10-phenanthroline) and [Cu(diptmp)₂]^{2+/+}, needs be prepared and utilized to measure self-exchange rate constants.

After solving the problems with the stereoisomers, employing steric bulk to mitigate pseudo-Jahn–Teller distortion and extend excited state lifetimes has the potential to diminish the reorganization energy associated with electron transfer, thus facilitating rapid shuttling—a characteristic of an effective acceptor species.

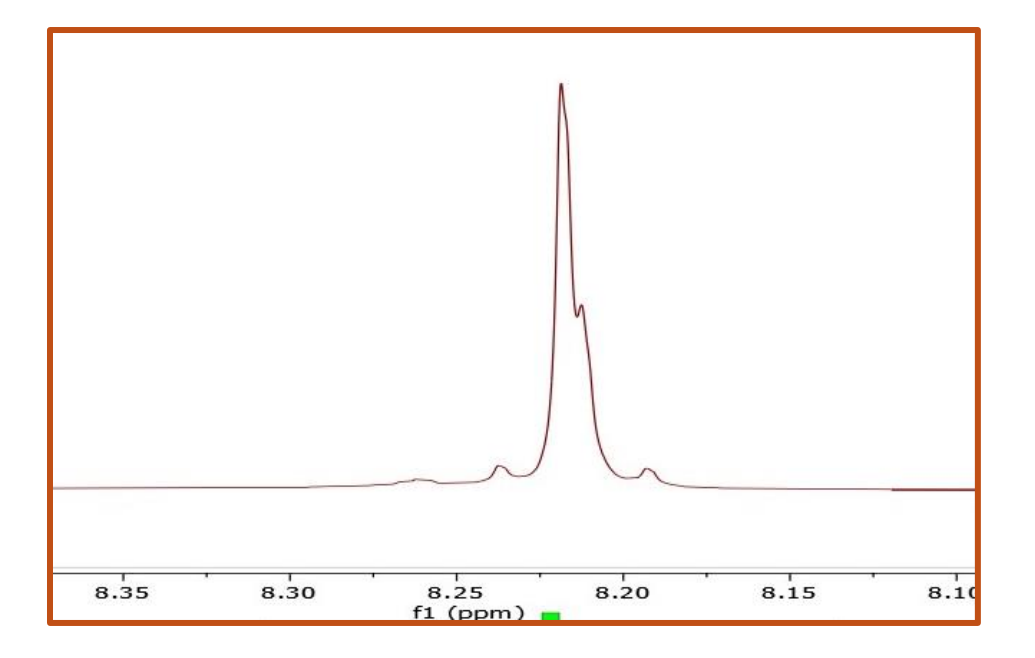


Figure 5.6: (1) ¹H-NMR of [Cu(dsbtmp)₂](PF₆) in CD₂Cl₂ showing the "pseudo-singlet" at 8.22 ppm which is actually a doublet due to the stereoisomerism in the complex.

REFERENCES

- (1) Sodergren, S.; Hagfeldt, A.; Olsson, J.; Lindquist, S. E. Theoretical Models for the Action Spectrum and the Current-Voltage Characteristics of Microporous Semiconductor Films in Photoelectrochemical Cells. Journal of physical chemistry **1994**, 98 (21), 5552–5556. https://doi.org/10.1021/J100072A023.
- (2) Schlichthörl, G.; Huang, S. Y.; Sprague, J.; Frank, A. J. Band Edge Movement and Recombination Kinetics in Dye-Sensitized Nanocrystalline TiO2 Solar Cells: A Study by Intensity Modulated Photovoltage Spectroscopy. Journal of Physical Chemistry B **1997**, 101 (41), 8141–8155. https://doi.org/10.1021/JP9714126.
- (3) Dloczik, L.; Ileperuma, O.; Lauermann, I.; Peter, L. M.; Ponomarev, E. A.; Redmond, G.; Shaw, N. J.; Uhlendorf, I. Dynamic Response of Dye-Sensitized Nanocrystalline Solar Cells: Characterization by Intensity-Modulated Photocurrent Spectroscopy. Journal of Physical Chemistry B **1997**, 101 (49), 10281–10289. https://doi.org/10.1021/JP972466I/ASSET/IMAGES/LARGE/JP972466IF00016.JPEG.
- (4) Schlichthörl, G.; Park, N. G.; Frank, A. J. Evaluation of the Charge-Collection Efficiency of Dye-Sensitized Nanocrystalline TiO2 Solar Cells. Journal of Physical Chemistry B **1999**, 103 (5), 782–791. https://doi.org/10.1021/JP9831177.
- (5) Donolato, C. A Reciprocity Theorem for Charge Collection. Appl Phys Lett **1985**, 46 (3), 270–272. https://doi.org/10.1063/1.95654.
- (6) Bertoluzzi, L.; Ma, S. On the Methods of Calculation of the Charge Collection Efficiency of Dye Sensitized Solar Cells. Physical Chemistry Chemical Physics **2013**, 15 (12), 4283–4285. https://doi.org/10.1039/C3CP44248A.
- (7) Clark, W. D. K.; Sutin, N. Spectral Sensitization of N-Type TiO2 Electrodes by Polypyridineruthenium(II) Complexes. J Am Chem Soc **1977**, 99 (14), 4676–4682. https://doi.org/10.1021/ja00456a025.
- (8) Marcus, R. A. Chemical and Electrochemical Electron-Transfer Theory. Annu Rev Phys Chem **1964**, 15 (1), 155–196. https://doi.org/10.1146/ANNUREV.PC.15.100164.001103.
- (9) Smolenaers, P. J.; Beattie, J. K. Proton NMR Investigation of the Electron-Exchange Reaction between Hexaammineruthenium(II) and Hexaammineruthenium(III) Ions. Inorg Chem 1986, 25 (13), 2259–2262. https://doi.org/10.1021/ic00233a033.
- (10) Jameson, D. L.; Anand, R. Examination of Electron Transfer Self-Exchange Rates Using NMR Line-Broadening Techniques: An Advanced Physical Inorganic Laboratory Experiment. J Chem Educ **2000**, 77 (1), 88. https://doi.org/10.1021/ed077p88.
- (11) Chandrasekhar, S.; Mcauley, A. Contribution from the Syntheses, Structure, and Reactivity of Cobalt and Nickel Complexes of 1,4,7-Trithiacyclodecane: Self-Exchange Rates for Co(S6)2+/3+ Couples from 59Co NMR Spectroscopy; 1992; Vol. 31. https://pubs.acs.org/sharingguidelines (accessed 2021-05-03).

- (12) Pearson, R. G.; Lanier, R. D. Rates of Rapid Ligand Exchange Reactions by Nuclear Magnetic Resonance Line Broadening Studies1a. J Am Chem Soc **1964**, 86 (5), 765–771. https://doi.org/10.1021/JA01059A004.
- (13) Thomas, S.; Reynolds, W. L. Solvation Number and Solvent Exchange Rate of Al(DMSO)N3+ in DMSO. J Chem Phys **1966**, 44 (8), 3148–3149. https://doi.org/10.1063/1.1727207.
- (14) Glaeser, H. H.; Dodgen, H. W.; Hunt, J. P. The Kinetics of Exchange of Ammonia with the Hexaamminecobalt(II) Complex in Anhydrous Ammonia. Inorg Chem **1965**, 4 (7), 1061–1063. https://doi.org/10.1021/IC50029A031.
- (15) Bulkin, B. J.; Rundell, C. A. Bonding in Coordination Compounds Containing Metal-Metal Bonds. Coord Chem Rev **1967**, 2 (3), 371–384. https://doi.org/10.1016/S0010-8545(00)80129-0.
- (16) Pregosin, P. S.; Rüegger, H. Nuclear Magnetic Resonance Spectroscopy. Comprehensive Coordination Chemistry II **2004**, 2, 1–35. https://doi.org/10.1002/chin.200427292.
- (17) Brunschwig, B. S.; Logan, J.; Newton, M. D.; Sutin, N. A Semiclassical Treatment of Electron-Exchange Reactions. Application to the Hexaaquoiron(II)-Hexaaquoiron(III) System. J Am Chem Soc **1980**, 102 (18), 5798–5809. https://doi.org/10.1021/JA00538A017.
- (18) Swift, T. J.; Stephenson, T. A. The Kinetics of Protonation of Nickel and Chromium Hexaaquo Cations in Aqueous Solution. Inorg Chem **1966**, 5 (7), 1100–1105. https://doi.org/10.1021/IC50041A004.
- (19) Rorabacher*, D. B. Electron Transfer by Copper Centers. Chem Rev **2004**, 104 (2), 651–697. https://doi.org/10.1021/CR020630E.
- (20) Blaskie, M. W.; McMillin, D. R. Photostudies of Copper(I) Systems. 6. Room-Temperature Emission and Quenching Studies of Bis(2,9-Dimethyl-1,10-Phenanthroline)Copper(I). Inorg Chem **2002**, 19 (11), 3519–3522. https://doi.org/10.1021/IC50213A062.
- (21) Raithel, A. L.; Kim, T. Y.; Nielsen, K. C.; Staples, R. J.; Hamann, T. W. Low-Spin Cobalt(Ii) Redox Shuttle by Isocyanide Coordination. Sustain Energy Fuels **2020**, 4 (5), 2497–2507. https://doi.org/10.1039/d0se00314j.
- (22) Marcus, R. A.; Sutin, N. Electron Transfers in Chemistry and Biology. BBA Reviews On Bioenergetics. Elsevier August 1, 1985, pp 265–322. https://doi.org/10.1016/0304-4173(85)90014-X.
- (23) German, E. D.; Kuznetsov, A. M. Outer Sphere Energy of Reorganization in Charge Transfer Processes. Electrochim Acta **1981**, 26 (11), 1595–1608. https://doi.org/10.1016/0013-4686(81)85133-X.
- (24) Marcus, R. A. On the Theory of Oxidation-Reduction Reactions Involving Electron Transfer. I. J Chem Phys **1956**, 24 (5), 966–978. https://doi.org/10.1063/1.1742723.

- (25) Brintzinger, H.; Hammes, G. G. Inner- and Outer-Sphere Complex Formation in Aqueous Solutions of Nickel(II)-Methyl Phosphate. Inorg Chem **1966**, 5 (7), 1286–1287. https://doi.org/10.1021/IC50041A050.
- (26) Kessinger, M. C.; Brillhart, C.; Vaissier Welborn, V.; Morris, A. J. The Effect of Inner-Sphere Reorganization on Charge Separated State Lifetimes at Sensitized TiO2interfaces. Journal of Chemical Physics **2020**, 153 (12). https://doi.org/10.1063/5.0023591.
- (27) Brunschwig, B. S.; Creutz, C.; MacArtney, D. H.; Sham, T. K.; Sutin, N. The Role of Inner-Sphere Configuration Changes in Electron-Exchange Reactions of Metal Complexes. Faraday Discuss Chem Soc **1982**, 74 (0), 113–127. https://doi.org/10.1039/DC9827400113.
- (28) Brunschwig, B. S.; Creutz, C.; MacArtney, D. H.; Sham, T. K.; Sutin, N. The Role of Inner-Sphere Configuration Changes in Electron-Exchange Reactions of Metal Complexes. Faraday Discuss Chem Soc **1982**, 74 (0), 113–127. https://doi.org/10.1039/DC9827400113.
- (29) Leandri, V.; Daniel, Q.; Chen, H.; Sun, L.; Gardner, J. M.; Kloo, L. Electronic and Structural Effects of Inner Sphere Coordination of Chloride to a Homoleptic Copper(II) Diimine Complex. Inorg Chem **2018**, 57 (8), 4556–4562. https://doi.org/10.1021/ACS.INORGCHEM.8B00225.
- (30) McCusker, C. E.; Castellano, F. N. Design of a Long-Lifetime, Earth-Abundant, Aqueous Compatible Cu(I) Photosensitizer Using Cooperative Steric Effects. Inorg Chem **2013**, 52 (14), 8114–8120. https://doi.org/10.1021/ic401213p.

Chapter 6: BiVO₄- Liquid Junction Solar Cells

6.1 Introduction

Bismuth vanadate (BiVO₄) has garnered significant attention as a promising photoanode material for various applications, particularly in solar energy conversion technologies such as photoelectrochemical (PEC) water splitting and dye-sensitized solar cells. Here are some key points about BiVO₄:

- 1. Optical Properties: BiVO₄ possesses desirable optical properties, including a suitable bandgap (around 2.4 eV) that allows absorption of a significant portion of the solar spectrum, particularly in the visible range. This feature makes it advantageous for solar energy conversion applications.¹
- 2. Photoelectrochemical Water Splitting: BiVO₄ is a notable candidate for photoelectrochemical water splitting, a process that utilizes sunlight to split water into hydrogen and oxygen. Its bandgap aligns well with the thermodynamic potential required for water oxidation, making it an efficient photoanode material for the oxygen evolution reaction (OER) in water splitting.²⁻
- 3. Stability and Durability: BiVO₄ exhibits good chemical stability under aqueous conditions, which is crucial for long-term performance in water-splitting devices. However, its stability can be further enhanced through various doping strategies and surface modifications.^{4,7}
- 4. Charge Carrier Transport: One challenge with BiVO₄ is its relatively low carrier mobility and high recombination rate of photogenerated charge carriers, which can limit its overall efficiency. Strategies such as heterojunction formation with other semiconductors or surface

- passivation techniques are being explored to mitigate these issues and improve charge transport properties.^{4,7}
- 5. Synthesis Methods: Various synthesis routes have been developed to fabricate BiVO₄ with controlled morphologies, crystalline structures, and surface properties. These include sol-gel methods, hydrothermal synthesis, electrodeposition, and chemical vapor deposition, among others. 1-4,6,7
- 6. Integration in Solar Cells: In addition to PEC water splitting, BiVO₄ has also been investigated for its potential application as a photoanode in dye-sensitized solar cells (DSSCs). Its light absorption properties and stability make it a promising candidate for enhancing the efficiency and stability of these solar cells.^{8,9}

Bismuth vanadate (BiVO₄) has emerged as a notable contender in the realm of dye-sensitized solar cells (DSSCs), offering promising avenues for enhancing device efficiency and stability.^{8,9} The history of BiVO₄ in DSSCs traces back to the early 2000s when researchers began exploring alternative photoanode materials to the prevalent titanium dioxide (TiO₂). TiO₂, while effective, has limitations such as a wide bandgap and limited visible light absorption, prompting the search for alternatives like BiVO₄.

Initially, BiVO₄ gained attention due to its suitable bandgap (around 2.4 eV), enabling absorption of a larger portion of the solar spectrum compared to TiO₂.^{10,11} This characteristic, coupled with its favorable electronic structure and chemical stability, rendered BiVO₄ an attractive candidate for incorporation into DSSCs. Researchers began investigating methods to integrate BiVO₄ into DSSC architectures, aiming to exploit its potential for enhanced light harvesting and charge transport.^{12,13}

Throughout the early stages of research, efforts focused on optimizing the synthesis and processing techniques to fabricate BiVO₄ films with desirable properties for DSSCs. Various methods, including sol-gel, electrodeposition, and chemical vapor deposition, were explored to tailor the morphology, crystallinity, and surface characteristics of BiVO₄ films to enhance their performance in solar cells.

As research progressed, studies delved deeper into understanding the fundamental photophysical and electrochemical processes occurring at the BiVO₄/electrolyte interface in DSSCs. Insights into charge transfer mechanisms, recombination processes, and interface engineering strategies were crucial for improving device efficiency and stability.

In recent years, advancements in material design and device architecture have led to notable progress in BiVO₄-based DSSCs. Strategies such as heterojunction formation, surface passivation, and co-sensitization with organic dyes have been explored to further enhance the performance of BiVO₄ photoanodes in DSSCs.

Today, BiVO₄ continues to be a subject of active research in the field of DSSCs, with ongoing efforts aimed at addressing remaining challenges such as improving charge transport properties, enhancing stability under prolonged exposure to light and electrolytes, and scaling up production processes for commercial viability. ^{3,6,8,14–17}

Despite its advances, the interaction of BiVO₄ electrodes with triiodide/iodide redox couple is not well studied. Therefore, this study was conducted with the help of Frank Osterloh et. al at the University of California Davis in order to elucidate the interaction of BiVO₄ electrodes with triiodide/iodide as a part of DSSCs.¹⁸

6.2 Methodology

Preparation of BiVO₄ Film:

The electrodes were prepared by Sahar Daemi and detailed fabrication can be found in our published paper. 18 The protocol for this was modified from previously established methods. 19 Initially, the FTO pieces with a surface area of 2.0 cm² underwent a thorough cleaning process involving sonication in a soap solution for 5 minutes, followed by sequential sonication in methanol, ethanol, isopropanol, and acetone for 15 minutes each. Subsequently, the BiVO₄/FTO composite was synthesized following a previously published protocol. To summarize, a 50 mL solution of 0.40 M KI with a pH of 1.7 (adjusted using 2.0 M HNO₃) was prepared. Separately, 0.970 grams of Bi(NO₃)₃·5 H₂O was dissolved in 50 mL of 0.4 M KI to yield a 0.040 M Bi(NO₃)₃ solution. This solution was then mixed with 20 mL of absolute ethanol containing 0.23 M pbenzoquinone. The electrodeposition process was carried out using a typical three-electrode cell setup, with FTO serving as the working electrode (WE), calomel (3.5 M KCl) as the reference electrode (RE), and platinum as the counter electrode (CE). BiOI electrodes were electrodeposited onto the FTO substrate for 3–5 minutes, followed by drop-coating 0.10 mL of a dimethyl sulfoxide (DMSO) solution containing 0.20 M vanadyl acetylacetonate (VO(acac)₂) onto the BiOI electrode. The resulting structure underwent calcination at 450 °C and subsequent etching in 1.0 M NaOH for 30 minutes to remove excess V₂O₅. Additionally, Mo-doped BiVO₄ was prepared by dropcoating VO(acac)₂ in DMSO containing 1 mol% Mo(acac)₂, followed by calcination at 450 °C and etching in 1.0 M NaOH for 30 minutes.

Platinum Counter Electrode: To create the platinum counter electrode, single holes were drilled into bare fluorine-doped tin oxide (FTO) sheets (TEC 8, Hartford), which were then cut into pieces measuring 1.5 × 1 cm. The FTO pieces underwent a rigorous cleaning process, involving

sonication in a soap solution for 5 minutes, followed by sonication in deionized (DI) water for 5 minutes. Subsequently, they were rinsed with a 0.10 M HCl solution in ethanol and sonicated in acetone for 10 minutes. Afterward, the FTO pieces were heated at 400 °C for 15 minutes. Platinum was deposited onto the FTO surface by coating a drop of 5.0 mM H2PtCl6 in isopropanol, which was then spread and dried for 5 minutes. The Pt-coated FTO pieces were further heated to 380 °C for 20 minutes and then allowed to cool to room temperature.

Cell Assembly:

The assembly of the solar cell involved sandwiching the BiVO₄ photoanode and the Pt counter electrode using 25 µm Surlyn films. These components were placed on a hot plate at 140 °C, and pressure was applied to facilitate bonding. The electrolyte was injected into the cell through the predrilled hole in the counter electrode, and a vacuum was applied. The cell was sealed with Surlyn film and a coverslip by melting the film edges with a soldering iron. Electrical contact was established with the cell using melted indium.

Electrolyte Preparation:

The electrolyte solution was prepared by first creating a 1.0 M phosphate-buffered stock solution (PBS) with a pH of 6.66. This was achieved by dissolving 3.40 g of KH₂PO₄ in 250 mL of water and adjusting the pH to 6.66 with a 2.0 M KOH solution. A 0.05 M PBS solution was then prepared by diluting the stock solution accordingly. The triiodide/iodide solution was formulated using 1.0 M potassium iodide (KI), 50 mM iodine (I₂), and 0.050 M potassium phosphate buffer (with a 95%/5% molar ratio) in water. The pH of this solution was adjusted to 6.66 using the 2.0 M KOH solution.

The schematic of the complete solar cell is given in figure 6.1.

Measurements:

Solar cell measurements were conducted using an Autolab PGSTAT 128N potentiostat with a xenon arc lamp. Sunlight simulation at 100 mW cm⁻² was achieved using an AM 1.5 solar filter, with light intensity calibrated using an Oriel Reference Solar Cell and Meter. IPCE (incident photon-to-electron conversion efficiency) measurements were performed using a Horiba Jobin Yvon MicroHR monochromator equipped with a 450 W xenon arc lamp. The photon flux of incident light on the cells was measured using a Nova II Ophir power meter, with a mask applied to the active area of the cells to define an area of 0.16 cm².

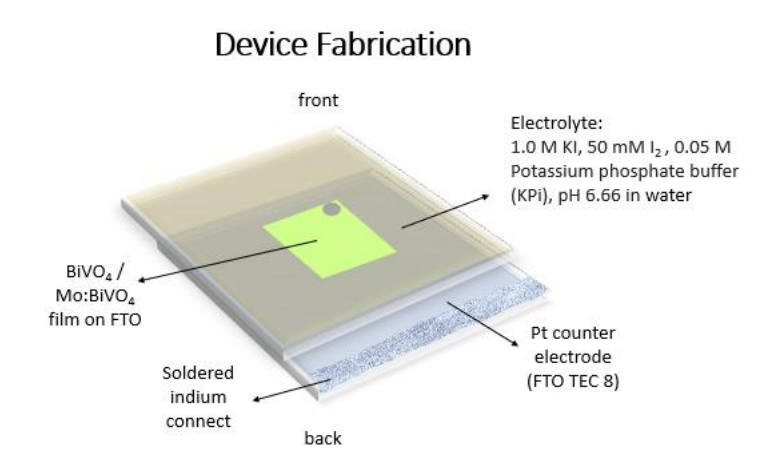


Figure 6.1: Representation of BiVO₄ sandwich solar cell.

6.3 Results and Discussion

Figure 6.2 a, b and c show the light and dark current density (J) vs applied potential (V) plots for the three different types of photoanodes under 1 sun illumination from the front side. Front side refers to the BiVO₄ substrate. Batch 1 refers to the BiVO₄ photoanodes made by 3 minutes of electrodeposition, Batch 2 refers to the BiVO₄ photoanodes made by 5 minutes of

electrodeposition and Batch 3 refers to the Mo doped BiVO₄ photoanodes made by 5 minutes of electrodeposition. The average short- circuit photocurrent density (J_{sc}), open-circuit potential (V_{oc}), fill factor (ff) and efficiency (η) of the respective batches of cells are given in Table 6.1.

(a)

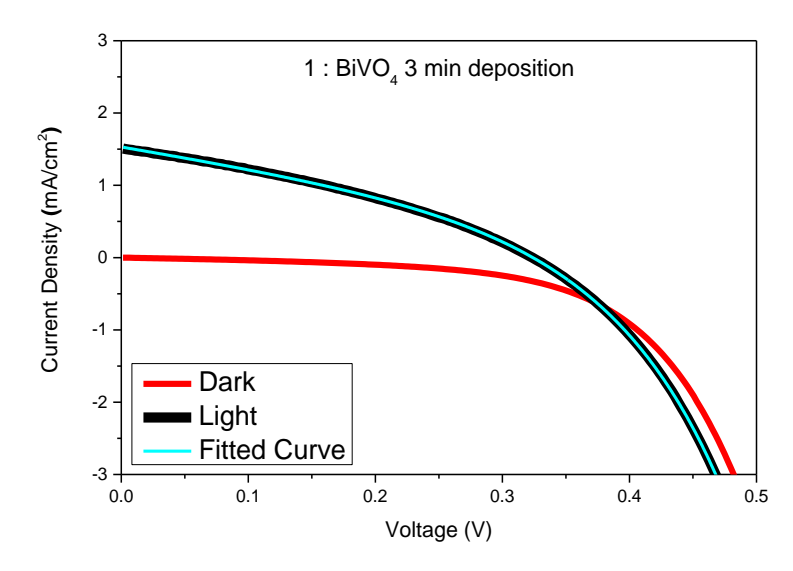
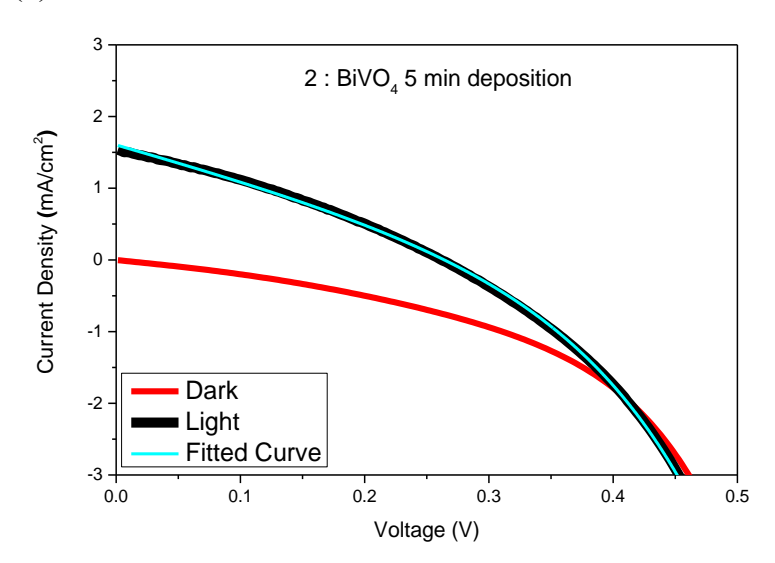


Figure 6.2: (a), (b), (c) Plots of J-V curves of DSSCs of Batch 1, Batch 2 and Batch 3 respectively for FS illumination. Light J-V curves are represented by black solid lines and dark J-V curves are represented by red lines. Blue lines represent the fitted curves for the light J-V plots.

Figure 6.2 (cont'd)





(c)

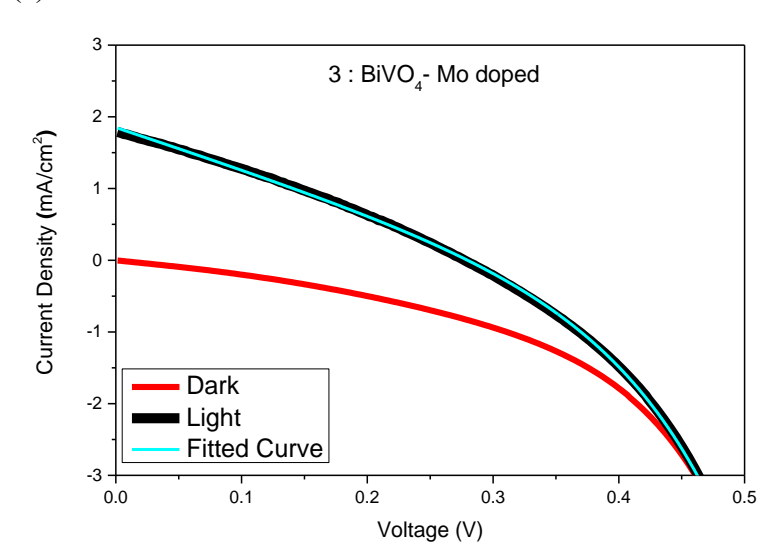


Table 6.1: Average J–V Characteristics of DSSCs under Simulated AM 1.5G Illumination (100 mW/cm²)

Sample	J_{SC}	V_{OC}	ff	η
	(mA/cm ²)	(V)		(%)
Batch 1 (3 min deposition)	1.58 ± 0.11	0.36 ± 0.04	0.39 ± 0.03	0.22 ± 0.04
Batch 2 (5 min deposition)	1.46 ± 0.17	0.32 ± 0.15	0.39 ± 0.02	0.17 ± 0.05
Batch 3 (Mo-doped 5 min	1.8 ± 0.17	-0.25 ± 0.03	0.31 ± 0.02	0.14 ± 0.03
deposition)				

Table 6.2: Average J–V Characteristics of DSSCs under Simulated AM 1.5G Illumination (100 mW/cm²)

		Diode quality
Sample	R _{shunt}	factor
		γ
Batch 1 (3 min deposition)	0.1737 ± 0.0013	3.396±
Buten 1 (5 mm deposition)	0.1737 = 0.0013	0.0066
Batch 2 (5 min deposition)	0.1630 ± 0.0054	3.858 ± 0.047
Batch 3 (Mo-doped 5 min deposition)	0.1736 ± 0.0013	3.246 ± 0.032

Figure 6.2 a, b and c show the incident photon to current efficiency (IPCE) plots of the respective batches of cells. Measurements were carried out from both sides of five cells from each batch. The

IPCE plots here correspond to one cell from each batch. The IPCE for the three batches show similar trend. The integrated IPCE gives J_{sc} values which agree with the measured J_{sc} , thus showing that the IPCE is in agreement with the J-V behavior. It is observed that the overall performance of the cells with BS illumination is worser than FS illumination, with the IPCE for back side illumination being significantly lower than the IPCE for front side illumination, indicating diffusion length limitations for the charge collection process.

(a)

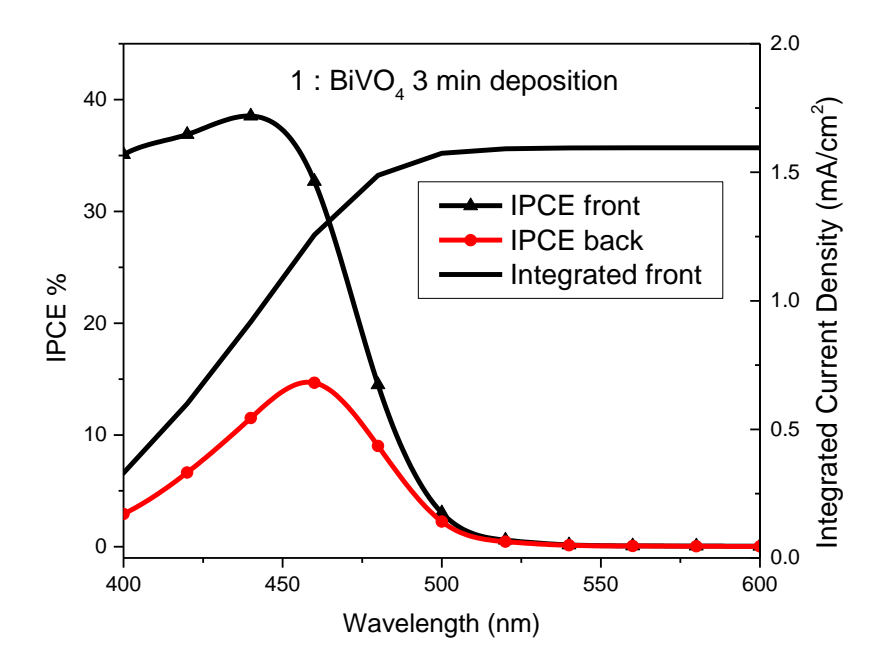
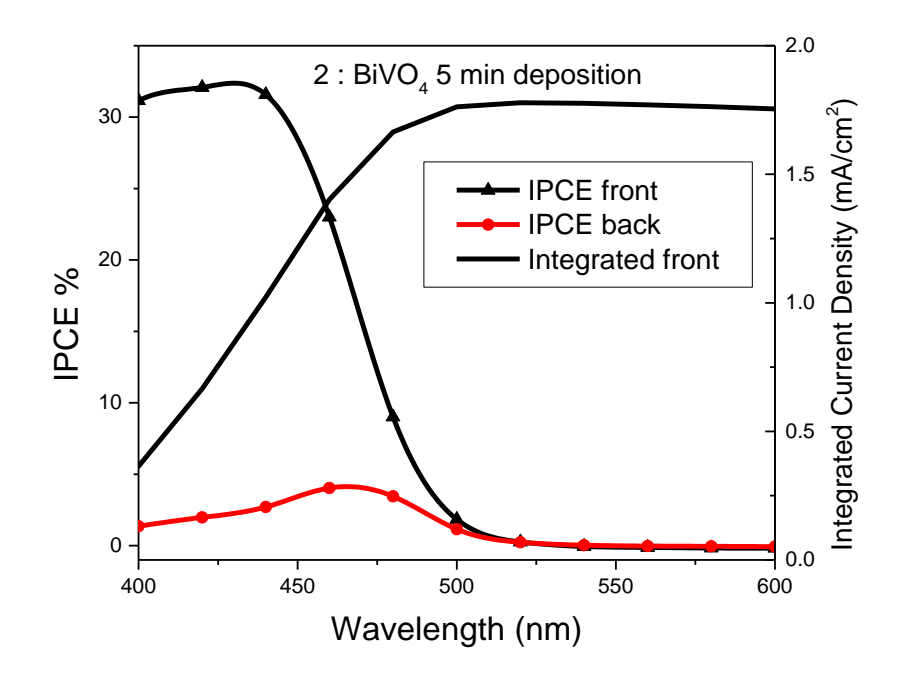


Figure 6.3: (a), (b), (c) IPCE curves for Batch 1, Batch 2 and Batch 3 respectively for front side (black line with triangles) and back side illumination (red line with circles) and front integrated current density plot (black line) on secondary axes.

Figure 6.3 (cont'd)

(b)



(c)

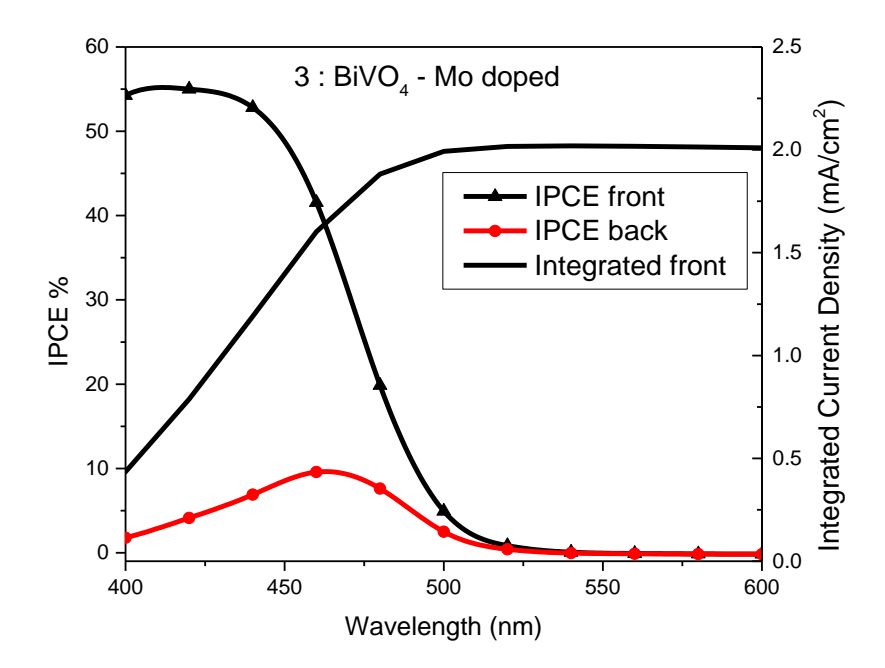


Figure 6.2 illustrates representative J-V curves under light and dark conditions and AM 1.5 illumination for one device each condition. Performance data, averaged over six devices, is

summarized in Table 6.1. The solar energy conversion efficiencies are measured at 0.14% for the Mo:BiVO₄ device and 0.17% for the BiVO₄ device. Notably, a slightly higher efficiency of 0.22% is observed for a thinner BiVO₄ film (Table 6.1). The open circuit potentials (OCPs) average at -0.32 ± 0.15 V for the BiVO₄ devices and -0.25 ± 0.03 V for the Mo:BiVO₄ device. The lower open circuit voltage of Mo:BiVO₄ corresponds with increased electron/hole recombination, as observed in the PEC data. However, the Mo:BiVO₄ devices exhibit larger short circuit photocurrents $(1.8 \pm 0.17 \text{ mA cm}^{-2})$ compared to the BiVO₄ devices $(1.46 \pm 0.17 \text{ mA cm}^{-2})$, owing to enhanced conductivity resulting from increased electron concentration after Mo doping.

The linear J–V response near short circuit (Figure 5.1 a,b,c) indicates significant shunting, likely due to the porosity of the BiVO₄ films, which permit direct contact between the underlying FTO substrate and the I^{3-/}I⁻ electrolyte. The J–V curves are fit to the modified diode equation, incorporating the shunt resistance (R_{shunt}):

$$J = \text{-}J_0 (exp(qV/nkT) \text{ - } V/R_{shunt} + J_{photo}$$

where is the exchange (recombination) current density, q is the charge of an electron, k is the Boltzmann constant, and T is temperature. The fitted J–V curves effectively describe the behavior with a shunt resistance and diode quality factors between 3 and 4 (Fig 5.1 a, b, c). The values for these measurements are given in Table 6.2. The larger diode quality factor and smaller shunt resistance align with the lower fill factor of the Mo-doped BiVO₄ film. Moreover, diode quality factors from the J–V curves exceed those from the SPV data¹⁸, possibly due to differing illumination conditions (front illumination for J–V and back illumination for SPV). SPV measurements were conducted without applied bias, while J–V curves were obtained under forward bias, leading to decreased band bending and improved conductivity of the BiVO₄ liquid junction.

The IPCE spectra in figure 5.3 a, b, c correlate closely with the optical absorption of BiVO₄. ¹⁸ Front illumination yields significantly higher IPCE values than back illumination through the electrolyte, primarily due to shading from the Pt counter electrode and the I^{3-/}I⁻ electrolyte. Platinum counter electrodes are known to cause approximately 10% uniform loss in transmittance. Even with a thin layer sandwich cell containing a diluted solution of 50 mM I³⁻, the strong absorption of the triiodide ion results in approximately 70% loss of transmitted light at 400 nm. The remaining difference in performance under back versus front illumination is attributed to slow electron diffusion in BiVO₄. However, electron transport is enhanced in the Mo:BiVO₄ device, resulting in a higher IPCE of 41% compared to 23% for the BiVO₄ device at 470 nm. As shown in figures 5.1 and 5.2, the integrated IPCE concurs with the measured short circuit current densities in the J-V curves.

6.4 Conclusion and Future Directions

In summary, the first example of a BiVO₄ photovoltaic cell has been provided. The devices employed a solid-liquid junction with an aqueous triiodide/iodide redox couple. The champion device achieved an energy conversion efficiency of 0.22%, a photovoltage of 0.36 V, and a photocurrent of 1.58 mA cm⁻² under AM 1.5 illumination. The performance was considerably below that of conventional dye-sensitized solar cells but has the potential for improvement. BiVO₄, with its 2.4 eV band gap, permits the absorption of only 12% of the solar flux and is limited by electron-hole recombination, as verified by IPCE measurements under front and back illumination. Mo-doped films produced higher photocurrents due to the higher donor concentration and conductivity but lower photovoltage due to increased recombination at Mo defects. The main photovoltage loss of these devices was caused by the mismatch between the BiVO₄ valence band and the triiodide/iodide standard reduction potential. Additional photovoltage losses resulted from

a detrimental junction at the FTO/Mo:BiVO $_4$ interface. Improved V_{OC} is possible by replacing the triiodide/iodide couple with a more oxidizing redox couple junction/back electron transfer problems at the FTO back contact.

Overall, the work demonstrated the possibility of photovoltaic devices using metal oxide absorbers in contact with aqueous electrolytes.

REFERENCES

- (1) Zhong, X.; Li, Y.; Wu, H.; Xie, R. Recent Progress in BiVO4-Based Heterojunction Nanomaterials for Photocatalytic Applications. Materials Science and Engineering: B **2023**, 289, 116278. https://doi.org/10.1016/J.MSEB.2023.116278.
- (2) Seabold, J. A.; Choi, K. S. Efficient and Stable Photo-Oxidation of Water by a Bismuth Vanadate Photoanode Coupled with an Iron Oxyhydroxide Oxygen Evolution Catalyst. J Am Chem Soc **2012**, 134 (4), 2186–2192. https://doi.org/10.1021/JA209001D/SUPPL FILE/JA209001D SI 001.PDF.
- (3) Wang, L.; Shi, X.; Jia, Y.; Cheng, H.; Wang, L.; Wang, Q. Recent Advances in Bismuth Vanadate-Based Photocatalysts for Photoelectrochemical Water Splitting. Chinese Chemical Letters **2021**, 32 (6), 1869–1878. https://doi.org/10.1016/J.CCLET.2020.11.065.
- (4) Kudo, A.; Miseki, Y. Heterogeneous Photocatalyst Materials for Water Splitting. Chem Soc Rev **2008**, 38 (1), 253–278. https://doi.org/10.1039/B800489G.
- (5) Wang, Q.; Hisatomi, T.; Suzuki, Y.; Pan, Z.; Seo, J.; Katayama, M.; Minegishi, T.; Nishiyama, H.; Takata, T.; Seki, K.; Kudo, A.; Yamada, T.; Domen, K. Particulate Photocatalyst Sheets Based on Carbon Conductor Layer for Efficient Z-Scheme Pure-Water Splitting at Ambient Pressure. J Am Chem Soc **2017**, 139 (4), 1675–1683. https://doi.org/10.1021/JACS.6B12164.
- Yaw, C. S.; Chong, M. N.; Soh, A. K. Bismuth Vanadate-Based Photoelectrodes for Photoelectrochemical Water Splitting: Synthesis and Characterisation. Advances in Science and Technology 2017, 99, 9–16. https://doi.org/10.4028/WWW.SCIENTIFIC.NET/AST.99.9.
- (7) Park, Y.; Mc Donald, K. J.; Choi, K. S. Progress in Bismuth Vanadate Photoanodes for Use in Solar Water Oxidation. Chem Soc Rev **2013**, 42 (6), 2321–2337. https://doi.org/10.1039/C2CS35260E.
- (8) Liu, Z.; Yan, F. The Application of Bismuth-Based Oxides in Organic-Inorganic Hybrid Photovoltaic Devices. J Am Ceram Soc **2012**, 95 (6), 1944–1948. https://doi.org/10.1111/j.1551-2916.2012.05088.x.
- (9) Zhang, J.; Luo, W.; Li, W.; Zhao, X.; Xue, G.; Yu, T.; Zhang, C.; Xiao, M.; Li, Z.; Zou, Z. A Dye-Free Photoelectrochemical Solar Cell Based on BiVO4 with a Long Lifetime of Photogenerated Carriers. Electrochem Commun 2012, 22 (1), 49–52. https://doi.org/10.1016/j.elecom.2012.05.027.
- (10) Walsh, A.; Yan, Y.; Huda, M. N.; Al-Jassim, M. M.; Wei, S. H. Band Edge Electronic Structure of BiVO4: Elucidating the Role of the Bi s and V d Orbitals. Chem Mater **2009**, 21 (3), 547–551. https://doi.org/10.1021/cm802894z.
- (11) Bhatt, M. D.; Lee, J. S. Recent Theoretical Progress in the Development of Photoanode Materials for Solar Water Splitting Photoelectrochemical Cells. J Mater Chem A Mater **2015**, 3 (20), 10632–10659. https://doi.org/10.1039/C5TA00257E.

- (12) Laser, D.; Bard, A. J. Semiconductor Electrodes: VI . A Photoelectrochemical Solar Cell Employing a Anode and Oxygen Cathode. J Electrochem Soc **1976**, 123 (7), 1027–1030. https://doi.org/10.1149/1.2132985.
- (13) Mavroides, J. G.; Tchernev, D. I.; Kafalas, J. A.; Kolesar, D. F. Photoelectrolysis of Water in Cells with TiO2 Anodes. Mater Res Bull **1975**, 10 (10), 1023–1030. https://doi.org/10.1016/0025-5408(75)90210-X.
- (14) Li, B.; Oldham, L. I.; Tian, L.; Zhou, G.; Selim, S.; Steier, L.; Durrant, J. R. Electrochemical versus Photoelectrochemical Water Oxidation Kinetics on Bismuth Vanadate (Photo)Anodes. J Am Chem Soc **2024**. https://doi.org/10.1021/JACS.4C03178.
- (15) Li, B.; Oldham, L. I.; Tian, L.; Zhou, G.; Selim, S.; Steier, L.; Durrant, J. R. Electrochemical versus Photoelectrochemical Water Oxidation Kinetics on Bismuth Vanadate (Photo)Anodes. J Am Chem Soc **2024**. https://doi.org/10.1021/JACS.4C03178.
- (16) Park, Y.; Mc Donald, K. J.; Choi, K. S. Progress in Bismuth Vanadate Photoanodes for Use in Solar Water Oxidation. Chem Soc Rev **2013**, 42 (6), 2321–2337. https://doi.org/10.1039/C2CS35260E.
- (17) Seabold, J. A.; Choi, K. S. Efficient and Stable Photo-Oxidation of Water by a Bismuth Vanadate Photoanode Coupled with an Iron Oxyhydroxide Oxygen Evolution Catalyst. J Am Chem Soc **2012**, 134 (4), 2186–2192. https://doi.org/10.1021/JA209001D.
- (18) Daemi, S.; Kaushik, S.; Das, S.; Hamann, T. W.; Osterloh, F. E. BiVO4-Liquid Junction Photovoltaic Cell with 0.2% Solar Energy Conversion Efficiency. J Am Chem Soc 2023, 145 (47), 25797–25805. https://doi.org/10.1021/JACS.3C09546/ASSET/IMAGES/LARGE/JA3C09546_0006.JPE G.
- (19) Kim, T. W.; Choi, K. S. Nanoporous BiVO4 Photoanodes with Dual-Layer Oxygen Evolution Catalysts for Solar Water Splitting. Science (1979) **2014**, 343 (6174), 990–994. https://doi.org/10.1126/SCIENCE.1246913.

Chapter 7: Exploring 2D Organic Single

Crystals: Properties, Synthesis, and Applications

7.1 Introduction

Organic semiconductors are central to the realms of organic electronics and photonics, which focus on developing technologies such as flexible, cost-effective electronics, organic photovoltaic cells, light-emitting displays, smart tags, and molecular sensors. 1–3 These materials are celebrated for their potential to produce lightweight, adaptable devices that can be produced at low costs. However, despite substantial advancements in applied organic electronics and a deep body of research into organic materials, there remains a significant gap in our comprehension of their fundamental properties.

This gap is largely due to the challenges associated with using polycrystalline and amorphous organic thin films, which often exhibit substantial disorder.⁴ Such disorder, including irregular grain boundaries and varying structural characteristics, significantly impacts the electrical and optical properties of these materials. This results in reduced charge-carrier mobility and exciton diffusion, making it difficult to reconcile experimental data with theoretical expectations and complicating the development of highly efficient devices.

Recently, however, the focus has shifted towards organic single crystals, which present a more refined alternative.^{3,5–7} Research into organic single crystals is crucial for several reasons. First, their exceptional structural order ensures that charge carriers move with greater efficiency, which is vital for creating high-performance electronic devices. Second, their high purity reduces the influence of impurities and defects, leading to more reliable and consistent performance. By

studying these materials, scientists can better understand the true potential of organic semiconductors, advancing both theoretical knowledge and practical applications. Over the past decade, electronic devices utilizing these single crystals—such as high-performance single-crystal transistors and photoconductors—have demonstrated unparalleled performance across key metrics. These include charge-carrier mobility, exciton diffusivity, defect concentration, and operational stability.

In terms of charge-carrier mobility, single-crystal organic semiconductors achieve significantly higher values compared to their polycrystalline or amorphous counterparts.^{8,9} This is due to their well-ordered crystalline structure, which facilitates more efficient charge transport. Additionally, the high exciton diffusivity in these materials allows for better energy transfer, which is crucial for applications in optoelectronics. The low concentration of defects within single crystals also contributes to their superior performance, as fewer imperfections lead to fewer traps and recombination centers that could otherwise hinder device efficiency.

Operational stability is another critical area where single-crystal organic semiconductors excel. ^{8,10,11}Their intrinsic structural quality results in greater resistance to degradation under various environmental conditions, making them more reliable for long-term use. As a result, devices built from these materials are not only more efficient but also more durable, enhancing their overall performance and longevity.

The investigation of organic single crystals represents a significant step forward in organic semiconductor research. Their inherent structural and chemical advantages provide a clearer understanding of fundamental properties, paving the way for the development of next-generation electronic and photonic devices. As research in this area progresses, it promises to unlock new opportunities and drive innovation in organic semiconductor technology.

In recent years, the field of materials science has witnessed a transformative shift with the emergence of two-dimensional (2D) materials, which are characterized by their ultrathin, planar structures. ^{12,13} Among these, 2D organic single crystals have garnered significant attention due to their unique blend of organic chemistry and advanced material properties. Unlike their inorganic counterparts, such as graphene and transition metal dichalcogenides, 2D organic single crystals are composed of organic molecules arranged in a well-defined two-dimensional lattice. They are thin, layered structures where organic molecules are organized in a two-dimensional lattice. Unlike traditional bulk crystals, these materials exhibit a high degree of anisotropy, where properties vary significantly in different directions. This characteristic is a result of their layered nature. They are essentially monolayers or few-layered structures where organic molecules are organized into a repeating lattice through strong covalent bonds within the layers and weaker van der Waals forces between the layers. This arrangement imparts a range of fascinating electronic, optical, and mechanical properties that are not typically observed in bulk organic materials. For instance, these crystals can exhibit high charge carrier mobilities, remarkable optical absorption and emission characteristics, and impressive mechanical flexibility, making them highly attractive for applications in organic electronics, optoelectronics, and sensing technologies. ^{6,14–16}

They can include a variety of compounds such as organic semiconductors, polymers, and small organic molecules. The unique structural arrangement of these crystals imparts distinctive electronic, optical, and mechanical properties that are not found in their bulk counterparts.

The synthesis of 2D organic single crystals involves precise control overgrowth conditions, including temperature, pressure, and solvent environment, to ensure the formation of high-quality, well-ordered structures. ^{3,6}Techniques such as vapor phase deposition, solution-based

crystallization, and self-assembly are employed to fabricate these crystals, each offering unique advantages and challenges.

Vapor Phase Transport: This method involves the sublimation of organic molecules followed by their deposition onto a substrate. The process is conducted under controlled temperatures and pressures, allowing for the formation of high-quality single crystals. Techniques such as chemical vapor deposition (CVD) and physical vapor deposition (PVD) fall under this category.

Solution-Based Methods: Solution shearing is a coating technique that involves using a shearing rod to spread a gel solution over a heated substrate. This meniscus-guided method is effective for producing thin films of different materials. Solution-based techniques, such as slow evaporation and solution shearing, involve dissolving organic molecules in a solvent and allowing them to crystallize slowly. This method is relatively simple and can produce large-area crystals. However, controlling the uniformity and quality of the crystals can be challenging.

Self-Assembly: Self-assembly techniques utilize the intrinsic interactions between organic molecules to form well-ordered structures. This method relies on non-covalent interactions such as hydrogen bonding, π - π stacking, and van der Waals forces. Self-assembly offers a pathway to fabricate complex and functional 2D organic single crystals with minimal external intervention. Melt growth: Melt growth involves the controlled solidification of a liquid phase into a crystalline structure, allowing for the fabrication of high-quality 2D materials such as graphene, transition metal dichalcogenides (TMDs), and other layered materials. This technique capitalizes on the unique properties of 2D materials, including their electronic, optical, and mechanical characteristics, which are significantly influenced by their crystalline quality.

The process typically begins with the melting of the precursor material, followed by careful cooling to promote crystal nucleation and growth. Parameters such as temperature gradient,

cooling rate, and ambient atmosphere play crucial roles in determining the size and quality of the resulting crystals. For instance, slow cooling rates often lead to larger, more uniform crystals with fewer defects, while rapid cooling can result in smaller, polycrystalline structures.

Research has shown that the incorporation of specific additives or the use of controlled atmospheres can further enhance crystal growth and quality. Techniques like zone melting and Bridgman growth have been adapted for 2D materials, allowing for precise control over the growth conditions. The resulting single crystals can be used in various applications, including electronics, photonics, and catalysis, due to their superior properties compared to polycrystalline counterparts. In summary, the melt growth technique for 2D single crystals presents a promising avenue for the development of high-quality materials with tailored properties, paving the way for advancements in multiple technological fields.

As research in this area advances, the potential applications of 2D organic single crystals continue to expand. Their use in organic field-effect transistors (OFETs), organic light-emitting diodes (OLEDs), and organic photovoltaic cells (OPVs) highlights their versatility and promise. Furthermore, their unique properties facilitate the development of advanced sensors and flexible electronic devices. 17–22

The synthesis of 2D organic single crystals involves precise control over the growth conditions to achieve high-quality crystals with well-defined properties. Several methods have been developed to grow these crystals, each with its advantages and limitations.

The properties of 2D organic single crystals are largely dictated by their structural and electronic characteristics:

Electronic Properties: 2D organic single crystals often exhibit high carrier mobilities due to their well-ordered structure, which facilitates efficient charge transport. This makes them suitable for applications in organic electronics, including transistors and sensors. 11,18,22–25

Optical Properties: These materials can display strong optical absorption and photoluminescence, which are advantageous for optoelectronic devices such as light-emitting diodes (LEDs) and photovoltaic cells. The tunability of their optical properties through molecular design allows for the development of materials with specific emission and absorption spectra. ^{26–29}

Mechanical Properties: Despite their thinness, 2D organic single crystals can possess remarkable mechanical strength and flexibility. This makes them suitable for applications in flexible electronics and wearable devices.^{7,30}

The unique properties of 2D organic single crystals have led to their exploration in a variety of applications:

Organic Electronics: Due to their high charge carrier mobility and flexibility, these materials are used in organic field-effect transistors (OFETs), organic light-emitting diodes (OLEDs), and organic photovoltaic cells (OPVs). Their ability to form large-area, uniform films makes them attractive for large-scale and flexible electronic devices. 18,19,23

Sensors: The high surface-to-volume ratio and sensitivity of 2D organic single crystals make them excellent candidates for sensing applications. They can be used to detect gases, biological molecules, and other substances with high accuracy. ^{31,32}

Optoelectronics: The tunable optical properties of 2D organic single crystals enable their use in a variety of optoelectronic devices, including photodetectors and light-emitting devices. Their

ability to emit and absorb light at specific wavelengths is particularly useful in designing devices with precise optical characteristics.^{33,34}

7.2 Solution Based Methods for crystal growth

The synthesis of large-size single crystals of organic semiconductors relies heavily on four critical parameters: the evaporation rate of the solvent, solution concentration, the interaction between the semiconductor and substrate, and shearing speed. While numerous studies have explored methods for synthesizing large-scale two-dimensional organic semiconductors (2D OSCs), models that effectively delineate the optimal growth conditions remain limited. The influence of the substrate temperature, latent heat of the solvent, and thermal conductivity is critical; these parameters collectively enhance crystal growth by increasing semiconductor solubility and solvent evaporation.

Notably, while rapid crystal deposition may seem advantageous, it can inadvertently lead to homogeneous nucleation, resulting in poorer crystallinity. Therefore, selecting an appropriate evaporation flux in the solution shearing process is vital. This relationship can be expressed through equations that capture the dynamics of temperature and vapor concentration during solvent evaporation. The interplay between crystal thickness and theoretical evaporation flux further elucidates how optimal shearing speeds can be determined through mass conservation principles. In practice, various experimental conditions, such as solution concentrations and substrate temperatures, can be systematically explored to achieve desired growth outcomes. For example, distinct shearing conditions have been defined to examine how different parameters impact the formation of 2D OSCs. Comparisons among these conditions revealed that specific combinations of concentration and temperature yielded films with larger domain sizes and more uniform characteristics. The first and second shearing processes employed varying concentrations and

temperatures, illustrating that the optimal conditions for producing monolayer crystals often involve a careful balance between dissolution and deposition dynamics.^{35–37}

Furthermore, it has been demonstrated that homogenous nucleation, which complicates the formation of organic crystals, is mitigated by maintaining a lower concentration of organic solutions compared to the solubility limit. The dual-solution shearing method has emerged as an effective strategy, employing semiconductor concentrations that approach the solubility limit to fabricate high-crystalline monolayer crystals. For example, C10-DNTT dissolved in tetralin has been used, and the initial shearing process was conducted at a substrate temperature of 85 °C. ^{38,39}Characterization techniques such as polarized optical microscopy provided insights into the resultant crystalline domains, revealing how different concentration values impacted the crystallization behavior.

The findings illustrate that under certain conditions, nearly complete coverage of monolayer single crystals can be achieved, particularly when using concentrations that closely approach the solubility limit. In terms of crystal growth, the selected shearing conditions not only influence the rate of dissolution and deposition but also determine the uniformity and size of the resulting monolayers. Overall, these investigations highlight the significance of optimizing shearing speed and concentration in the solution-based growth of 2D OSCs, with practical implications for developing high-performance organic electronic devices. The application of solution shearing techniques has also been successfully extended to other organic semiconductors, such as TIPS-PEN and diF TES-ADT, demonstrating the versatility and effectiveness of these methods in producing high-quality 2D materials. 40,41

7.3 Motivation Behind the Work

electro-optic device architectures, encompassing both passive and active optical elements as well as electroactive devices. These lightweight, flexible polymer and organic solid layers offer significant potential for use in wearable devices, such as smart glasses, due to their conformability and comfort, which make them ideal candidates for advanced technologies like virtual and augmented reality devices that benefit from a comfortable and adjustable form factor. 42-44 Despite recent advancements, there remains a need for polymer and organic solid materials with enhanced optical properties. These desired properties include a controllable refractive index, tunable birefringence, improved optical clarity, and high transparency. Such materials can be fabricated into thin films, which can be further stacked to form multilayer structures, enhancing their functionality. This project aims to address challenges associated with lightweight materials capable of modulating properties like refractive index. Various techniques have been used to create layers of organic solid crystal materials through both gas- and liquid-phase epitaxial and nonepitaxial methods. However, achieving a single-crystal organic solid crystal (OSC) has been challenging, as most previous materials developed were polycrystalline. This project advances the field by developing single-crystal OSC thin films, which have promising applications in diverse optical systems and devices. 44,45

Polymers and other organic materials are increasingly being integrated into various optical and

The potential applications of this technology are extensive. For instance, an optical assembly incorporating a lens system with a circular reflective polarizer and a multilayer OSC thin film could enhance performance. Each biaxial OSC layer possesses three orthogonal refractive indices, providing higher signal efficiency and superior ghost image suppression compared to architectures

that utilize traditional materials. Additionally, OSC thin films can be applied as brightness enhancement layers in various projectors, further broadening their practical use.

This research explores the tunable optical properties of OSC materials. The OSC layer demonstrates a first refractive index in one biased state and a second refractive index in an alternative biased state, enabling active tuning across a range of refractive index values. Various crystallizable organic semiconductors were employed to develop OSC thin films, encompassing a diverse set of small molecules, including p-type, n-type, and ambipolar polycyclic aromatic hydrocarbons like anthracene and phenanthrene. These materials provide functionalities for applications in phase modulation, beam steering, wave-front shaping and correction, optical communication, optical computation, and holography. Their unique optical and mechanical properties make them attractive for high-performance devices that could eventually replace traditional systems based on polymers, inorganic materials, and liquid crystals.

The close-packed structures of these organic molecules exhibit desirable optical properties, such as a high, tunable refractive index and significant birefringence. Anisotropic organic solid materials displayed preferred molecular orientations, yielding high-refractive-index OSC thin films with smooth surfaces. This research particularly emphasizes organic thin films and the devices they enable, focusing on single-crystal OSC thin films and their fabrication methods. High-refractive-index and highly birefringent organic semiconductor materials were created as either free-standing articles or thin films deposited onto substrates. Both epitaxial and non-epitaxial growth processes were employed to form OSC layers on suitable substrates, pushing the boundaries of performance in optical devices.

A potential source of active refractive index modulation in organic solid crystals stemmed from changes in the polarizability of molecules that contained charge due to hole or electron injection.

In organic molecules, the time required for repolarization upon charge injection is found to be significantly shorter than the residence time of the charge. Within the OSC materials, the charge could remain on a molecule long enough for that molecule to modulate its electron cloud, as well as the electron clouds of neighboring molecules. This alteration in the local electronic structure of the crystal led to changes in both polarizability and refractive index.

When a charge is introduced into an organic material, polarization occurs due to a redistribution

of electrons within the molecule, causing a slight separation of positive and negative charges

within the molecule, essentially creating a temporary dipole moment, even if the molecule was originally non-polar; this happens because the electrons in the molecule are attracted to the introduced charge, distorting the electron cloud and creating a polarized region around it. Polarization energies in organics upon introduction of a charge has been widely studied. ^{46–51} The primary mechanism is the distortion of the electron cloud around the atoms in the organic molecule when an external charge is nearby, causing a slight positive charge on one side of the molecule and a slight negative charge on the other. ⁵¹ This distortion results in a temporary dipole moment, which is a measure of the separation of positive and negative charges within the molecule. ^{46,49,51} The extent of polarization depends on the molecular structure and the polarizability of the molecule, which is determined by how easily the electron cloud can be

Understanding polarization is crucial in various organic electronic devices like organic lightemitting diodes (OLEDs) and organic solar cells, as it affects charge carrier mobility and device performance.

distorted. 4,47–49,51

Electron hopping in organic materials refers to a mechanism where electrons move through a molecule or a collection of molecules by jumping from one localized site to another, typically between adjacent redox centers, rather than flowing through a continuous medium, which is commonly observed in organic semiconductors due to their weak intermolecular interactions and localized electronic states. ^{2,52–56} In organic molecules, electrons are often localized on specific functional groups or atoms, creating discrete "hopping sites" where the electron can reside temporarily. ^{53,56} Electron hopping usually requires thermal energy to overcome the energy barrier between these localized sites, allowing the electron to jump to a neighboring site. ^{52,54} The relatively weak van der Waals forces between organic molecules facilitate the hopping mechanism, as it allows for some degree of molecular movement needed for electron transfer. ^{2,52} Compared to inorganic semiconductors, electron hopping in organic materials typically leads to lower charge carrier mobility due to the discontinuous nature of the electron transport. ^{54–57}

7.4 Experimental and discussion

The first step towards synthesizing these films involved exploring various techniques for single-crystal thin film growth, beginning with anthracene. Due to its extensive study in literature, anthracene served as an ideal material to establish a standard. For reference, the Becke line method study reported refractive indices of $n_1 \approx 1.553$ and $n_2 \approx 1.810$ for anthracene at a wavelength of 540 nm. ⁵⁸

For film growth, two main approaches were employed: developing free-standing crystals and growing films on a substrate. Glass was selected as the substrate because of its cost-effectiveness and availability. The following chart illustrates these methods and the types of crystals produced. Each type was grown using two methods: solvent evaporation and thermal growth.

In the solvent evaporation method, a saturated solution of the material was placed in a sealed container with evenly spaced holes to allow controlled evaporation. This setup was placed in a glass box with regulated ventilation to prevent rapid evaporation.

For thermal growth, a Linkam stage was used. This specialized microscope stage allows temperature-controlled analysis, enabling precise heating or cooling of samples under microscopic observation. For anthracene, a saturated solution of anthracene and toluene was sealed and heated to 40°C at a rate of 1°C/min, held at 40°C for 6 hours, and then gradually cooled to room temperature at 0.05°C/min. Specific temperature controls and gradients were applied to the crystallization front of the nascent thin film to promote nucleation and crystal growth, with conditions adjusted according to the material's properties.

While free-standing crystals were successfully grown, they exhibited large thickness and size variations that made reproducing the work challenging. These crystals measured approximately 0.1 mm and displayed surface deformities. Fine polishing pads were used to clean the surfaces, with before-and-after images shown in Figure 7.2. Due to these challenges, the focus shifted to thermal growth on substrates, which produced films with grain boundaries that require further investigation to reduce defects. Figure 7.1 shows the various types of anthracene films that were successfully synthesized.

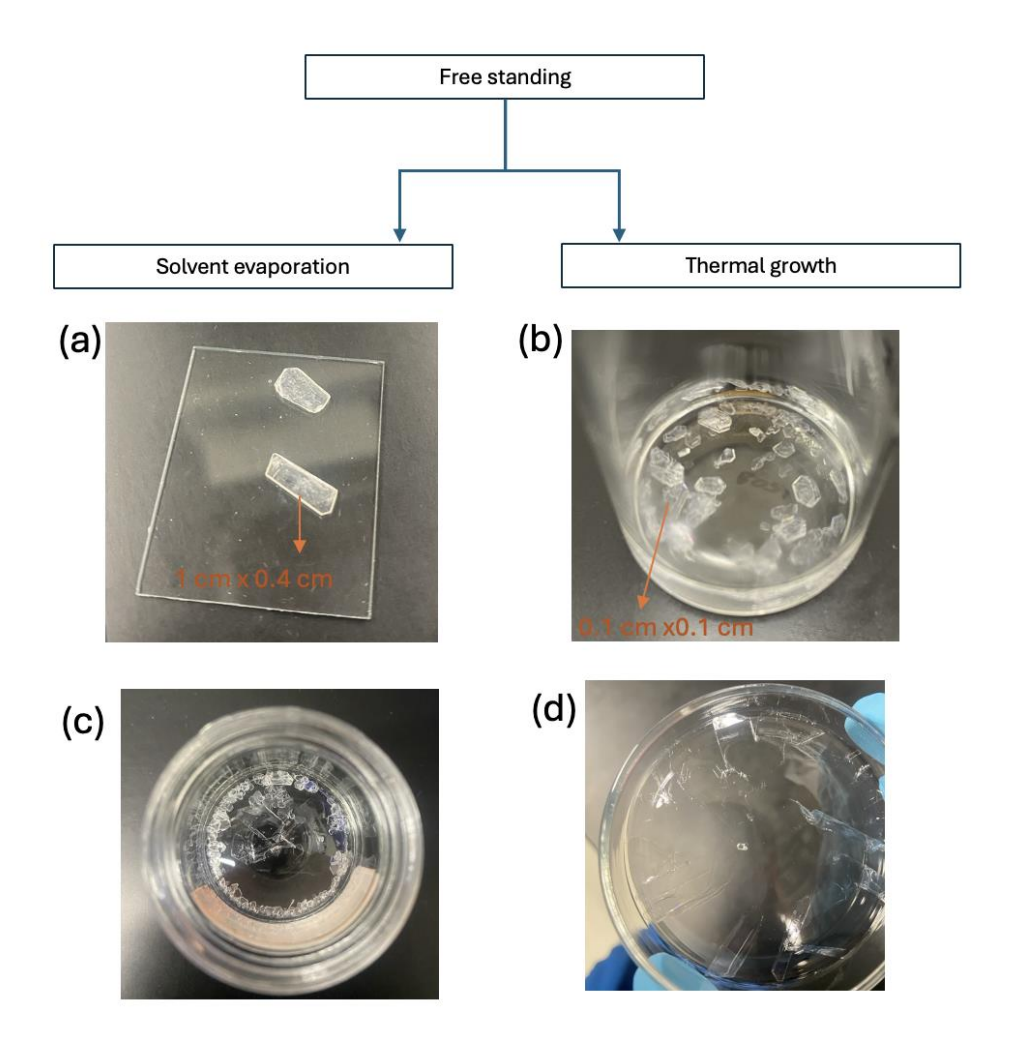


Figure 7.1: (a), (c) Free standing anthracene crystals synthesized by solvent evaporation where a saturated solution of anthracene was placed in a sealed container with equally spaced holes from which the solvent evaporation took place. The container was placed in a glass box with regulated ventilation. (b), (d) Free standing anthracene crystals synthesized by thermal cooling where a container of saturated anthracene solution (in toluene) was subjected to heating to40°C at a rate of 1°C/min, holding the temperature at 40°C for 6 hours, and then gradually cooling to room temperature at 0.05°C/min.

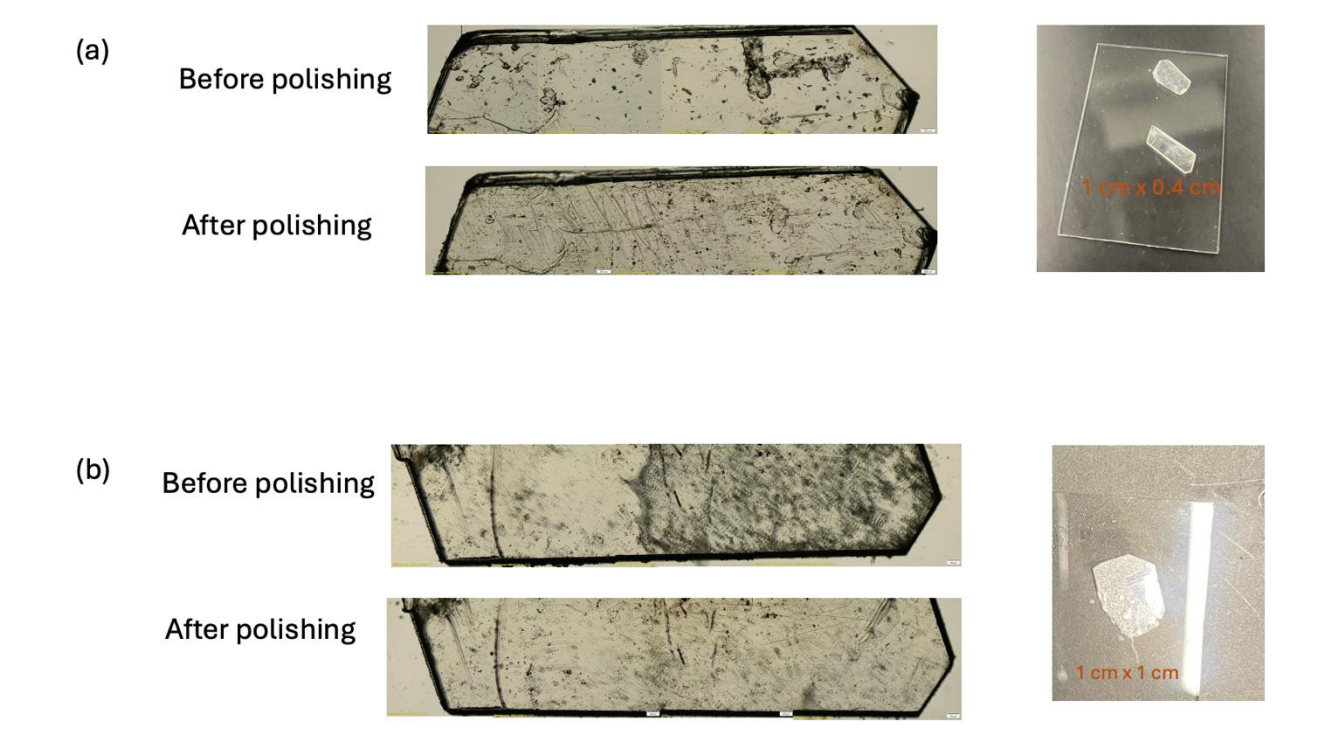


Figure 7.2: Free standing anthracene crystals being polished to remove crystal surface deformities. Pictures show optical images before and after polishing the two different crystals.

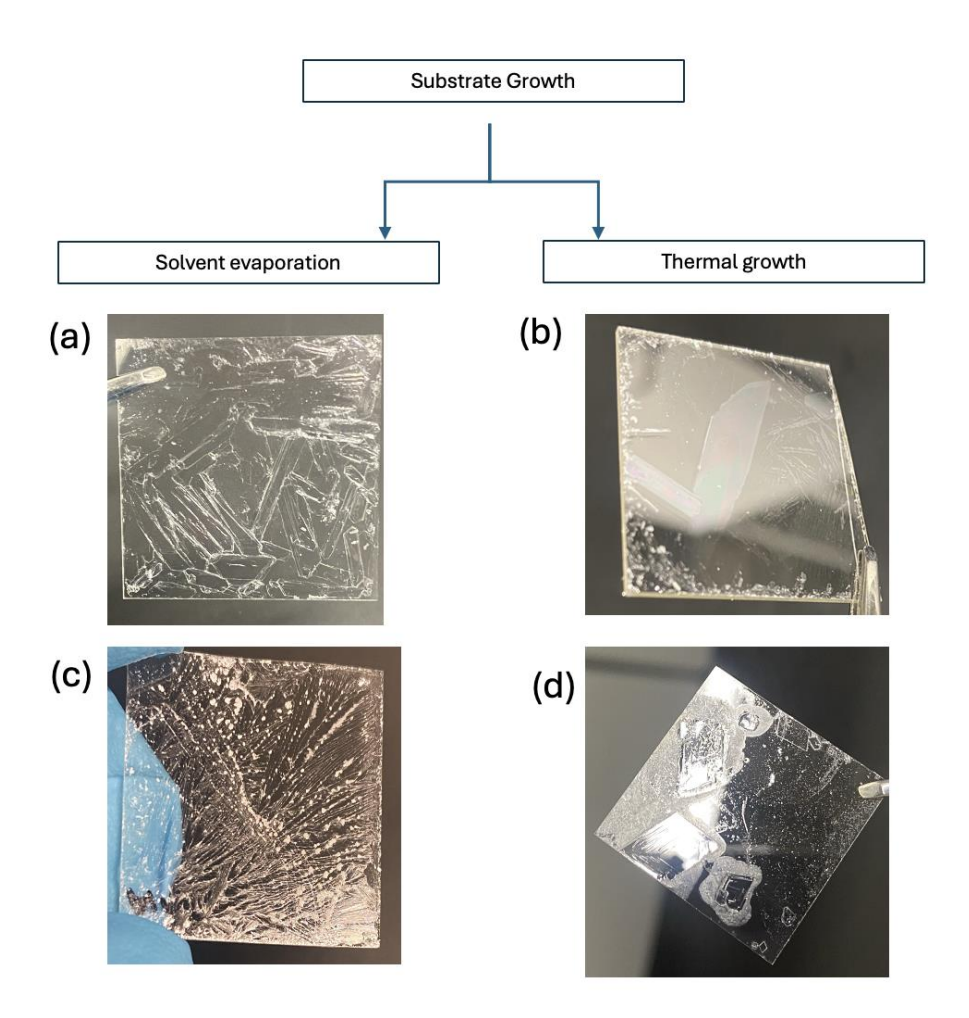


Figure 7.3: (a), (c) Substrate grown anthracene crystals synthesized by solvent evaporation where a saturated solution of anthracene was placed on top of the substrate in a sealed container. The cap of the container had equally spaced holes from which the solvent evaporation took place. The container was placed in a glass box with regulated ventilation. (b), (d) Substrate grown anthracene crystals synthesized by thermal cooling where a container of saturated anthracene solution (in toluene) was subjected to heating to 40°C at a rate of 1°C/min, holding the temperature at 40°C for 6 hours, and then gradually cooling to room temperature at 0.05°C/min.

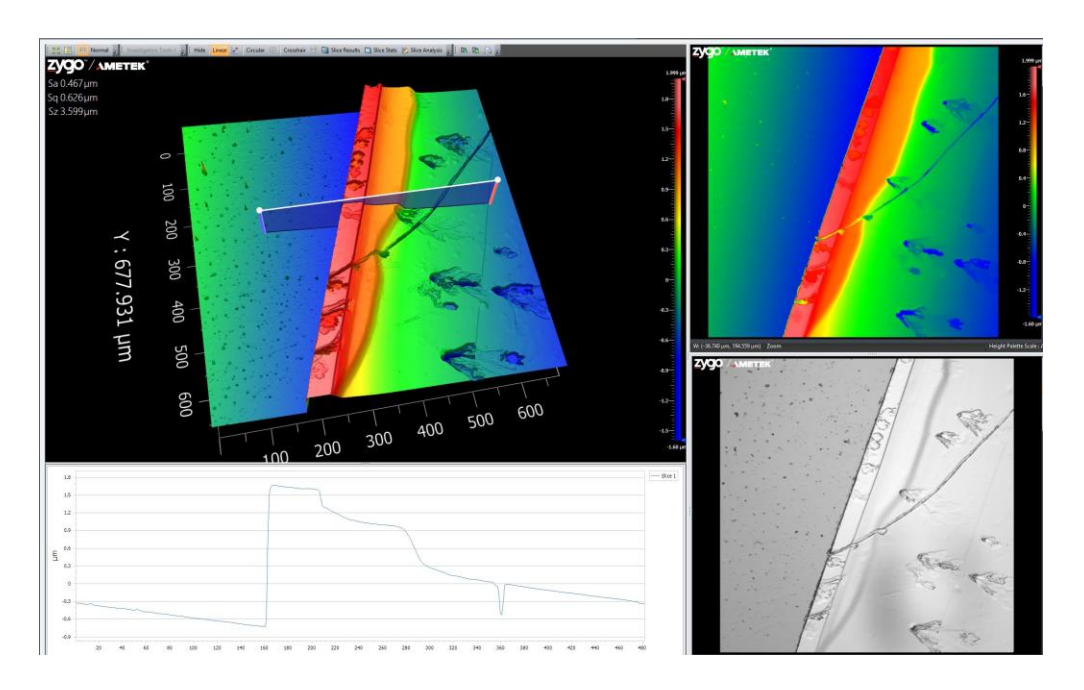


Figure 7.4: Profilometry measurement of thickness of the anthracene film on glass substrate.

After characterizing the single-crystal films with a profilometer (see Figure 7.4), it was determined that anthracene typically forms films around 0.6 µm in thickness, an ideal dimension for device applications. To test the active properties of these materials, a Schottky diode-type device was fabricated. This device serves as an optical modulator, where an organic single-crystal (OSC) layer is placed between two electrodes. In certain configurations, a dielectric layer may be added between the OSC and one or both electrodes to modulate the current or voltage applied to the OSC. Gold and indium tin oxide (ITO) were selected as electrodes due to their favorable energy alignment with anthracene. To achieve this, anthracene needed to be grown directly on gold. The difference in surface energy between glass and gold posed challenges for directly translating

the growth process, so the gold surface required passivation. Various passivation techniques were tested, with plasma treatment and thiophenol surface activation proving effective for promoting OSC growth.

In parallel, another material, "FRL 108," was investigated for thin-film formation. FRL 108 has a higher refractive index (2.1, 1.7, and 1.6) than anthracene, and generally demonstrated improved

film coverage (see Figure 7.5 (a)), likely due to its higher solubility and better wettability. FRL 108 films formed with a thickness of about 0.8 µm, closely comparable to anthracene.

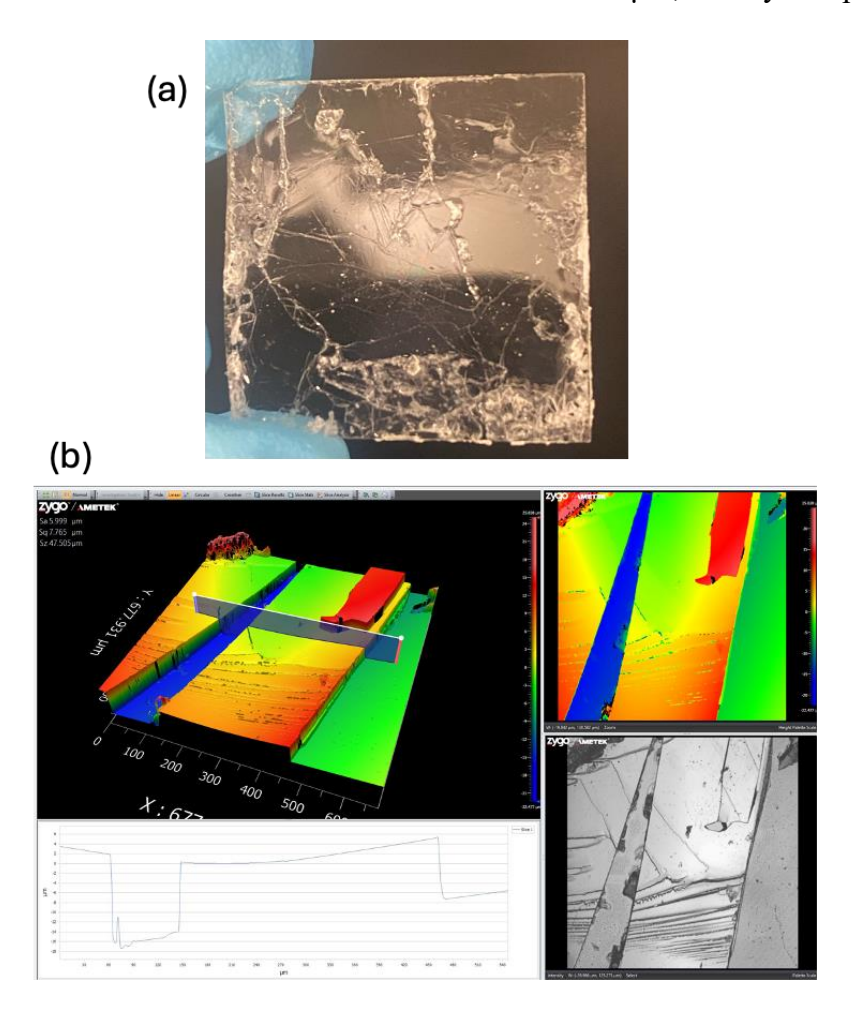


Figure 7.5: (a) Image of FRL 108 film on glass substrate. Image shows surface coverage of the film on glass. (b) Profilometry measurement of thickness of the FRL 108 film on glass substrate.

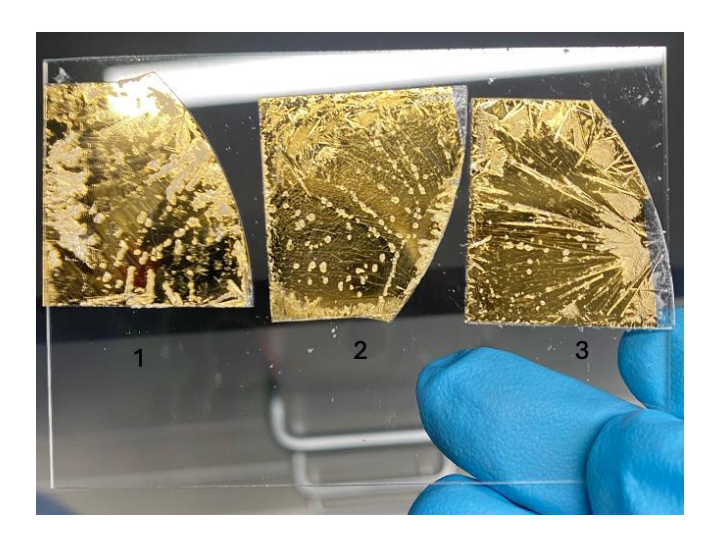


Figure 7.6: Image of FRL 108 films on gold substrate. Image shows surface patterns formed on the film.

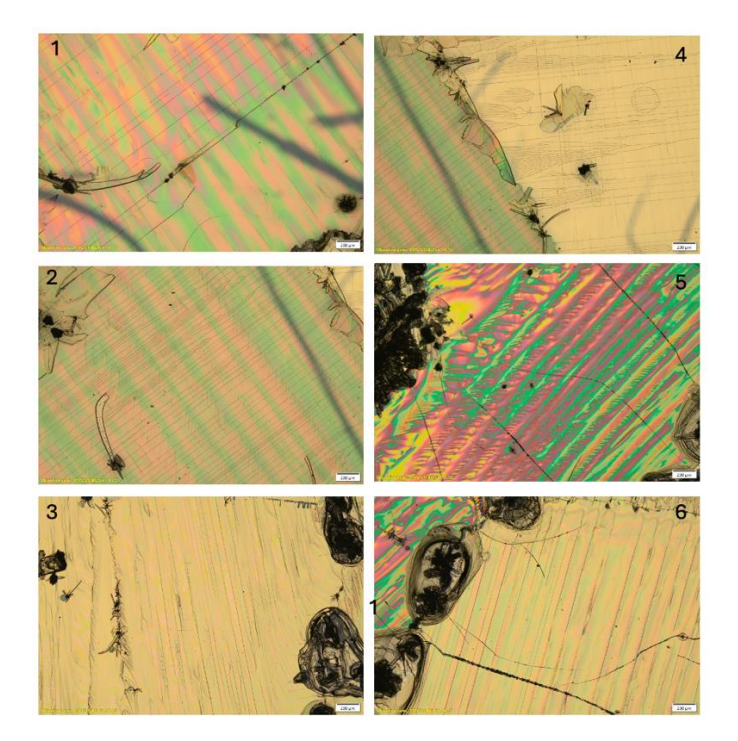


Figure 7.7: Optical images of the three different kinds of film striations formed by FRL 108 on gold substrate. Three distinct types of striations were observed: alternately colored bands (1,5), grey lines along these colored patterns(3,6) and dark black lines (5,7).

An intriguing observation in the films of both anthracene and FRL 108 was the formation of striations (see Figure 7.7 and 7.8). The regularity of these patterns was assessed using profilometry, revealing a consistent structure. These formations present a promising feature that could be harnessed in future grating design applications.

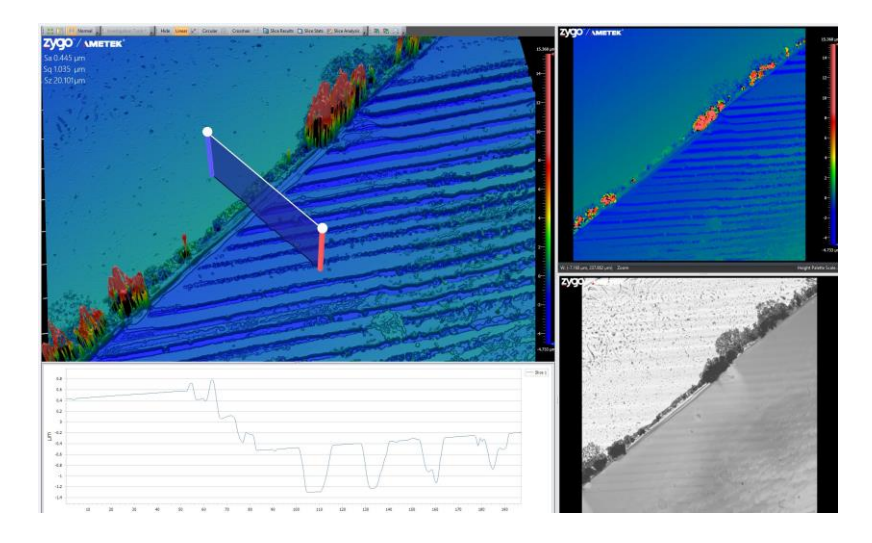


Figure 7.8: Profilometry measurement of thickness of the FRL 108 film on gold substrate. Striations on the surface can be detected by the profilometer.

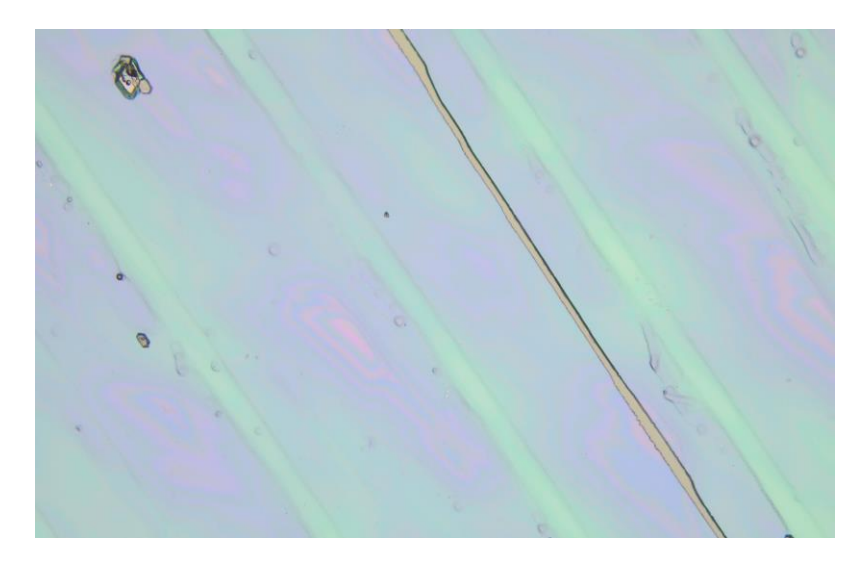


Figure 7.9: Optical microscopy image of striations of anthracene on glass substrate.

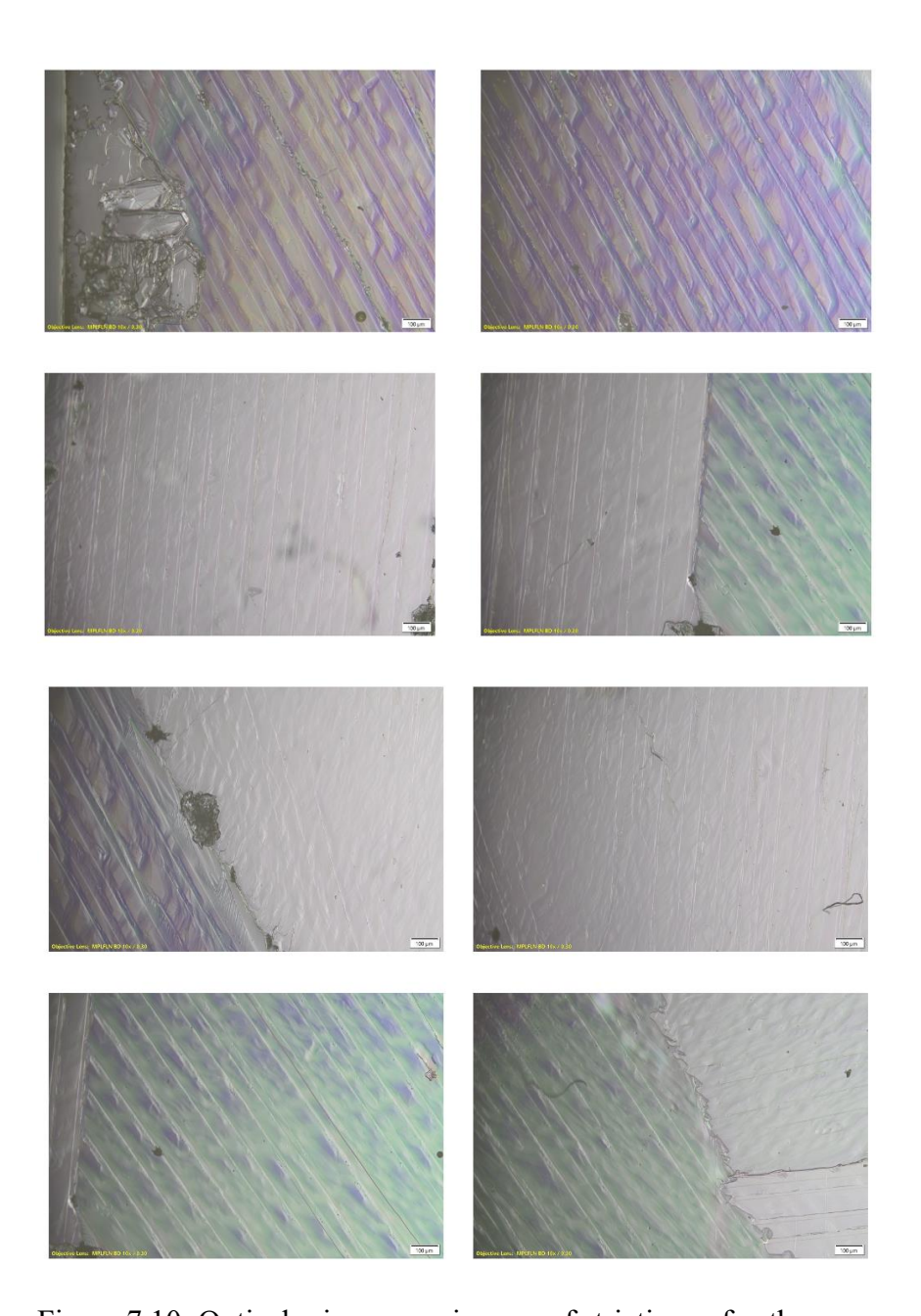


Figure 7.10: Optical microscopy images of striations of anthracene on glass substrate.

As shown in Figure 7,7, three distinct types of striations were observed: alternately colored bands, grey lines along these colored patterns, and dark black lines. Further investigation using AFM spectroscopy (Figure 7.11) revealed that these striations varied in height. Optical microscopy later indicated that the grey lines were stress lines aligned with the crystal orientation, marking the direction of solvent evaporation. The black lines were cracks extending

down to the substrate. The colored bands, however, represented step growth of the single crystals, illustrating the process by which the crystal formed. Together, AFM and optical microscopy provided key insights into the crystal formation process and underscored the potential for controlled single-crystal growth.

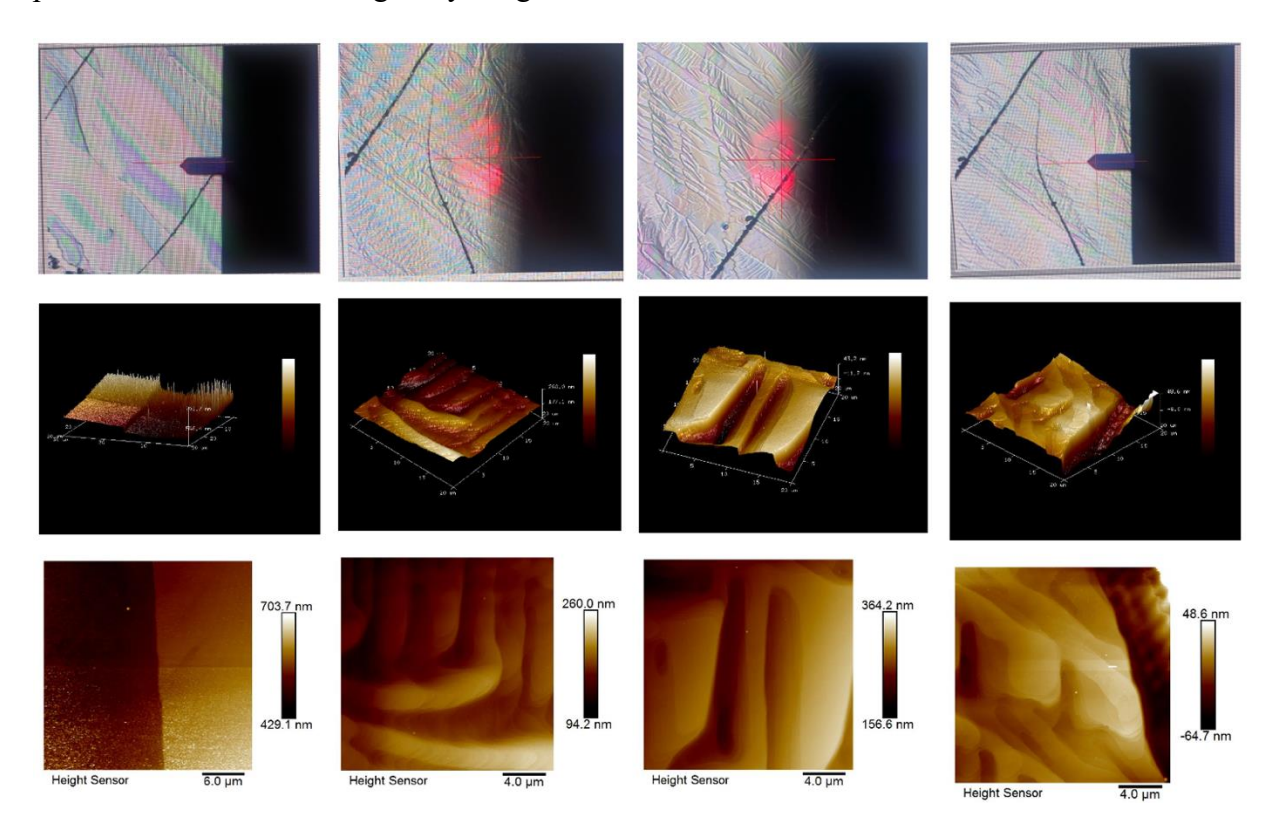


Figure 7.11: Atomic force microscopy (AFM) images of striations of FRL 108 on gold substrate. Images reveal the various heights of the striations indicating that the method of crystal formation being a 2D step growth type.

To further analyze the grey stress lines, the substrate was heated at various temperatures and for different time periods and it was found that the stress lines disappeared, meaning the crystals coalesced into one single crystal after heating it at 100°C for 5 days. Figure 7.12 shows the optical images of before and after heating.

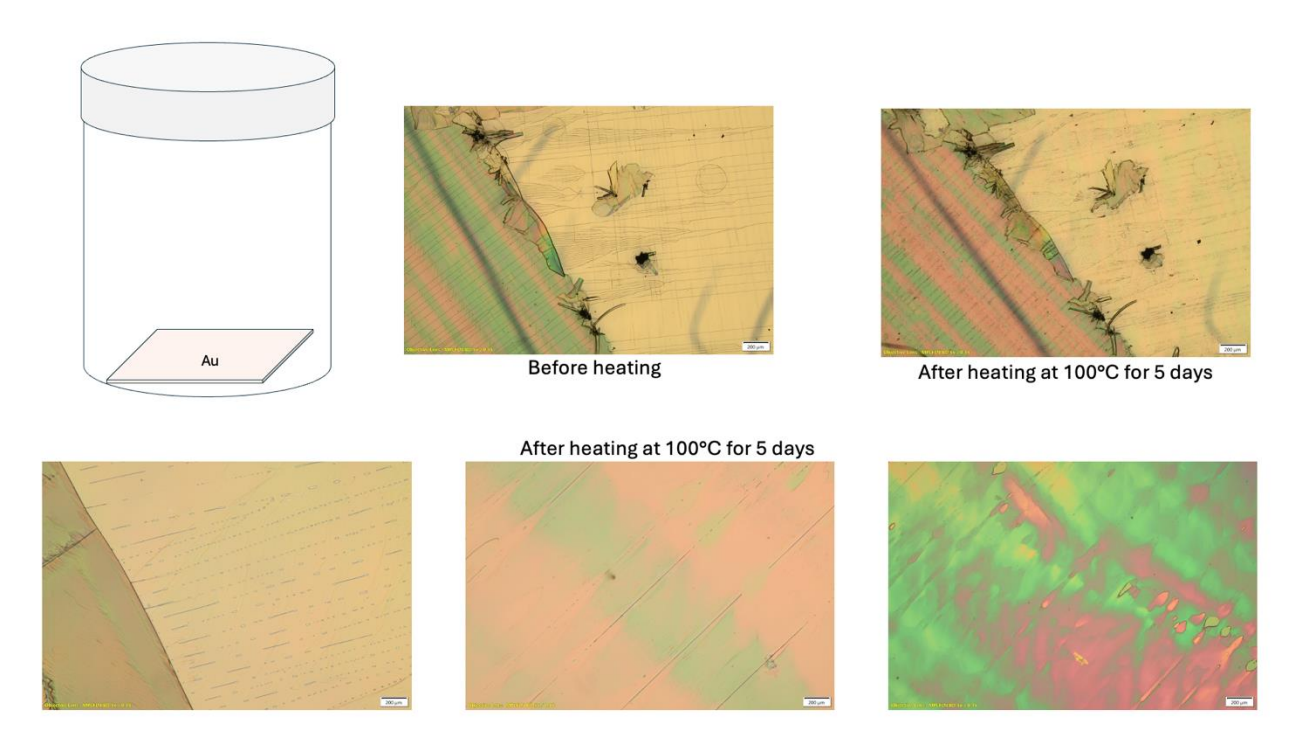


Figure 7.12: Optical microscopy images of FRL 108 film on gold substrate, before and after heating at 100°C for 5 days. Images indicate that the crystals coalesce to form one continuous single crystal.

The figure 7.12 also shows the experimental setup for crystal growth, where a sealed container holding the substrate and solution was placed on the Linkam stage. A significant drawback of this setup was that condensed solvent droplets would fall back onto the substrate, interrupting stable film growth. To address this issue, a modified setup was designed with a slanted piece of glass that allowed condensed particles to flow down the sides of the container, as illustrated in the figure 7.13. This improved design enabled the formation of larger single-crystal films and made the process reproducible.

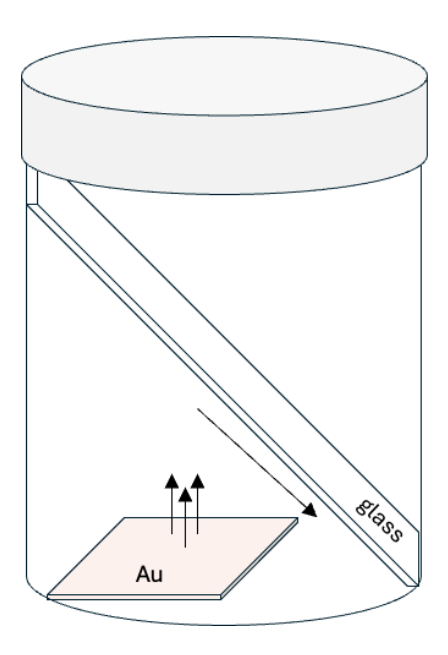


Figure 7.13: Experimental set up of crystal growth where a tilted glass is introduced to the container to prevent condensed solvent particles to directly drop back onto the substrate.



Figure 7.14: Optical microscopy image showing successful continuous single organic solid crystal film growth.

The best way to test the active properties of the materials was to fabricate a Schottky diode type device. This would act as an optical modulator which includes a layer of organic solid crystal situated between a pair of electrodes. In certain designs, a dielectric layer could also be placed between the OSC layer and one or more electrodes, serving to mediate the current or voltage applied to the OSC.

The structure and performance of an OSC-containing optical modulator was evaluated, featuring a layer of anthracene positioned between two indium tin oxide electrodes. This anthracene layer was developed into a single crystal for optimal charge injection. Measurements indicated a correlation between shifts in peak positions recorded by ellipsometry and the applied voltage, displaying a defined decay corresponding to the removal of the voltage. The observed peak shifts were linked to changes in refractive index and/or birefringence in the OSC layer.

7.5 Conclusion

This project demonstrates the successful development of single-crystal organic thin films with notable optical transparency and minimal bulk haze. The films achieved approximately 80% transmissivity within the visible spectrum for a given thickness. Here, "haze" refers to the scattering of light within the material, often due to secondary phases or internal porosity.

Several deposition methods were explored for forming organic solid crystals, including vaporphase and solution-based growth. These methods often involved inducing shear during coating, which aided in aligning the crystallites and molecules within the films. Epitaxial growth techniques further enabled the organic crystal layer to align with the crystalline structure of the deposition surface, improving the films' optical characteristics.

Throughout this study, the control of crystallite size, surface roughness, and molecular orientation within organic solid crystal thin films and fibers emerged as essential factors for optimizing their

performance in photonic applications. Active modulation of the refractive index, in particular, was highlighted as a crucial parameter for enhancing functionality in optical devices like waveguides, resonators, and other active optical components.

This research paves the way for integrating organic solid crystals into a broad spectrum of optical components and systems, broadening their applicability across fields such as telecommunications, sensors, and advanced photonics. By refining the control of crystal orientation and optical properties, these materials could significantly enhance device efficiency and open new possibilities for applications in optics and beyond.

7.6 Future Directions

To achieve more uniform films, molds can be employed to guide the growth process, providing controlled boundaries for film formation. Another promising approach to explore is vapor deposition, which could yield films with greater consistency and fine-tuned properties.

In manufacturing architectures for creating organic single-crystal thin films, seed crystals can play a critical role. By depositing a seed crystal precursor between mold surfaces or onto a substrate, it is possible to initiate and guide the growth of the thin film into the desired structure. However, using seed crystals introduces unique challenges—particularly the requirement for thin-film seed crystals with a specific molecular orientation, as the alignment significantly influences the optical and electronic properties of the final film.

Achieving the desired orientation and thickness in seed crystals necessitates a deeper molecular-level study of crystal growth dynamics. Understanding factors like intermolecular forces, lattice matching, and the influence of surface energy can inform the design of seed crystals that facilitate uniform and highly oriented thin-film growth. These insights could refine the use of molds and vapor deposition techniques, potentially leading to advanced processes for producing highly

uniform, orientation-controlled organic crystal films suitable for high-performance optical and electronic devices.

REFERENCES

- (1) Wang, Y.; Liu, T.; Liu, J.; Li, C.; Chen, Z.; Bo, S.; Wang, Y.; Liu, T.; Liu, J. Y.; Li, C. B.; Chen, Z.; Bo, S. H. Organic Electro-Optic Polymer Materials and Organic-Based Hybrid Electro-Optic Modulators. J. Semicond 2022 (10), 101301. https://doi.org/10.1088/1674-4926/43/10/101301.
- (2) Forrest, S. R. Charge Transport in Organic Semiconductors. Org Electron 2020, 171–292. https://doi.org/10.1093/OSO/9780198529729.003.0004.
- (3) Chen, Z.; Duan, S.; Zhang, X.; Hu, W. Growing Two-Dimensional Single Crystals of Organic Semiconductors on Liquid Surfaces. Appl Phys Lett 2021, 119 (21). https://doi.org/10.1063/5.0067274/40783.
- (4) Noguchi, Y.; Tanaka, Y.; Ishii, H.; Brütting, W. Understanding Spontaneous Orientation Polarization of Amorphous Organic Semiconducting Films and Its Application to Devices. Synth Met 2022, 288, 117101. https://doi.org/10.1016/J.SYNTHMET.2022.117101.
- (5) Cui, G.; Qi, J.; Liang, Z.; Zeng, F.; Zhang, X.; Xu, X.; Liu, K. Growth of Noncentrosymmetric Two-Dimensional Single Crystals. Precision Chemistry 2024, 2 (7), 330–354. https://doi.org/10.1021/PRECHEM.3C00122.
- (6) Zhang, L.; Mehedi Hasan, M.; Tang, Y.; Raza Khan, A.; Yan, H.; Yildirim, T.; Sun, X.; Zhang, J.; Zhu, J.; Zhang, Y.; Lu, Y. 2D Organic Single Crystals: Synthesis, Novel Physics, High-Performance Optoelectronic Devices and Integration. Materials Today 2021, 50, 442–475. https://doi.org/10.1016/J.MATTOD.2021.02.021.
- (7) Xiao, D.; Jin, Z.; Sheng, G.; Chen, L.; Xiao, X.; Shan, T.; Wang, J.; Navik, R.; Xu, J.; Zhou, L.; Guo, Q. H.; Li, G.; Zhu, Y.; Stoddart, J. F.; Huang, F. Single Crystals of Purely Organic Free-Standing Two-Dimensional Woven Polymer Networks. Nature Chemistry 2024 16:11 2024, 16 (11), 1906–1914. https://doi.org/10.1038/s41557-024-01580-3.
- (8) Sawatzki-Park, M.; Wang, S. J.; Kleemann, H.; Leo, K. Highly Ordered Small Molecule Organic Semiconductor Thin-Films Enabling Complex, High-Performance Multi-Junction Devices. Chem Rev 2023, 123 (13), 8232. https://doi.org/10.1021/ACS.CHEMREV.2C00844.
- (9) Coropceanu, V.; Cornil, J.; da Silva Filho, D. A.; Olivier, Y.; Silbey, R.; Brédas, J. L. Charge Transport in Organic Semiconductors. Chem Rev 2007, 107 (4), 926–952. https://doi.org/10.1021/CR050140X/ASSET/CR050140X.FP.PNG V03.
- (10) Silinsh, E. A.; Čápek, V. Organic Molecular Crystals: Interaction, Localization, and Transport Phenomena. 1994.
- (11) Podzorov, V. Organic Single Crystals: Addressing the Fundamentals of Organic Electronics. MRS Bull 2013, 38 (1), 15–24. https://doi.org/10.1557/MRS.2012.306.
- (12) Liu, X.; Luo, X.; Nan, H.; Guo, H.; Wang, P.; Zhang, L.; Zhou, M.; Yang, Z.; Shi, Y.; Hu, W.; Ni, Z.; Qiu, T.; Yu, Z.; Xu, J. Bin; Wang, X. Epitaxial Ultrathin Organic Crystals on Graphene for High-Efficiency Phototransistors. Advanced Materials 2016, 28 (26), 5200–5205. https://doi.org/10.1002/ADMA.201600400.

- (13) Wu, B.; Zhao, Y.; Nan, H.; Yang, Z.; Zhang, Y.; Zhao, H.; He, D.; Jiang, Z.; Liu, X.; Li, Y.; Shi, Y.; Ni, Z.; Wang, J.; Xu, J. Bin; Wang, X. Precise, Self-Limited Epitaxy of Ultrathin Organic Semiconductors and Heterojunctions Tailored by van Der Waals Interactions. Nano Lett 2016, 16 (6), 3754–3759. https://doi.org/10.1021/ACS.NANOLETT.6B01108.
- (14) Yadav, A.; Kumar, H.; Shrama, R.; Kumari, R. Synthesis, Processing, and Applications of 2D (Nano)Materials: A Sustainable Approach. Surfaces and Interfaces 2023, 39. https://doi.org/10.1016/j.surfin.2023.102925.
- (15) Fu, B.; Wang, C.; Sun, Y.; Yao, J.; Wang, Y.; Ge, F.; Yang, F.; Liu, Z.; Dang, Y.; Zhang, X.; Shao, X.; Li, R.; Hu, W. A "Phase Separation" Molecular Design Strategy Towards Large-Area 2D Molecular Crystals. Advanced Materials 2019, 31 (35). https://doi.org/10.1002/adma.201901437.
- (16) Zhang, Y.; Yang, S.; Wang, W.; Zhang, S.; Wang, Z.; Niu, Z.; Guo, Y.; Li, G.; Li, R.; Hu, W. Molecularly Thin 2D Organic Single Crystals: A New Platform for High-Performance Polarization-Sensitive Phototransistors. ACS Appl Mater Interfaces 2024. https://doi.org/10.1021/ACSAMI.3C17868.
- (17) Zhu, K.; Wen, C.; Aljarb, A. A.; Xue, F.; Xu, X.; Tung, V.; Zhang, X.; Alshareef, H. N.; Lanza, M. The Development of Integrated Circuits Based on Two-Dimensional Materials. Nat. Electron. 2021, 4 (11), 775–785. https://doi.org/10.1038/s41928-021-00672-z.
- (18) Zhang, X.; Dong, H.; Hu, W. Organic Semiconductor Single Crystals for Electronics and Photonics. Adv. Mater. 2018, 30 (44), e1801048. https://doi.org/10.1002/adma.201801048.
- (19) Zidan, M. A.; Strachan, J. P.; Lu, W. D. The Future of Electronics Based on Memristive Systems. Nat. Electron. 2018, 1 (1), 22–29. https://doi.org/10.1038/s41928-017-0006-8.
- (20) Qian, F.; Bu, X.; Wang, J.; Lv, Z.; Han, S. T.; Zhou, Y. Evolutionary 2D Organic Crystals for Optoelectronic Transistors and Neuromorphic Computing. Neuromorphic Computing and Engineering 2022, 2 (1), 012001. https://doi.org/10.1088/2634-4386/AC4A84.
- (21) Fan, Y.; Liu, J.; Hu, W.; Liu, Y.; Jiang, L. The Effect of Thickness on the Optoelectronic Properties of Organic Field-Effect Transistors: Towards Molecular Crystals at Monolayer Limit. J. Mater. Chem. C 2020, 8 (38), 13154–13168. https://doi.org/10.1039/d0tc03193c.
- Wang, H.; Wang, Q.; Li, Y. Two-Dimensional Organic Materials and Their Electronic Applications. Chem. Lett. 2019, 48 (1), 14–21. https://doi.org/10.1246/cl.180811.
- (23) Jiang, H.; Hu, W. The Emergence of Organic Single-crystal Electronics. Angew. Chem., Int. Ed. 2020, 59 (4), 1408–1428. https://doi.org/10.1002/anie.201814439.
- (24) Karl, N.; Farchioni, R.; Grosso, G. Organic Electronic Materials. 2001.
- (25) Pope, M.; Swenberg, C. E. Electronic Processes in Organic Crystals and Polymers. Electronic Processes in Organic Crystals and Polymers 1999. https://doi.org/10.1093/OSO/9780195129632.001.0001.
- (26) Heng, L.; Wang, X.; Tian, D.; Zhai, J.; Tang, B.; Jiang, L. Optical Waveguides Based on Single-Crystalline Organic Micro-Tiles. Advanced Materials 2010, 22 (42), 4716–4720. https://doi.org/10.1002/ADMA.201000444.

- (27) Zhang, C.; Yan, Y.; Jing, Y. Y.; Shi, Q.; Zhao, Y. S.; Yao, J. One-Dimensional Organic Photonic Heterostructures: Rational Construction and Spatial Engineering of Excitonic Emission. Advanced Materials 2012, 24 (13), 1703–1708. https://doi.org/10.1002/ADMA.201104326.
- (28) Ma, Y.; Zong, Y.; Yin, H.; Lin, H.; Chen, S.; Wang, X. D. 2D Optical Waveguides Based on Hierarchical Organic Semiconductor Single Crystals. Adv Opt Mater 2021, 9 (22), 2101481. https://doi.org/10.1002/ADOM.202101481.
- (29) Kalaji, M.; Peter, L. M. Optical and Electrical A.C. Response of Polyaniline Films. Journal of the Chemical Society, Faraday Transactions 1991, 87 (6), 853–860. https://doi.org/10.1039/FT9918700853.
- (30) Yang, Y.; Liang, B.; Kreie, J.; Hambsch, M.; Liang, Z.; Wang, C.; Huang, S.; Dong, X.; Gong, L.; Liang, C.; Lou, D.; Zhou, Z.; Lu, J.; Yang, Y.; Zhuang, X.; Qi, H.; Kaiser, U.; Mannsfeld, S. C. B.; Liu, W.; Gölzhäuser, A.; Zheng, Z. Elastic Films of Single-Crystal Two-Dimensional Covalent Organic Frameworks. Nature 2024, 630 (8018), 878–883. https://doi.org/10.1038/S41586-024-07505-X.
- (31) Hassan, J. Z.; Raza, A.; Din Babar, Z. U.; Qumar, U.; Kaner, N. T.; Cassinese, A. 2D Material-Based Sensing Devices: An Update. J Mater Chem A Mater 2023, 11 (12), 6016–6063. https://doi.org/10.1039/D2TA07653E.
- (32) Yan, X.; Zhao, Y.; Cao, G.; Li, X.; Gao, C.; Liu, L.; Ahmed, S.; Altaf, F.; Tan, H.; Ma, X.; Xie, Z.; Zhang, H. 2D Organic Materials: Status and Challenges. Advanced Science 2023, 10 (7). https://doi.org/10.1002/ADVS.202203889.
- (33) Lee, D. M.; Jung, J. H.; Lee, Y. J.; Yu, C. J.; Kim, J. H. Brightness Enhancement of 3D Display through Patterning Linearly Polarized OLED. Dig Tech Pap 2017, 48 (1), 2018–2020. https://doi.org/10.1002/SDTP.12062.
- (34) An, M.-H.; Ding, R.; Ding, R.; Zhang, X.-L.; Chen, S.-N.; Wang, Y.-N.; Ye, G.-D.; Zhu, Q.-C.; Chen, N.-K.; Liu, Y.; Feng, J.; Feng, J.; Sun, H.-B.; Sun, H.-B.; Sun, H.-B. Highly Polarized Emission from Organic Single-Crystal Light-Emitting Devices with a Polarization Ratio of 176. Optica, Vol. 9, Issue 1, pp. 121-129 2022, 9 (1), 121–129. https://doi.org/10.1364/OPTICA.442016.
- (35) Neupane, G. P.; Ma, W.; Yildirim, T.; Tang, Y.; Zhang, L.; Lu, Y. 2D Organic Semiconductors, the Future of Green Nanotechnology. Nano Materials Science 2019, 1 (4), 246–259. https://doi.org/10.1016/J.NANOMS.2019.10.002.
- (36) Li, Y.; Ji, D.; Liu, J.; Yao, Y.; Fu, X.; Zhu, W.; Xu, C.; Dong, H.; Li, J.; Hu, W. Quick Fabrication of Large-Area Organic Semiconductor Single Crystal Arrays with a Rapid Annealing Self-Solution-Shearing Method. Scientific Reports 2015 5:1 2015, 5 (1), 1–9. https://doi.org/10.1038/srep13195.
- (37) Xu, C.; He, P.; Liu, J.; Cui, A.; Dong, H.; Zhen, Y.; Chen, W.; Hu, W. A General Method for Growing Two-Dimensional Crystals of Organic Semiconductors by "Solution Epitaxy." Angew Chem Int Ed Engl 2016, 55 (33), 9519–9523. https://doi.org/10.1002/ANIE.201602781.

- (38) Qian, F.; Bu, X.; Wang, J.; Lv, Z.; Han, S. T.; Zhou, Y. Evolutionary 2D Organic Crystals for Optoelectronic Transistors and Neuromorphic Computing. Neuromorphic Computing and Engineering 2022, 2 (1), 012001. https://doi.org/10.1088/2634-4386/AC4A84.
- (39) Sun, L.; Li, Y.; Xie, J.; Liqi Zhou, |; Wang, P.; Xu, J.-B.; Shi, Y.; Wang, | Xinran; He, D. Modulating Contact Properties by Molecular Layers in Organic Thin-Film Transistors. Electron 2023, 1 (2), e7. https://doi.org/10.1002/ELT2.7.
- (40) Giri, G.; Miller, E.; Bao, Z. Selective Solution Shearing Deposition of High Performance TIPS-Pentacene Polymorphs through Chemical Patterning. J Mater Res 2014, 29 (22), 2615–2624. https://doi.org/10.1557/JMR.2014.305.
- (41) Salzillo, T.; D'Amico, F.; Montes, N.; Pfattner, R.; Mas-Torrent, M. Influence of Polymer Binder on the Performance of DiF-TES-ADT Based Organic Field Effect Transistor. CrystEngComm 2021, 23 (4), 1043–1051. https://doi.org/10.1039/D0CE01467B.
- (42) Enami, Y.; Seki, A.; Masuda, S.; Joichi, T.; Luo, J.; Jen, A. K. Y. Bandwidth Optimization for Mach-Zehnder Polymer/Sol-Gel Modulators. Journal of Lightwave Technology 2018, 36 (18), 4181–4189. https://doi.org/10.1109/JLT.2018.2860924.
- (43) Lebby, M. S. Naturally Fast and Low Power Electro-Optic Polymer Optical Devices Are Ideally Positioned for the next-Generation Internet Photonics Roadmap (Conference Presentation). 2020, 100. https://doi.org/10.1117/12.2571129.
- (44) Electro-Optic Polymers Improve Speed and Power Efficiency | Features | Aug 2020 | Photonics Spectra. https://www.photonics.com/Articles/Electro-Optic_Polymers_Improve_Speed_and_Power/a65902 (accessed 2024-10-30).
- (45) Hammond, S. R.; O'malley, K. M.; Xu, H.; Elder, D. L.; Johnson, L. E. Organic Electro-Optic Materials Combining Extraordinary Nonlinearity with Exceptional Stability to Enable Commercial Applications.
- (46) Ueda, Y.; Tanaka, M.; Nakanotani, H.; Adachi, C. A Polar Transition of Spontaneous Orientation Polarization in Organic Amorphous Thin Films. Chem Phys Lett 2023, 833, 140915. https://doi.org/10.1016/J.CPLETT.2023.140915.
- (47) Iwamoto, M.; Manaka, T. Interfacial Polarization Phenomena in Organic Molecular Films. Anal Chim Acta 2006, 568 (1–2), 65–69. https://doi.org/10.1016/J.ACA.2005.12.018.
- (48) Lukin, L. V. Electric Polarization of Electron-Hole Pairs in Organic Semiconductors Induced by Picosecond Pulses of an Electromagnetic Wave: Consideration of Small-Molecule Semiconductors with a Negligibly Small Concentration of Traps. Chem Phys 2019, 527, 110456. https://doi.org/10.1016/J.CHEMPHYS.2019.110456.
- (49) Soos, Z. G.; Tsiper, E. V.; Pascal, R. A. Charge Redistribution and Electronic Polarization in Organic Molecular Crystals. Chem Phys Lett 2001, 342 (5–6), 652–658. https://doi.org/10.1016/S0009-2614(01)00661-3.
- (50) Noguchi, Y.; Tanaka, Y.; Ishii, H.; Brütting, W. Understanding Spontaneous Orientation Polarization of Amorphous Organic Semiconducting Films and Its Application to Devices. Synth Met 2022, 288, 117101. https://doi.org/10.1016/J.SYNTHMET.2022.117101.

- (51) Noguchi, Y.; Miyazaki, Y.; Tanaka, Y.; Sato, N.; Nakayama, Y.; Schmidt, T. D.; Brütting, W.; Ishii, H. Charge Accumulation at Organic Semiconductor Interfaces Due to a Permanent Dipole Moment and Its Orientational Order in Bilayer Devices. J Appl Phys 2012, 111 (11), 114508. https://doi.org/10.1063/1.4724349/898337.
- (52) Ela, A. H. A. El; Afifi, H. H. Hopping Transport in Organic Semiconductor System. Journal of Physics and Chemistry of Solids 1979, 40 (4), 257–259. https://doi.org/10.1016/0022-3697(79)90100-8.
- (53) Bai, Y.; Sun, T.; Angenent, L. T.; Haderlein, S. B.; Kappler, A. Electron Hopping Enables Rapid Electron Transfer between Quinone-/Hydroquinone-Containing Organic Molecules in Microbial Iron(III) Mineral Reduction. Environ Sci Technol 2020, 54 (17), 10646– 10653. https://doi.org/10.1021/ACS.EST.0C02521/ASSET/IMAGES/MEDIUM/ES0C02521_M0 12.GIF.
- (54) Michaeli, K.; Beratan, D. N.; Waldeck, D. H.; Naaman, R. Voltage-Induced Long-Range Coherent Electron Transfer through Organic Molecules. Proc Natl Acad Sci U S A 2019, 116 (13), 5931–5936. https://doi.org/10.1073/PNAS.1816956116/SUPPL_FILE/PNAS.1816956116.SAPP.PDF.
- (55) Kou, B.; Yuan, Y.; Zhu, X.; Ke, Y.; Wang, H.; Yu, T.; Tan, W. Effect of Soil Organic Matter-Mediated Electron Transfer on Heavy Metal Remediation: Current Status and Perspectives. Science of The Total Environment 2024, 917, 170451. https://doi.org/10.1016/J.SCITOTENV.2024.170451.
- (56) Castner, A. T.; Su, H.; Svensson Grape, E.; Inge, A. K.; Johnson, B. A.; Ahlquist, M. S. G.; Ott, S. Microscopic Insights into Cation-Coupled Electron Hopping Transport in a Metal-Organic Framework. J Am Chem Soc 2022, 144 (13), 5910–5920. https://doi.org/10.1021/JACS.1C13377/ASSET/IMAGES/LARGE/JA1C13377_0009.JPE G.
- (57) Chemcomm, J. :; Lin, S.; Usov, P. M.; Morris, A. J. The Role of Redox Hopping in Metal-Organic Framework Electrocatalysis. J. Name 2013, 00, 1–3. https://doi.org/10.1039/x0xx00000x.
- (58) Nakada, I. The Optical Properties of Anthracene Single Crystals. https://doi.org/10.1143/JPSJ.17.113 2013, 17 (1), 113–118. https://doi.org/10.1143/JPSJ.17.113.

APPENDIX

This research was conducted at Meta Reality Labs, Redmond, WA, under the guidance of Dr. Lafe Purvis as part of an optional internship program from May 2024 to October 2024. It is conducted with a strong emphasis on innovation, precision, and confidentiality. The team works on cuttingedge advancements in materials science and device fabrication, integrating state-of-the-art techniques to push technological boundaries. Due to the highly sensitive and proprietary nature of the work, all research details, methodologies, and findings remain strictly confidential. Employees and collaborators operate under rigorous non-disclosure agreements (NDAs) to ensure intellectual property protection and maintain Meta's competitive edge. As such, specific information about the research, including experimental data, materials used, and project objectives, cannot be disclosed.